Evolutions microstructurales au cours du laminage à chaud d'aciers bas carbone microalliés

Alexis Graux

N° d'ordre NNT : 2019LYSEI120

THESE de DOCTORAT DE L'UNIVERSITE DE LYON
opérée au sein de
L'Institut National des Sciences Appliquées de Lyon

Ecole Doctorale N° EDA 034
Matériaux de Lyon

Spécialité de doctorat : Matériaux

Soutenue publiquement le 13/12/2019, par :
Alexis Graux

Evolutions microstructurales au cours du laminage à chaud d'aciers bas carbone microalliés

***

Microstructure evolutions during hot rolling of low carbon microalloyed steels

---

Devant le jury composé de :

Yves BRECHET	Professeur, Monash Univesity	Président
Francisca CABALLERO	Research Professor, CENIM-CSIC	Rapporteure
Sébastien ALLAIN	Professeur, Institut Jean Lamour	Rapporteur
Sophie CAZOTTES	Maitre de conférences, MATEIS	Examinatrice (encadrante)
Michel PEREZ	Professeur, MATEIS	Directeur de thèse
Damien FABREGUE	Professeur, MATEIS	Directeur de thèse
Carlos CAPDEVILA	Senior Scientist, CENIM-CSIC	Invité
Frédéric DANOIX	Chargé de recherches, GPM	Invité

Département FEDORA – INSA Lyon - Ecoles Doctorales – Quinquennal 2016-2020

SIGLE	ECOLE DOCTORALE	NOM ET COORDONNEES DU RESPONSABLE
CHIMIE	**CHIMIE DE LYON** **http://www.edchimie-lyon.fr** Sec : Renée EL MELHEM Bat Blaise Pascal 3e etage secretariat@edchimie-lyon.fr Insa : R. GOURDON	M. Stéphane DANIELE Institut de Recherches sur la Catalyse et l'Environnement de Lyon IRCELYON-UMR 5256 Équipe CDFA 2 avenue Albert Einstein 69626 Villeurbanne cedex directeur@edchimie-lyon.fr
E.E.A.	**ELECTRONIQUE, ELECTROTECHNIQUE, AUTOMATIQUE** **http://edeea.ec-lyon.fr** Sec : M.C. HAVGOUDOUKIAN Ecole-Doctorale.eea@ec-lyon.fr	M. Gérard SCORLETTI Ecole Centrale de Lyon 36 avenue Guy de Collongue 69134 ECULLY Tél : 04.72.18 60.97 Fax : 04 78 43 37 17 Gerard.scorletti@ec-lyon.fr
E2M2	**EVOLUTION, ECOSYSTEME, MICROBIOLOGIE, MODELISATION** **http://e2m2.universite-lyon.fr** Sec : Sylvie ROBERJOT Bât Atrium - UCB Lyon 1 04.72.44.83.62 Insa : H. CHARLES secretariat.e2m2@univ-lyon1.fr	M. Fabrice CORDEY CNRS UMR 5276 Lab. de géologie de Lyon Université Claude Bernard Lyon 1 Bât Géode 2 rue Raphaël Dubois 69622 VILLEURBANNE Cédex Tél : 06.07.53.89.13 cordey@univ-lyon1.fr
EDISS	**INTERDISCIPLINAIRE SCIENCES-SANTE** **http://www.ediss-lyon.fr** Sec : Sylvie ROBERJOT Bât Atrium - UCB Lyon 1 04.72.44.83.62 Insa : M. LAGARDE secretariat.ediss@univ-lyon1.fr	Mme Emmanuelle CANET-SOULAS INSERM U1060, CarMeN lab, Univ. Lyon 1 Bâtiment IMBL 11 avenue Jean Capelle INSA de Lyon 696621 Villeurbanne Tél : 04.72.68.49.09 Fax :04 72 68 49 16 Emmanuelle.canet@univ-lyon1.fr
INFOMATHS	**INFORMATIQUE ET MATHEMATIQUES** **http://infomaths.univ-lyon1.fr** Sec :Renée EL MELHEM Bat Blaise Pascal, 3e étage Tél : 04.72. 43. 80. 46 Fax : 04.72.43.16.87 infomaths@univ-lyon1.fr	M. Luca ZAMBONI Bâtiment Braconnier 43 Boulevard du 11 novembre 1918 69622 VILLEURBANNE Cedex Tél :04 26 23 45 52 zamboni@maths.univ-lyon1.fr
Matériaux	**MATERIAUX DE LYON** **http://ed34.universite-lyon.fr** Sec : Marion COMBE Tél:04-72-43-71-70 –Fax : 87.12 Bat. Direction ed.materiaux@insa-lyon.fr	M. Jean-Yves BUFFIERE INSA de Lyon MATEIS Bâtiment Saint Exupéry 7 avenue Jean Capelle 69621 VILLEURBANNE Cedex Tél : 04.72.43 71.70 Fax 04 72 43 85 28 Ed.materiaux@insa-lyon.fr
MEGA	**MECANIQUE, ENERGETIQUE, GENIE CIVIL, ACOUSTIQUE** **http://mega.universite-lyon.fr** Sec : Marion COMBE Tél:04-72-43-71-70 –Fax : 87.12 Bat. Direction mega@insa-lyon.fr	M. Philippe BOISSE INSA de Lyon Laboratoire LAMCOS Bâtiment Jacquard 25 bis avenue Jean Capelle 69621 VILLEURBANNE Cedex Tél : 04.72 .43.71.70 Fax : 04 72 43 72 37 Philippe.boisse@insa-lyon.fr
ScSo	**ScSo*** **http://recherche.univ-lyon2.fr/scso/** Sec : Viviane POLSINELLI Brigitte DUBOIS Insa : J.Y. TOUSSAINT Tél : 04 78 69 72 76 viviane.polsinelli@univ-lyon2.fr	M. Christian MONTES Université Lyon 2 86 rue Pasteur 69365 LYON Cedex 07 Christian.montes@univ-lyon2.fr

*ScSo : Histoire, Géographie, Aménagement, Urbanisme, Archéologie, Science politique, Sociologie, Anthropologie

Contents

List of Abbreviations

AHSS	Advanced High Strength Steels
APT	Atom Probe Tomography
BSE	BackScattered Electrons
CCT	Continuous Cooling Transformation
CP	Complex Phase
DCCT	Deformed Continuous Cooling Transformation
DP	Dual Phase
EDX	Energy Dispersive X-Ray spectroscopy
FCC	Face-Centered Cubic
FEG	Field Emission Gun
HAADF	High Angle Annular Dark Field
HE	Hole Expansion
HER	Hole Expansion Ratio
HSLA	High Strength Low Alloy
ICP-MS	Inductively Coupled Plasma Mass Spectrometry
JMAK	Johnson-Mehl-Avrami-Kolgomorov
KAM	Kernel Average Misorientation
MA	Martensite/Austenite
ND	Normal Direction
PAG	Prior Austenite Grain(s)
PAGB	Prior Austenite Grain Boundaries
PAGS	Prior Austenite Grain Sizes
RD	Rolling Direction
RTT	Recrystallization-Time-Temperature
RPTT	Recrystallization-Precipitation-Time-Temperature
SAED	Selected Area Electron Diffraction
SEM	Scanning Electron Microscope/Microscopy
STEM	Scanning Transmission Electron Microscopy
TAP	Tomographic Atom probe
TEM	Transmission Electron Microscope/Microscopy
UTS	Ultimate Tensile Strength
YS	Yield Strength

Résumé en français

Cette partie est un résumé étendu en français, donnant le contexte et les objectifs des travaux, les principaux résultats et conclusions de chaque chapitre, ainsi que les principales perspectives. Pour accéder à l'intégralité des travaux, le lecteur est prié de se référer au reste du manuscrit, rédigé en anglais.

Contexte industriel et scientifique

Les constructeurs automobiles font face à une pression croissante de la part des instances européennes concernant la réduction des émissions de gaz à effet de serre. Pour répondre aux demandes de l'industrie automobile, les aciéristes développent des aciers à plus haute résistance. L'emploi d'aciers à haute résistance permet de réduire la masse globale des véhicules sans compromettre la sécurité, et ainsi de contribuer à réduire la consommation des véhicules. De nombreuses pièces automobiles sont fabriquées par des procédés d'emboutissage ou de formage à froid à partir de tôles. L'acier doit donc également présenter une bonne formabilité. Cependant, de manière générale, la formabilité des aciers décroit lorsque leur résistance augmente. Réussir à augmenter la résistance sans compromettre la formabilité est donc un défi.

Les constructeurs automobiles et les aciéristes s'intéressent notamment à une propriété particulière de formabilité: **l'aptitude à l'étirement des bordures**[1], évaluée lors d'essais d'expansion de trou[2]. L'aptitude à l'étirement des borduress est donnée par le **degré d'expansion de trou**, exprimé en pourcentage, qu'il est possible d'atteindre sans que l'acier ne se fissure. Cette propriété est très sensible à la microstructure des aciers, et notamment à la présence de grands écarts de dureté entre les différentes phases de l'acier. Cela pousse au développement d'aciers présentant des microstructures homogènes, et à la réduction des hétérogénéités de dureté dans les aciers présentant différentes phases.

Ce travail de doctorat s'inscrit dans le cadre du projet de recherche européen NANOFORM (voir Annex A), financé par le Research Fund for Coal and Steel et incluant partenaires académiques et industriels. Le projet NANOFORM a pour but de développer des aciers dits à phases complexes, microalliés et bas carbone, dont la microstructure est principalement bainitique. Un bon compromis entre résistance et aptitude à l'étirement des bordures est attendu, avec une résistance maximale en traction d'au minimum 800 MPa et un degré d'expansion de trou minimum de 70 %. Le projet

[1] En anglais: stretch flangeability.
[2] En anglais: hole expansion ratio.

NANOFORM est un projet complet de design de nouvelles nuances d'aciers, depuis l'échelle du laboratoire jusqu'à l'échelle industrielle. Un essai sur la ligne de production industrielle de l'un des partenaires du projet est en effet planifié à la fin du projet, dans le but d'établir la faisabilité industrielle des aciers conçus.

Dans le projet NANOFORM, les plaques d'aciers sont destinées à être produites par **laminage à chaud** à partir de brames. Le procédé commence par le **réchauffage** des brames, durant lequel ces dernières sont insérées dans un four qui les porte à haute température dans le domaine de stabilité de l'austénite. Ensuite vient le **laminage** à chaud, qui vise à réduire l'épaisseur des brames en leur faisant subir différentes passes de déformation lors de leur passage dans des cages de laminoir. Le laminage s'effectue généralement en deux étapes distinctes: le dégrossissage et la finition. A la fin du laminage, la tôle atteint son épaisseur finale et subit un **refroidissement accéléré** jusqu'à une température cible sur une table de sortie. La tôle est enfin enroulée pour former une bobine, lors de la dernière étape: le **bobinage**. Les différentes étapes du laminage à chaud sont schématisées sur la Figure 1.

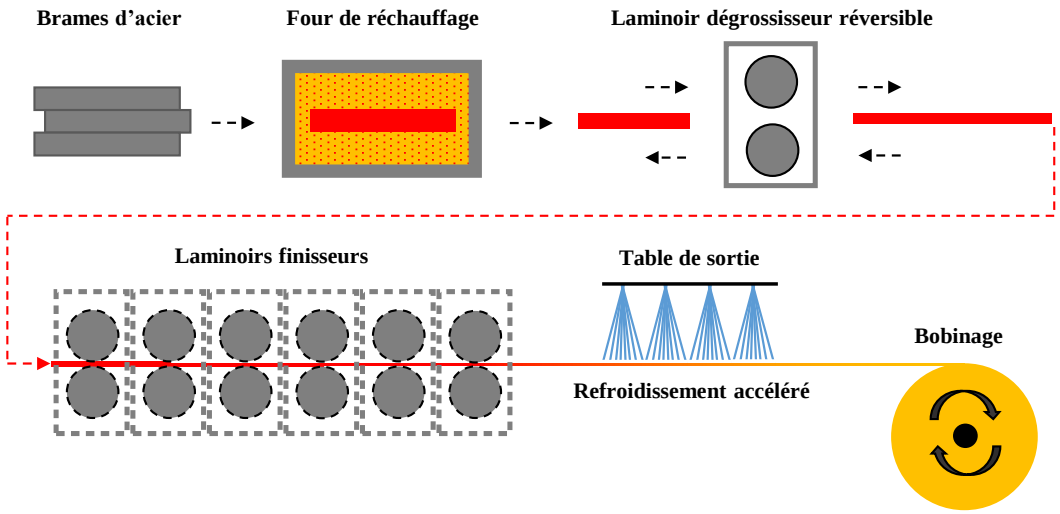

Figure 1: Représentation schématique des principales étapes du procédé de laminage à chaud.

La composition des aciers ainsi que les paramètres de laminage à chaud déterminent les microstructures et les propriétés mécaniques finales. Le projet NANOFORM avait pour objectif d'optimiser la composition et le procédé pour obtenir des microstructures homogènes, principalement constituées de bainite, et atteindre les objectifs quant aux propriétés mécaniques. Ainsi, un total de 11 nuances ont été étudiées dans le cadre du projet. Les évolutions microstructurales à chaque étape du procédé de laminage à chaud ont été examinées, en incluant de façon non-exhaustive:

(i) Des calculs d'équilibre thermodynamique.

(ii) L'évolution des tailles de grains austénitiques et de la précipitation lors du réchauffage des brames.

(iii) Les évolutions ayant lieu durant ou après la déformation à chaud de l'austénite: restauration, recristallisation et précipitation induite par la déformation.

(iv) Les transformations de phase.

(v) La production par laminage à chaud des aciers sur une usine pilote (à l'échelle du laboratoire) et sur une réelle ligne industrielle.

(vi) Une caractérisation détaillée des microstructures et propriétés mécaniques résultantes.

Objectifs et organisation du manuscrit

Ce travail de doctorat a pour but de décrire et de comprendre les évolutions microstructurales ayant lieu au cours des différentes étapes du laminage à chaud. Le manuscrit contient trois chapitres indépendants et pouvant être lus séparément. Bien que 11 nuances aient été étudiées au cours du projet, les travaux présentés ici portent principalement sur l'une de ces nuances, dénommée 0.04Nb-0.09Ti. Dans le second chapitre, deux alliages additionnels ont été également étudiés. Les compositions des nuances sont données dans le Tableau 1. Le laminage à chaud constitue le fil conducteur du manuscrit, comme l'illustre la Figure 2:

(i) Le chapitre 1 se concentre sur l'étape de réchauffage des brames. L'évolution des tailles de grains austénitiques et de l'état de précipitation au cours de traitements thermiques isothermes sont caractérisés expérimentalement. Un modèle de précipitation a été développé et couplé à un modèle simple de croissance de grains basé sur la théorie de l'épinglage Zener.

(ii) Le chapitre 2 est lié à l'étape de laminage à chaud. Dans ce chapitre, les cinétiques de recristallisation et de précipitation ont été déterminés expérimentalement par des essais de relaxation de contrainte et des observations expérimentales directes. Ce chapitre comprend également des travaux de modélisation portant sur la recristallisation et la précipitation.

(iii) Le chapitre 3 se concentre sur la description des relations entre les paramètres de laminage à chaud, la microstructure et les propriétés mécaniques obtenues. Six procédés de fabrication différents ont été appliqués sur un laminoir de laboratoire pour simuler le laminage à chaud. Les microstructures et les propriétés mécaniques des plaques laminées à chaud y sont caractérisées.

Elément	**C**	**Mn**	**Si**	**Ti**	**Nb**	**V**	**Mo**	**Al**	**Cr**	**N**
0.04Nb-0.09Ti	0.062	1.91	0.50	**0.085**	**0.039**	**0.002**	0.212	0.065	0.013	0.006
0.04Nb-0.09Ti-0.1V	0.087	1.94	0.50	**0.093**	**0.039**	**0.105**	0.209	0.067	0.014	0.006
0.04Nb-0.05Ti-0.2V	0.085	1.95	0.50	**0.046**	**0.039**	**0.206**	0.209	0.070	0.014	0.006

Tableau 1: Compositions des trois aciers microalliés étudiés (pourcentage massique).

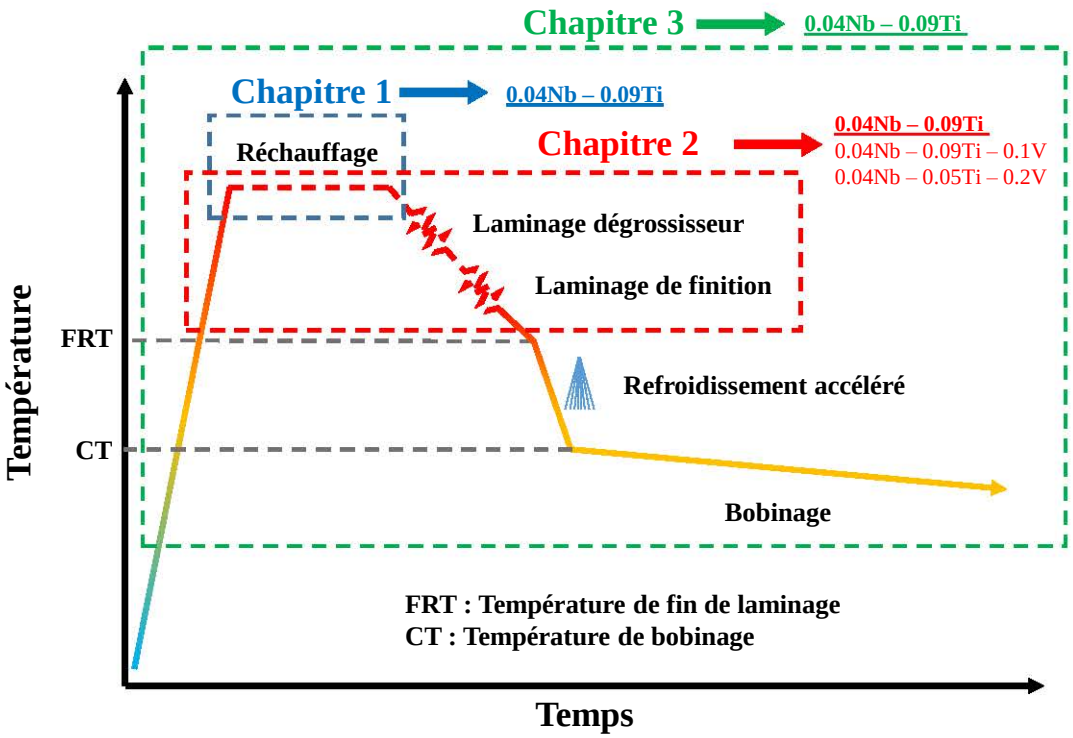

Figure 2: Organisation du manuscrit par rapport au procédé de laminage à chaud.

Chapitre 1: Évolution de l'état de précipitation et croissance des grains austénitiques lors du réchauffage

La température de réchauffage des brames détermine la taille des grains austénitiques et la quantité de précipités remis en solution à la fin du réchauffage. Ainsi, celle-ci doit être sélectionnée avec soin car elle influencera les évolutions microstructurales subséquentes, telles que les cinétiques de recristallisation de l'austénite lors de la déformation à chaud, ou la quantité de précipités formés lors du refroidissement et du bobinage. Dans ce premier chapitre, les évolutions de l'état de précipitation et de la taille des grains austénitiques au cours du réchauffage des brames ont été étudiées pour la nuance 0.04Nb-0.09Ti, en associant caractérisations expérimentales et travaux de modélisation.

Partant d'un état de réception complètement précipité, des traitements thermiques isothermes ont été effectués entre 950 et 1250 °C. Les états de précipitation ont été caractérisés de façon approfondie par microscopie électronique en balayage et en transmission. Quatre populations différentes de précipités ont été identifiées. Parmi ces populations, seule la population de (Ti,Nb)C présentait une fraction volumique suffisamment importante et des tailles de précipités suffisamment fines pour contrôler significativement la croissance des grains austénitiques. L'étude s'est donc focalisée sur ces (Ti,Nb)C. Parallèlement, les grains austénitiques ont été révélés par attaque thermique et leurs tailles ont été mesurées pour ces différentes températures de réchauffage.

Une approche originale a été suivie pour estimer la fraction volumique des (Ti,Nb)C en utilisant la sonde atomique tomographique (SAT). Les mesures de SAT ont permis d'estimer la quantité

totale de Ti et de Nb disponible pour former les (Ti,Nb)C ainsi que de mesurer la quantité de Ti et de Nb en solution solide dans l'austénite à différentes températures. La fraction volumique de (Ti,Nb)C a donc été estimée indirectement par un bilan de masse se basant sur la composition de la matrice austénitique. De telles mesures sont possibles grâce aux évolutions considérables qu'a connu la sonde atomique tomographique ces 20 dernières années: il est aujourd'hui possible d'analyser plusieurs dizaines de millions d'ions par expérience.

En se basant sur les résultats expérimentaux générés (types de précipités, tailles, fraction volumiques) un modèle de précipitation multi-classe a été implémenté et utilisé pour modéliser l'évolution de la distribution de taille des (Ti,Nb)C au cours des traitements thermiques. La distribution initiale de (Ti,Nb)C considérée par le modèle est basée sur les distributions expérimentales mesurées par MEB/MET. La composition et le domaine de stabilité des (Ti,Nb)C ont été calculés à partir de la base de données TCFE8 de Thermo-Calc. Les distributions de tailles de précipités issues du modèle de précipitation servent de données d'entrée à un modèle simple de croissance de grains basé sur la théorie de l'épinglage des joints de grains. La vitesse de croissance des grains austénitiques y est calculée par:

$$\frac{dD}{dt} = \begin{cases} M_0 \exp\left(\frac{-Q_{GG}}{R_g T}\right)(P_D - P_P) & \text{si} \quad P_D - P_P > 0 \\ 0 & \text{si} \quad P_D - P_P < 0 \end{cases} \tag{1}$$

où $M_0 \exp\left(\frac{-Q_{GG}}{R_g T}\right)$ est la mobilité des joints de grains (thermiquement activée), P_D est la pression motrice pour la croissance de grains, et P_P est la pression d'épinglage exercée par les précipités sur les joints de grains. Deux expressions différentes de P_P, données par les théories de Zener [SMI 48, HUA 16b] et de Rios [RIO 87], ont été comparées. Ces deux théories considèrent des interactions entre joints de grains et précipités de natures différentes: la théorie de Zener considère que le joint de grains passe au travers du précipité (*pass-through mechanism*), tandis que Rios base sa théorie sur un franchissement par contournement (*enveloping mechanism*).

Les modèles de précipitation et de croissance des grains ne contenaient aucun paramètre ajustable, sauf le facteur pré-exponentiel du terme de mobilité des joints de grains M_0. Tous les autres paramètres de modélisation ont été extraits de bases de données thermodynamiques ou de la littérature.

Les travaux expérimentaux et de modélisation réalisés dans ce chapitre sont résumés graphiquement dans la Figure 3.

Le modèle de croissance de grains prend en compte la distribution de tailles complète des précipités pour le calcul de la pression d'épinglage, plutôt que de considérer des valeurs moyennes (f_v et $\langle r \rangle$). Cette prise en compte influence significativement les pressions d'épinglage calculées: l'utilisation de valeurs moyennes mène à une surestimation de l'épinglage de précipités. La Figure 4 compare les prédictions du modèle avec les tailles de grains austénitiques mesurées expérimentalement. Les prédictions du modèle sont en accord avec les données expérimentales. Les mesures se trouvent entre les prédictions considérant les théories de Zener et de Rios.

Suite à cette étude, une température de réchauffage des brames de 1250 °C a été sélectionnée pour le procédé, et a donc été appliquée dans les deux chapitres suivants. Une telle température de réchauffage mène à la remise en solution des précipités contrôlant la taille de grains. Des tailles

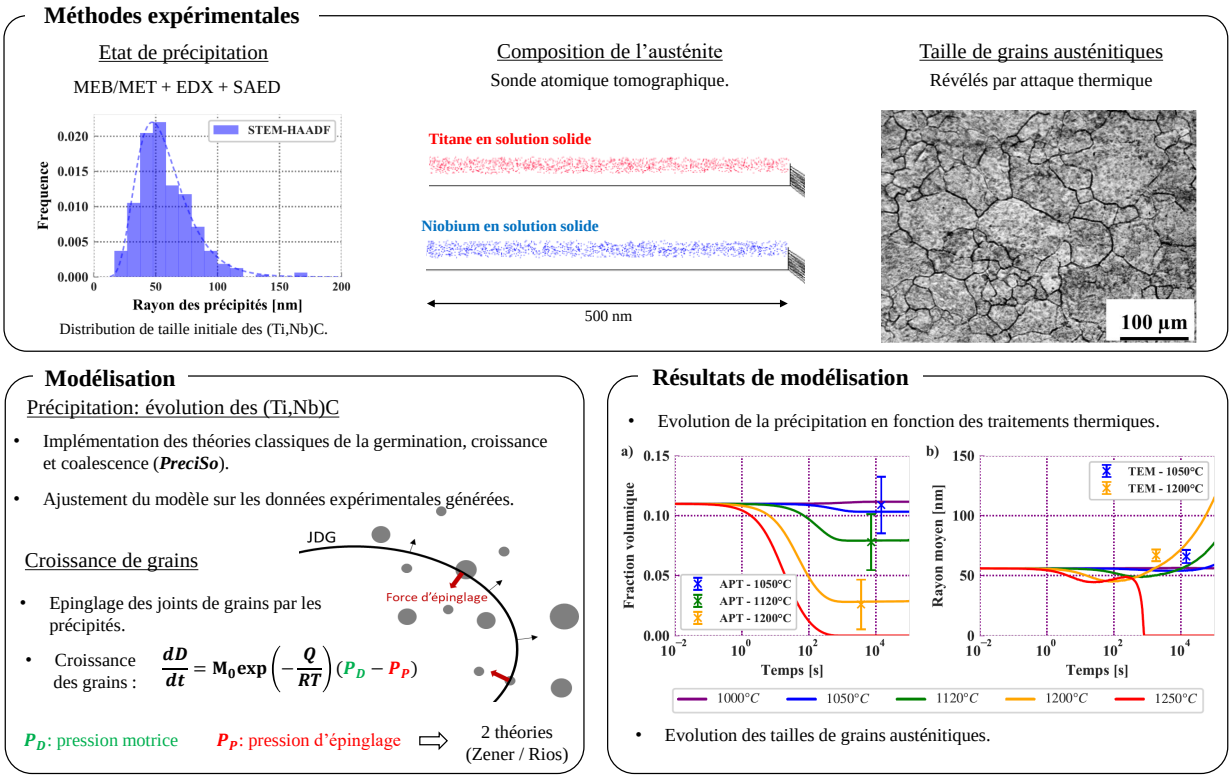

Figure 3: Résumé graphique des travaux expérimentaux réalisés dans le chapitre 1.

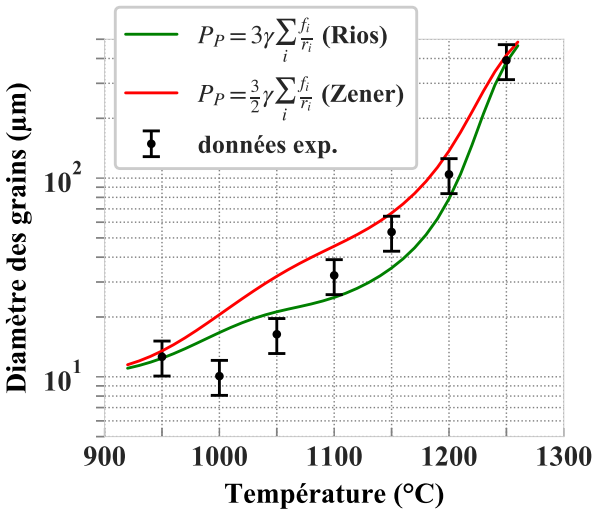

Figure 4: Tailles des grains austénitiques prédites par le modèle et mesurées expérimentalement pour des traitements thermiques isothermes de 10 min.

de grains austénitiques conséquentes sont donc obtenues à la fin du réchauffage (Figure 4). Elles pourront cependant être affinées par recristallisation lors du laminage à chaud (prochaine étape du

procédé).

Chapitre 2: Cinétiques de recristallisation et de précipitation après déformation à chaud de l'austénite

Au cours du laminage à chaud, les brames subissent une succession de passes de déformation dans le domaine austénitique. La déformation appliquée à chaque passe augmente la densité de dislocations dans l'austénite, ce qui permet ensuite à plusieurs évolutions microstructurales de se produire: restauration, recristallisation, et précipitation induite par la déformation. Dans ce second chapitre ces phénomènes ont été étudiés dans trois aciers microalliés présentant des additions de Ti, Nb et V (voir Tableau 1).

Après une étape de réchauffage à 1250 °C, les évolutions microstructurales susmentionnées ont été suivie par des essais de relaxation de contrainte réalisés entre 900 et 1100 °C, en faisant varier les déformations et vitesses de déformation appliquées. Les essais de relaxation de contrainte permettent de suivre les évolutions microstructurales de façon indirecte, via l'évolution de la contrainte en fonction du temps. Ils ont donc été complétés par des observations microstructurales directes de la précipitation et des tailles de grains austénitiques.

Les cinétiques de recristallisation et de précipitation ont été établies pour les trois aciers étudiés, permettant ainsi la construction des diagrammes de Recristallisation - Précipitation - Temps - Température. Pour des faibles niveaux de déformation ($\varepsilon = 0.1$), la force motrice pour la recristallisation est trop faible et seules la restauration et la précipitation sont observées. Pour une déformation plus élevée ($\varepsilon = 0.3$), la recristallisation est observée pour des températures supérieures ou égales à 1000 °C, tandis seules la restauration et la précipitation sont observées à 950 °C.

A haute température, les éléments de microalliage (Ti, Nb et V) interagissent avec la recristallisation par la formation de précipités (pression d'épinglage) et l'effet de trainée de solutés. A haute température, les cinétiques de recristallisation sont contrôlées par l'effet de trainée de solutés. En particulier, l'ajout de vanadium retarde significativement les cinétiques de recristallisation. A plus basse température, la recristallisation intervient pour des temps assez courts (t <100 s), avant que la recristallisation n'ait pû avoir lieu. La formation de ces précipités retarde ensuite la recristallisation par l'exertion d'une pression d'épinglage des joints de grains, de telle sorte que la recristallisation n'est pas observée pour les temps de traitements thermiques réalisés. Les cinétiques de recristallisation sont accélérées lorsque la vitesse de recristallisation augmente de 0.1 à 5 s^{-1}. Cela est dû à la plus grande densité de dislocation dans le matériau écroui à forte vitesse, donnant une force motrice pour la recristallisation plus importante.

Ces travaux expérimentaux ont été complétés par des travaux de modélisation des cinétiques de recristallisation et précipitation pour la nuance 0.04Nb-0.09Ti. Le modèle de recristallisation est basé sur une loi JMAK dans laquelle sont introduits des paramètres physiques tels que la mobilité des joints de grains et la force motrice pour la recristallisation. La force motrice pour la recristallisation est calculée à partir de l'augmentation de la contrainte d'écoulement mesurée lors de la compression des éprouvettes. Les travaux de modélisation de la précipitation présentés dans le chapitre 1 ont également été étendus pour améliorer la compréhension de la précipitation

induite par la déformation. Les résultats de modélisation tendent à confirmer que la détection de la précipitation par les essais de relaxation de contrainte est liée à la densité numérique de précipités plutôt qu'à leur fraction volumique ou à leur pression d'épinglage.

Les travaux réalisés dans ce second chapitre sont résumés graphiquement dans la Figure 5.

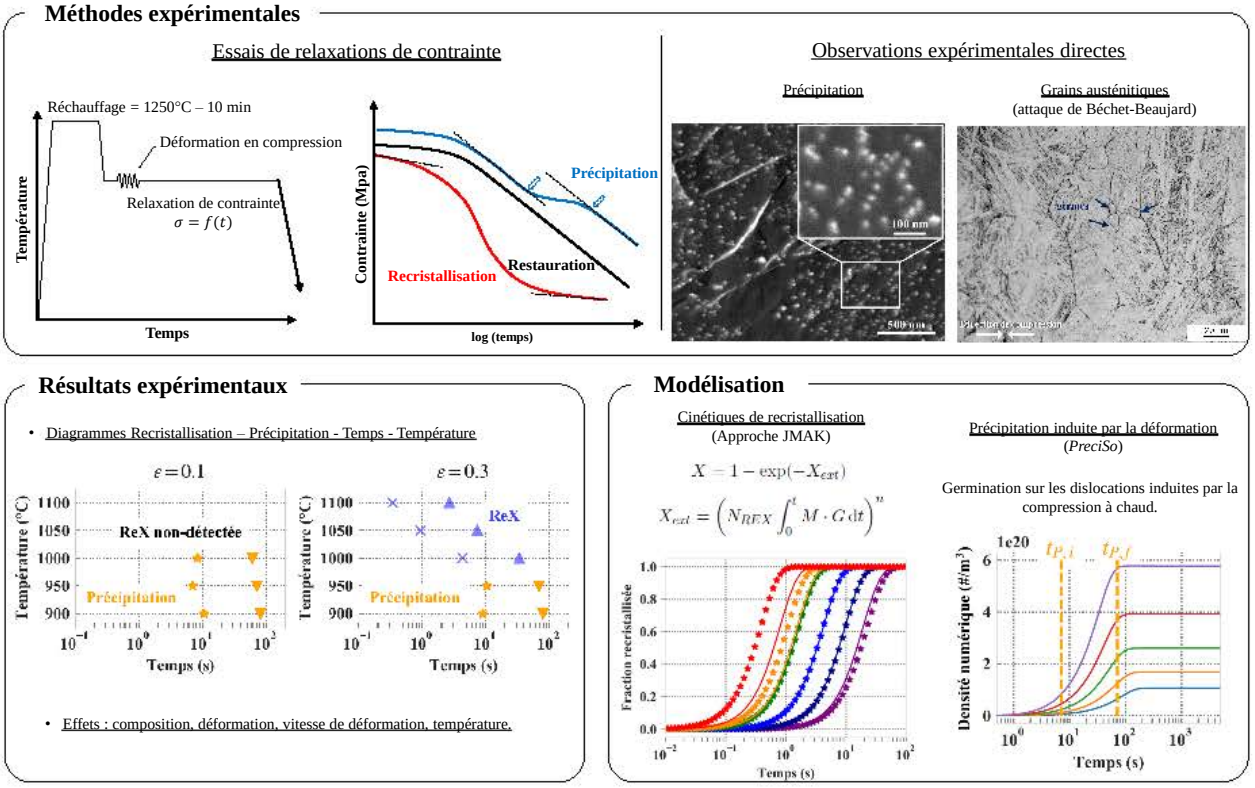

Figure 5: Résumé graphique des travaux expérimentaux réalisés dans le chapitre 2.

L'état métallurgique de l'austénite (taille de grain, densité de dislocations) influence la nature, la morphologie et la taille des phases formées lors des étapes suivantes du procédé (refroidissement accéléré et bobinage). Les résultats expérimentaux et de modélisation générés dans ce chapitre sont donc des données essentielles pour l'optimisation du laminage à chaud dans le but de contrôler les microstructures finales.

Chapitre 3: Conception d'aciers à phase complexe par laminage à chaud

Ces travaux visaient à générer une microstructure complexe principalement composée de bainite par laminage à chaud et bobinage entre 500 et 650 °C. Ce troisième et dernier chapitre se concentre ainsi sur les relations entre les paramètres de laminage à chaud, les microstructures finales et les propriétés mécaniques obtenues.

Le comportement en transformation de phase de l'acier 0.04Nb-0.09Ti a tout d'abord été suivi

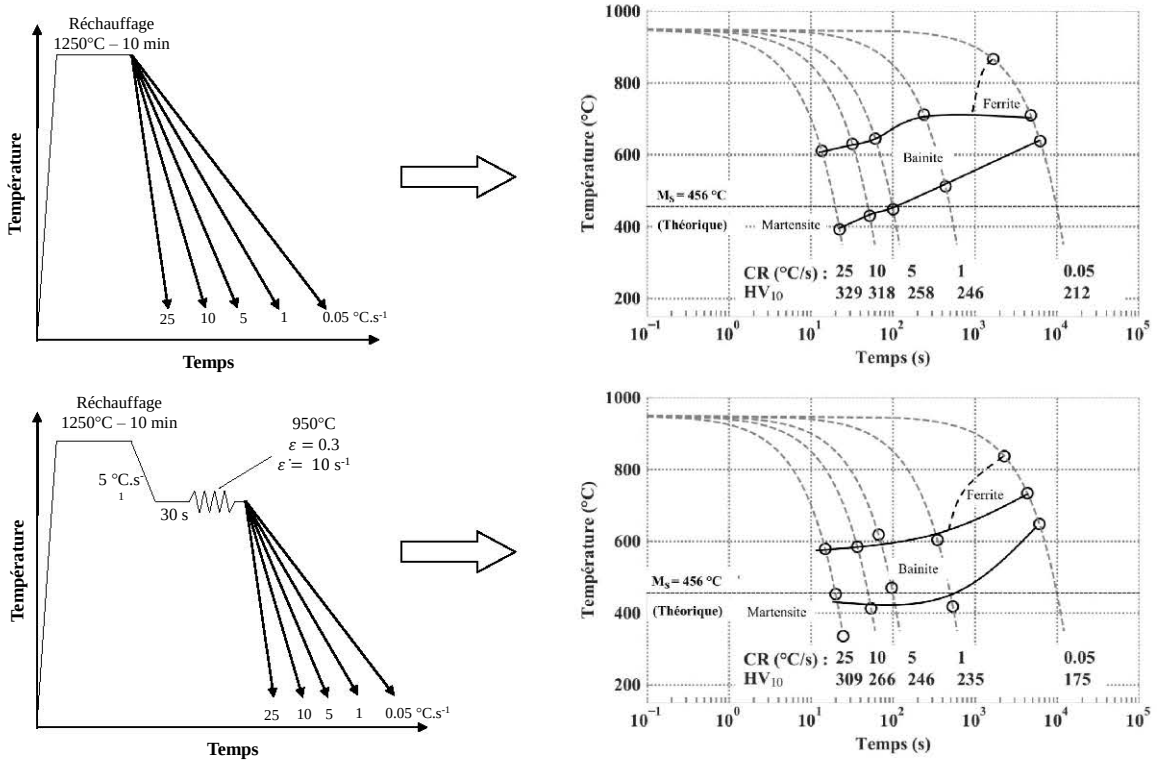

Figure 6: Diagrammes de transformations en refroidissement continu (TRC) partant d'une austenite non déformée ou déformée à 950 °C avec $\varepsilon = 0.3$ et $\dot{\varepsilon}$ =10 s^{-1}.

par dilatométrie lors d'essais de refroidissements continus (voir Figure 6), partant d'une austénite recristallisée (non-déformée) ou déformée à 950 °C ($\varepsilon = 0.3$ et $\dot{\varepsilon}$ =10 s^{-1}). Des microstructures bainitiques ont été obtenues pour une large gamme de vitesses de refroidissement. Des vitesses de refroidissement aussi faibles que 1 °C s^{-1} ont conduit à des microstructures entièrement bainitiques (principalement granulaire), montrant que la composition étudiée est particulièrement appropriée pour favoriser la transformation bainitique. Pour des vitesses de refroidissement plus élevées, des microstructures en lattes sont plutôt observées. La déformation de l'austénite dans la région de non-recristallisation étend le domaine de formation de la bainite granulaire au détriment de la bainite en lattes. Concernant la bainite en lattes, la déformation mène à des microstructures plus grossières (lattes plus courtes et plus larges), présentant des duretés plus faibles que les microstructures obtenues à partir d'austénite non-déformée.

Par la suite, des tôles d'acier ont été produites par laminage à chaud sur un laminoir de laboratoire, en utilisant des conditions proches des conditions de laminage industriel. Différentes stratégies ont été testées. Premièrement, les passes de déformation ont été effectuées dans des domaines de température différents, en suivant trois programmes distincts:

(i) HOT, pour lequel toutes les passes de déformation sont effectuées dans le domaine de température où l'austénite a le temps de recristalliser entre chaque passe.

(ii) MIXED, pour lequel les passes de dégrossissage ont été effectuées dans la région de recristallisation et les passes de finition ont été effectuées entre 1050 et 880 °C.

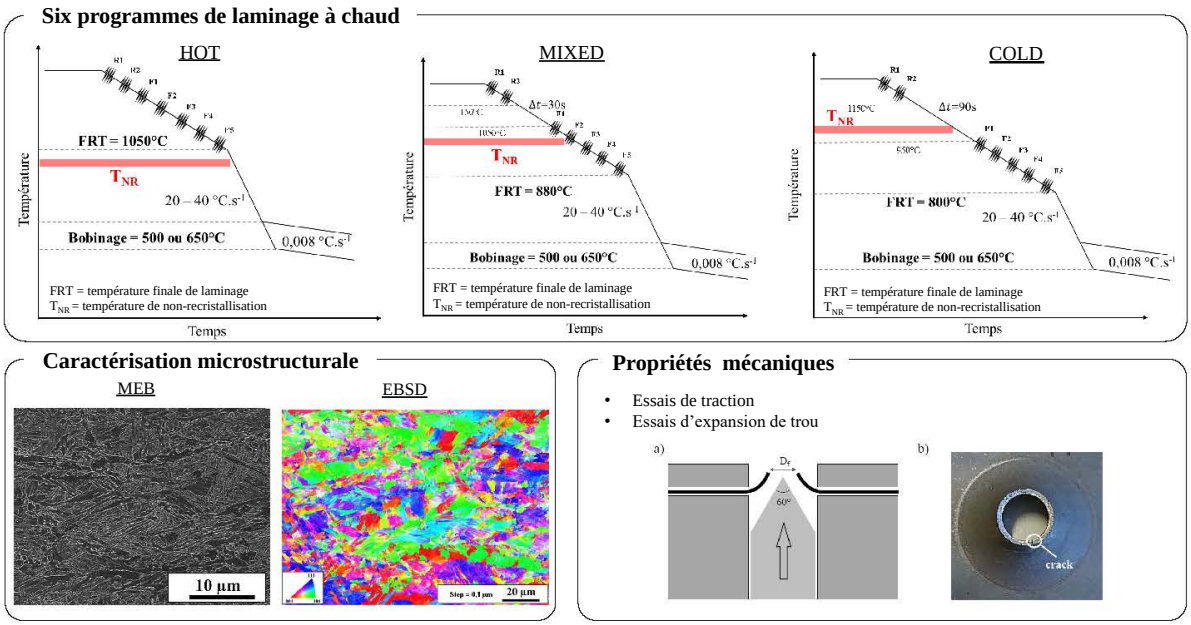

Figure 7: Production de plaques d'acier par six programmes de laminage à chaud différents, et caractérisations microstructurale et mécanique correspondantes.

(iii) COLD, similaire au programme MIXED, mais avec des passes de finition effectuées à plus basse température, entre 950 et 800 °C.

Deuxièmement, deux températures de bobinage différentes ont été appliquées : 500 et 650 °C. Ainsi, six programmes de laminage à chaud différents ont été testés. Pour chacune des plaques obtenues, la microstructure a été finement caractérisée au MEB et par EBSD, et les propriétés de traction et d'aptitude à l'étirement des bordures ont été déterminées. Ces tâches sont résumées graphiquement sur la Figure 7.

Pour tous les programmes de laminage à chaud testés, les microstructures résultantes sont principalement constituées de bainite, associée à de faibles quantités de ferrite. La déformation de l'austénite dans son domaine de non-recristallisation a favorisé la formation de ferrite, principalement localisée aux anciens joints de grains austénitiques. Des microstructures bainitiques en lattes ont été obtenues pour les programmes HOT - 500 °C et MIXED - 500 °C, tandis que la bainite granulaire domine les microstructures obtenues pour les autres programmes de laminage à chaud.

Des résistances maximales supérieures à 800 MPa ont été obtenues pour toutes les plaques laminées à chaud, atteignant ainsi l'objectif initial du projet NANOFORM. Les limites d'élasticité atteintes sont également élevées, avec des rapports YS/UTS compris entre 0.81 et 0.97. Des niveaux de ductilité en traction limités sont atteints.

Aucune de plaques obtenues n'atteint l'objectif de 70 % de degré d'expansion de trou. Cependant, des aptitudes à l'étirement des bordures raisonnables ont été obtenues, avec des degrés d'expansion de trous compris entre 40 et 60 %. Les microstructures bainitiques granulaires, principalement obtenues par bobinage à 650 °C, présentent les plus faibles degrés d'expansion de trous. Les microstructures en lattes, HOT - 500 °C et MIXED - 500 °C, sont plus favorables à l'obtention de

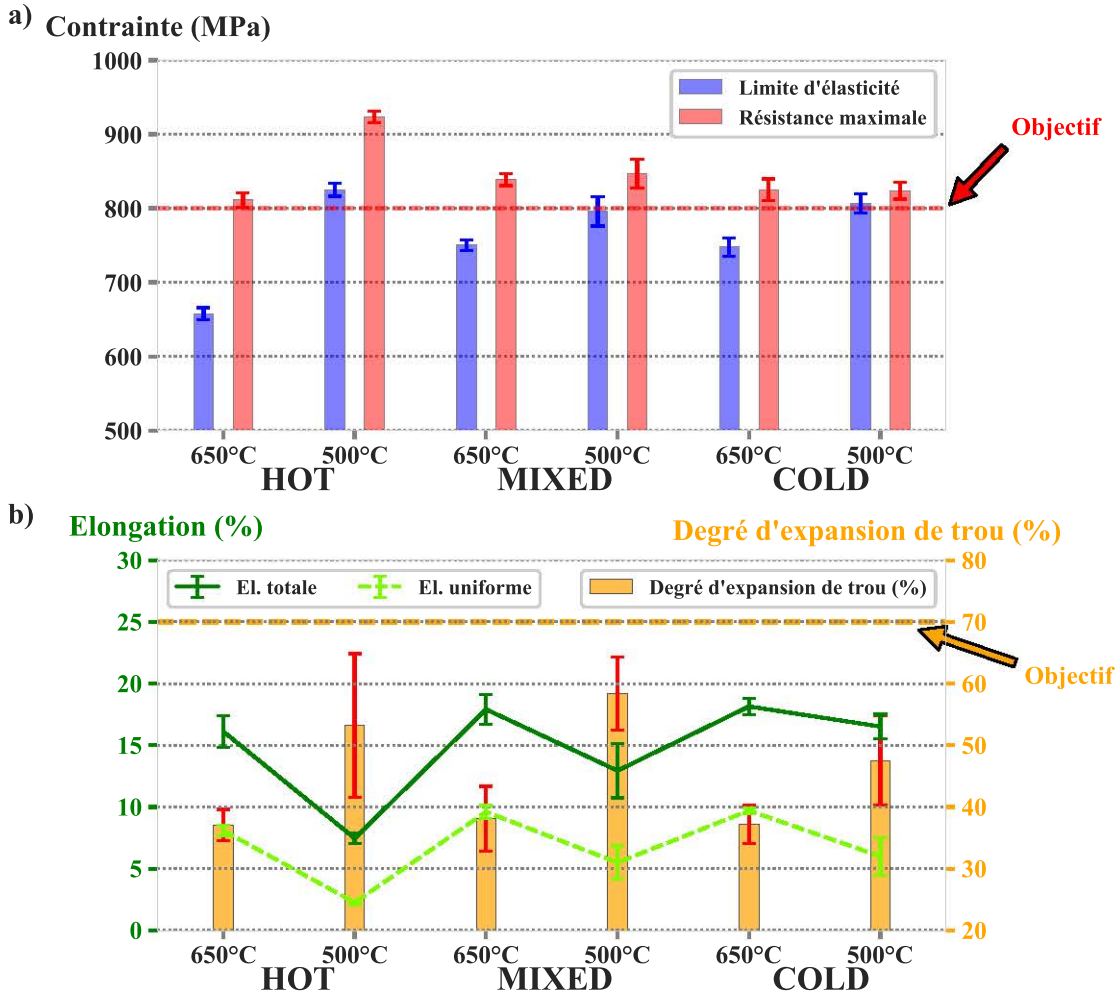

Figure 8: Propriétés mécaniques moyennes des plaques laminées à chaud. (a) Limites d'élasticité et résistances maximales. (b) Propriétés de ductilité en traction et degrés d'expansion de trous.

bonnes aptitudes à l'étirement des bordures. Cela est principalement dû à la présence néfaste d'îlots de martensite/austénite dans les microstructures granulaires.

Perspectives

Ces travaux de thèse ont porté sur les évolutions microstructurales d'acier bas carbone micro-alliés au cours du laminage à chaud. Le premier chapitre s'est concentré sur les phénomènes de réversion de la précipitation et la croissance de grains austénitiques lors du réchauffage des brames. Le second chapitre a permis l'étude de la restauration, de la recristallisation et de la précipitation induite par la déformation lors du laminage à chaud. Dans le troisième et dernier chapitre, les transformations de phase lors d'essais en refroidissement continu et de laminage à chaud ont été étudiées.

A l'issue de ces travaux, plusieurs perspectives peuvent être établies:

(i) **Production industrielle des aciers NANOFORM**

Bien que prometteurs, les résultats du chapitre 3 n'ont pas permis d'établir la faisabilité industrielle des aciers conçus au cours du projet NANOFORM. Ainsi, l'acier 0.04Nb-0.09Ti, qui a fait l'objet de la plupart des travaux présentés dans ce manuscrit, a été sélectionné pour des essais finaux sur la ligne industrielle de Salzgitter Mannesmann Forschung GmbH. Différents programmes ont été testés dans le but de chercher les propriétés mécaniques optimales. A l'heure de l'écriture de ce manuscrit, ces essais de production viennent d'être réalisés. Des combinaisons intéressantes de propriétés mécaniques ont été obtenues pour deux des tôles produites industriellement, l'une d'entre elle atteignant les objectifs initiaux du projet (UTS $\geq 800\,\mathrm{MPa}$ et HER $\geq 70\,\%$).

A court terme, les microstructures de ces tôles seront caractérisées dans le but de comprendre l'origine des propriétés mécaniques. Ces tôles subiront également une caractérisation plus poussée, incluant des essais de soudabilité, de galvanisation et de pliabilité. A plus long terme, si les essais de caractérisation finaux sont concluants, il est possible que ces aciers se retrouvent sur le marché dans quelques années.

(ii) **Amélioration des travaux de modélisation**
Le modèle de précipitation / croissance de grains présenté dans le premier chapitre pourrait être amélioré. Des efforts devraient notamment être faits pour réduire la quantité de données expérimentales nécessaires à la calibration du modèle. L'un des points clefs est l'estimation de la quantité réelle d'éléments de microalliage piégée dans des précipités dont les tailles sont trop importantes pour participer efficacement au contrôle de la taille des grains.

Dans le chapitre 2, des modèles décrivant la recristallisation de l'austénite et la précipitation induite par la déformation ont été présentés. Pour aller plus loin, ces modèles devraient être couplés entre eux, en prenant en compte les nombreuses interactions entre restauration, recristallisations et précipitation. Cela pourrait se faire sur la base des travaux présentés par Zurob [ZUR 03], ce qui permettrait une meilleure compréhension des courbes de relaxation de contrainte obtenues expérimentalement.

Il serait enfin très utile de développer un modèle complet, incluant à la fois les phénomènes dynamiques prenant place durant la compression, et les phénomènes statiques ayant lieu après la déformation.

(iii) **Optimisation de la composition des aciers**
L'acier 0.04Nb-0.09Ti étudié présente des taux de Ti et de N qui mènent à la formation de TiN très grossiers, atteignant plusieurs micromètres. Il est probable que ces TiN soient la principale source de germination des fissures lors d'essais d'expansion de trou. La composition étudiée pourrait donc ne pas être optimale pour atteindre une bonne aptitude à l'étirement des bordures.

Bien que cela ait déjà été rapporté dans la littérature, il convient d'abord de confirmer expérimentalement que ces TiN sont la principale source de formation des fissures dans l'acier étudié. L'analyse des faciès de rupture des échantillons d'essais d'expansion de trou devrait confirmer cette hypothèse. Il serait alors intéressant de tester d'autres compositions similaires mais ayant des teneurs plus faibles de Ti et de N pour éviter la formation de ces TiN grossiers. Il faudrait cependant conserver une composition susceptible de favoriser la transformation

bainitique pour atteindre les propriétés de résistance mécanique visées.

Il serait intéressant d'adopter une approche de métallurgie combinatoire pour trouver la composition optimale. Il faudrait tout d'abord produire des matériaux à gradient de composition en un ou plusieurs éléments [DES 18] et leur faire subir des traitements de laminage à chaud similaires à ceux présentés dans le chapitre 3. Une large gamme de compositions pourrait ainsi être analysée, et la composition menant à des propriétés optimales pourrait alors être déterminée.

General introduction

Industrial context

Over the last 20 years, car designers have been facing increasing challenges concerning passenger safety, vehicle performance and fuel economy. To meet the demands of the automotive industry, steelmakers have developed higher strength steel grades named Advanced High Strength Steels (AHSS). Two main driving forces for the development of AHSS are identified [BOU 13, NAN 16].

The first one is related to safety issue: increasing both yield strength and ultimate tensile strength leads to enhanced crash performances. Components made of AHSS can provide better energy absorption performance and anti-intrusion properties than conventional steels. The second driving force is related to the need to reduce vehicle greenhouse gas emissions. Automotive industries are directly exposed to financial penalties in case of non-compliance with European Union directives concerning greenhouse gas emissions. European Union defined targets of 130 g CO_2/km for 2015 and 95 g CO_2/km for 2021 for the average emissions of new passenger cars, whereas the new passengers cars in the EU in 2016 had average CO_2 emissions of 118.1 g of CO_2/km. Reducing the weight of a vehicle without losing strength is one of the possible successful strategies to reduce fuel consumption and CO_2 emissions, together with improved engines and aerodynamics. A reduction of 10 % of a vehicle mass results in a fuel consumption reduction ranging from 3 to 7 % [MOD 14].

In this context, steel is also competing on some parts with lower density materials, such as aluminum or magnesium alloys. In order to properly determine the impact of light-weighting, one needs to consider the total embodied energy of the materials, notably accounting for the energy cost of material production. It appears that light-weighting generally requires higher energy due to material production. In particular, the primary energy demand for the production of aluminum and magnesium alloys can be significantly higher than for steel: 47 MJ/kg for steel, against 141 MJ/kg for wrought aluminum and 360 MJ/kg for magnesium [KIM 13]. In addition, magnesium has high production costs, so that only aluminum and steel can be considered for large-scale use in the automotive industry. Nonetheless, a recent global study [MOD 14] showed that both high strength steels and aluminum alloys are viable solutions to reduce the green house gas emissions in future years.

As a side remark, one should note that despite a growing use of high strength steels and aluminum alloys in automotive industry, the average weight of vehicles has not decreased over the last two decades [KOL 15, VED 17]. Figure 1 a) shows selected data on the average mass of private cars in the UE on this time period. The average mass of new vehicles registered in Europe seems to be reaching a plateau, but does not decrease. This is mainly due the increase of comfort equipments

and user/buyer preference for larger vehicles. In addition, European legislation is quite flexible, since CO_2 emission targets are modulated by the average weight of cars [VED 17]. A heavy/large car is allowed to emit more CO_2 than a lighter/smaller car, which does not encourage manufacturers to produce cars of more reasonable sizes. However, as observed on Figure 1 b), the average CO_2 emissions have considerably decreased over the same time period. This reduction is therefore mainly related to other factors, such as engine efficiency or improved aerodynamics.

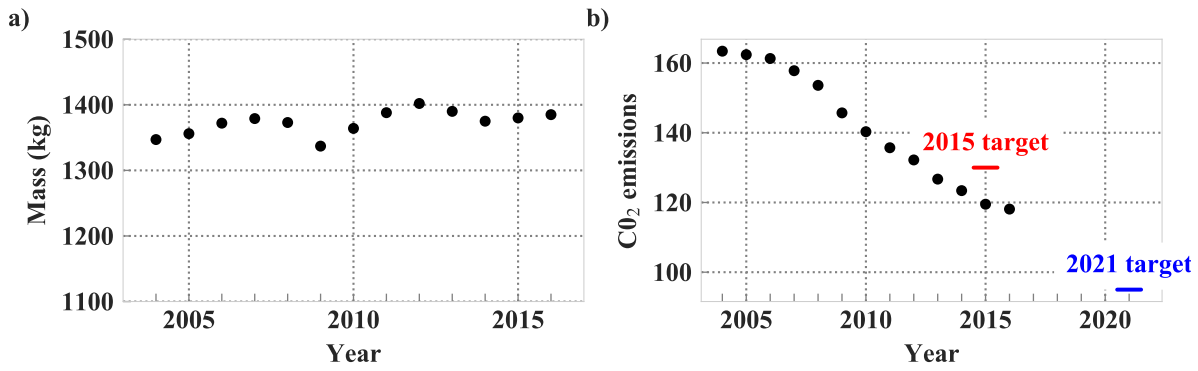

Figure 1: Evolution of (a) the average $C0_2$ emissions and (b) the average mass (kg) of new private wars sold in European Union. The data is extracted from [VED 17].

Development and classification of Advanced High strength steels

Numerous families of Advanced High Strength steels (AHHS) have been developed and can answer the demands of the automotive industry. AHSS present enhanced mechanical properties compared to conventional high strength steels. AHSS are generally classified into categories referred to as generations [KWO 10, MAT 12, HIL 15, NAN 16], according to their date of development.

The term ***first generation*** AHSS refers to different steel types developed since the beginning of the 1980s, based on ferritic microstructures. It includes dual phase (DP), transformation induced plasticity (TRIP), complex phase (CP) and martensitic (MART) steels. Despite a significant improvement of strength in comparison to conventional steels, the main disadvantage of the first generation of AHSS is their limited ductility and formability [BOU 13].

In the 1990s, in order to overcome the weaknesses of the first generation of AHSS, the steelmakers developed the ***second generation*** of AHSS, that present an outstanding combination of strength and ductility. This second generation contains austenitic stainless steels (AUST. SS), Twinning Induced Plasticity (TWIP) steels, and lightweight steels with induced plasticity (L-IP). Unlike the first generation, the second generation AHSS is based on fully austenitic microstructures. The austenitic microstructure is reached through considerable additions of alloying elements that stabilize austenite, such as manganese and nickel. Despite their excellent balance of strength and ductility, these steels suffers several drawbacks: they are significantly more expensive, present a tendency to cracking after elaboration and have a poor weldability [HIL 15, NAN 16]. Thus, their use in automotive industry is very limited.

Because of the drawbacks of first and second generations, the ***third generation*** of AHSS is currently under development. The strategies adopted to develop this generation are based on an enhancement of the mechanical properties of first generation ones. In other words, third generation AHSS are expected to be an extension of first generation AHSS. The improvement of DP steels, the use of new processing routes like quenching and partitioning (Q&P) or the enhancement of existing ones, the development of ultra-fine bainite microstructures, and the modification of the conventional processing routes of TRIP steels are some examples of the possible followed approaches [MAT 09, MAT 12, NAN 16].

Figure 2 presents a summary of the strength and elongation data for conventional high strength steels (HSS) as well as for various AHSS grades. The gap between the properties of first generation AHSS and those of second generation AHSS allows the definition of the desired properties for the ***third generation*** of AHSS.

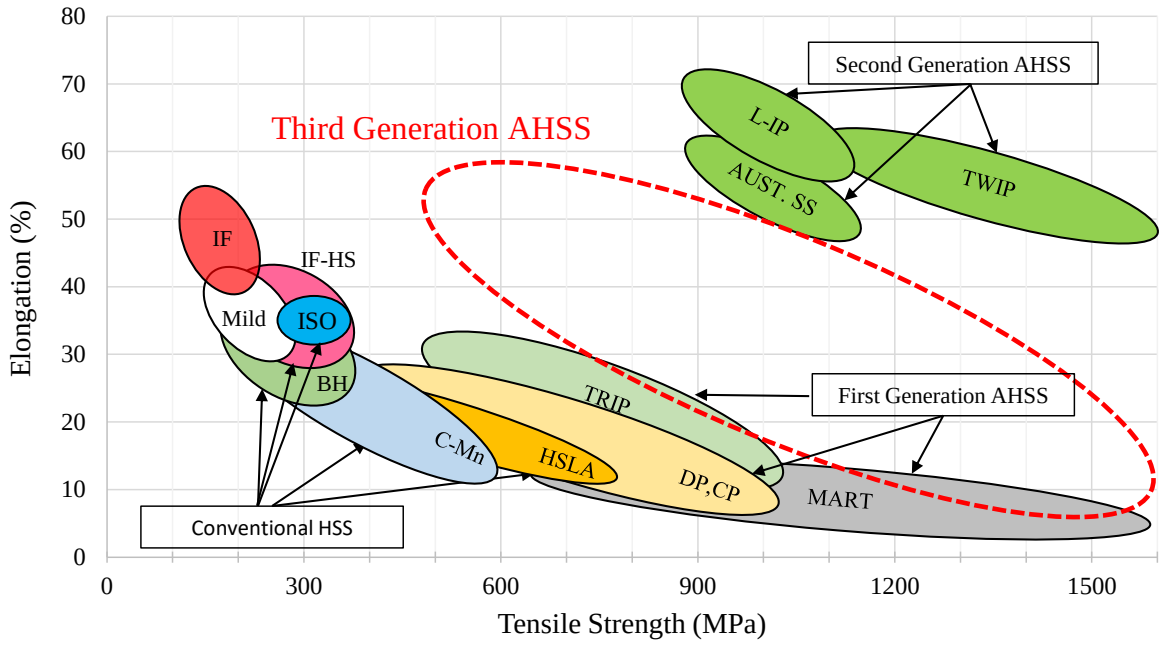

Figure 2: Overview of tensile strength and total elongation for various high strength (HSS) and advanced high strength steels (AHSS) grades. Based on data extracted from [KWO 10, MAT 12, NAN 16].

Brief definition and history of Microalloyed steels

The terminology "Microalloyed steels", also referred to as high strength low alloy (HSLA) steels, is used for steels containing low amounts of denominated microalloying elements, giving them superior strength as compared to conventional carbon-manganese steels. The metallurgical principles on which these steels are based have been the subject of a considerable amount of publications, so that performing an exhaustive review of the metallurgical concepts is impossible.

In an attempt to summarize, microalloyed steels are low carbon - manganese steels to which are added small quantities of strong carbonitride-forming elements such as Ti, Nb, and V. Such elements, referred to as microalloying elements, are added for their benefecial effect on strength. They act through three main mechanisms [GLA 02]:

- By controlling austenite grain size during high temperature processing, thus leading to a general grain refinement of the final microstructure.
- By increasing the strength through precipitation hardening when fine carbides are formed in the ferritic microstructures.
- By increasing the hardness and influencing the phase transformation behavior (hardenability) when in solid solution.

Strictly speaking, the concept of microalloying was discovered in the 1920s, as studies reported the beneficial effects of small additions of zirconium to plain carbon steels [BEC 23, FEI 23]. In 1959, Breiser [BEI 59] democratized the concept and created the term *microalloying* by reporting the effect of Nb addition to carbon steels. Thus, from the end of the 1950s until the beginning of the 1980s, microalloyed steels have remarkably developed. During these years, the literature and industrial developments were almost exclusively focused on low-hardenability steels presenting ferrite-pearlite microstructures, with yield stress up to 420 MPa [PIC 92, GLA 02, DEA 09, BAK 16]. Starting from the beginning of the 1980s, due to the increasing demands of pipeline and automotive industry for steels with higher strengths, microalloyed steels gradually diversified. The microstructures gradually transformed from high-temperature transformation products (ferrite and pearlite) to a mixture of low-temperature transformation products such as acicular ferrite and bainite [PIC 92, GLA 02, DEA 09, BAK 16]. From a processing perspective, this evolution towards low-temperature transformation products was made possible by the enhancement of hot rolling practices and the apparition of new techniques, such as accelerating cooling after hot rolling.

Thus, today's microalloyed steels present a very broad range of properties and microstructures, ranging from ferrite-pearlite microstructures to more complex ones mixing several austenite transformation products. The modern complex phase (CP) steels, whose tensile properties are shown in Figure 2, are nothing more than the results of the evolution of microalloyed steels towards low-temperature austenite transformation products.

Aims of the NANOFORM project

Due to the aforementioned driving forces, the use of AHSS has gradually increased in automotive industry. However, increasing strength generally leads to a reduction in ductility and formability of steels. As a consequence, the use of AHSS was initially limited to parts with rather simple shapes [HAS 04]. Numerous body-in-white car parts present shapes that need to be manufactured by cold forming. This implies that the used steels must present good formability properties, including stretch flangeability, which is generally evaluated by hole expansion tests.

Dual phase steels are the most widely used AHSS for body-in-white car parts. They exhibit a very good balance of strength and elongation due to a high strengthening rate. Thus, they present a low YS/UTS (yield strength/ ultimate tensile strength), which is quite a drawback because body-in-white parts should resist to intrusion [FON 15]. Another drawback of DP steels is their limited

formability, which arises from the very high difference in hardness between ferrite and martensite [HAS 04]. Therefore, there is a demand for AHSS presenting the same level of strength than DP steels but enhanced formability properties and higher YS/UTS ratio.

The concept of complex phase (CP) steels have emerged to address the lack of stretch flangeability of DP steels. This term refers to steels presenting a strength superior to 800 MPa with a "complex" microstructure composed of a mixture of bainite, ferrite, martensite and precipitates [FON 15]. In order to increase the stretch flangeability, it is recommended the lower the difference of hardness between the phases present in the microstructure. A homogeneous microstructure thus leads to better hole expansion ratios. Additionally, CP steels containing a high fraction of bainite are expected to present an enhanced stretch flangeability because bainite present a strength between those of ferrite and martensite. This category of steel also presents a higher YS/UTS ratio than DP or TRIP steels.

In this scientific and industrial context, the NANOFORM RFCS[3] project aims at designing new grades of **complex phase low carbon microalloyed steels** with **enhanced stretch flangeability** in comparison with existing steels with similar levels of strength. The targeted ultimate tensile strength level ranges from **800 MPa to 1000 MPa**. Regarding stretch-flangeability, a **hole expansion ratio** of **70 %** is targeted. These steels are intended to be manufactured through hot rolling, accelerated cooling and coiling between 500 °C and 650 °C.

Figure 3 describes the hot rolling process by which the steel sheets of the project are manufactured. In hot rolling steel plants, the manufacturing process of steel sheets starts with slabs that come from the casting process. These slabs are inserted in the slab **reheating** furnace, whose primary purpose is to ensure that the slab is ductile enough to be hot rolled. During this reheating stage, the steel is brought to a fully austenitic state. In the case of microalloyed steels, reheating ensures that primary coarse precipitates are dissolved before hot rolling, to optimize the effects of microalloying additions.

After the reheating stage comes the proper **hot rolling**, that aims at reducing the slab thickness to get the targeted thickness of the final steel sheet. Hot rolling is divided into two stages, referred as roughing and finishing. Depending on the deformation temperatures, the levels of strain and strain rates applied, as well as the times between each deformation pass (interpass time), the microstructural state obtained at the end of hot rolling can strongly vary. This state will influence the phase transformations occurring in the later stages of the process, and thus must be carefully optimized.

Right after hot rolling, the steel sheet reaches its final thickness. This process ends with **accelerated cooling** on a run-out table. The steel sheet is rapidly cooled down to a target temperature and coiled at this temperature. Accelerated cooling practice aims at avoiding the formation of high temperature austenite transformation products, such as ferrite and pearlite. Depending on the cooling rate applied and the **coiling** temperature, the final microstructure can be adapted.

The composition of the steel as well as the hot rolling parameters determine the final microstructure and mechanical properties obtained. The NANOFORM project aims to optimize both the composition and the hot rolling process in order to develop rather homogeneous microstructures

[3]RFCS: Research Fund for Coal and Steel.

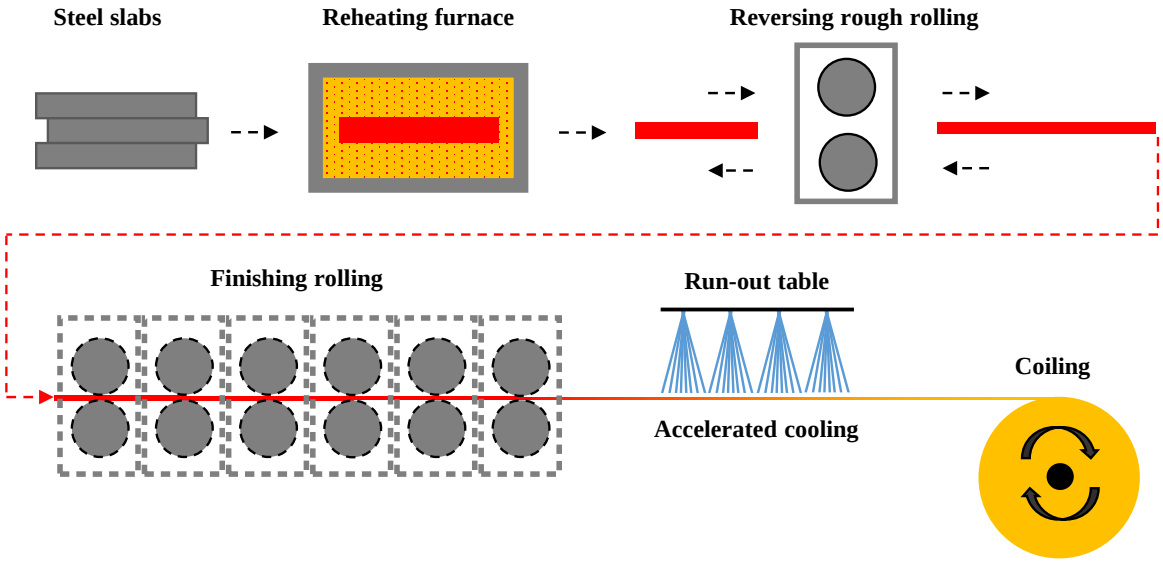

Figure 3: Manufacturing process targeted in the NANOFORM project for the production of AHSS steels plates.

mainly consisting of bainite and reach the targeted mechanical properties. Thus, a total of 11 different compositions were studied. The microstructural evolutions at each stage of the process were studied, non-exhaustively including:

(i) thermodynamic equilibrium calculations.

(ii) the evolution of austenite grain sizes and precipitation state during reheating.

(iii) the microstructural evolutions taking place during and after hot deformation of austenite: recovery, recrystallization and strain-induced precipitation.

(iv) the phase transformation behavior.

(v) the hot rolling production of these steels on a pilot plant (lab scale) and on an industrial scale.

(vi) a detailed characterization of the resulting microstructures and mechanical properties.

For a better understanding of the context of this PhD-work, an overview of the organization and progress of the NANOFORM project is given in Appendix A.

Objectives of the PhD and outline

This PhD thesis fits into the context of the NANOFORM project. It aims at describing and understanding of microstructural evolutions during the various stages of the manufacturing process schematically represented in Figure 3. Although a total of 11 steels were studied in the framework of the NANOFORM project, this work mainly[4] focuses on one of the steel grades studied in the project, referred to as 0.04Nb-0.09Ti steel. The manuscript is organized in three independent chapters, which can be read separately. The hot rolling process links the different chapters, as shown in Figure 4.

[4]In chapter 2, two other steel grades are also studied.

(i) Chapter 1 is related to the reheating stage of the manufacturing process. It presents an experimental study aiming at describing the evolution of austenite grain growth and precipitation state during during isothermal treatments. A precipitation model was developed and coupled to a simple grain growth model based on Zener pinning to describe microstructural evolutions that occur during reheating.

(ii) Chapter 2 is related to the hot rolling stage of the manufacturing process. In this chapter, the kinetics of austenite recrystallization and precipitation in austenite were studied by application of the stress relaxation method. This chapter also includes a modeling work on the kinetics of recrystallization and precipitation.

(iii) Chapter 3 focuses on the description of the relationships between the manufacturing process, the microstructure, and the mechanical properties obtained. Six varying manufacturing processes were applied on a pilot plant to simulate hot rolling. The obtained microstructures and mechanical properties of the resulting hot-rolled plates were characterized.

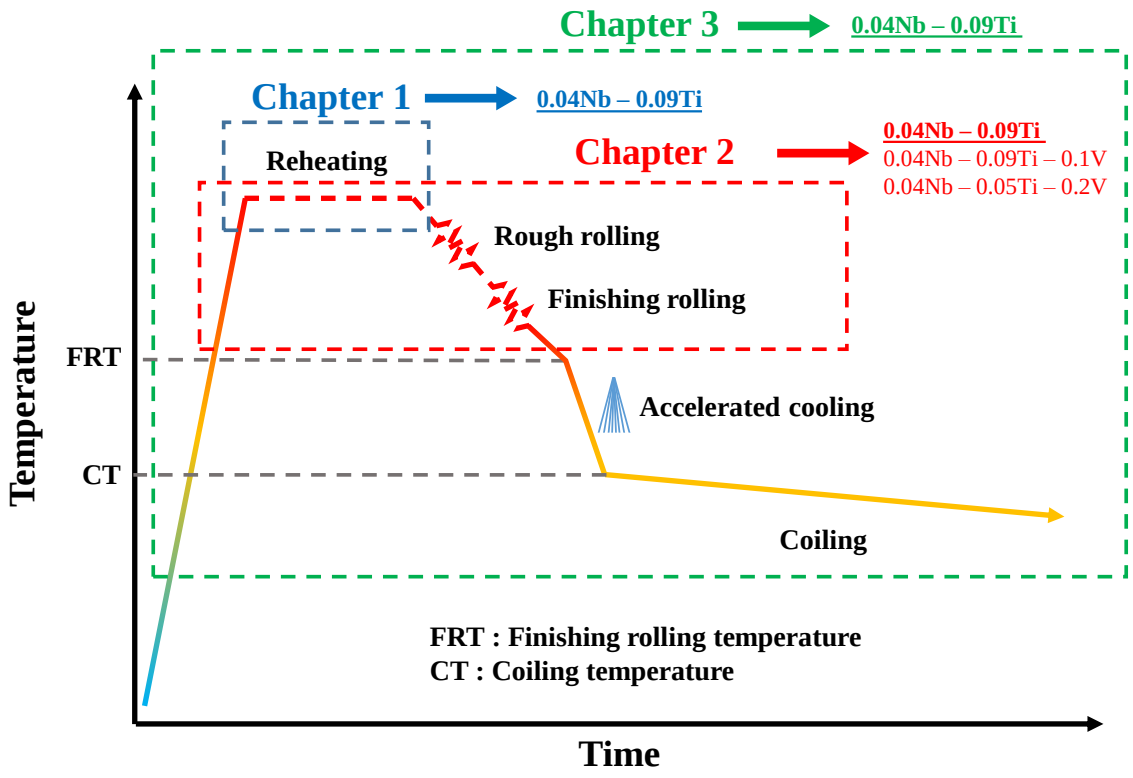

Figure 4: Structure of the PhD manuscript with respect to the different stages of the hot rolling process.

Chapter 1

Evolution of precipitation state and austenite grain growth during reheating

Contents

1.1 Introduction

Microalloyed steels, also referred to as high strength low alloy (HSLA) steels, present small additions of strong carbonitride-forming elements such as Ti, Nb and V. In austenite, the precipitates formed control the grain sizes through a grain boundary pinning mechanism during the high temperature processing. Regardless of the intended phase transformations from the austenitic domain, the resulting mechanical properties depend on the prior austenite grain size. Indeed, austenite grain boundaries (GB) act as nucleation sites for ferrite, bainite and/or martensite. A finer austenitic microstructure thus results in a finer ultimate microstructure, with enhanced strength and toughness.

During hot rolling process, the reheating temperature prior to hot rolling must be carefully selected to optimize the effects of microalloying elements. A high soaking temperature ensures a complete dissolution of the pre-existing precipitates, leading to the formation of finer precipitates during and after hot rolling. However, it also results in coarser austenite microstructures. On the other hand, a low soaking temperature would maintain a fine austenite microstructure but may not dissolve existing coarse precipitates, decreasing the potential for precipitation strengthening during the following steps. The choice of the soaking temperature and duration is generally the result of many years of practical feedback. There is a demand to replace an essentially experience-based approach with thermodynamic and kinetic models.

Grain growth is an important field of study in materials science and has been the subject of a considerable amount of work [HUM 17, RIO 18]. Numerous studies intend to develop numerical models for austenite grain growth kinetics in steels. Phenomenological approaches are widely used for their simplicity [SEL 79, SHO 04, LEE 08a, XU 12, ZHA 11, YAN 14], the grain diameter following empirical equations of the type:

$$D^n - D_0^n = At \exp\left(\frac{-Q_{GG}}{R_g T}\right) \tag{1.1}$$

where D is the final grain diameter, D_0 is the initial grain diameter, A and n are empirical parameters, Q_{GG} is the activation energy for grain growth, R_g is the ideal gas constant, T is the temperature, and t is the soaking duration. However, these types of models do not account for the pinning effect of precipitates. Other studies adopt physically based approaches that take into account the influence of pinning precipitates on grain growth [AND 95, MAN 96a, BAN 10, MAA 12]. The austenite grain size is shown to result from the competition between a driving pressure for grain growth and a pinning pressure, induced by precipitates, that evolves during heat treatments. In particular, Banerjee *et al.* [BAN 10] and Maalekian *et al.* [MAA 12] presented models coupling the evolution of precipitation with austenite grain growth. The pinning effect of different precipitate species are added up to calculate the global pinning pressure. Although Maalekian *et al.* [MAA 12] present a multi-class description of the precipitation state, the pinning pressures are calculated using the mean volume fraction f of precipitate, and the mean radius of precipitates $\langle r \rangle$. More recently, Razzak *et al.* [RAZ 12, RAZ 14] showed the importance of using the size distribution of precipitates for the calculation of pinning pressure in an abnormal grain growth model. Considering only averaged values may lead to erroneous calculated pinning pressure, especially in cases where precipitate size distribution is broad and/or bimodal.

In the present chapter, the evolution of the precipitation state and austenite grain growth were studied in a Ti-Nb microalloyed steel during reversion treatments, *i.e.* starting from a fully precipitated state and performing thermal treatments between 950 °C and 1250 °C. A Kampmann-Wagner Numerical (KWN) type precipitation model [WAG 05] was coupled with a grain growth model to predict the austenite grain size obtained after several heat treatments. The evolution of a pre-existing population of (Ti,Nb)C precipitates was modeled using a multi-class description of the precipitation state. Thermodynamic databases were used, accounting for the alloy thermal history, to estimate the solubility product of (Ti,Nb)C precipitates.

1.2 Background

In the following, the fundamentals of the solubility of microalloying elements in austenite and of grain growth control by precipitates are reviewed.

1.2.1 Solubility of microalloying elements in austenite

The solubility of a MX compound, where M is a metallic element (Ti, Nb, or V) and X is an interstitial element (C or N), is often described by its solubility product, K_S. The value of K_S is given by the concentration of the elements in solid solution by:

$$K_S = [M] \cdot [X] \tag{1.2}$$

where $[M]$ and $[X]$ should be, strictly speaking, the molar fraction of M and X dissolved in matrix [GLA 02]. For convenient reasons, $[M]$ and $[X]$ are generally expressed in terms of weight percentage. The temperature dependence of K_S is historically expressed by a condensed form of an Arrhenius relationship:

$$\log_{10}(K_S) = A - B/T \tag{1.3}$$

where A and B are constant for a given MX compound and T is the temperature (K). Figure 1.1 compares the solubility products of microalloying elements carbides and nitrides. It is worth noticing that for each microalloying element, the nitride is more stable than the corresponding carbide in austenite. TiN is markedly the most stable precipitate in austenite, whereas VC is the least stable. Thus, in the case of multiple microalloying additions, TiN tends to form at very high temperatures and to precipitate before other microalloy carbides and nitrides, consuming the available nitrogen in the alloy.

All carbides and nitrides of Ti, Nb, and V share the same face-centered cubic (FCC) crystalline structure with very similar lattice parameters [GLA 02]. Therefore, mixed carbo-nitrides (Ti,Nb,V)(C,N) can form when the steel presents multiple microalloying additions. In this case, thermodynamic databases in commercial softwares such as Thermo-Calc [AND 02a] are particularly useful for the estimation of the solubility products of these complex compounds.

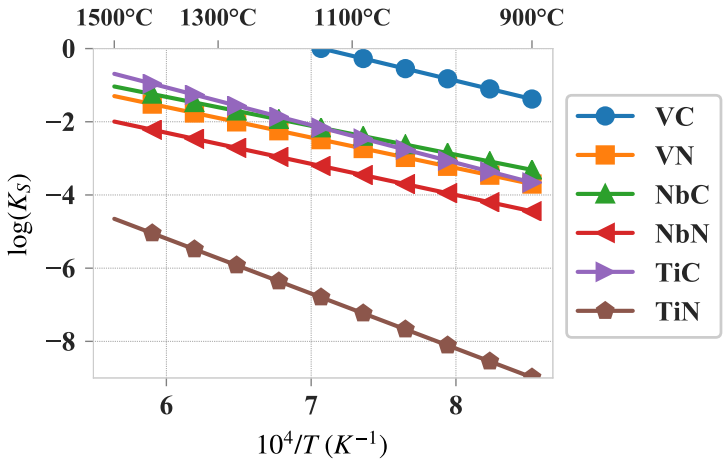

Figure 1.1: Comparison of the solubility products of microalloy carbides and nitrides. Data is extracted from [GLA 02].

1.2.2 Grain growth control by precipitates

Grain growth occurs at sufficiently high temperature in metallic materials in order to reduce the total interfacial energy of the polycrystalline material. In microalloyed steels, microalloying elements may interact with the motion of grain boundaries in two ways. First of all, a dispersion of precipitates exerts a retarding pressure on grain boundaries, which has a pronounced effect on grain growth. Secondly, a migrating interface drags a local segregation (atmosphere) of solute elements, which exerts a retarding force on it. Thus, solute elements may largely reduce the grain boundary mobility and the grain growth kinetics. This phenomenon is generally referred to as solute drag effect [CAH 62, HER 14]. In the case of high velocity grain boundaries, the solute elements can no longer keep up with the grain boundaries. Thus, in the case of high temperature heat treatments, the solute-drag effect stays limited and precipitate pinning forces prevail.

In 1948, Zener first formulated an expression for the pinning pressure exerted by precipitates on grain boundaries, in a paper written by Smith [SMI 48] after a personal communication with Zener. Zener's theory has been widely adopted and modified ever since, so that dozens of precipitate pinning expressions can be found nowadays [HUA 16b]. In the following sections, we will detail two particularly relevant theories: the original Zener's theory [SMI 48], and the one formulated by Rios [RIO 87]. Both theories are given for a randomly distributed population of precipitates presenting the same radius r and a volume fraction f_v.

1.2.2.1 Driving pressure for grain growth

Both theories consider that the driving pressure for grain growth arises from the reduction of boundary area coming with grain growth and is given by:

$$P_D = \beta \frac{\gamma}{D_\gamma} \tag{1.4}$$

Where β is a coefficient, γ is the austenite interfacial energy and D_γ is the mean grain diameter. The value of β is subject to discussion in literature. Few details are given in Smith's 1948 founding article, but the most likely assumption[1] is that Zener considered that $\beta = 2$. This value seems actually overestimated as several experimental and modeling works tend to prove that the correct expression of the driving pressure for grain growth in polycrystalline materials is four times lower [PAT 92, RIO 96, RIO 04, RIO 10]. In his theory, Rios considered that $\beta = 1$.

1.2.2.2 Pinning pressure exerted by precipitates

Zener and Rios considered fundamentally different interaction mechanisms between precipitates and grain boundaries [RIO 10]:

(i) Zener's theory [SMI 48] is based on the *pass-through mechanism*, which assumes that grain boundaries go through the pinning particles (Figure 1.2 a)). Schematically, if a precipitate occupies a fraction area of the grain boundary, this area has to be created if the interface moves away from the precipitate. The force exerted by one spherical precipitate of radius r is thus given by:

$$F_{Zener} = \pi r \gamma \tag{1.5}$$

(ii) Rios [RIO 87] developed his own model on the *enveloping mechanism*, in which the moving grain boundary bends around and envelops the precipitate (Figure 1.2 b)). It is supposed that the precipitate/matrix interface is not replaced but an additional grain boundary area equal to the surface of the precipitate has to be created. The process is analogous to Orowan looping of a dislocation bypassing a precipitate. The model assumes that the energy required to bypass the precipitate is equal to the energy required to create the new enclosing surface. The force exerted by one spherical precipitate of radius r is then twice the one calculated by Zener:

$$F_{Rios} = 2\pi r \gamma \tag{1.6}$$

For a given volume fraction f_v of randomly distributed inclusions, and assuming that all particles present the same radius r, the number density of particles (number per unit volume) N_v is given by:

$$N_v = \frac{f_v}{\frac{4}{3}\pi r^3} \tag{1.7}$$

From this total number density of particles, it is now necessary to calculate N_s, the surface density of particles that interact with the grain boundary. Zener considered that $N_s = r \cdot N_v$ without giving any explanation of this assumption. It actually seems more appropriate to postulate that a particle interact with the grain boundary when the center of the particle lies within $\pm\, r$ of the grain boundary, as explained by Nes *et al.* [NES 85]. Thus Rios considered that N_s is equal to $2rN_v$.

The actual pinning pressure P_p applied by the particle distribution per unit surface of grain boundary is then derived by:

[1] For more details, the lecture of the review written by Manohar *et al.* [MAN 98] is recommended.

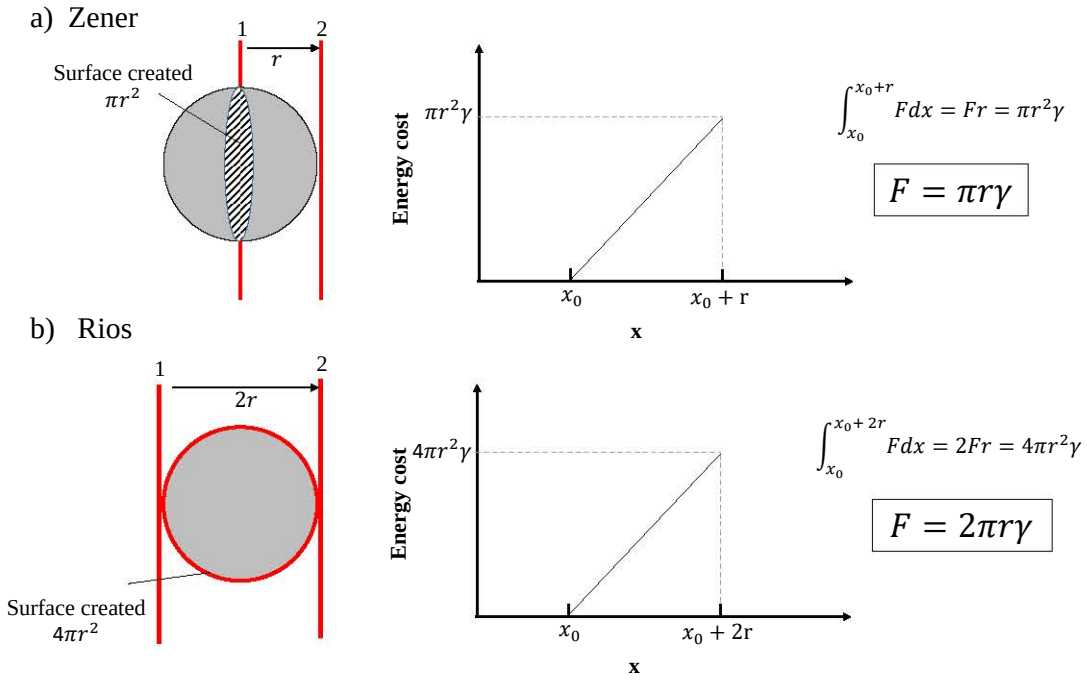

Figure 1.2: Comparison of Zener (a) and Rios (b) theories for the interaction between a grain boundary (red) and a spherical (grey) precipitate of radius r.

$$P_P = N_s \cdot F \tag{1.8}$$

where F is the force applied by one precipitate, either given by equation 1.5 or 1.6.

A limiting grain diameter D_L is reached when the driving pressure for grain growth equals the pinning pressure exerted by the precipitate distribution: $P_D = P_P$. It should be noted that Rios found a critical diameter 8 times lower than the one originally found by Zener. The confrontation of experimental data with Zener and Rios expressions shows that exaggerated grain sizes are obtained through the formulation originally given by Zener [RIO 87, MAN 98]. As Rios [RIO 10] suggested, a corrected Zener's theory is thus considered. Zener's corrected theory considers Zener's calculation of the pinning force applied by one precipitate on a grain boundary, but with corrected N_s and β values. Table 1.1 compares the expressions of D_L found in three different cases: Zener's original theory, corrected Zener's theory, and Rios's theory. Most of the experimental data lies between the corrected Zener's theory and Rios's theory [RIO 10]. Therefore, these two theories somehow define a lower and an upper limit for the pinning pressure.

Theory	Original Zener	Corrected Zener	Rios
Driving pressure P_D	$\frac{2\gamma}{D_\gamma}$	$\frac{\gamma}{D_\gamma}$	$\frac{\gamma}{D_\gamma}$
Number of particles / unit surface of GB N_s	$r \cdot N_V$	$2r \cdot N_V$	$2r \cdot N_V$
Pinning pressure P_P	$\frac{3f_v\gamma}{4r}$	$\frac{3f_v\gamma}{2r}$	$\frac{3f_v\gamma}{r}$
Limiting diameter D_L	$\frac{8r}{3f_v}$	$\frac{2r}{3f_v}$	$\frac{r}{3f_v}$

Table 1.1: Comparison of Zener and Rios expressions for grain boundary pinning by precipitates.

1.3 Material & methods

1.3.1 Studied material

The alloy used in this study was produced by vacuum induction melting. An ingot of approximate dimensions 140 × 150 × 50 mm^3 was obtained. The ingot was homogenized at 1200 °C for 2 hours before hot rolling. Seven passes were applied, giving a plate of 450 × 150 × 15 mm^3. The alloy composition was measured by inductively coupled plasma mass spectrometry (ICP-MS). The key alloying elements are listed in Table 1.2. The microstructure of the as-received state is mainly composed of granular bainite and is homogeneous (Figure 1.3). No notable texture was observed.

Element	**C**	**Mn**	**Si**	**Ti**	**Nb**	**V**	**Mo**	**Al**	**Cr**	**N**	**S**
wt%	0.062	1.91	0.50	**0.085**	**0.039**	0.002	0.212	0.065	0.013	0.006	0.003
at%	0.286	1.93	0.99	**0.098**	**0.023**	0.002	0.122	0.134	0.013	0.023	0.005

Table 1.2: Bulk composition of the steel determined by ICP-MS.

1.3.2 Grain growth measurements[2]

Cylindrical samples of 10 mm length and 4 mm diameter were machined from the steel plate and used to determine austenite grain sizes. A Bähr 805 DIL dilatometer was used to perform heat treatments consisting of a 5 °C/s ramp up to the austenitisation temperature T_A (950 °C< T_A <1250 °C), followed by a 10 min holding at T_A and cooling. After austenitisation, the heating was switched off and the samples cooled down to room temperature with an average cooling rate of 10 °C/s. A 2 mm wide flat surface was prepared along the sample length by mechanical grinding and polishing, finishing with 1 μm diamond solution. The temperature was controlled by welding a type K thermocouple in the middle of the samples. For all temperatures except 1250 °C, the austenite grain size was determined by the thermal etching method [AND 02b]. During the heat treatments, grooves were formed at the intersection of austenite grain boundaries with the flat surface [MUL 57, HAL 63]. At 1250 °C, thermal etching turned out to be unsuccessful, and a Béchet-Beaujard etching [Bé 55] was

[2]The heat treatments, thermal/chemical etching, and optical microscopy observations were performed by the partners from CENIM in Madrid.

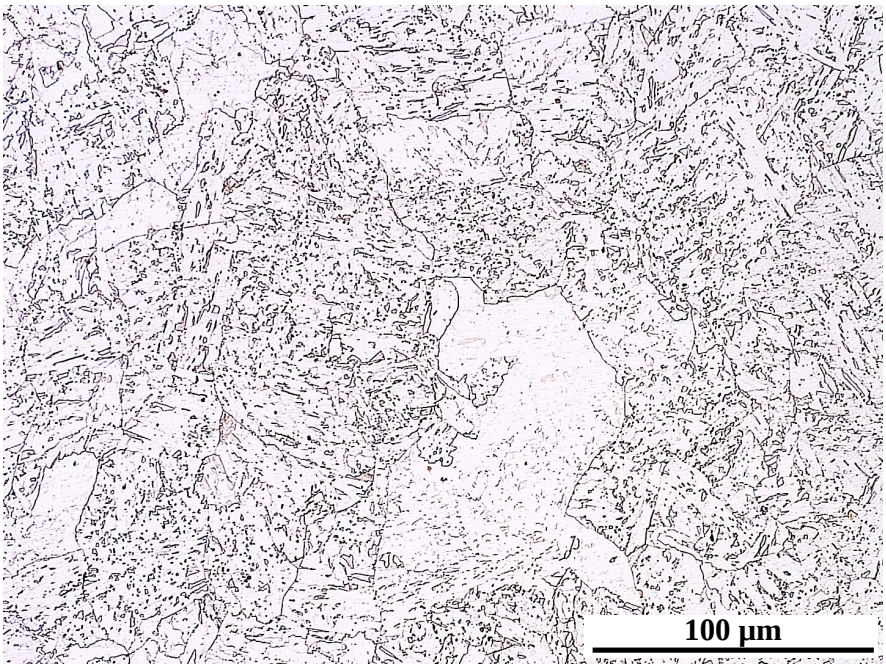

Figure 1.3: Optical micrograph of the as-received steel microstructure, etched with Nital. An homogeneous granular bainite microstructure showing no particular texture is observed.

performed instead. Since a martensitic microstructure is needed for Béchet-Beaujard etching, the sample was quenched (cooling rate of 100 °C/s) with helium after the isohermal holding at 1250 °C.

Etched samples were then observed using a Nikon Epiphot 200 optical microscope. For the thermally eched samples, Nomarski microscopy under bright field reflection illumination was used. This technique allows highlighting micro-topographic features, like the thermal grooves [SAN 10]. In order to avoid any inaccuracies on the temperature measurement due to the temperature gradient in the dilatometer, observations were performed on the same layer as where the thermocouple was welded. The areas of at least 50 grains were determined using FIJI [SCH 12] by manual detouring (Figure 1.4). The equivalent area diameter D_A of circular grain was calculated from each measured grain area A:

$$D_A = \sqrt{\frac{4A}{\pi}} \tag{1.9}$$

In order to account for the intercept effects, the mean grain size D was estimated by multiplying the number-based mean equivalent area diameter D_A by 1.2, in accordance with [GIU 99].

1.3.3 Additional heat treatments for precipitation and austenite composition characterization

Several heat treatments were performed in the austenite stability domain between 1050 °C and 1280 °C, using parallelepiped samples machined from the as-received steel plate. In order to avoid excessive oxidation and decarburization, heat treatments were either performed under dynamic

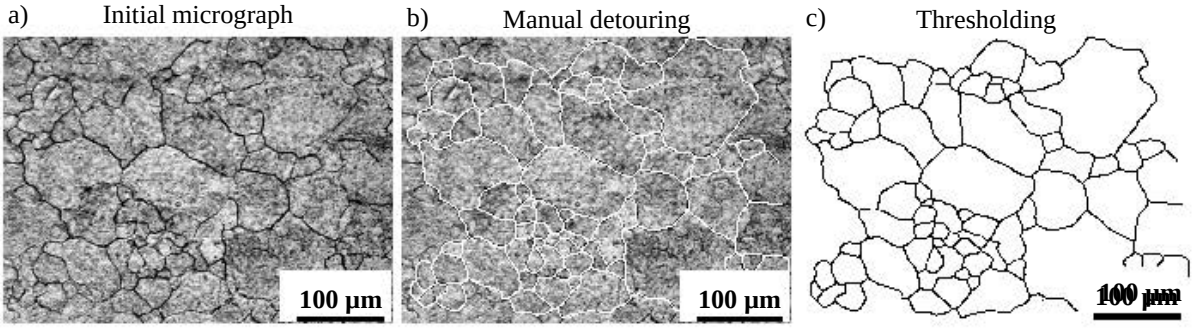

Figure 1.4: Image analysis procedure for the determination of the equivalent area diameter of the austenite grains. Starting from a thermal etching optical micrograph (a), grains were manually detoured (b) and the image thresholded (c).

secondary vacuum or in primary vacuum sealed quartz tube. The samples were directly inserted in the furnace heated up to the target temperature. After heat treatment, the samples underwent water quenching and martensitic microstructures were obtained.

1.3.4 Precipitation characterization

The precipitation state of the as-received condition and heat treated samples were investigated by means of scanning (SEM) and transmission electron microscopy (TEM).

1.3.4.1 Bulk samples

Bulk samples were investigated for the analysis of precipitates presenting micrometric sizes. After polishing down to 1 μm, samples were etched with a nital 2 % solution and observed in a ZEISS Supra 55VP field emission gun (FEG) scanning electron microscope (SEM). Energy-dispersive X-ray (EDX) analysis was carried out using an Oxford EDX analyser with silicon drift detector.

1.3.4.2 Carbon extractive replicas

Precipitates presenting nanometric sizes were collected for investigation on carbon extractive replicas. After polishing down to 1 μm and nital (4 %) etching, a carbon layer was deposited on the etched sample using a SCD500 BALTEC carbon evaporator. Squares of approximately $2 \times 2\,\mathrm{mm}^2$ were drawn on the carbon-coated surface using a cutter blade. Samples were thereafter placed in a 4 % nital solution until the sliced carbon films start delaminating from the sample surface. A carbon layer containing the precipitates was thus obtained. Afterwards, the carbon replicas were rinsed in three successive ethanol baths, and placed on nickel or copper grids.

The precipitates were characterized in scanning transmission electron microscopy mode (STEM) - high angle annular dark field (HAADF) imaging. The STEM-HAADF technique provides a Z-contrast [WIL 09], which facilitates the observations: a large contrast appears between the carbon layer (dark) and the precipitates (bright). Other observations were performed on carbon replicas using a ZEISS Supra 55VP FEG-SEM. Using backscattered electrons (BSE) mode, a chemical

contrast was also obtained.

Using FIJI [SCH 12], an image analysis procedure was developed to determine the precipitate sizes. The projected surface of precipitates A_P was determined and an equivalent radius was calculated:

$$r = \sqrt{\frac{A_P}{\pi}} \tag{1.10}$$

Both TEM and SEM were equipped with Oxford EDX analyzers with silicon drift detectors. EDX measurements were used to determine the relative contents of the metallic species such as Ti, Nb and S. Lighter elements such as C and N cannot be correctly quantified by EDX. Moreover, carbon quantification was hindered by the presence of the carbon layer of the replicas. However, nitrogen can be detected if present in the precipitates.

Finally, the crystallographic nature of the precipitates was investigated using selected area electron diffraction (SAED) on a JEOL 2010F TEM operating at 200 kV. The composition of each precipitate analyzed by SAED was checked by EDX. The crystallography data used for indexing the SAED patterns are extracted from [WYC 63], available on [GRA 09]. $Ti_4C_2S_2$ precipitates present an hexagonal structure of space group $P6_3/mmc$ with $a = b = 0.3210$ nm and $c = 1.120$ nm. TiN, TiC and NbC all share the same face-centered cubic (fcc) structure of space group $Fm\bar{3}m$ with respectively $a = 0.4235$ nm, $a = 0.4319$ nm, and $a = 0.4469$ nm.

1.3.5 Atom probe tomography[3]

Atom probe tomography (APT) was applied to measure the austenite composition in Ti/Nb. The samples used for this APT work were resulting from isothermal heat treatments followed by water quenching, as presented in part 1.3.3. The measurements were therefore performed on martensitic microstructures obtained after quenching. Due to the diffusion-less nature of its transformation mechanism, the composition of martensite is that of the parent austenite. Table 1.3 lists the heat treatments performed for APT measurements.

Temperature (°C)	1050	1120	1200	1280
Time (min)	240	120	60	60

Table 1.3: Heat treatments performed for APT measurements of austenite composition.

The specimen tips were prepared using a classical electro-polishing method. First, the tips were thinned using a solution of 75 % acetic acid and 25 % perchloric acid. Then, a final polishing was completed using a mixture of 2 % perchloric acid in 98 % 2 butoxyethanol at 15 V until separation of the rod into two pieces with a needle tip radius smaller than 50 nm. The experiments were carried out on a LEAP® 4000HR device from CAMECA, the reconstruction procedure was conducted using IVAS 3.6 software package. The peaks superimposition on the experimental mass spectrum was manually corrected from the isotopes ratios. In order to get enough precision in the quantification of microalloying additions, several tens of millions of atoms were collected per heat treated condition.

[3]Atom probe measurements were performed in GPM Rouen, by Frédéric Danoix.

In the experimental mass spectrum generated, a peak convolution is observed between the principal isotope of Ti ($^{48}Ti^{2+}$) and a peak from carbon molecular ions ((^{12}C - $^{12}C)^{+}$), that both are around 24 Da. Therefore, the principal peak of Ti, representing approximately 75 % of the total Ti amount was not used for quantification of the Ti. The measurement of Ti in solid solution relied on the peaks of the two first isotopes ($^{46}Ti^{2+}$ and $^{47}Ti^{2+}$) representing 15 % of the total Ti amount.

If the atoms are randomly distributed, the standard deviation associated with the measurement of a composition by APT is given by [DAN 07]:

$$\sigma = \sqrt{\frac{C(1-C)(1-Q)}{N}} \tag{1.11}$$

with C the measured composition, N the total number of atoms collected, and Q the detection efficiency. For several millions of atoms, this standard deviation becomes negligible.

Another source of error on this composition measurement can arise from APT very local nature, thus sensitive to possible heterogeneities in composition. For each heat-treated state, several samples were analyzed. The error on composition measurement is reported by the standard error on the different experiment values obtained ($\sigma_{\bar{x}}$):

$$\sigma_{\bar{x}} = \sqrt{\frac{\sum_i (C_i - C_m)^2}{n}} \tag{1.12}$$

where C_m is the average composition measured, C_i the different individual composition measured, and n is the number of observations.

1.4 Experimental results

1.4.1 Austenite grain size measurements

Figure 1.5 displays optical micrographs from heat treatments showing prior austenite grain boundaries (PAGB) revealed by the thermal etching method. Most of these micrographs allowed an accurate tracking of the austenite grain boundaries. For the lower temperatures (950 °C and 1000 °C), thermal etching was less effective and prior austenite grain sizes (PAGS) determination was more tedious. Figure 1.6 shows the PAGB revealed by a Béchet-Beaujard etching for the 1250 °C heat treatment. For all temperatures, some austenite grain boundaries were not revealed, leading to uncertainties, that were estimated to be 20 %.

Figure 1.7 shows the resulting average PAGS measurements after 10 min isothermal heat treatments at temperature ranging from 950 °C to 1250 °C. As expected, raising temperature results in increasing PAGS. Up to 1050 °C, PAGS remains roughly constant, with values between 10 and 20 µm. Starting from 1100 °C, a substantial austenite grain growth occurs. At 1250 °C, coarse grains were obtained, with a final grain diameter around 400 µm.

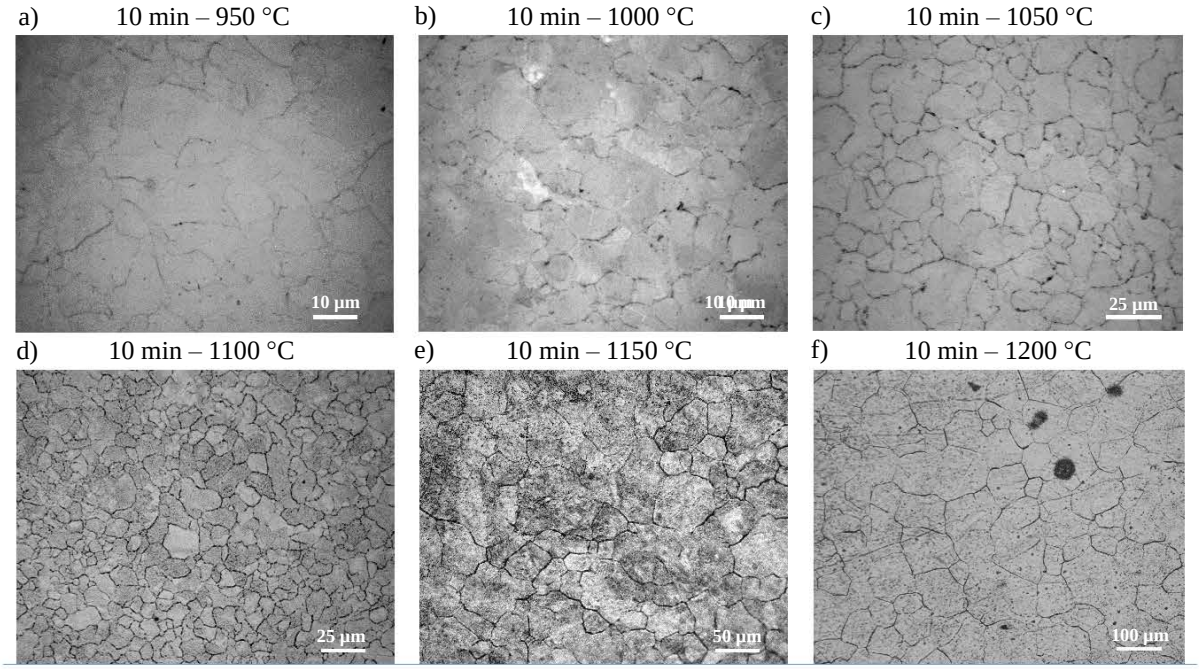

Figure 1.5: Optical micrographs showing PAGB revealed by thermal etching for 10 min holding treatments at 950 °C, 1000 °C, 1050 °C, 1100 °C, 1150 °C, and 1200 °C.

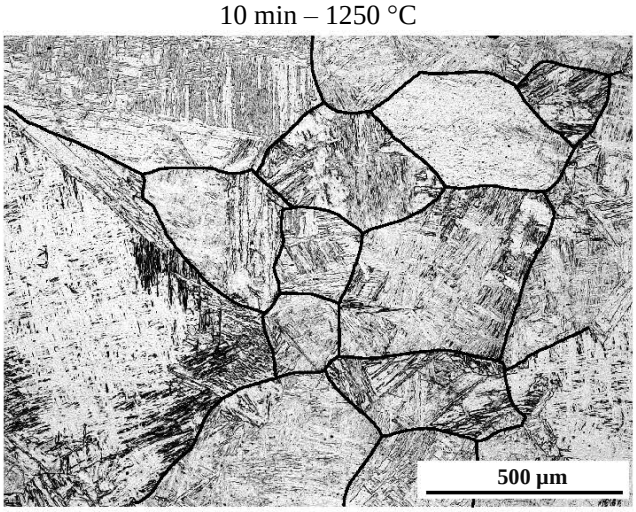

Figure 1.6: Optical micrograph showing PAGB revealed by Bechet-Beaujard etching after a 10 min holding treatment at 1250 °C. The PAGB were manually underlined in order to facilitate their identification.

1.4.2 Precipitation characterization

1.4.2.1 As-received condition

Nature of precipitates observed

On bulk samples, complex carbonitrides (Ti,Nb)(C,N) with micrometric sizes were found. As seen

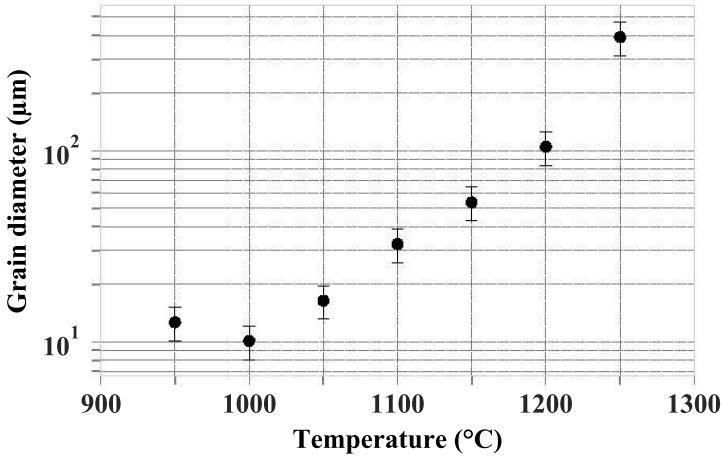

Figure 1.7: Evolution of PAGS for 10 minutes heat treatments at temperatures ranging from 950 °C to 1250 °C

in Figure 1.8, Ti and N are the main elements detected in these precipitates. Lower amounts of Nb and C were detected. In the following, this population is referred to as (Ti,Nb)(C,N)$_{large}$. Other complex assemblies of precipitates were observed on bulk samples. These are composed of (Ti,Nb)(C,N)$_{large}$ and manganese sulphides MnS that often nucleate on aluminum oxide particles (Figure 1.9).

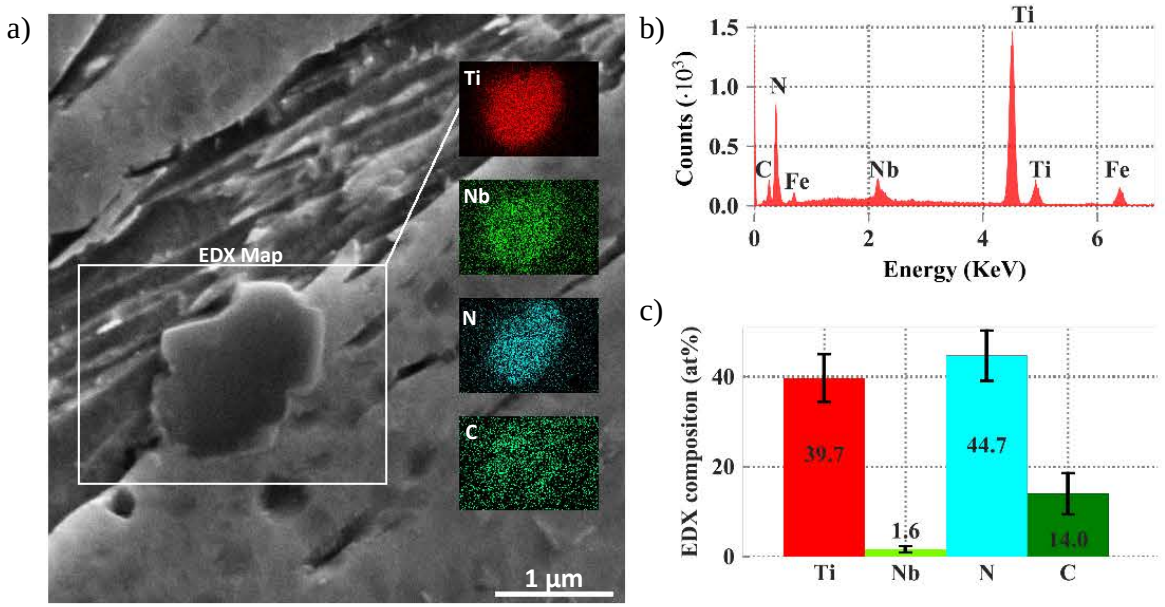

Figure 1.8: (Ti,Nb)(C,N)$_{large}$ population observed on bulk samples. a) Displays a SEM micrograph showing a (Ti,Nb)(C,N)$_{large}$ precipitate with its corresponding EDX map. b) shows its associated EDX spectra and (c) gives the mean EDX composition of this population, determined on 13 different precipitates.

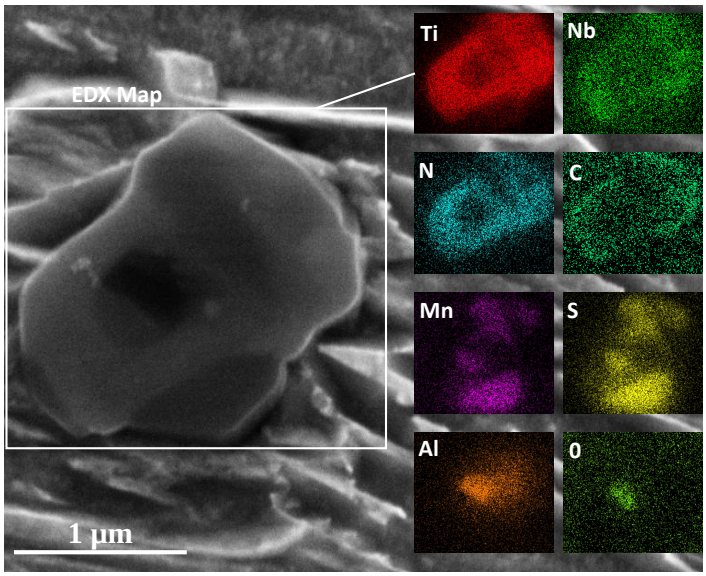

Figure 1.9: Complex precipitate composed of (Ti,Nb)N and MnS nucleated on an aluminum oxide, observed on bulk samples by SEM, with associated EDX map.

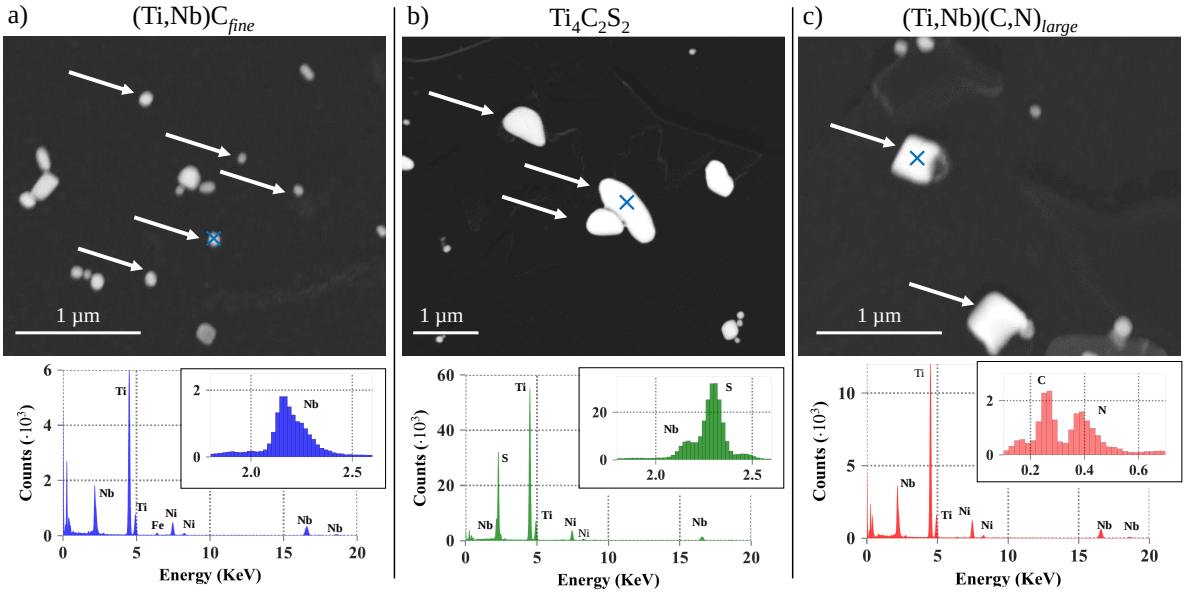

Figure 1.10: STEM-HAADF observation of the three populations of precipitates found in as-received steel on carbon replicas, with associated EDX spectra. The Ni lines appearing in the spectra correspond to the grid holding the carbon replica. The blue crosses indicate the precipitates on which EDX was performed.

Smaller precipitates, presenting sub-micrometer sizes, were collected and analyzed on carbon replicas. Three types of precipitates were identified on carbon replicas in the initial state, combining STEM-HAADF observations and EDX (Figure 1.10) with bright field observations and SAED (Figure 1.11):

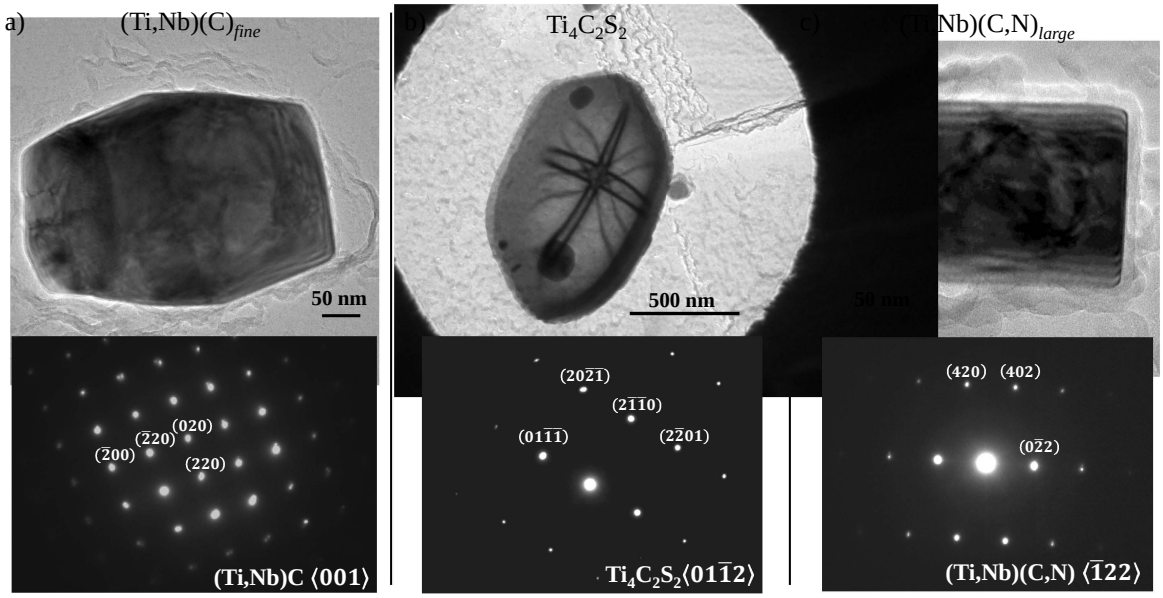

Figure 1.11: Bright field TEM observation of the 3 populations of precipitates found in as-received steel, with associated Selected area diffraction patterns.

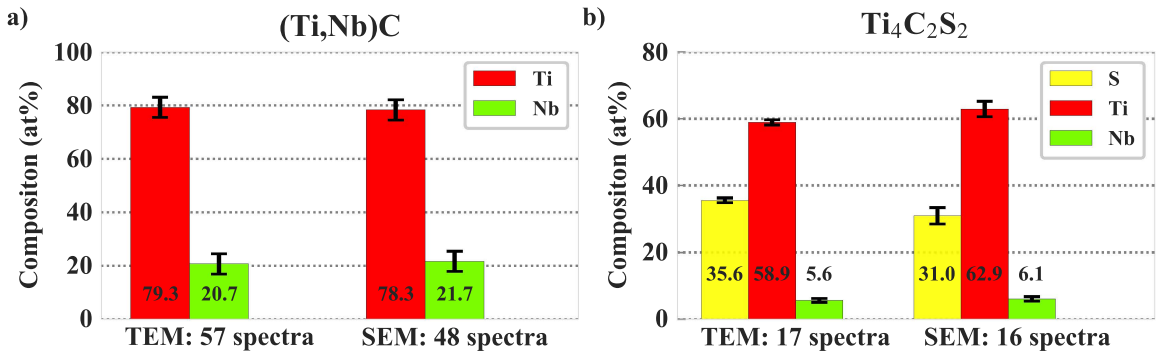

Figure 1.12: Mean EDX composition of (a) (Ti,Nb)C$_{fine}$ and (b) $Ti_4C_2S_2$ precipitates in as-received condition determined on carbon replicas in TEM and SEM.

(i) The main population observed was composed of precipitates whose radii approximately range from a few tens of nm to 150 nm. They exhibited various geometrical forms, but were mainly spherical and cuboidal (Figure 1.10 a)). Their mean composition in heavy elements were determined by EDX in SEM and TEM. Approximately 80 at% of Ti and 20 at% of Nb were detected. Measurements in SEM and TEM gave similar values (see Figure 1.12 a)). The indexation of SAED patterns confirms that these populations present a fcc structure of space group Fm$\bar{3}$m, like TiC and NbC (Figure 1.11 a)). Although no peak of N emerges from the EDX spectra acquired from these precipitates, it is not possible to exclude the presence of N in quantities below the detection limit. As a first approximation, it can be stated that these precipitates are mixed titanium-niobium carbides (Ti,Nb)C. In the following, this population

is referred to as (Ti,Nb)C_{fine}.

(ii) Some precipitates presenting larger sizes and mainly containing Ti and S were found. Small amounts of Nb were also detected in these precipitates. SAED patterns show that they exhibit a hexagonal structure of space group $P6_3/mmc$ (Figure 1.11 b). Their mean composition was determined by EDX (Figure 1.12 b)). SEM and TEM measurements were once again similar. The composition is compatible with $Ti_4C_2S_2$ (Ti /S $\approx$ 2), leaving no doubt on the nature of this population.

(iii) Finally, some (Ti,Nb)$(C,N)_{large}$ precipitates were also identified on carbon replicas. Due to the presence of the carbon layer, it was not possible to quantify C by EDX. They present a fcc structure of space group $Fm\bar{3}m$ (Figure 1.11 c)), like TiC and TiN.

These three populations are visually distinguishable because they present very different sizes and geometrical aspects. They can as well be distinguished by performing EDX measurements, based on nitrogen or sulphur peaks.

Initial size distribution of (Ti,Nb)C_{fine}

The titanium-niobium carbides (Ti,Nb)C_{fine} were the most frequently observed precipitates, and also the smaller ones. Therefore, they are likely to be the ones governing austenite grain growth during soaking at high temperature. Using the analysis routine developed on FIJI, the particle size distribution was determined from a series of images taken randomly at the same magnification in both SEM (BSE mode) and TEM (STEM-HAADF mode). The resulting precipitate size distributions are shown in Figure 1.13. Log-normal laws accurately fit experimental size distributions for both SEM and TEM. The mean precipitates radius are equal (56 nm for BSE and 58 nm for STEM-HAADF). However, the size distribution determined by SEM is slightly larger than the TEM one, which could be explained by the lower spatial resolution of SEM observations.

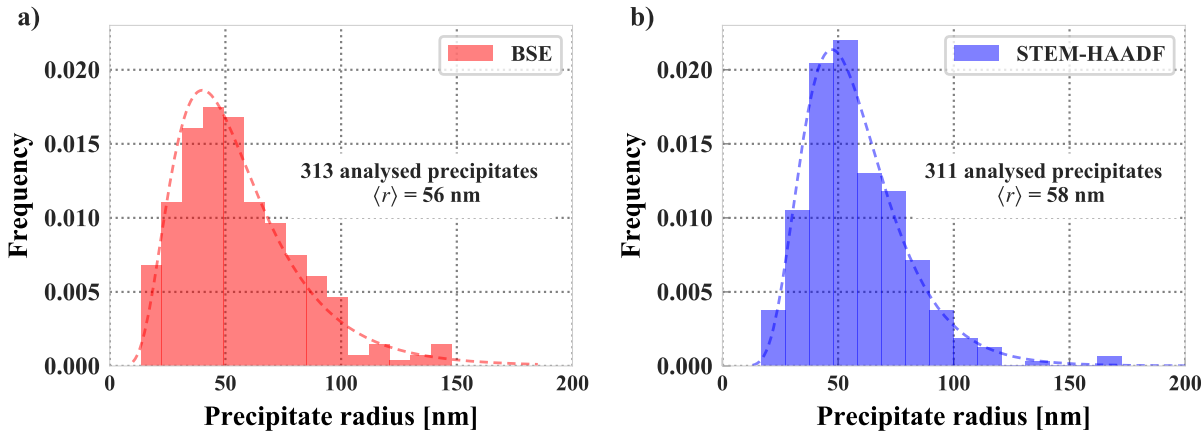

Figure 1.13: Initial distribution of (Ti,Nb)C_{fine} precipitates characterized by MEB-BSE and STEM-HAADF

1.4.2.2 Heat-treated samples

The thermal stability of the four different types of precipitates was studied by investigation of the precipitation state after isothermal heat treatments at four different temperatures: 1050 °C, 1120 °C, 1200 °C, and 1280 °C. Below 1280 °C, the same four types of precipitates found in the as-received state were still present. At 1280 °C, there was no trace of (Ti,Nb)C_{fine} nor $Ti_4C_2S_2$ on carbon replicas, showing that these two populations of precipitates are no longer stable and completely dissolved at 1280 °C. A summary of the different precipitates found after each heat treatments is given in Table 1.4.

Heat treatment	**Temperature (°C)**	**1050**	**1120**	**1200**	**1280**
	Time (min)	240	120	30, 60	10, 30, 60
Precipitates observed (✓= yes / ✗= no)	**(Ti,Nb)C_{fine}**	✓	✓	✓	✗
	(Ti,Nb)$(C,N)_{large}$	✓	✓	✓	✓
	$Ti_4C_2S_2$	✓	✓	✓	✗
	MnS	✓	✓	✓	✓

Table 1.4: Precipitates observed for each heat treatment performed.

The EDX composition of (Ti,Nb)C_{fine} after varying heat treatments are very close to the one determined in the initial condition (Figure 1.14). Thus the composition of these population does not evolve significantly over the temperature range studied. Additionally, the mean radius of (Ti,Nb)C_{fine} was measured after 240 min at 1050 °C and 30 min at 1200 °C (Figure 1.15). Mean radii of 66 nm and 67 nm were respectively found.

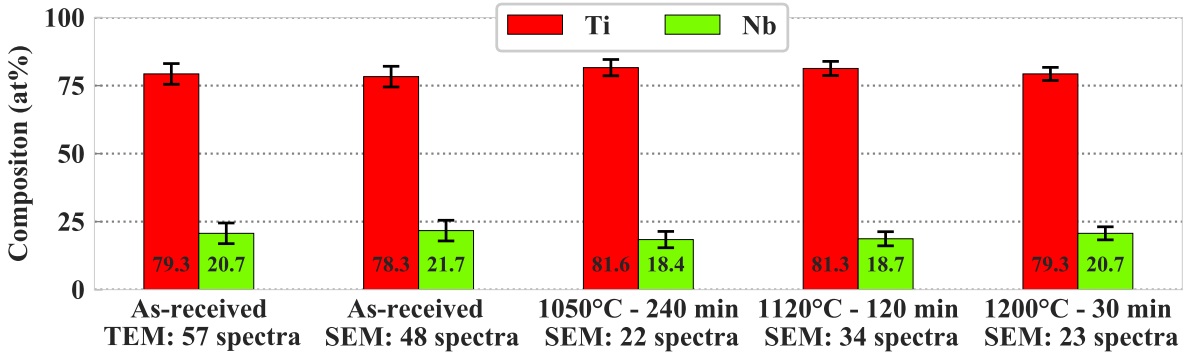

Figure 1.14: Mean EDX composition of (Ti,Nb)C_{fine} found on carbon replicas in as-received state and after varying heat treatments.

1.4.3 Atom probe tomography measurements of austenite composition

1.4.3.1 Austenite composition

APT was applied to measure the austenite composition after four heat treatments at 1050 , 1120 , 1200 , and 1280 °C. The total number of analyzed ions for each conditions can be retrieved in Table

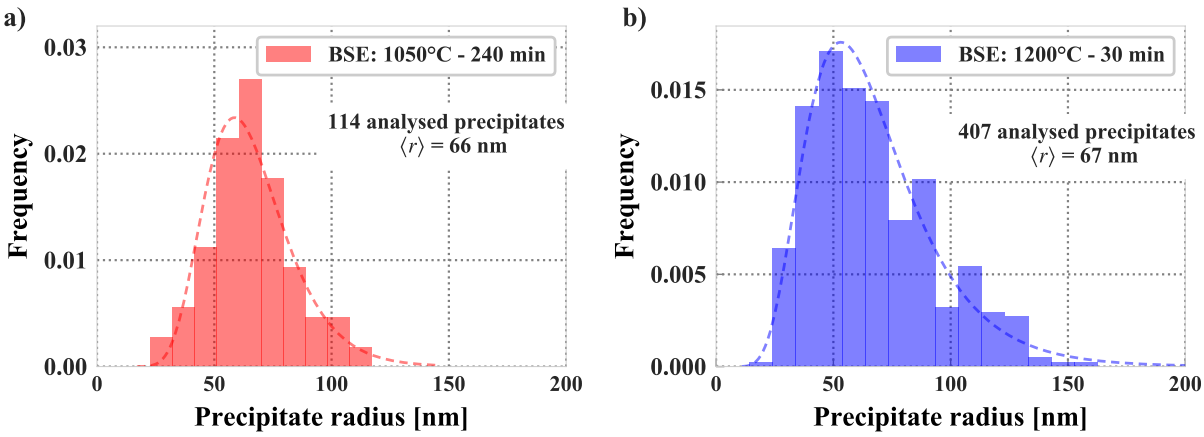

Figure 1.15: Experimental (Ti,Nb)C$_{fine}$ size distributions after (a) 240 min at 1050 °C and (b) 30 min at 1200 °C.

1.5. The amount of Ti and Nb in austenite increases with increasing temperature, indicating the dissolution of (Ti,Nb)C$_{fine}$ precipitates. Figure 1.16 displays the reconstructed positions of carbon, titanium, and niobium within a specimen heat treated at 1200 °C.

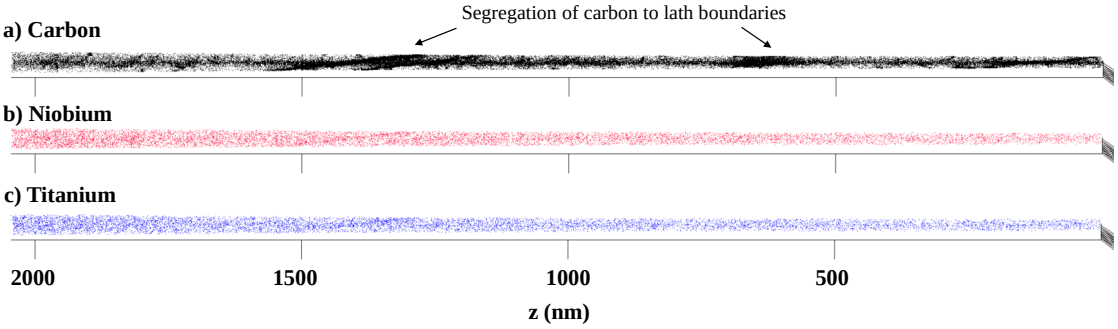

Figure 1.16: Reconstructed atomic positions of (a) carbon, (b) niobium and (c) titanium of an APT sample heat treated 60 minutes at 1200 °C.

The specimen is nearly 2 microns long, so that several martensite laths formed during quenching are analyzed. As expected for martensitic steels, a segregation of carbon is observed at lath boundaries. The distribution of niobium and titanium is homogeneous throughout the sample. No precipitate was intercepted during analyzes, therefore the whole tip composition measurement is representative of the matrix composition.

1.4.3.2 (Ti,Nb)C$_{fine}$ composition

An estimation of the composition of the (Ti,Nb)C$_{fine}$ population is proposed in this section. For the sake of clarity, (Ti,Nb)C$_{fine}$ are referred to as (Ti$_x$,Nb$_{1-x}$)C in the following, where x is the unknown to determine. The total amount of Ti and Nb available for the formation of (Ti$_x$,Nb$_{1-x}$)C,

Heat treatment	Temperature (°C)	1050	1120	1200	1280
	Time (min)	240	120	60	60
Austenite composition	Analyzed ions ($\cdot 10^6$)	17.9	60.2	100.4	47.5
	Nb (ppm)	**4**	**61**	**155**	**201**
	std error of the mean (%)	12.2	9.3	6.9	10.9
	Ti (ppm)	**141**	**290**	**412**	**531**
	std error of the mean (%)	10.9	2.5	8.0	12.5

Table 1.5: Total number of ions analyzed by APT, and austenite Ti and Nb solute content for each heat treatment performed.

respectively X^0_{Ti} and X^0_{Nb}, are also estimated.

A composition close to $(Ti_{0.80},Nb_{0.20})C$ was determined by EDX. This chemical content is inconsistent with the composition of solid solution measured by APT (see Table 1.5). It is therefore proposed here to derive the value of x from the evolution of austenite composition measured by APT.

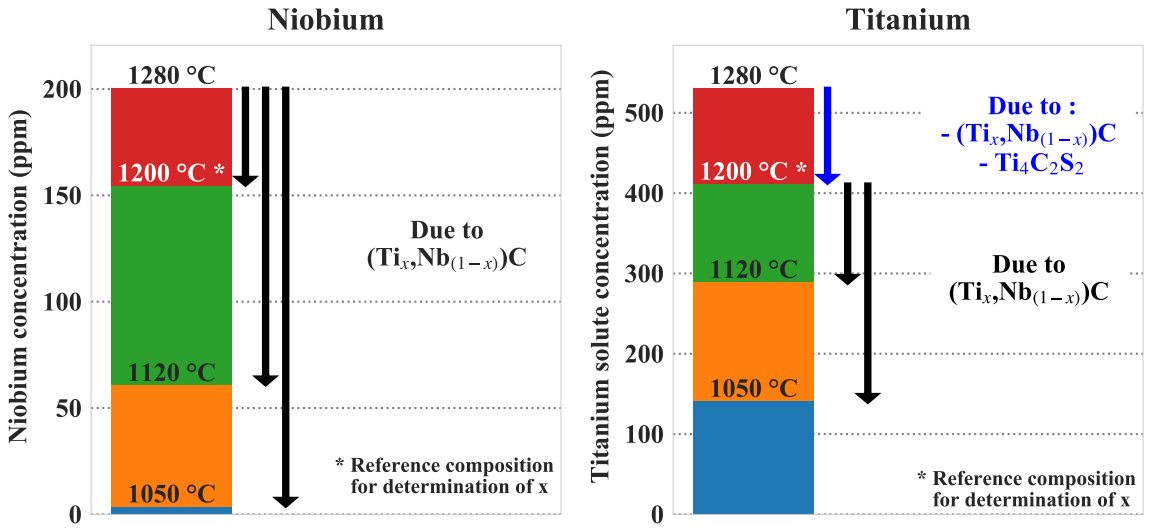

Figure 1.17: Niobium and titanium amounts in solid solution in austenite between 1050 °C and 1280 °C. Niobium evolution is only related to the formation of $(Ti_x,Nb_{1-x})C$ whereas titanium is affected by the formation of $(Ti_x,Nb_{1-x})C$ and $Ti_4C_2S_2$ between 1280 °C and 1200 °C.

As shown in part 1.4.2, the Ti evolution from 1200 °C to 1280 °C is affected by the dissolution of both $(Ti_x,Nb_{1-x})C$ and $Ti_4C_2S_2$ (Figure 1.17). The amount of Ti involved in both population is *a priori* unknown. Below 1200 °C, it is however reasonable to assume that the evolution of Ti and Nb in solid solution is only related to the dissolution of $(Ti_x,Nb_{1-x})C$. Thus, the APT measurement at 1200 °C are taken as the reference composition for the derivation of x, X^0_{Ti}, and X^0_{Nb}.

At 1050 and 1120 °C, the differences in Nb and Ti concentrations relative to the reference, ΔNb and ΔTi, are calculated. Assuming that the evolution of the amount of Ti and Nb in solid solution

are only related to the $(Ti_x,Nb_{1-x})C$, the value of x can be estimated from the ratio $R = \Delta Ti/\Delta Nb$:

$$x = \frac{R}{1+R} \tag{1.13}$$

$x = 0.57$ and $x = 0.64$ are found at 1050 °C and 1120 °C, respectively. Thus, the precipitate composition coherent with the respective evolutions of Ti and Nb is $x = 0.61 \pm 0.04$.

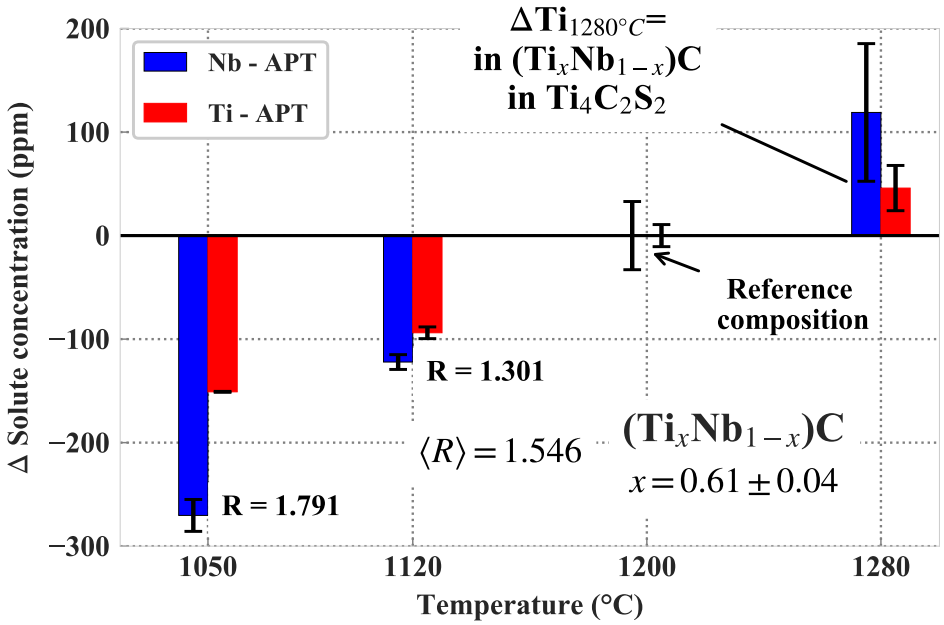

Figure 1.18: Determination of x based on the respective evolution of Ti and Nb in solid solution below 1200 °C. The total amount of Ti and Nb available for $(Ti_x,Nb_{1-x})C$ are deduced from the analysis.

Since Nb evolution is only related to the $(Ti_x,Nb_{1-x})C$, the total amount of Nb available for the formation of $(Ti_x,Nb_{1-x})C$ is directly given by the APT measurement at 1280 °C:

$$X^0_{Nb} = X^{SS}_{Nb,APT}(1280\,°C) = 201 \text{ ppm} \tag{1.14}$$

The total amount of Ti available for the formation of $(Ti_x,Nb_{1-x})C$ is estimated using the mean R ratio, $\langle R \rangle$:

$$X^0_{Ti} = X^{SS}_{Ti,APT}(1200\,°C) + \langle R \rangle \cdot (X^0_{Nb} - X^{SS}_{Nb,APT}(1200\,°C)) = 483 \text{ ppm} \tag{1.15}$$

1.4.4 Estimation of $(Ti_x,Nb_{1-x})C$ volume fraction

The evolution of Nb solute content was used as the reference for the calculation of volume fraction. The volume fraction f_v was estimated by:

$$f_v = \frac{X^0_{Nb} - X^{SS}_{Nb}}{X^P_{Nb}\alpha_v - X^{SS}_{Nb}\alpha_v} \tag{1.16}$$

where X^P_{Nb} is the atomic fraction of Nb within $(\mathrm{Ti}_x\mathrm{Nb}_{1-x})C$, and α_v is the ratio between the atomic volume of austenite, v^{at}_γ, and the one of $(\mathrm{Ti}_x,\mathrm{Nb}_{1-x})\mathrm{C}$, v^{at}_P:

$$\alpha_v = \frac{v^{at}_\gamma}{v^{at}_P} \tag{1.17}$$

Here, $v^{at}_\gamma = 1.227 \times 10^{-29}\,\mathrm{m}^3$ [TCF] and v^{at}_P was calculated by a law of mixture between that of pure TiC and NbC:

$$v^{at}_P = x \cdot v^{at}_{TiC} + (1-x) \cdot v^{at}_{NbC} \tag{1.18}$$

with $v^{at}_{TiC} = 1.100 \times 10^{-29}\,\mathrm{m}^3$, $v^{at}_{NbC} = 1.181 \times 10^{-29}\,\mathrm{m}^3$ [TCF] and $x = 0.61$.

Neglecting the uncertainty of α_v, the uncertainty on the volume fraction, Δf_v, is given from the partial derivatives of f_v:

$$\Delta f_v = \left|\frac{\partial f_v}{\partial X^0_{\mathrm{Nb}}}\right| \cdot \Delta X^0_{\mathrm{Nb}} + \left|\frac{\partial f_v}{\partial X^{SS}_{\mathrm{Nb}}}\right| \cdot \Delta X^{SS}_{\mathrm{Nb}} + \left|\frac{\partial f_v}{\partial X^P_{\mathrm{Nb}}}\right| \cdot \Delta X^P_{\mathrm{Nb}} \tag{1.19}$$

with:

$$\frac{\partial f_v}{\partial X^0_{\mathrm{Nb}}} = \frac{1}{\alpha_v \cdot (X^P_{\mathrm{Nb}} - X^{SS}_{\mathrm{Nb}})} \tag{1.20}$$

$$\frac{\partial f_v}{\partial X^{SS}_{\mathrm{Nb}}} = \frac{X^P_{\mathrm{Nb}} + X^0_{\mathrm{Nb}}}{\alpha_v \cdot (X^P_{\mathrm{Nb}} - X^{SS}_{\mathrm{Nb}})^2} \tag{1.21}$$

$$\frac{\partial f_v}{\partial X^P_{\mathrm{Nb}}} = \frac{X^{SS}_{\mathrm{Nb}} - X^0_{\mathrm{Nb}}}{\alpha_v \cdot (X^P_{\mathrm{Nb}} - X^{SS}_{\mathrm{Nb}})^2} \tag{1.22}$$

The relative uncertainties on X^{SS}_{Nb} were given in Table 1.5. The uncertainty on ΔX^0_{Nb} is equal to the one of X^{SS}_{Nb} at 1280 °C. Following the precipitate chemistry, X^P_{Nb} is equal to $x/2$. Thus, the uncertainty on X^P_{Nb} is estimated to 0.02 (0.04/2) according to the estimation of x presented in part 1.4.3.2.

The calculated volume fraction after isothermal heat treatments can be retrieved in Table 1.6. Logically, the precipitated volume fraction increases as the heat treatment temperature decreases.

Temperature (°C)	**1050**	**1120**	**1200**
Time (min)	240	120	60
Volume fraction of (Ti,Nb)C$_{fine}$ (%)	0.109 ± 0.024	0.078 ± 0.023	0.026 ± 0.021

Table 1.6: Calculated volume fraction of (Ti,Nb)C$_{fine}$ from APT for each heat treatment performed.

1.5 Model

1.5.1 Equilibrium calculations

Modeling the evolution of precipitation state with time and temperature requires having a correct estimate of the stability domain of phases. In particular, the solubility product of the precipitates is an essential parameter. In the present case, the key population is (Ti,Nb)C$_{fine}$, whose size makes it effective for grain boundary pinning. A correct modeling requires to know the actual amount of solute elements available to form (Ti,Nb)C$_{fine}$. Two types of calculations were performed and compared to estimate the stability of precipitates. Both calculations were carried out in austenite domain using the commercial Thermo-Calc software [AND 02a] with TCFE8 Steels/Fe-alloys database [TCF].

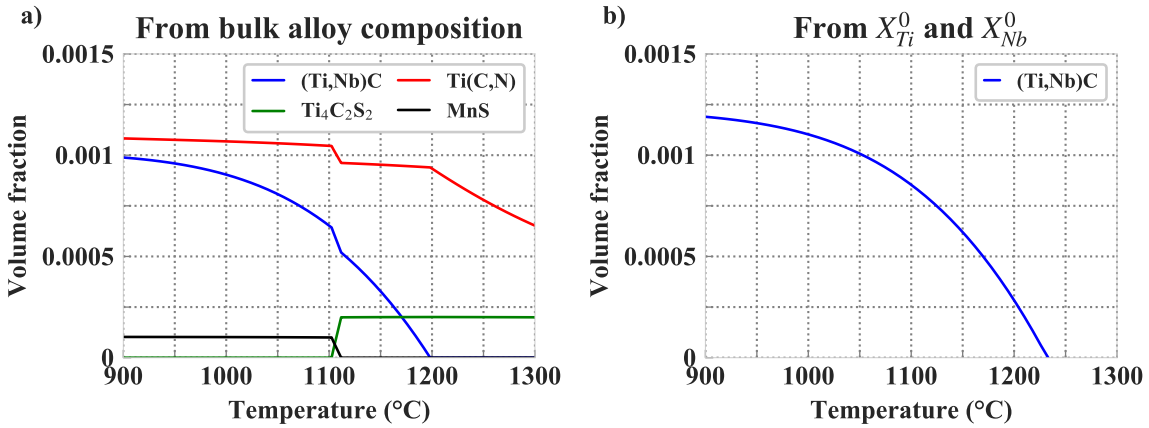

Figure 1.19: Equilibrium volume fractions of precipitates (a) resulting from Thermo-Calc calculations with TCFE8 using bulk alloy composition and (b) starting from X_{Ti}^0 and X_{Nb}^0 for calculating the solubility product of (Ti,Nb)C.

The first calculations were performed assuming full-equilibrium, using the ICP-MS composition given in Table 1.2. Four populations are coexisting with austenite: (Ti,Nb)C, Ti(C,N), $Ti_4C_2S_2$, and MnS (Figure 1.19 a)). MnS is found stable in the lower temperature range, whereas $Ti_4C_2S_2$ is stable at high temperatures. Between 1102 and 1112 °C, MnS are gradually dissolved and replaced by $Ti_4C_2S_2$. The stability of (Ti,Nb)C phase goes up to 1198 °C and the maximum volume fraction remains below 0.001. The volume fraction of Ti(C,N) population stays roughly constant around 0.001 and start decreasing once the (Ti,Nb)C population is not stable anymore. Both the volume fractions of Ti(C,N) and (Ti,Nb)C are affected by the progressive replacement of MnS by $Ti_4C_2S_2$ around 1100 °C.

These first full-equilibrium calculations do not seem to reflect the experimental results shown in section 1.3.4 for two main reasons:

(i) The respective stabilities of $Ti_4C_2S_2$ and MnS are in contradiction with the experiments. It has been shown experimentally that $Ti_4C_2S_2$ are no longer stable at 1280 °C, whereas MnS are.

(ii) The calculations also predict a complete dissolution of (Ti,Nb)C around 1200 °C whereas an intensive population of these precipitates were found on carbon replicas after heat treatments of 30 and 60 min at this temperature.

Thus, these full-equilibrium thermodynamics calculations do not allow the determination of the actual stability domain of the key (Ti,Nb)C_{fine} population. This is mainly due to the fact that the alloy's thermal history starting from high temperatures was not accounted for. In fact the (Ti,Nb)(C,N)$_{large}$ population observed experimentally is very stable and probably formed at very high temperatures or during the casting process [SCH 08]. A large proportion of Ti and Nb is therefore removed and no longer available for the formation of other precipitates.

As a consequence, the stability domain of (Ti,Nb)C_{fine} population was recalculated starting from the actual amounts of Ti and Nb available for their formation, X^0_{Ti} and X^0_{Nb}, that were determined in section 1.4.3.2. Sulfur and nitrogen are not considered in these calculations, assuming that they are contained in (Ti,Nb)(C,N)$_{large}$ and $Ti_4C_2S_2$. The composition of other alloying elements are extracted from the ICP-MS bulk composition given in Table 1.2. The resulting stability domain of (Ti,Nb)C is shown in Figure 1.19 b).

The dissolution temperature of (Ti,Nb)C calculated with Thermo-Calc is 1233 °C, which is more consistent with experimental observations. The maximum volume fraction of precipitates formed is slightly below 0.0012. TCFE8 database [TCF] gave a relatively constant composition of (Ti,Nb)C over the studied temperature range: $(Ti_{0.66\pm0.05},Nb_{0.34\pm0.05})C_{0.93\pm0.02}$. Thus, a simplified average composition between 900 °C and the dissolution temperature was taken. It was also assumed that the number of metallic (Ti and Nb) atoms was equal to the number of carbon atoms (no vacancy in precipitates), giving the following precipitate composition: $(Ti_{0.68},Nb_{0.32})C$.

Using the evolution of austenite composition with temperature, the solubility product was evaluated at each temperature using:

$$K_S = (X^{eq}_{\mathrm{Ti}})^{0.68}(X^{eq}_{\mathrm{Nb}})^{0.32}X^{eq}_{\mathrm{C}} \tag{1.23}$$

with X^{eq}_i the atomic fraction of the element i in austenite.

Then by linearly fitting the evolution of $\log_{10} K_S$ with $1/T$, the following expression was taken for the solubility product of (Ti,Nb)C:

$$\log_{10} K_S = -\frac{9612.4}{T(K)} + 0.40115 \tag{1.24}$$

1.5.2 Grain growth model

A Zener-type model accounting for the competition between driving pressure for grain growth P_D and precipitate pinning pressure P_P was used. Under the influence of pinning precipitates, the grain diameter D growth rate can be expressed by:

$$\frac{dD}{dt} = \begin{cases} M(P_D - P_P) & \text{if} \quad P_D - P_P > 0 \\ 0 & \text{if} \quad P_D - P_P < 0 \end{cases} \tag{1.25}$$

M is the interface boundary mobility, described by an Arrhenius law:

$$M = M_0 \exp\left(\frac{-Q_{GG}}{R_g T}\right) \tag{1.26}$$

Here M_0 is a pre-exponential factor, R_g is the gas constant and Q_{GG} is the activation energy for grain boundary mobility.

In the present model, both the corrected Zener theory and Rios theory, presented in part 1.2, are used and compared. The driving pressure for grain growth is calculated from equation 1.4 with $\beta = 1$.

In order to take into account the effect of several classes of precipitates with different sizes instead of adopting a mean-radius approach, the expression for pinning pressure was thus modified as:

$$P_P = \alpha\gamma \sum_i \frac{f_{vi}}{r_i} \tag{1.27}$$

where i is a summation index representing all the present precipitate classes of different radius r_i and having the volume fraction f_{vi}. $\alpha = 3/2$ in Zener's corrected theory, whereas $\alpha = 3$ in Rios's theory (as presented in Table 1.1).

1.5.3 Precipitation model

In this work, the software *PreciSo* [PER 08, PER 09] was used to follow the evolution of precipitation state during heat treatments. It is based on the classical nucleation, growth and coarsening theories, fully described in [WAG 05]. The precipitation state was characterized by the whole precipitate size distribution (Lagrange-like approach). It has to be noted that only reversion (precipitate dissolution) experiments are to be modeled, during which nucleation does not take place. However, we present the model as a whole, including the description of the nucleation step.

1.5.3.1 Nucleation

The formation of a precipitate from a supersaturated solution is associated with a variation of the Gibbs free energy $\Delta G(r)$. For a spherical precipitate of radius r, $\Delta G(r)$ is given by:

$$\Delta G(r) = \frac{4\pi}{3} r^3 \Delta g_{ch} + 4\pi r^2 \gamma_P \tag{1.28}$$

with γ_P the precipitate/matrix interfacial energy and Δg_{ch} the chemical driving force. In this expression, the elastic energy contribution is neglected. Equation 1.28 translates a competition between two antagonist energies: a beneficial volume energy (formation of a more stable phase) against a detrimental surface energy (creation of a new interface between precipitate and matrix). The radius value that maximizes $\Delta G(r)$ is called nucleation critical radius and is noted r^*:

$$r^* = \frac{-2\gamma_P}{\Delta g_{ch}} \tag{1.29}$$

The radius at which precipitates nucleate at a temperature T is noted $r^*_{k_{B,T}}$ and is given by [PER 08]:

$$r^*_{k_{B,T}} = r^* + \frac{1}{2}\sqrt{\frac{k_B T}{\pi \gamma_P}} \tag{1.30}$$

with k_B the Boltzmann constant. By introducing r^* into equation 1.28, the thermodynamic barrier for nucleation ΔG^* is derived:

$$\Delta G^* = \frac{16\pi\gamma_P}{3\Delta g_{ch}} \tag{1.31}$$

The chemical driving force Δg_{ch} is calculated from the solid solution supersaturation s. It represents the excess of solute elements beside the equilibrium conditions. For a $(\mathrm{Ti}_x, \mathrm{Nb}_{1-x})\mathrm{C}$ precipitate, s is given by:

$$s = \ln \frac{(X^{SS}_{\mathrm{Ti}})^x (X^{SS}_{\mathrm{Nb}})^{1-x} (X^{SS}_{\mathrm{C}})}{(X^{eq}_{\mathrm{Ti}})^x (X^{eq}_{\mathrm{Nb}})^{1-x} (X^{eq}_{\mathrm{C}})} \tag{1.32}$$

where X_i^{SS} is the atomic fraction of the element i in solid solution and X_i^{eq} is the atomic fraction of the element i in equilibrium conditions. The chemical driving force for nucleation Δg_{ch} is then directly proportional to the supersaturation:

$$\Delta g_{ch} = -\frac{k_B T}{v^p_{at}} s \tag{1.33}$$

where v^p_{at} is the atomic volume of the precipitate. Equilibrium conditions are dictated by the solubility product of the precipitates K_S. For $(\mathrm{Ti}_x, \mathrm{Nb}_{1-x})\mathrm{C}$, K_S is given by:

$$K_S = (X^{eq}_{\mathrm{Ti}})^x (X^{eq}_{\mathrm{Nb}})^{1-x} (X^{eq}_{\mathrm{C}}) \tag{1.34}$$

Please note that the solubility product is defined though the use of molar fractions here, instead of weight percentage that are common in literature. The solubility product K_S is temperature-dependent and is expressed in terms of two parameters A^{at} and B^{at}:

$$\log K_S = -\frac{A^{at}}{T} + B^{at} \tag{1.35}$$

The nucleation rate (*i.e.* the number of supercritical precipitates formed per unit of time and volume) is expressed by Kampmann and Wagner's equation [WAG 05]:

$$\frac{dN}{dt} = N_0 Z \beta^* \exp(-\frac{\Delta G^*}{k_B T})(1 - \exp(-\frac{t}{\tau})) \tag{1.36}$$

N_0 is a normalization constant and represents the number of available nucleation sites. β^* is the frequency at which atoms are added to the critical nucleus [PER 09] and is equal to:

$$\beta^* = \frac{4\pi r^{*2}}{a^4} (\sum_i \frac{X_i^P}{D_i X_i^m})^{-1} \tag{1.37}$$

This expression takes into account the diffusion of the solute elements by considering their diffusion coefficient D_i, the solute atomic fraction in the matrix X_i^m, the solute atomic fraction in the precipitate X_i^P and the matrix lattice parameter a.

τ is the incubation time,, given by [PER 08]:

$$\tau = \frac{2}{\pi \beta^* Z^2} \tag{1.38}$$

Z the Zeldovich factor, expressed for spherical particles by [PER 09]:

$$Z = \frac{v_{at}^p}{2\pi r^{*2}} \sqrt{\frac{\gamma_P}{k_B T}} \tag{1.39}$$

1.5.3.2 Growth and coarsening

The diffusion of solute elements governs the growth of nucleated precipitates. The diffusion coefficient of an element i, noted D_i, follows an Arrhenius law $D_i^0 \exp(-Q_i/(R_g T))$. D_i^0 is the pre-exponential factor, and Q_i is the activation energy. The growth rate of a precipitate is given for element i by:

$$\frac{dr}{dt} = \frac{D_i}{r} \frac{X_i^{SS} - X_i^{eq}(r)}{\alpha_v X_i^P(r) - X_i^{eq}(r)} \tag{1.40}$$

α_v is equal to v_{at}^m / v_{at}^p and $X_i^P(r)$ is the atomic fraction of element i at the interface between matrix and a precipitate of radius r.

In fact, the presence of an interface between matrix and precipitates (*i.e.* the interface curvature) modifies the local equilibrium and atomic fractions at the interface (Gibbs-Thomson effect [PER 05]). Thus, the concentrations of solute elements at the interface of a $(\mathrm{Ti}_x, \mathrm{Nb}_{1-x})\mathrm{C}$ precipitate are given by the solubility product modified by a factor traducing the effect of interface curvature:

$$X_{\mathrm{Ti}}^{eq}(r)^x \cdot X_{\mathrm{Nb}}^{eq}(r)^{1-x} \cdot X_{\mathrm{C}}^{eq}(r) = K_S \exp\left(\frac{2\gamma_P (x + 1 - x + 1) v_{at}^p}{r k_B T}\right) = K_S \exp\left(\frac{4\gamma_P v_{at}^p}{r k_B T}\right) \tag{1.41}$$

Eqs. 1.40 and 1.41 provide a system of 4 equations (3 diffusion equations plus solubility product) with 4 unknown (dr/dt and X_i^{eq}).

At each timestep, growth of all existing classes is performed using eqs. 1.40 and 1.41. Consequently, precipitate coarsening (Ostwald ripening) is implicitly accounted for in this approach.

1.5.3.3 Mass balance

Finally, mass balance is performed to update the new solute content of all elements:

$$X_i^m = \frac{X_i^0 - \alpha_v f_v X_i^P}{1 - \alpha_v f_v} \tag{1.42}$$

where X_i^0 is the total amount of solute i.

1.5.4 Coupling between precipitation and grain growth models

Precipitation and grain growth models are coupled but run separately. The precipitation model was first run, providing the precipitate size distributions at each time step in the form of a large output file. Then, in a second stage, this file is read and, at each time step, the pinning pressure is calculated and the grain growth equation (eq.1.25) is integrated.

1.5.5 Model parameters

The evolution of precipitation was modeled for several holding treatments and coupled with the grain growth model, with the aim of reproducing the results obtained in section 1.4.1. Only (Ti,Nb)C$_{fine}$ precipitates were considered in the precipitation model. Given their respective sizes and number densities (see section 1.4.2), (Ti,Nb)(C,N)$_{large}$, $Ti_4C_2S_2$ and complex (Ti,Nb)(C,N)$_{large}$/MnS assemblies populations have a very limited pinning effect.

Parameter	**Value**	**Source/Comment**
M_0	10^4 m^{4}J^{-1}s^{-1}	Fit parameter.
Q_{GG}	390 kJ/mol	Uhm *et al.* [UHM 04].
Initial austenite grain diameter	10 µm	Grain growth measurements.
Austenite grain boundary energy	0.5 J m^{-2}	-
(Ti,Nb)C$_{fine}$ solubility product	$\log_{10} K_S = -9612.4\ K/T + 0.40115$	See equation 1.24.
(Ti,Nb)C$_{fine}$ initial volume fraction	0.0011	Close to maximum.
(Ti,Nb)C$_{fine}$ initial distribution	$\mu = 3.99$ and $\sigma = 0.369$	STEM-HAADF (Figure 1.13 a)).
(Ti,Nb)C$_{fine}$ interfacial energy γ_P	$0.955 - 4.27 \cdot 10^{-4} \cdot T(K)$ J m^{-2}	From [YON 89].

Table 1.7: Modeling parameters used.

The precipitation model only considers C, Ti, and Nb. Their respective amount are set according to the APT calculation of X^0_{Ti} and X^0_{Nb}. The precipitation model uses the solubility product given in equation 1.24. The diffusion coefficients of alloying elements were calculated from the MOBFE3 Steels/Fe-Alloys Mobility Database [MOB] (see Table 1.8).

Element	Content (wt.%)	D_0 [m^2 s^{-1}]	Q [J mol^{-1}]
C	0.0612	2.4×10^{-5}	147800
Ti	0.0415	1.5×10^{-5}	251000
Nb	0.0334	8.9×10^{-5}	266400

Table 1.8: Austenite content in alloying elements and diffusion coefficients used in the precipitation model. The diffusion data are calculated from the MOBFE3 mobility database of Thermo-Calc.

The (Ti,Nb)C$_{fine}$/matrix interfacial energy γ_P is not a critical parameter in the case of reversion heat treatments, since no nucleation takes place during reversion. γ_P was estimated using the temperature-dependent formulas calculated by misfitting dislocation theory in the work of Yong *et*

al.. [YON 89]:

$$\gamma_{TiC} = 0.9304 - 4.16 \cdot 10^{-4} \cdot T(K) \tag{1.43}$$

$$\gamma_{NbC} = 1.0058 - 4.49 \cdot 10^{-4} \cdot T(K) \tag{1.44}$$

The interfacial energy of (Ti,Nb)C_{fine} is calculated by a rule of mixtures between that of pure TiC and NbC, using $x = 0.68$ (mean composition of the precipitates given by Thermo-Calc):

$$\gamma_P = x \cdot \gamma_{TiC} + (1 - x) \cdot \gamma_{NbC} \tag{1.45}$$

The initial distribution of (Ti,Nb)C_{fine} precipitates experimentally determined by TEM (Figure 1.13 b)) serves as an input for the precipitation model. The STEM-HAADF distribution was used because of the better precision and resolution of TEM measurements compared to SEM ones. Based on a log-normal fitting curve, a theoretical precipitate distribution of 100 classes was calculated. The following expression was used for the probability density function:

$$f(r, \mu, \sigma) = \frac{1}{r\sigma\sqrt{2\pi}} \exp\left(-\frac{(\ln(r/\text{nm}) - \mu)^2}{2\sigma^2}\right) \tag{1.46}$$

with μ =3.991 nm and σ =0.369 nm. The total number of precipitates was adjusted in order to give an initial volume fraction of (Ti,Nb)C of 0.11 %, which is close to the maximum precipitate volume fraction given by mass balance.

An initial austenite grain diameter of 10 µm was considered, based on the experimental results given in section 1.4.1. An austenite grain boundary energy of 0.5 J/m^2 was assumed. Concerning grain boundary mobility, Uhm *et al.* [UHM 04] determined an expression of the activation energy by multiple regression analysis for steels containing C, Mn, Ni, Cr, Mo and Si. Based on this study, a value of 390 kJ/mol was used. The mobility factor M_0 is the only fitting parameter: the best agreement with experimentally determined PAGS was obtained with $M_0 = 10^4$ m^{4}J^{-1}s^{-1}.

1.6 Modeling Results

1.6.1 Precipitation

Several reversion heat treatments were simulated in the stability domain of (Ti,Nb)C_{fine} in austenite. Figure 1.20 shows the main outputs of the precipitation model for several reversion heat treatments ranging from 1000 °C to 1250 °C. Experimentally determined mean radii are also plotted.

For high temperatures, the volume fraction of (Ti,Nb)C_{fine} rapidly decreases as a result of the dissolution process. Meanwhile, a slight decrease of the mean precipitate radius and a consequent decrease of their number density (*i.e.* the number of precipitates per cubic meter) are observed. After precipitate shrinkage, coarsening occurs, causing a decrease in precipitate number density, and an increase in mean radius, while volume fraction remains constant. Eventually, the volume fraction reaches the equilibrium value given by the solubility product. The kinetics of precipitate dissolution is temperature-dependent: higher temperature leads to faster dissolution. At 1250 °C, the precipitates are finally completely dissolved. The kinetics of precipitate growth is also temperature-dependent: as expected, higher temperature leads to faster growth kinetics.

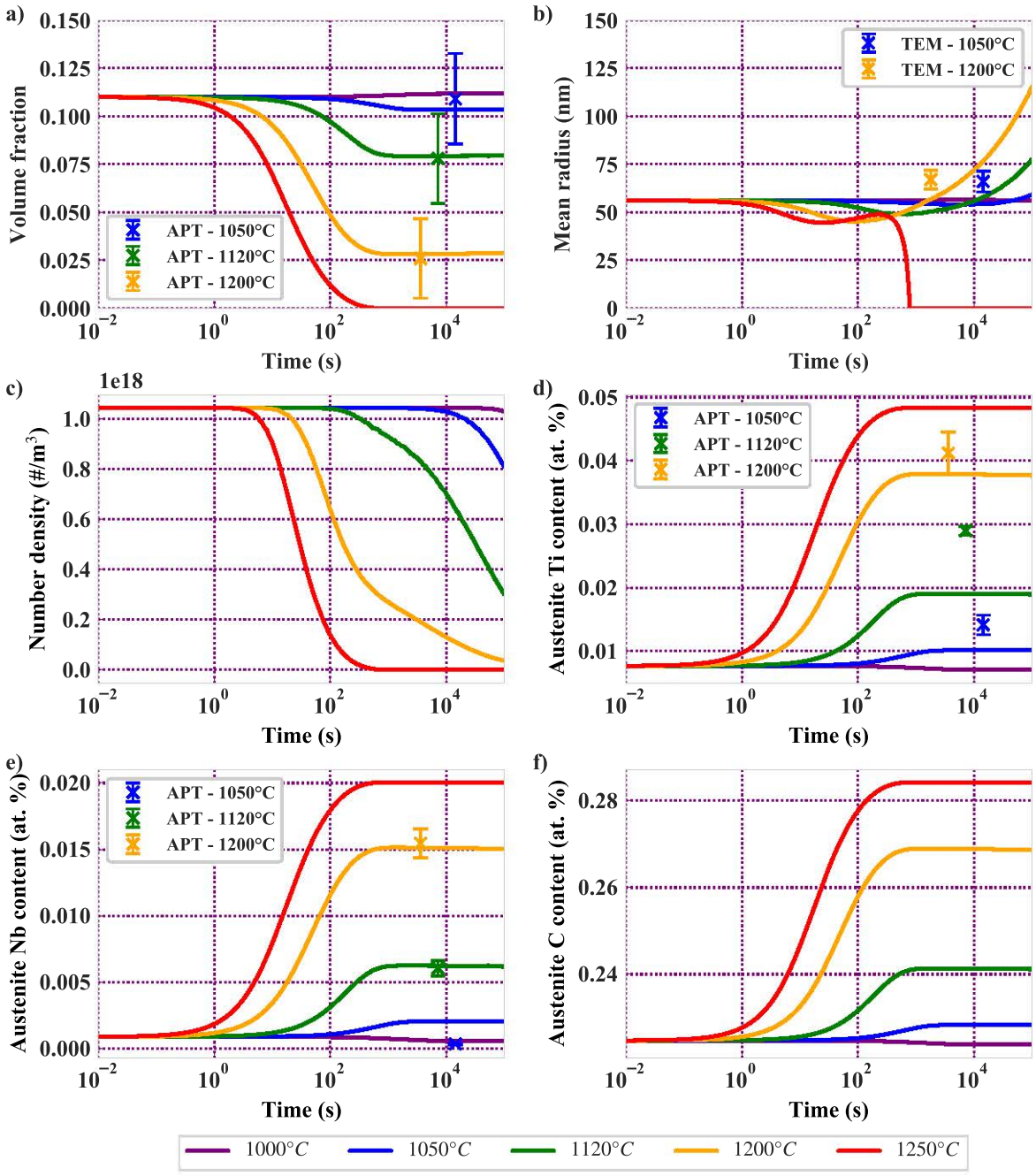

Figure 1.20: Simulated evolution of (Ti,Nb)C$_{fine}$ volume fraction (a), mean radius (b), number density (c), and austenite composition (d-f) for isothermal heat treatments.

Meanwhile, microalloying elements are released in solid solution in the austenite phase due to the dissolution of precipitates.

A correct agreement is obtained between the modeling results and the experimental measurements of the volume fractions, mean precipitate radii, and Nb solid solution content. A larger difference is obtained concerning the titanium content. This mainly arises to the apparent disagreement between the precipitate composition estimated via the atom probe measurements ($x = 0.61 \pm 0.04$) and that considered in the model ($x = 0.68$).

Figure 1.21 shows the evolution of (Ti,Nb)C_{fine} size distribution during isothermal holding at 1200 °C. It can be observed that the number density of precipitates decreases sharply during the modeled heat treatment.

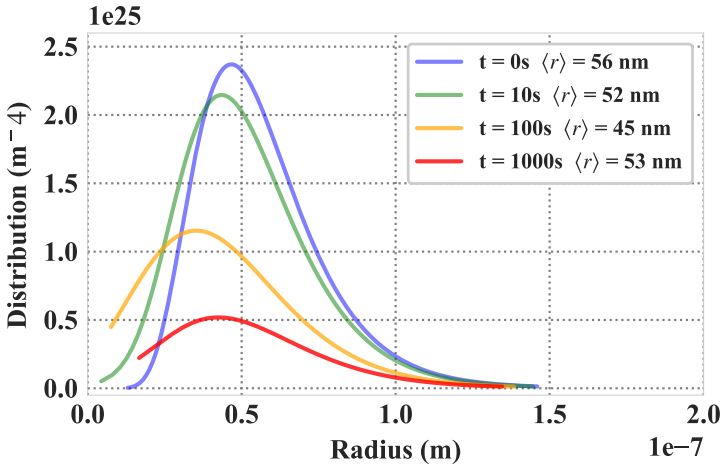

Figure 1.21: Evolution of the precipitate size distribution of (Ti,Nb)C_{fine} with time for a 1200 °C isothermal holding.

1.6.2 Austenite grain growth

The pinning effect of (Ti,Nb)C_{fine} particles is largely affected during heat treatments due to the massive evolution of the precipitation state. Figure 1.22 illustrates the effect of the evolution of the precipitation state on pinning pressure at 1200 °C. On this figure, the pinning pressure was calculated according to Rios ($\alpha = 3$). The effect of the α coefficient was discussed in section 1.7. Figure 1.22 a) shows the evolution of the pinning ratio (defined as either from averaged values $f/\langle r \rangle$, or from the actual size distribution ($\sum_i f_i/r_i$). Taking averaged parameters f and $\langle r \rangle$ leads to an overestimation of the initial pinning pressure of more than 26 %.

Figure 1.22 b) shows the time evolution of driving and pinning pressures. Pinning pressure exerted by (Ti,Nb)C_{fine} particles decreases during holding, as the precipitate number density decreases. The difference between the driving pressure for grain growth and the pinning pressure on grain boundaries is positive, leading thus to grain growth (according to equation 1.25), as illustrated in Figure 1.22 c). As the austenite grain diameter increases, the driving pressure decreases, until both pressures balance each other.

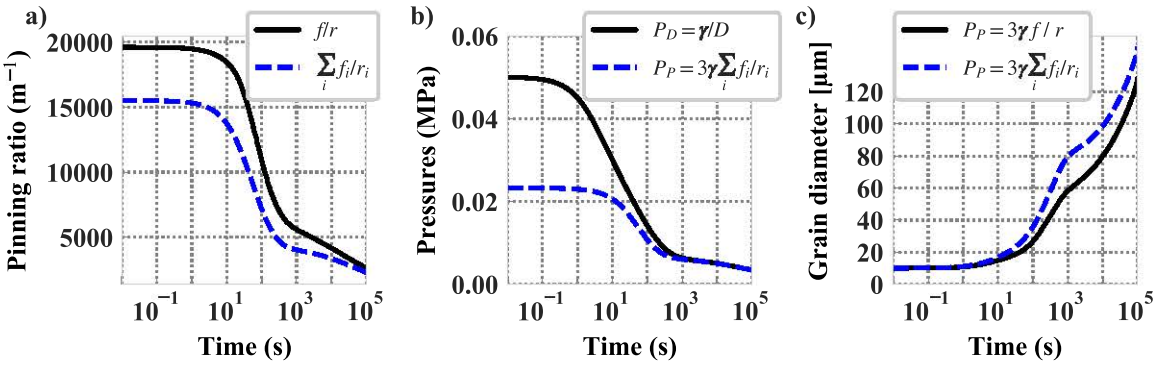

Figure 1.22: Evolution of pinning parameter (a), driving and pinning pressure induced by (Ti,Nb)C_{fine} (b) and austenite grain diameter (c) during a thermal treatment at 1200 °C, considering the expression of pinning pressure given by Rios [RIO 87].

1.7 Discussion

1.7.1 APT as a tool for measuring precipitate volume fraction

Both the volume fraction f_v and precipitate radii are critical parameters to determine the impact of precipitation on microstructure evolution and/or mechanical properties.

Transmission electron microscopy (TEM) techniques directly allow the determination of the frequency distribution of precipitate sizes. The determination of f_v by TEM is however much less precise. For thin foils observations, it is difficult to measure precisely the local thickness of the foil [ALL 81] in order to calculate the observed volume of matrix. Moreover, for low volume fraction, the number of observed precipitates in a single field of view drops to values that hinders any statistical analysis. This procedure then often turns out to be inaccurate. The estimation of volume fraction using extracting replicas [ASH 66] also imposes to estimate the etched volume of matrix, which depends on the studied material, etching time and many other (unknown) experimental factors. Other techniques are thus needed to estimate the volume fraction of precipitates.

The most common method is to resort to selective matrix dissolution techniques coupled with inductively coupled plasma (ICP) spectroscopy [MAU 04, ACE 05, LU 11]. These aim at isolating the precipitates present in the steel by chemical or electrolytic dissolution of the matrix. Both the precipitates isolated by filtration, and the resulting solution (dissolved matrix) are then analyzed to determine the respective proportions of elements present in precipitates and in solid solution. Selective matrix dissolution has the advantage of providing a global composition of large samples but requires a strong experience in sample preparation, etching solutions and precipitate filtering.

Small Angle X-rays Scattering (SAXS) and Small Angle Neutron Scattering (SANS) also allow to measure precipitate volume fraction [DEG 12, DES 13]. With these techniques, the detection limit depends on the type of precipitates. In some cases, volume fraction of approximately 0.1 % can be difficult to quantity. It is also hard to distinguish different types of precipitates if they present similar sizes.

In this PhD work, the volume fraction was indirectly derived through composition measurements

of the matrix by APT. The use of APT for this purpose is much less widespread than selective matrix dissolution coupled with ICP mass spectrometry. In literature, a few examples of APT used for f_v determination can be found, in high speed steels [RON 92] or Al-Zn-Mg alloy [DUM 05]. In these studies, volume fractions of precipitates were rather large (of the order of 1 to 10 %), leading to low relative uncertainties.

In 1994, Palmière *et al.* [PAL 94] applied atom probe field ion microscopy (APFIM), the 1D ancestor of current APT, to study the evolution of Nb solute content in austenite for various heat treatments in Nb-microalloyed steels. Although original and promising, this methodology was then limited by the volume sizes and thus the number of atoms analyzed, the mass resolution of the instrument, and its one-dimensional nature. At last, the instruments they used only provided 1D concentration profiles, rather than 3D reconstruction. As a consequence, they developed a procedure to discriminate between matrix and precipitates. Their procedure can be questioned, but is no longer necessary nowadays, with true 3D atomic reconstruction. At the time of Palmière *et al.* study, 10 to 15 samples were needed to collect a total of 100 000 analysed ions. Thus, the standard deviation associated with each experiment was very large, since it is related to the total number of collected ions (see equation 1.11). The measurement of a concentration of 100 ppm with a total of 10 000 ions collected (per experiment) means that on average, only one solute atom is collected per experiment. Considering a total of 100 000 ions, the standard deviation associated with the measurement of 100 ppm is 22 ppm.

In addition, a satisfactory mass resolution is needed to discriminate elements on the mass spectrum because many alloying elements are present in commercial steels. At the time of the study of Palmière *et al.* [PAL 94], the mass resolution was too limited to well separate all addition elements that are present in commercial steels. Thus, superimposition of peaks on the mass spectrum could bias the composition measurement.

During the last two decades, APT has evolved considerably in terms of analyzed volume size (total number of analyzed ions per sample) as well as in mass resolution [MIL 12, MOO 16]. This technique is nowadays capable of analyzing tens of millions of ions in a single sample, leading to negligible standard deviations for each experiments. These evolutions have opened new perspective for using TAP as a quantitative tool for solid solution analysis.

Although the analyzed volumes have largely increased (typically around $50 \times 50 \times 1000\,\mathrm{nm}^3$ for this study), these measurements remain very local. By way of comparison, a few grams of material are analyzed with selective dissolution techniques, which represents a volume 10^{13} to 10^{14} times larger than those analyzed by APT. APT is thus much more sensitive to heterogeneities in matrix composition, due for example to segregations. Nevertheless, in the present case, the standard deviations observed on several samples of the same state remained limited, of the order of 10 to 20 % of the measured composition. The measurements therefore seems to remain fairly precise, with a limited uncertainty.

It should be noted, however, that these uncertainty calculations based on the standard deviation between several measurements do not accurately reflect the intrinsic uncertainties of the measurement. In particular, the measurement of the Ti content, which is made from two minor Ti peaks in the mass spectrum, should actually be affected by a greater uncertainty than that calculated

with the standard deviations. The estimation of the intrinsic uncertainties of the composition measurement by APT is a complicated task that has not been realized at the time of writing this manuscript.

A mass balance is used to estimate the volume fraction of precipitates. Thus, the volume fraction is affected by the uncertainties related to the matrix composition, X_{Nb}^{SS}, and also by those related to the determination of the total quantity of Nb available to form these precipitates, X_{Nb}^{0}. A poor estimate of X_{Nb}^{0} can lead to completely erroneous estimates of the volume fraction. Therefore, the uncertainty on the volume fraction is greater than that on the composition measurements.

The volume fraction measurement is based on the fact that only matrix is considered, any single precipitate can be identified on 3D reconstructions. This is even less of a problem in this study, with the considered sizes and volume fraction. Indeed, assuming spherical, mono-dispersed, and randomly distributed precipitates of radius r and volume fraction f_v, the probability of analyzing a precipitate in a cuboid volume of dimensions $L \times l \times l$ is given by the number density of precipitates multiplied by the analyzed volume:

$$P = \frac{f_v}{4/3\pi r^3} \cdot (L + r) \cdot (l + r)^2 \tag{1.47}$$

Figure 1.23 represents this probability for L =1000 nm and l =50 nm, as a function of r and f_v, for typical ranges of r and f_v met in microalloyed steels: $5 < r < 100$ nm and $f_v < 0.2\,\%$. It can be observed that the APT analysis performed in this work is particularly suited for precipitates larger than 20 to 30 nm for this range of volume fraction. In this study, the (Ti,Nb)C$_{fine}$ presented mean radius larger than 50 nm, which explains why no precipitates were intercepted during APT measurements.

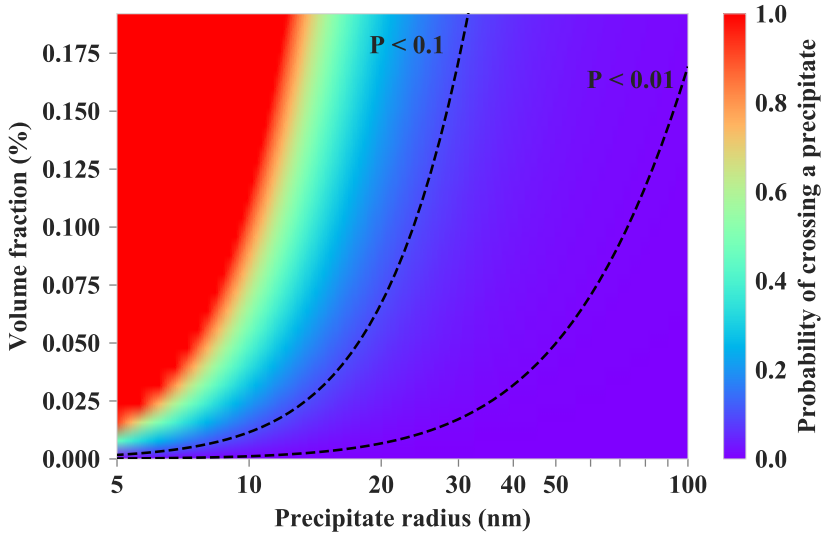

Figure 1.23: Probability of crossing a precipitate during the APT analysis, for a cuboid sample of length L =1000 nm and width l =50 nm, as a function of precipitate radius and volume fraction.

1.7.2 Precipitation and grain growth modeling

Almost all modeling parameters were extracted from literature and/or thermodynamic databases. The pre-exponential factor of the grain boundary mobility, M_0, was the only adjusted modelling parameter. However, another parameter was unknown: the initial volume fraction of (Ti,Nb)C$_{fine}$. It was chosen to set this value at 0.11 %, which is close to the maximum volume fraction. Since the initial state was obtained through hot rolling and air cooling, there is a high probability that the precipitate volume fraction is maximum. The precipitate/matrix interfacial energies were derived from the work of Yong *et al.* [YON 89] and not adjusted. It should however be remembered that this interfacial energy has only little influence on reversion kinetics, since nucleation does not take place during reversion.

Figure 1.24 compares measured (see section 1.4.1) and predicted grain sizes for 10 minutes heat treatments at temperatures ranging from 950 °C to 1250 °C. At 1000 and 1050 °C, the model slightly overestimates the austenite grain sizes. Above 1050 °C, the model shows a fairly good agreement with experimental data. The experimental data globally lie between the values predicted using Zener ($\alpha = 3/2$) and Rios ($\alpha = 3$) approaches.

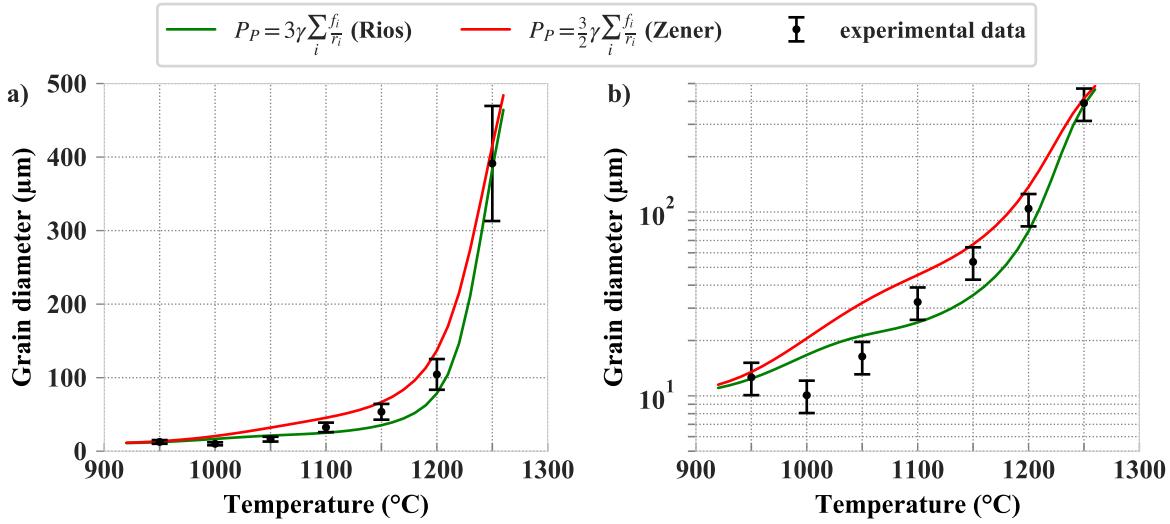

Figure 1.24: Predicted and experimentally determined austenite grain diameter for 10 minutes isothermal heat treatments. The data is represented in both linear (a) and logarithmic scale (b).

Note that the whole precipitate size distribution was used to evaluate the pinning pressure, whereas many other authors used averaged volume fractions and radii [BAN 10, MAA 12, KAR 14, AND 95]. It has been shown (Figure 1.22 a)) that using averaged parameters leads to an overestimation of the pinning pressure. Figure 1.22 c) compares the austenite grain growth kinetics at 1200 °C obtained using averaged parameters or size distribution for pinning pressure calculations. The gap between the two kinetics is non negligible.

In order to investigate the effect of the distribution shape on grain growth kinetics, three different precipitate size distributions with exact same mean radius and volume fraction were compared (see Figure 1.25). While a pinning pressure equal to 0.03 MPa was obtained (Rios's approach)

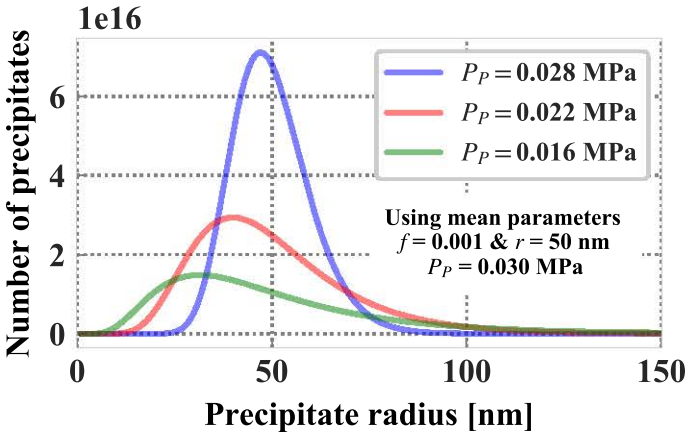

Figure 1.25: Comparison of the pinning pressure (Rios's approach) induced by three different size distributions of precipitates. The three size distributions present a mean radius of 50 nm and a mean volume fraction of 0.001 , showing that mean values are not appropriate.

using averaged parameters, the actual pinning pressures resulting from the three different size distributions can be significantly lower. For narrow size distributions, the error remained small, but significantly increased for wider size distributions. This error could be even greater in the case of more complex distributions such as multimodal ones. Accounting for the whole size distribution is therefore important for the calculation of pinning pressures, and thus grain growth kinetics.

The present grain growth model neglected the pinning effect of the larger (Ti,Nb)(C,N)$_{large}$, MnS and $Ti_4C_2S_2$ precipitates. It was considered that only (Ti,Nb)C$_{fine}$ are have sufficient number density to be effective pinning particles. These populations presented radii that often exceeded 500 nm for a total volume fraction around 0.1 %. Assuming for their mean radius is 500 nm, their maximum pinning effect is estimated to be 0.003 MPa using averaged parameters and Rios's theory. It represents approximately 10 % of the initial pinning contribution of the (Ti,Nb)C$_{fine}$ population. Thus, the error resulting from not considering the pinning effect of these large precipitates is more likely to remain limited, particularly for relatively short treatment times.

1.8 Conclusions

In the present chapter, the evolution of the precipitation state and austenite grain growth were studied in a Ti-Nb microalloyed steel during reversion treatments.

The precipitation state was extensively characterized using electron microscopy techniques. Four populations of precipitates were highlighted. Of these populations, only one has sufficiently fine sizes to provide effective austenite grain growth control: (Ti,Nb)C$_{fine}$. The study therefore mainly focused on this population.

An original approach was followed to experimentally measure the volume fraction of (Ti,Nb)C$_{fine}$ by APT. APT allowed to estimate the total amounts of Ti and Nb available to form (Ti,Nb)C$_{fine}$,

as well as to measure the austenite composition after heat treatments at various temperatures. The volume fraction of precipitates was calculated indirectly from the matrix composition, through mass balance. This type of measurement is made possible by the considerable improvements that atom probe tomography has undergone for the last 20 years. Several tens of millions atoms can be analyzed in a single experiment nowadays.

Based on acquired experimental data (precipitate types, sizes, and volume fractions), a multi-class precipitation model was developed and used to predict the evolution of (Ti,Nb)C_{fine} size distribution during thermal treatments. SEM and TEM characterization led to similar initial precipitate size distributions, which served as initial distributions in the precipitation model. The chemistry and stability of (Ti,Nb)C_{fine} precipitates was calculated using the TCFE8 thermodynamic database. The precipitate size distributions issued from the precipitation model served as entry parameters to a simple grain growth model based on Zener pinning.

Both precipitation and grain growth models did not contain any adjustable parameter, except the mobility factor M_0. All other parameters were extracted either from thermodynamic databases, or from literature.

The grain growth model accounted for the whole precipitate size distribution for calculation of the pinning pressure exerted on grain boundaries, rather than using average values. Accounting for the actual precipitation size distribution significantly influenced the calculated pinning pressure. The modeled austenite grain diameters were consistent with the experiments for all investigated heat treatments, justifying the original selected approach.

Chapter 2

Recrystallization and precipitation kinetics after hot deformation

Contents

2.1 Introduction

During hot rolling, steels slabs undergo a succession of deformation passes in the austenitic domain. This process primarily aims at reducing the slab thickness to obtain plates. The dislocation density of austenite strongly increases during each deformation pass. This allows several microstructural evolutions subsequently: recovery, recrystallization, and strain-induced precipitation. In the case of microalloyed steels, microalloying additions can interact with recovery and recrystallization through solute drag effect and precipitate pinning.

The metallurgical state of austenite influences the phase transformation behavior upon cooling. Indeed, the nature, morphology, and size of the phases formed are influenced by austenite grain size and dislocation density. The characterization of recovery, recrystallization, and precipitation in austenite after deformation allows optimizing the hot rolling process, in order to generate controlled final microstructures with targeted mechanical properties.

In the present work, the progress of recovery, static recrystallization and strain-induced precipitation were studied in three microalloyed steels, presenting Nb, Ti, and V additions. These microstructural evolutions were indirectly followed by stress relaxation tests after compression. The effects of strain, strain rate, temperature, and steel composition were analyzed. Recrystallization was also studied by means of direct metallographic observations, while strain-induced precipitates were characterized by TEM. Recrystallization and precipitation models were developed, based on the experimental data generated, providing a better understanding of the microstructural evolutions of austenite after deformation. This will allow a simultaneous optimization of the steel composition and of the thermomechanical path.

2.2 Background

The following part provides a short literature review of the metallurgical phenomena operating during and after the deformation of austenite. It focuses on recovery, recrystallization and precipitation, and describes the complex interactions between them. An overview of the experimental techniques used for the characterization of these metallurgical phenomena is also provided.

2.2.1 Austenite evolution during hot rolling process

A widespread objective of high strength steel processing is to refine the final microstructures, independently of the intended phase transformations from the austenite domain. Austenite phase transformation products nucleates on defects such as austenite grain boundaries, deformation bands, and incoherent twin boundaries [DEA 01b, DEA 03a]. Thus, a general grain refinement can be achieved by increasing the total interfacial area of near planar crystalline defects that act as nucleation sites for ferritic phases, S_V.

During hot rolling, austenite undergoes successive deformation passes in order to reduce the plate thickness. Depending on the temperature, strain, and strain rate applied, recrystallization can occur dynamically during the pass and/or in a static/metadynamic way after the deformation (Figure 2.1).

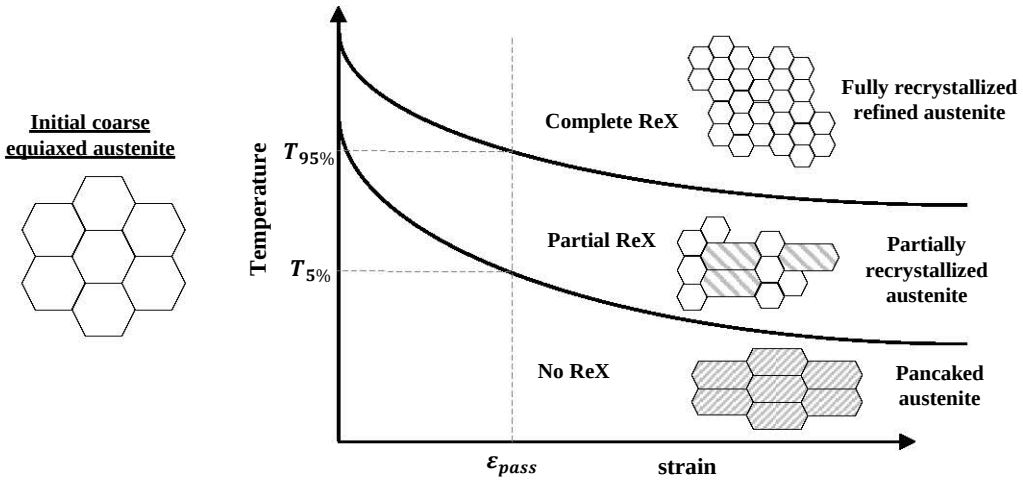

Figure 2.1: Illustration of evolution of austenitic microstructures resulting from various deformation conditions, after Deardo *et al.* [DEA 01a]. $T_{5\%}$ and $T_{95\%}$ are the temperatures for 5 and 95 % recrystallization, respectively.

(i) When recrystallization occurs, deformed grains are replaced by finer undeformed grains which nucleate and grow until the structure is fully recrystallized. Recrystallization thus leads to refinement of austenite grains.

(ii) When recrystallization does not take place due to an insufficient temperature or applied stress, austenite grains are deformed and show an elongated shape, often described as *pancaked austenite*.

(iii) At intermediate temperatures, a mixed grain structure is obtained. Recrystallized grains coexist with pancaked ones.

Both recrystallization and pancaking lead to an increase of the number of potential nucleation sites for ferritic phase. Refining the austenite size leads to an increase of total area of austenite grain boundaries. Pancaking also increases the area of austenite grain boundaries and creates inter-granular defects such as deformation bands and twin boundaries.

Thus, several industrial approaches can be followed for achieving a finer final microstructure. These approaches are generally distinguished by introducing the **concept of the temperature of no-recrystallization,** T_{NR}. The T_{NR} is defined as the temperature below which static or metadynamic recrystallization can no longer reach completion between two rolling passes (*i.e.* for a given interpass time) [DEA 01b, DEA 03a, VER 12]. Among these approaches, two are commonly used for processing micro-alloyed steels :

(i) Thermo-mechanical controlled processing (TMCP) [VER 12] (Figure 2.2 a)): Because slab reheating is generally performed at elevated temperatures, coarse austenitic microstructures are obtained after reheating. Thus, the roughing rolling is first performed above T_{NR} in order to refine the austenite grains. Then, the finishing rolling is performed in a low temperature austenite region, under T_{NR}. This leads to an increased number of potential nucleation sites for γ to α transformation. Note that one can also perform the last deformation passes in the

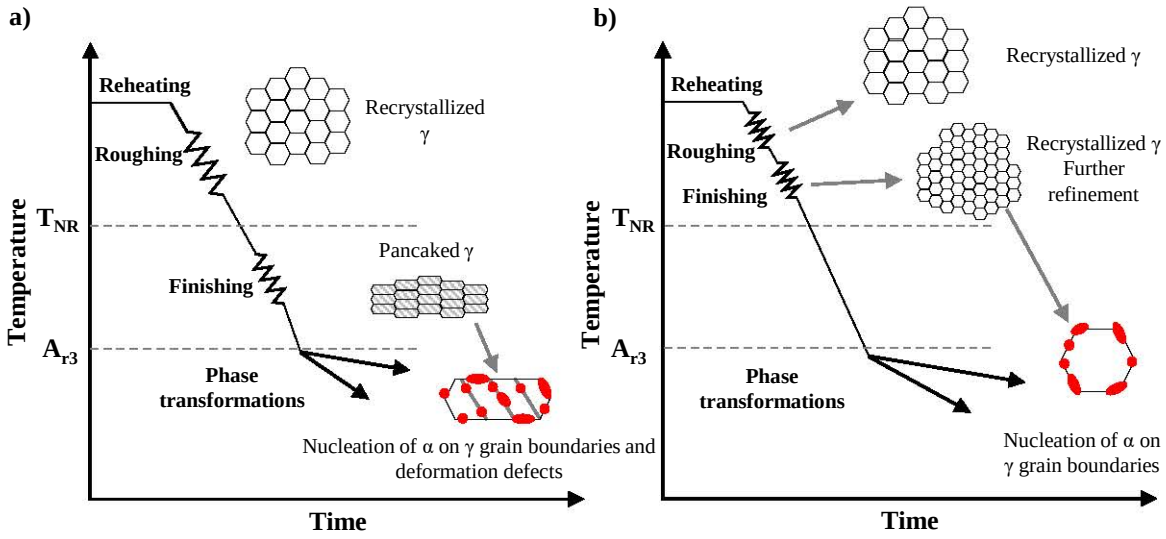

Figure 2.2: Differences between (a) thermo-mechanical controlled processing (TMCP) and (b) recrystallization controlled rolling (RCR).

intercritical ($\alpha + \gamma$) domain. In this case, the formation of ferrite during the final finishing passes is favored.

(ii) Recrystallization controlled rolling (RCR) [SIW 92] (Figure 2.2 b)): in this particular case, the finishing rolling temperature is set above T_{NR}. Both roughing and finishing are performed at elevated temperatures so that fine austenite grains are obtained. This approach can be attractive because it minimizes the rolling loads applied during deformation, since deformation is performed in a higher temperature range.

Both approaches are followed by different cooling procedures to obtain the desired ferritic microstructures. Microalloying elements play a major role in both rolling schedules since they set the value of T_{NR}. They also limit austenite grain growth during the relatively long cooling period between the finishing rolling temperature down to $Ar3$ during RCR. Moreover, the alloying elements will influence the potential precipitation occurring during rolling or during the cooling stage. The effects of microalloying elements on recrystallization kinetics are reviewed in part 2.2.3.

2.2.2 Recovery and recrystallization

During deformation, the free energy of a metallic material is raised by the introduction of deformation defects (mainly dislocations, but also vacancies), so that the material is thus put into a thermodynamically unstable state [HUM 17]. If the temperature is high enough to activate thermally activated mechanisms such as solid state diffusion, the defects introduced by deformation may be removed or rearranged into configurations of lower energies.

The mechanisms by which a deformed material returns into a thermodynamically more stable state are generally distinguished into two categories: **recovery** and **recrystallization** [DOH 97, HUM 17].

(i) Recovery refers to all annealing phenomena occurring in a strained material that eliminate deformation defects and that occur without the migration of high angle grain boundaries.

(ii) Recrystallization refers to the formation of new strain-free grains by the migration of high angle grain boundaries.

Both recovery and recrystallization are competing processes since both are driven by the energy stored during deformation.

2.2.2.1 Recovery

The microstructure and properties of metallic materials can be partially retrieved by recovery, during which annihilation and rearrangement of dislocations take place. The microstructural changes brought by recovery are generally homogeneous and do not involve any migration of grain boundaries. Only a partial restoration of properties is generally reached, because the dislocation structure is not completely removed. Dislocations rearrange and form substructures, so that the material reaches a metastable state. Figure 2.3 details the different stages occurring during recovery. These microstructural rearrangements may take place either during annealing after a deformation or dynamically, during deformation. The recovery processes are then referred to as *static recovery* and *dynamic recovery*, respectively.

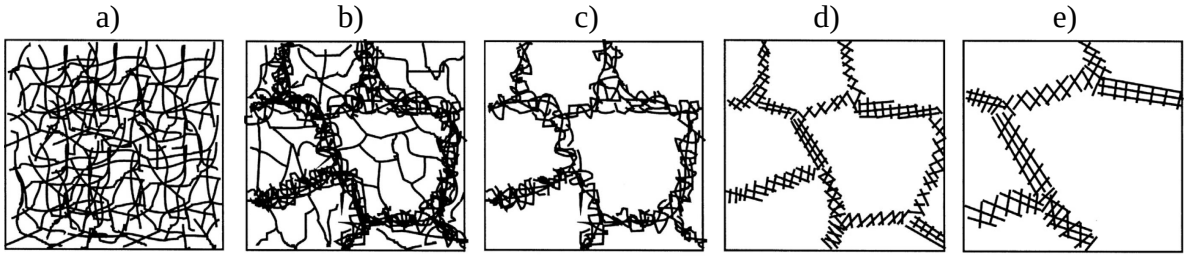

Figure 2.3: Stages of the recovery process of a deformed metallic material: (a) Initial dislocation tangles ; (b) formation of dislocation cells ; (c) Annihilation of dislocations within cells ; (d) sub-grain formation ; (e) sub-grain growth. Extracted from Humphreys *et al.* [HUM 17].

2.2.2.2 Recrystallization

Recrystallization is concomitant with recovery. This restoration process involves the migration of high angle grain boundaries and leads to the formation of new dislocation-free grains, formed within the recovered or deformed structure. When completed, recrystallization results in a new grain microstructure with a low dislocation density. When a metallic material is deformed at elevated temperatures, several recrystallization processes may take place, and need to be distinguished [DOH 97, HUA 16a, HUM 17]:

(i) **Static recrystallization** refers to the recrystallization process taking place during annealing ***after*** deformation. A minimum strain is needed to initiate static recrystallization.

(ii) **Dynamic recrystallization** refers to when the recrystallization occurs ***during*** the deformation. During deformation, news grains nucleates at the old grain boundaries. Since the

deformation process continues, the dislocation densities of the new grains increase, which reduces the driving pressure for further growth. The growth of news grains may also be limited by the nucleation of other grains at grain boundaries. Dynamic recrystallization is characterized by repeated nucleation and growth events.

(iii) **Meta-dynamic recrystallization** refers to a specific case: if the applied strain is larger than the critical strain for dynamic recrystallization, recrystallization nuclei are formed within the material. If the straining stops but the material is still annealed, the formed nuclei will grow without any incubation time into the partially dynamically recrystallized matrix. This phenomenon is sometimes also referred to as post-dynamic recrystallization.

The driving pressure for recrystallization, G, arises from the difference in dislocation densities before and after the displacement of a grain boundary during recrystallization, i.e. the difference in dislocation density between a work-hardened grain (ρ) and a recrystallized grain (ρ_0).

$$G = \frac{1}{2}\mu b^2(\rho - \rho_0) \tag{2.1}$$

Where μ is the shear modulus, and b the burgers vector. Generally, ρ is orders of magnitude larger than ρ_0 and the following approximation is performed: $\rho - \rho_0 \approx \rho$.

2.2.3 Interactions between recovery, recrystallization, and precipitation

In the case of microalloying additions, the microstructural evolutions of austenite after deformation are complex since they are influenced by the interactions between four mechanisms: recovery, recrystallization, solute drag and precipitation. All these mechanisms are inter-dependent and influenced by the parameters of deformation. Vervynckt *et al.* [VER 12] proposed a schematic illustration that allows a global view of the interactions between the deformation parameters, recovery, recrystallization, and precipitation. This schematic illustration is reproduced in Figure 2.4.

The addition of microalloying elements may interact with softening mechanisms by two different ways:

(i) **In solid solution**: small solute additions can segregate on moving grain boundaries or dislocations. The local segregation of microalloying elements exerts a dragging force, and therefore reduces their mobility. This mechanism is called solute drag effect [CAH 62]. Thus, solute drag effect can slow down the recovery or recrystallization rates.

(ii) **By the formation of precipitates**: As seen in Chapter 1, fine precipitate distributions exerts a pinning pressure on grain boundaries. Recovery is also influenced by the presence of precipitates, that are obstacles to the movement of dislocations.

2.2.3.1 Effects of deformation parameters

The deformation conditions naturally play a significant role in subsequent microstructural evolutions. Increasing temperature increases the rates of recrystallization and recovery. If the deformation temperature is below the dissolution temperature of precipitates, precipitation can take place on the generated dislocations. This is generally referred to as strain-induced precipitation [DUT 92, HON 02]. Increasing strain and strain rates generally leads to faster recrystallization

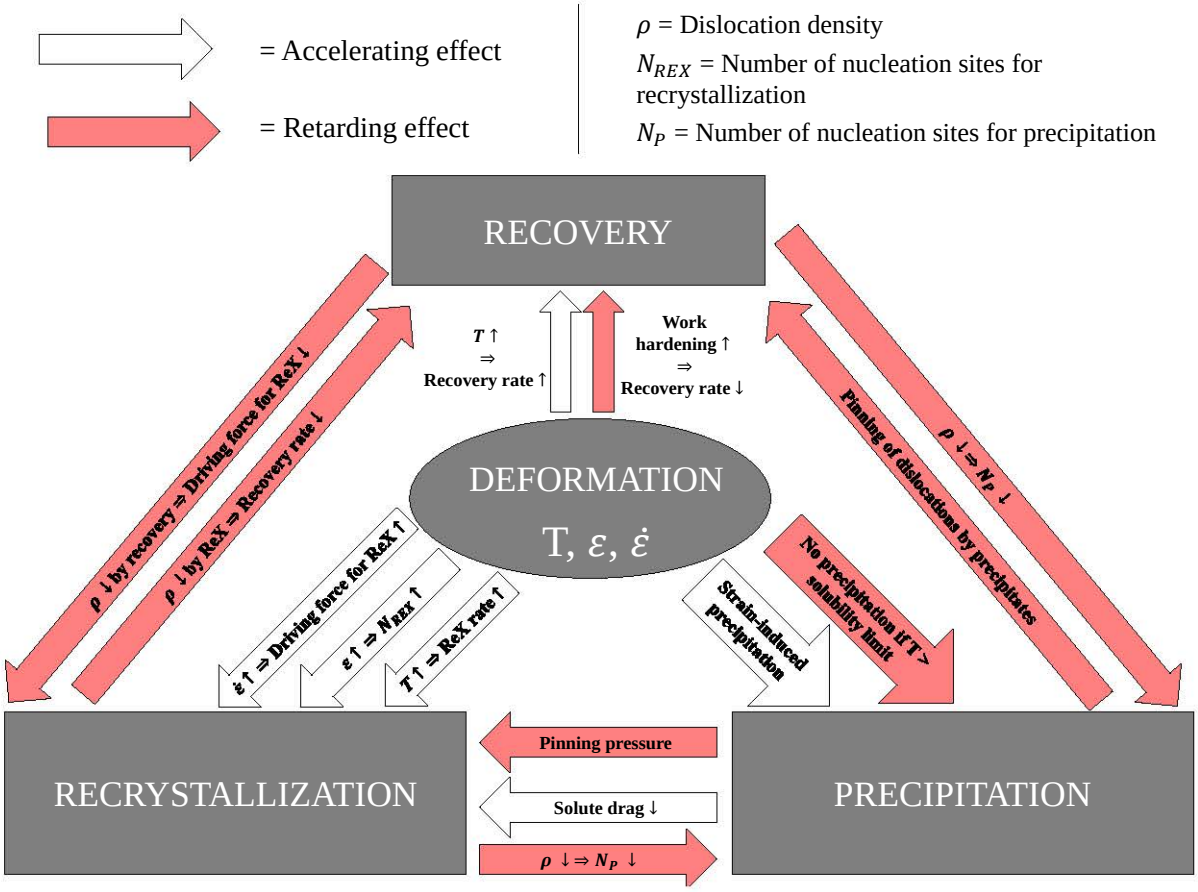

Figure 2.4: Schematic illustration of the interactions between deformation parameters, recovery, recrystallization, and precipitation. Based on Vervynckt *et al.* [VER 12].

kinetics [LAA 91, AI 00]. This is due to the fact that increasing strain or strain rates increases stored dislocation densities, and consequently the driving pressure for recrystallization.

2.2.3.2 Interactions between recovery and recrystallization

Since both are related to the stored energy due to the increase of dislocation density during deformation, recrystallization and recovery are two competing softening processes. Recovery decreases the dislocation density of the deformed austenite, which reduces the driving pressure for recrystallization.

2.2.3.3 Interactions between precipitation and recrystallization

Recrystallization and precipitation can interact in three main ways [VER 12]. First, recrystallization reduces the dislocation density, and consequently the number of nucleation sites for precipitation. Thus, recrystallization can delay the progress of precipitation. Second, the formation of precipitates exerts a pinning pressure on grain boundaries, which have the potential to slow down or interrupt the progress of recrystallization. The pinning pressure exerted by precipitates were discussed in part 1.2.2. Lastly, due to the solute drag effect, the grain boundary mobility depends on the austenite

solute concentration. Precipitation reduces the austenite solute content, and therefore lowers the solute drag effect. In the case were coarse precipitates are formed, the pinning pressure is very limited, and recrystallization is only slightly delayed.

In order to take into account the pinning pressure induced by precipitate, equation 2.1 is generally modified [ZUR 02, GÓM 05]:

$$G_{eff} = \frac{1}{2}\mu b^2(\rho - \rho_0 - P_P) \tag{2.2}$$

where P_P is the pinning pressure exerted by precipitates.

2.2.3.4 Interactions between recovery and precipitation

Interactions between recovery and precipitation are quite similar to the ones between recrystallization and precipitation. Dislocations provide nucleation sites for precipitates and well as fast-diffusion paths for solute elements. The progress of recovery can therefore delay the progress of precipitation by lowering the dislocation density. Conversely, precipitates are obstacles to dislocation motion and can therefore slow down the progress of recovery or even interrupt it. Moreover, microalloying elements may also provide a solute drag effect on dislocation mobility.

2.2.4 Experimental techniques used for the study of recrystallization

Two types of techniques can be used for investigating the static recrystallization kinetics of austenite [Dž 04, VER 10a]: direct metallographic techniques and hot deformation test investigating for flow stress restoration. One may also directly measure austenite grain sizes during heat treatments by laser ultrasonics method [MIL 13]. However, this technique requires special experimental devices as well as an advanced expertise in post-treating the results and will not be considered in the following.

2.2.4.1 Metallographic techniques

One may directly measure the recrystallization progress by quenching and applying metallographic techniques. Although direct, this option suffers from several disadvantages. First, it is very time-consuming since it is necessary to prepare a sample for each studied time. Secondly, because austenite transforms into martensite upon quenching, a technique for reconstructing the prior austenite grains boundaries (PAGB) is needed: either a Béchet-Beaujard [Bé 55] type etching or EBSD. Béchet-Beaujard type etching are particularly sensitive and difficult to perform with success, especially on low carbon steels and on deformed microstructures. The construction of PAGB through EBSD is also quite complex on deformed microstructures. Thirdly, even when PAGB are successfully revealed, distinguishing recrystallized grains from deformed grains can still remain difficult.

2.2.4.2 Mechanical testing

Since direct metallographic studies are time consuming and complicated when applied to austenite, hot mechanical tests are generally preferred over metallographic methods. For mechanical tests, the progress of recrystallization or recovery is indirectly studied through the restoration of flow stress after a deformation event. Two types of mechanical tests are generally used for the study

of recrystallization, either in torsion or compression: interrupted double hit deformation tests and stress relaxation tests.

It has to be noted that both tests are theoretically sensitive to all microstructural events that influence the time evolution of flow stress after a deformation. Thus, recrystallization, restoration and precipitation can all be studied by these techniques. However, it is quite complicated to uncorrelate them if they appear to be concomitant.

Double hit deformation tests

The principle of a double hit test is illustrated in Figure 2.5. After a reheating treatment and cooling down to the tested temperature, a first deformation pass is performed. After this deformation, the stress is lowered down to a minimum value, and the sample is kept in position for varying interpass times, Δt. Then, a second deformation is given with the same set of parameters.

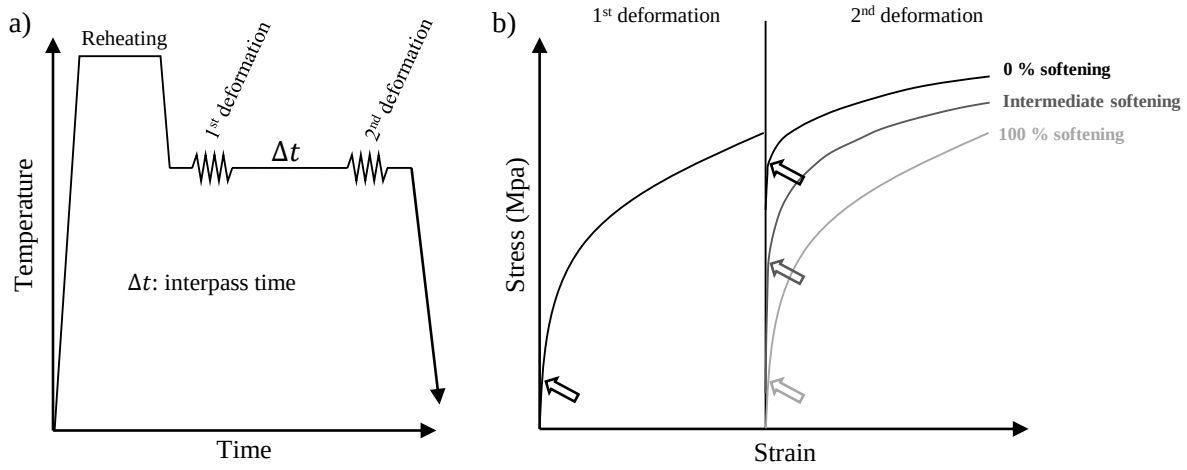

Figure 2.5: Principle of interrupted double hit tests. (a) Thermo-mechanical treatment applied. (b) Schematic evolution of stress-strain behavior for various degrees of softening.

The softening fraction can be determined by comparing the two different stress-strain curves [DŽU 04, LIN 08, VER 10b]. Depending on Δt, the shape of the second deformation curve varies. For very short interpass times, the second flow curve appears as an extrapolation of the first flow curve, showing no softening. Conversely, if Δt is long enough to allow a complete softening, the second flow curve should be identical to the first one.

Several different methods are applied and discussed in literature to analyze these interrupted mechanical tests [DŽU 04, VER 10b]. These different methods of post-processing give rise to significantly different resulting recrystallization kinetics, which constitutes one important drawback of the method. Another drawback of the technique is that it is also quite time consuming. Several double hit tests are needed for determining a complete recrystallization curve in a given set of deformation parameters.

Stress relaxation tests

Stress relaxation is the second mechanical method frequently used to study the softening kinetics after a deformation event. After a reheating treatment and cooling down to the tested temperature, the sample undergoes hot deformation, either in torsion or in compression. After deformation, the sample is kept in a fixed position, and the evolution of the stress as a function of time is recorded. Figure 2.6 a) illustrates the thermo-mechanical treatment applied during stress relaxation tests.

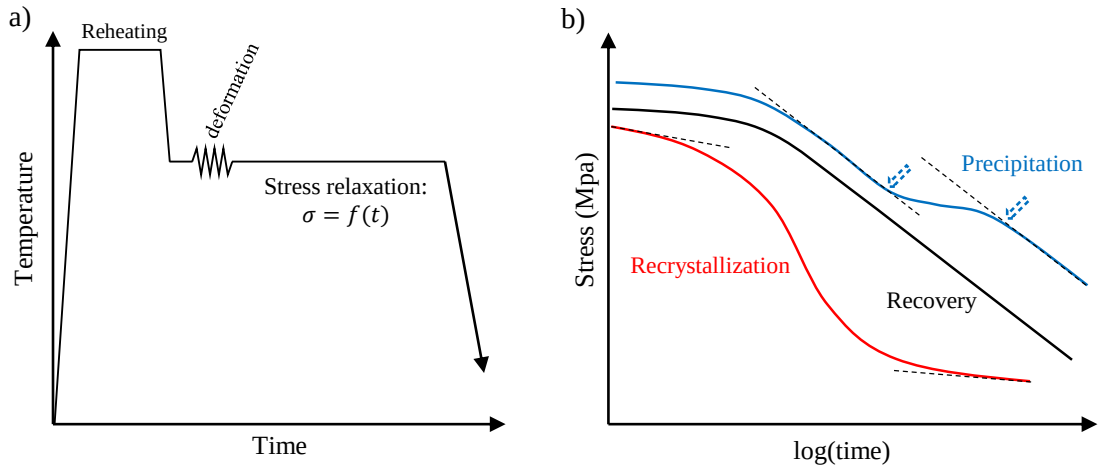

Figure 2.6: Principle of stress relaxation tests to study recovery, precipitation, and recrystallization. (a) Thermo-mechanical treatment applied. (b) Schematic evolution of relaxation stress when precipitation, recovery, and recrystallization occur.

Stress relaxation is a very sensitive technique that have been applied to follow numerous microstructural evolutions including recovery, precipitation, recrystallization, or even phase transformation. This method is sensitive to microstructural evolutions because the relaxation stress measured during testing is related to the dislocation density in the specimen [LIU 12].

This technique was first developed during the second half of 1980s by Liu and Jonas [LIU 88a, LIU 88b] to follow the precipitation kinetics of carbonitrides in austenite. When recovery is the only softening mechanism, Liu and Jonas demonstrated [LIU 88a] that for sufficiently long time, the stress decreases linearly as a function of the logarithm of time:

$$\sigma = \sigma_0 - \alpha \log(t) \tag{2.3}$$

These authors also found out that the linear decrease of stress was stopped when carbonitrides precipitation took place [LIU 88a, LIU 88b]. A plateau appears in the relaxation curve, and the precipitation start and finish times can be derived from the deviation from the linear behavior. This phenomenon is schematically represented in 2.6 b). After this pioneer work, the technique was applied in numerous studies to monitor precipitation in various alloys. Surprisingly, as pointed out by H. Zurob [ZUR 03], only one study [ARI 94] applying stress relaxation to study the recovery process in microalloyed steels can be found in literature.

Later, in the mid-1990s, Karjailen *et al.* [KAR 95] demonstrated the ability of the stress relaxation technique to monitor the kinetics of recrystallization after deformation. The authors found

out that when recrystallization occurs, the stress relaxation curve presents three distinct parts. The first part of the curve follows a linear decrease that is attributed to recovery. In the second part of the curve, a large drop of stress, attributed to recrystallization, is observed. The last part of the curve also follows a linear decrease, that corresponds to the grain growth behavior of the recrystallized material.

Whatever the studied phenomenon, stress relaxation tests have the advantage of being much more rapid than double hit tests: a single test allows determining a complete recrystallization kinetics under a given set of deformation parameters. However, several authors pointed out that stress relaxation tests are more difficult to carry out and require a very precise control of the temperature and deformation system [DŽU 04, VER 10b]. The same authors also reported that accelerated recrystallization kinetics are found using stress relaxation, compared to double hit tests.

2.3 Materials and methods

2.3.1 Studied materials

In this chapter, three different microalloyed steels were studied. They were produced by vacuum induction melting, following the procedure presented in part 1.3.1. Their respective compositions are listed in Table 2.3.1. In terms of microalloying elements, they all present the same amount of Nb, but different Ti and V contents. The other alloying elements are kept in similar ranges. In order to ease the understanding throughout the chapter, the three steels were named after their Nb, Ti, and V content.

Element	C	Mn	Si	Nb	Ti	V	Mo	Al	Cr	N
0.04Nb-0.09Ti	0.062	1.91	0.50	**0.039**	**0.085**	**0.002**	0.212	0.065	0.013	0.006
0.04Nb-0.09Ti-0.1V	0.087	1.94	0.50	**0.039**	**0.093**	**0.105**	0.209	0.067	0.014	0.006
0.04Nb-0.05Ti-0.2V	0.085	1.95	0.50	**0.039**	**0.046**	**0.206**	0.209	0.070	0.014	0.006

Table 2.1: Composition of the three microalloyed steels studied (wt.%).

2.3.2 Stress relaxation tests

Stress relaxations tests were applied to follow austenite microstructural evolutions after deformation. A Gleeble 3500 thermo-mechanical simulator in compression mode was used to deform cylindrical samples of 12 mm length and 8 mm diameter that were machined from the steel plates. Gleeble simulators are not particularly suited for long isothermal heat treatments (t>100 s). Thus, additional tests were undertaken at lower temperatures, using a Bähr 805 DIL dilatometer[1] on samples of 10 mm length and 5 mm diameter.

The heat treatment performed for stress relaxation tests is represented in Figure 2.7. The stress relaxation test begins with a reheating treatment of 10 min at 1250 °C that aims at dissolving most of the existing (Ti,Nb)C precipitates found in the initial condition of the steel (see Chapter 1). The

[1]These additional stress relaxation tests were performed by the partners from Eurecat in Manresa, Spain.

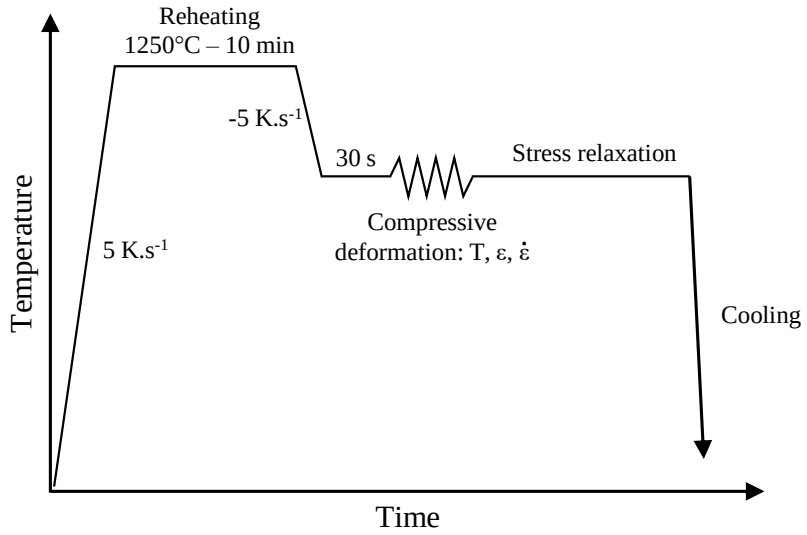

Figure 2.7: Stress relaxation test performed on Gleeble 3500 thermo-mechanical simulator.

sample is subsequently cooled down to the deformation temperature with a $5\,°C\,s^{-1}$ cooling rate and held 30 s for homogenization before compression. After compression, the anvils remain fixed in their positions and hold the sample during a certain time period. During that time period, the evolution of stress is recorded and stress relaxation occurs as a result of softening. The temperature was controlled by welding a thermocouple in the middle of the samples.

Table 2.2 summarizes the parameters of the various tests carried out in the Gleeble and/or dilatometer. The deformation temperatures applied range from 900 °C to 1100 °C. Two different strains (0.1 and 0.3) and two strain rates ($0.1\,s^{-1}$ and $5\,s^{-1}$) were applied. These conditions are supposed to represent hot rolling steps during industrial process. The dilatometer was only used for tests at lower temperatures and for $\dot{\varepsilon}$ =$0.1\,s^{-1}$.

T (°C)	**900**		**950**				**1000**				**1050**				**1100**	
Strain	**0.1**	**0.3**	**0.1**		**0.3**		**0.1**		**0.3**		**0.1**		**0.3**		**0.3**	
Strain rate (s^{-1})	**0.1**		**0.1**	**5**	**0.1**	**5**	**0.1**	**5**	**0.1**	**5**	**0.1**	**5**	**0.1**	**5**	**0.1**	**5**
0.04Nb-0.09Ti	✓	✓	✓	✓	✓	✓	✓	✓	✓	✓	✓	✓	✓	✓	✓	✓
0.04Nb-0.09Ti-0.1V	✓	✓	-	-	✓	✓	✓	✓	✓	✓	✓	-	✓	✓	✓	✓
0.04Nb-0.05Ti-0.2V	✓	✓	✓	✓	✓	✓	✓	✓	✓	✓	✓	✓	✓	✓	✓	✓
Equipment	D	D	D/G	G	D/G	G	D/G	D/G	G	G	G	G	G	G	G	G

Table 2.2: Stress relaxation tests parameters performed on the 3 investigated steels. The equipment used is given on the last line: G stands for Gleeble and D stands for dilatometer.

Figure 2.8 shows an example of the different microstructural phenomena observable on the stress relaxation curve in the present study. If both temperature and driving force are high enough, the recrystallization can be observed (Figure 2.8 a)). The curves were then analyzed following the method described in [KAR 95]. The beginning of the curve can be accurately described by a straight line ($\sigma_1 - \alpha_1 \cdot \log(t)$), corresponding to the recovery/creep behavior of the strained

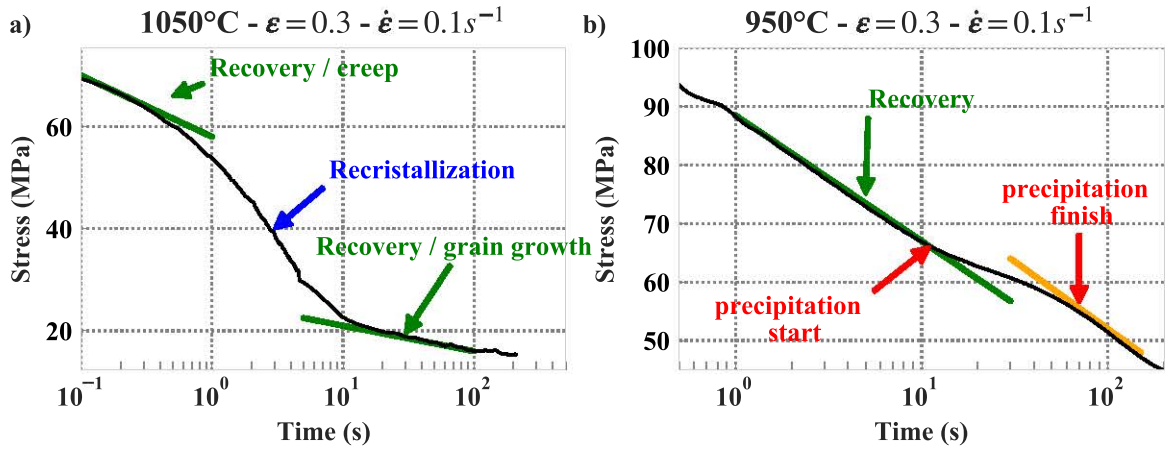

Figure 2.8: Illustration of the stress relaxation curves obtained at (a) 1050 °C and (b) 950 °C for $\epsilon = 0.3$ and $\dot{\epsilon} = 0.1\,\mathrm{s}^{-1}$.

material. Then, the curve typically exhibits a rapid and sharp drop related to the rapid softening due to recrystallization. The end of the curve also follows a linear shape, that mainly corresponds to the grain growth behavior of the recrystallized material ($\sigma_2 - \alpha_2 \cdot \log(t)$). Assuming that a partially recrystallized material consists of a mixture of two phases (work-hardened austenite and fully recrystallized austenite), a simple rule of mixtures is applied. Thus, the instantaneous value of stress is derived through the following equation:

$$\sigma = (1 - X) \cdot (\sigma_1 - \alpha_1 \cdot \log(t)) + X \cdot (\sigma_2 - \alpha_2 \cdot \log(t)) \tag{2.4}$$

where X is the recrystallized fraction. From 2.4, it can be derived that:

$$X = \frac{\sigma_1 - \alpha_1 \cdot \log(t) - \sigma}{(\sigma_1 - \sigma_2) + (\alpha_2 - \alpha_1) \cdot \log(t))} \tag{2.5}$$

At lower temperatures or for insufficient driving forces, recrystallization does not take place (Figure 2.8 b)). The softening observed is due to the recovery of the strained austenite. When precipitation occurs, a temporary increase in stress can be observed [LIU 88a]. The beginning and end of the precipitation process are detected from the deviation from the linear behavior.

For each test performed, the compression $\sigma - \varepsilon$ curve was also analyzed to determine the yield stress $\sigma_{0.2\%}$ and the rise in flow stress during work hardening $\Delta\sigma$ (see Figure 2.9) defined as:

$$\Delta\sigma = \sigma_{max} - \sigma_{0.2\%} \tag{2.6}$$

where σ_{max} is the maximum flow stress reached in the $\sigma - \varepsilon$ curve.

2.3.3 Metallographic examinations

Additional interrupted tests were run in order to perform metallographic examinations on 0.04Nb-0.5Ti-0.2V. After deformation, the samples were held for a certain time at the deformation temperature before being quenched with water. A Béchet-Beaujard etching [Bé 55] was performed to

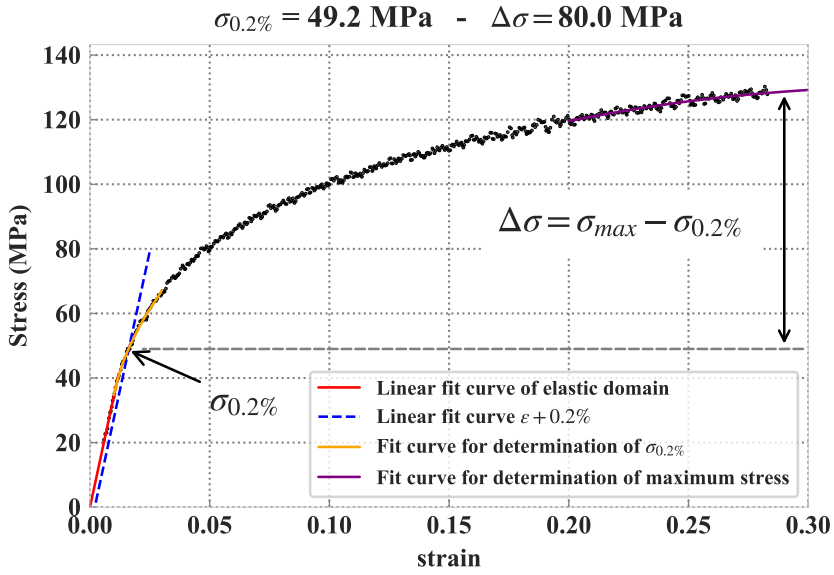

Figure 2.9: Analysis procedure of the compression curves, prior to the stress relaxation test. The yield stress $\sigma_{0.2\%}$ and the increase in flow stress $\Delta\sigma$ are determined.

reveal the austenite grain boundaries using an optical microscope. Austenite grain boundaries were manually detoured using FIJI [SCH 12]. The equivalent area diameter D_A of a circular grain was calculated from each measured grain area A:

$$D_A = \sqrt{\frac{4A}{\pi}} \tag{2.7}$$

The mean grain size D was estimated by multiplying the number-based mean equivalent area diameter D_A by 1.2, in accordance with [GIU 99]. Each optical micrographs were captured by placing the deformation direction horizontally. After manual detouring, ellipses were fitted on the obtained grain boundaries by a routine analysis performed on FIJI. Two other parameters were extracted from the analysis of austenite grain boundaries: the aspect ratio and the angle β between the long ellipse axis and the horizontal direction. The β angle allows to determine the orientation of the grains with respect to the direction of deformation.

2.4 Experimental results

2.4.1 Strain hardening during compression

Prior to stress relaxation, all samples underwent a compression test. The resulting compression curves were analyzed in order to determine the increase in flow stress $\Delta\sigma$ for the maximal ε reached during the test. No stress drop in the compression curves was observed in all the test performed, indicating that dynamic recrystallization did not take place for the strain levels applied in this study. Figure 2.11 shows the evolution of $\Delta\sigma$ as a function of testing temperature, strain, and strain rate

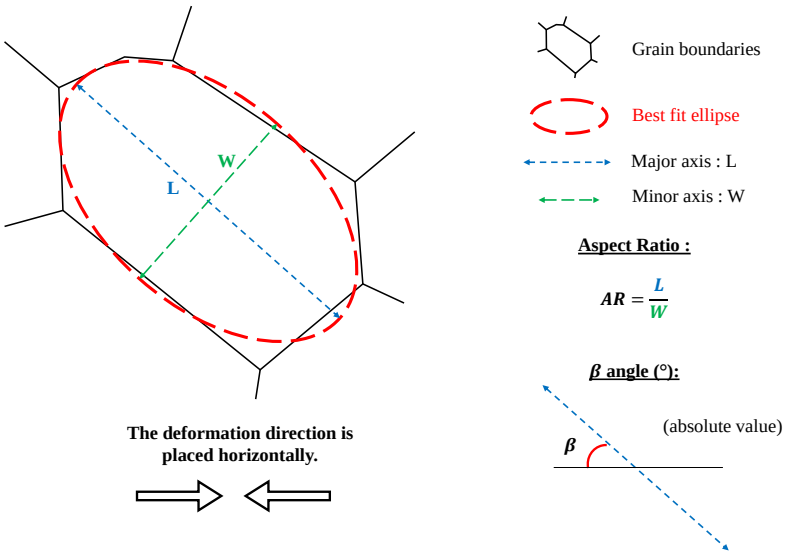

Figure 2.10: Definition of aspect ratio and β angle determined on FIJI.

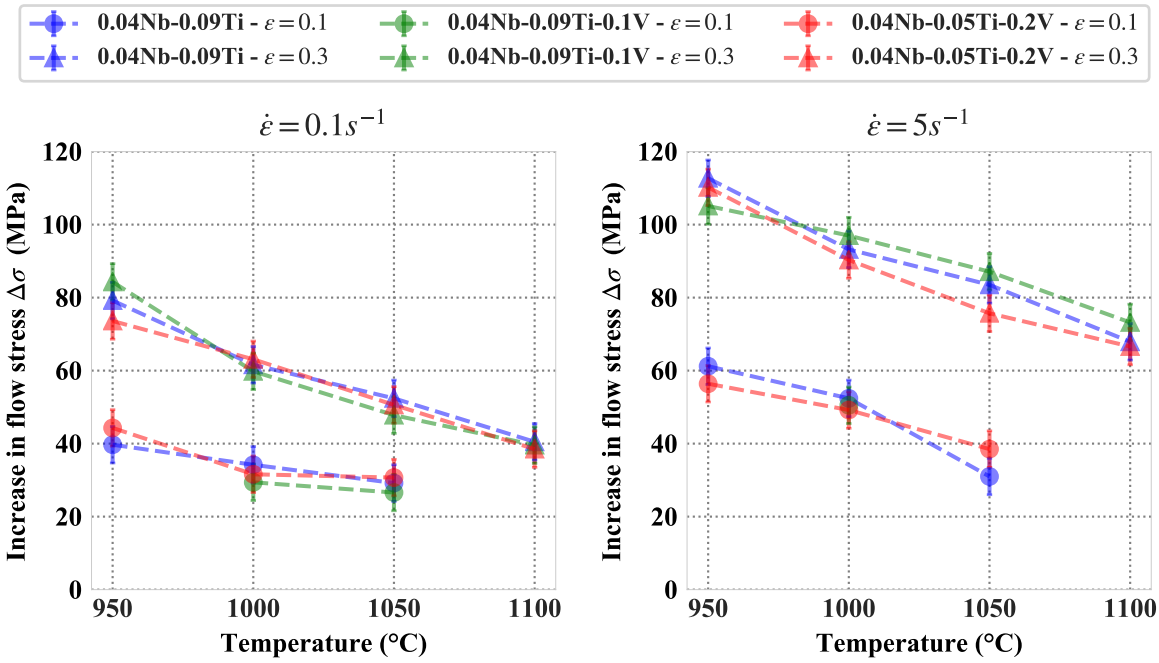

Figure 2.11: Evolution of the increase in flow stress during compression tests for the three studied steels, as a function of temperature and strain, for applied strain rates of $0.1\,s^{-1}$ and $5\,s^{-1}$.

applied during the compression tests performed with the Gleeble thermo-mechanical simulator. Increasing strain and strain rates results in a increase of $\Delta\sigma$. On the contrary, the higher the applied temperature, the lower $\Delta\sigma$ gets. It appeared that the three steels studied showed similar compression behaviors, which seems consistent since they present very similar compositions. Slight variations in Ti and V contents did not imply any significant change in $\sigma - \varepsilon$ behaviors.

2.4.2 Recrystallization kinetics

2.4.2.1 Stress relaxation curves

The raw stress relaxation curves obtained after deformation between 950 and 1100 °C are shown in Figure 2.12 for the three studied steels. Depending on the deformation parameters applied (temperature, strain, and strain rate), two types of softening mechanism are observed:

(i) When the driving force for recrystallization or the temperature is too low, the stress evolves linearly as a function of $\log_{10}(t)$. This type of behavior reflects the recovery process, and was observed for all steels for $\varepsilon = 0.1$ at all temperatures, and at 950 °C for $\varepsilon = 0.3$.

(ii) When both the driving force and temperature are high enough, the stress relaxation curves exhibit rapid drops in the form of sigmoids, indicating that recrystallization occurred. Recrystallization was typically observed in the three studied steel for an applied strain of $\varepsilon = 0.3$ and starting from 1000 °C.

These results show that an applied strain of 0.1 is below the critical strain for recrystallization initiation. For $\varepsilon = 0.3$, stress relaxation curves showed a change is the softening mechanism from recovery to recrystallization between 950 and 1000 °C. For conditions where recrystallization was observed ($\varepsilon = 0.3$ and $T \geq 1000$ °C) on the stress relaxation curves, the evolutions of the recrystallized fractions were calculated via equation 2.5, using the procedure showed in Figure 2.8 a). The recrystallization kinetics obtained are plotted in Figure 2.13. Some experimental dispersion can be observed for the raw data. In order to smooth these data, the raw curves were fitted by empirical JMAK laws, using $n = 1.5$:

$$X = 1 - \exp\left(-0.693 \cdot \left(\frac{t}{t_{1/2}}\right)^n\right) \tag{2.8}$$

All determined recrystallization half-times, $t_{1/2}$, can be retrieved in Table 2.3. In the following results, the recrystallization kinetics were always given using these empirical JMAK laws.

Temperature (°C)	1000		1050		1100	
Strain rate (s^{-1})	0.1	5	0.1	5	0.1	5
0.04Nb-0.09Ti	15.1	7.6	3.3	1.3	1.2	0.62
0.04Nb-0.09Ti-0.1V	25.9	13	9.3	5.4	3.2	0.93
0.04Nb-0.05Ti-0.2V	17.6	13	4.2	4.6	2.6	0.87

Table 2.3: Recrystallization half-times, $t_{1/2}$ (s), of the three studied steels obtained with $\varepsilon = 0.3$.

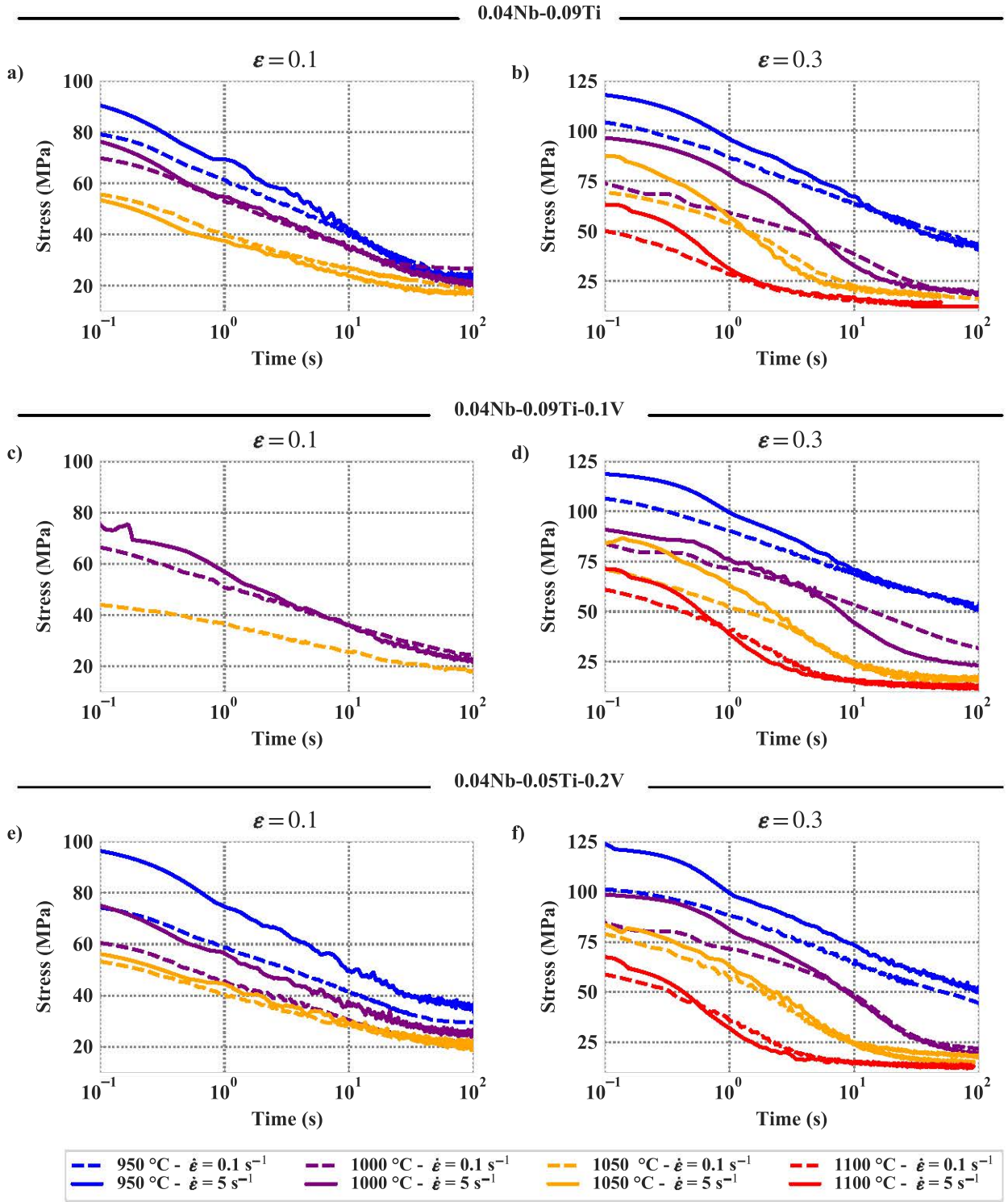

Figure 2.12: Raw stress relaxation curves obtained for 0.04Nb-0.09Ti (a-b), 0.04Nb-0.09Ti-0.1V (c-d), and 0.04Nb-0.09Ti-0.2V (e-f) steels.

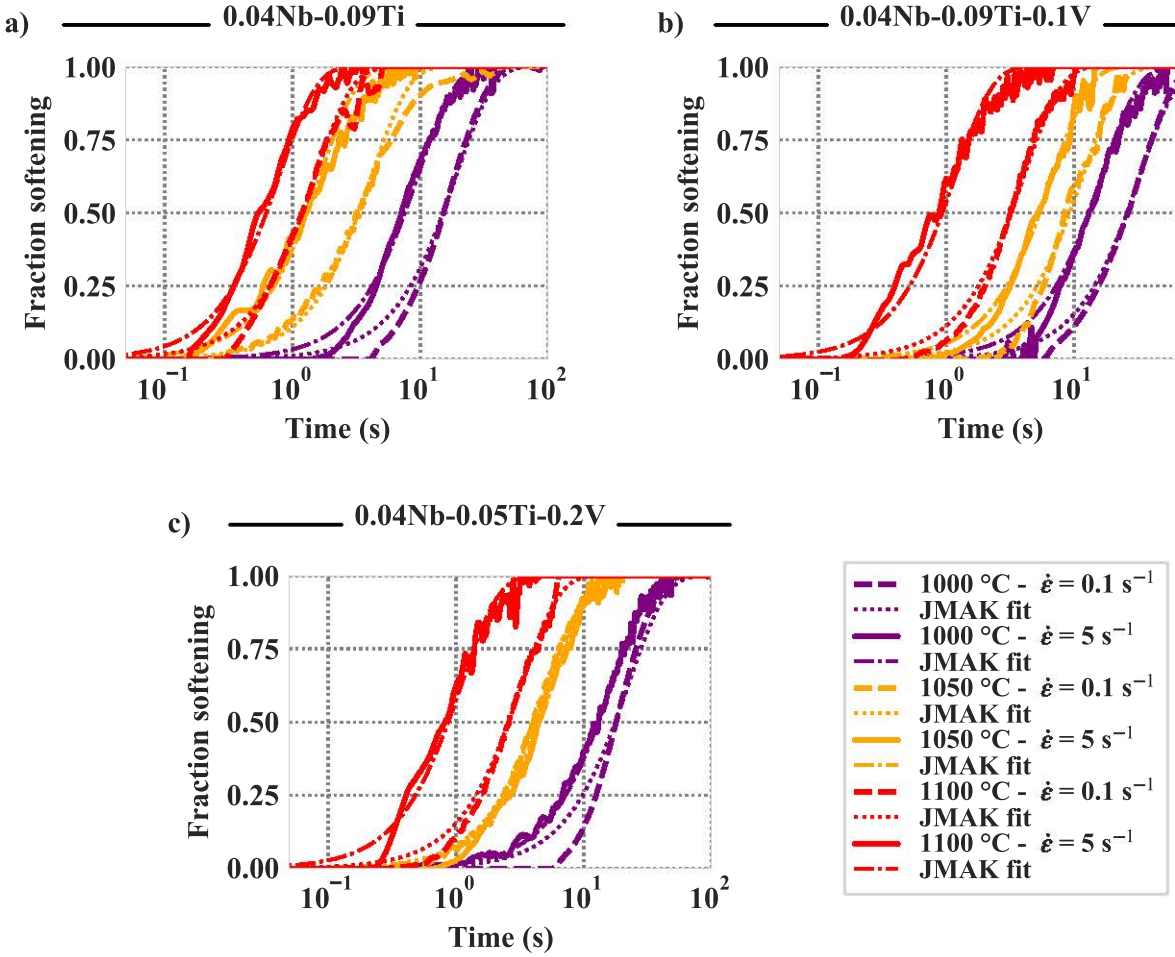

Figure 2.13: Softening fractions due to recrystallization during stress relaxation in (a) 0.04Nb-0.09Ti, (b) 0.04Nb-0.09Ti-0.1V, and (c) 0.04Nb-0.09Ti-0.2V steels. The raw data is represented together with fitted JMAK law curves obtained with a fixed parameter $n = 1.5$.

2.4.2.2 Austenitic microstructures

Stress relaxation tests allow indirect detection of recrystallization phenomena, via the evolution of stress. On the other hand, they do not, in themselves, provide any direct proof that recrystallization is the microstructural phenomenon responsible for the observed evolution of stress. Thus, austenitic microstructures were investigated by metallography before and during stress relaxation tests. Although the investigated microstructures are martensitic, only the prior austenite grains revealed by Béchet-Beaujard etching were investigated. For practical convenience, 0.04Nb-0.09Ti-0.2V was selected to perform these investigations, as it presents slower recrystallization kinetics compared to the two other studied steels. A water quenching device was added to the experimental setup in order to interrupt stress relaxation trials. As a consequence of the water quenching device, deteriorated levels of vacuum were obtained. The reheating stage at 1250 °C was thus limited to 3 min instead of 10 min, in order to limit oxidation. At the end of reheating, an equiaxed microstructure was obtained (see Figure 2.14), with a mean equivalent diameter of 85 µm.

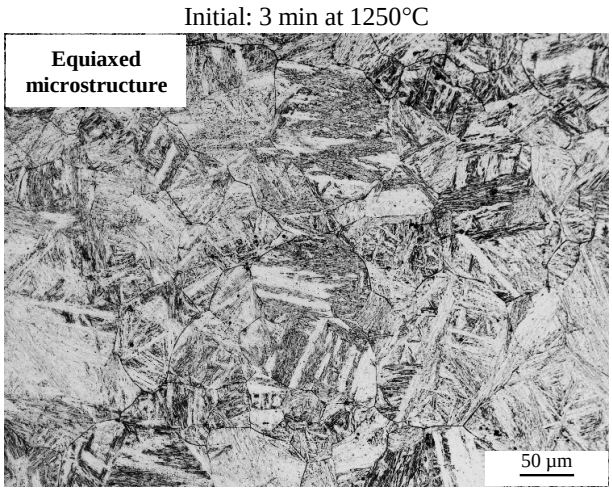

Figure 2.14: Initial austenitic microstructure revealed by Béchet-Beaujard etching for 0.04Nb-0.05Ti-0.2V steel, after 3 min at 1250 °C, prior to compression and stress relaxation.

Subsequently, the evolution of austenitic microstructures were followed during stress relaxation. Two distinct cases were investigated (see Figure 2.15):

(i) At 1050 °C, where the stress relaxation exhibits a sigmoidal shape indicating that austenite recrystallization is occurring.

(ii) At 950 °C, where the stress decreases linearly as a function of log(t), which is rather characteristic of the recovery process.

For each condition, three samples at different relaxation times were analyzed. The realized stress relaxation tests showed a very good reproducibility in terms of evolution of stress with time.

Figure 2.16 displays selected prior austenite grains obtained after quenching for the two stress relaxations tests performed. It should be noted here that all the micrographs were taken by placing the compression direction horizontally. For quasi-immediate quenching (0.1 s delay) after the end of the compression stage, austenite grains showed elongated shapes (Figure 2.16 a) and b)). The elongation direction is perpendicular to the compression direction. The grain boundaries exhibit irregular shapes, which contrasts with the fairly regular grain boundaries observed in the case of an undeformed equiaxed microstructure (Figure 2.14). These irregular grain boundary shapes may result from the strain-induced grain boundary migration phenomena, during which parts of a pre-existing grain boundary bulge to form regions with a lower dislocation contents [HUM 17]. At 1050 °C, some nucleus have formed, mainly at grain boundary triple junctions.

At 950 °C, 5 s after the end of compression, austenite grains still show elongated shapes (Figure 2.16 c)). Some nucleus have formed at grain boundary triple junctions. After 50 s at 950 °C, elongated grains are found together with rather equiaxed ones (Figure 2.16 e)). This indicates that the recrystallization process is only partial. On the contrary, recrystallization takes place rapidly at 1050 °C, as it can be observed on Figure 2.16 d) and f). After 3 s at 1050 °C, it becomes difficult to distinguish deformed grains from recrystallized ones. Eventually, a fully-recrystallized microstructure is obtained after 20 s at 1050 °C.

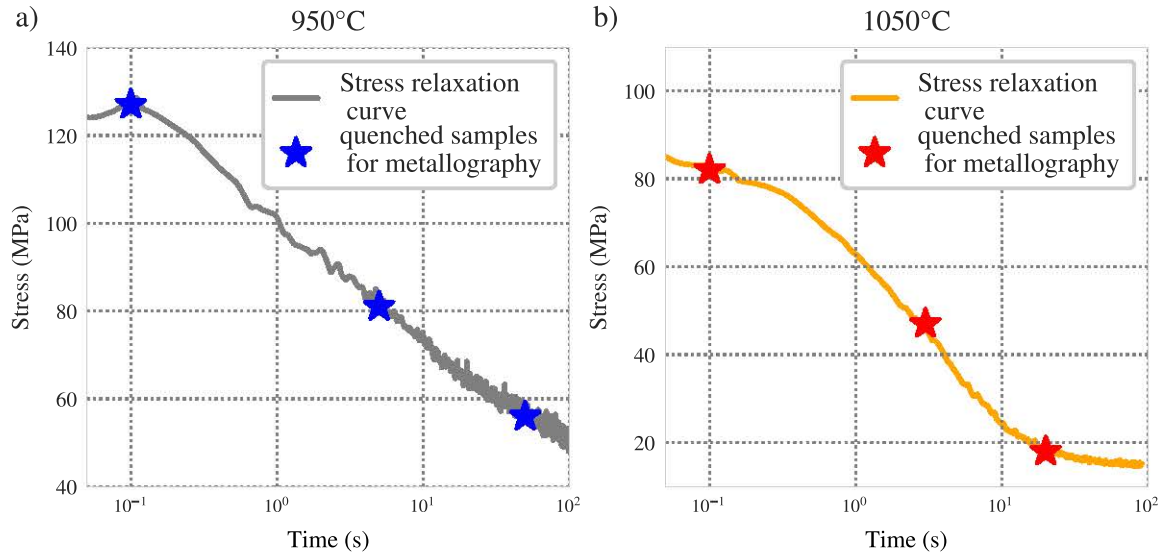

Figure 2.15: Selected conditions for metallographic examination of austenitic microstructures revealed by Béchet-Beaujard etching. Austenitic microstructures are investigated directly (0.1 s) after compression and during stress relaxation, at (a) 950 and (b) 1050 °C with $\varepsilon = 0.3$ and $\dot{\varepsilon} = 5\,s^{-1}$.

The microstructural evolutions of austenite can be followed by quantitative parameters that are displayed on Figure 2.17: (a) equivalent spherical grain diameter, (b) aspect ratio, and (c) β angle that allows the determination of the grain orientation with respect to the direction of deformation.

Starting from an initial 85 µm equivalent diameter, final grain diameter of approximately 40 µm are obtained at both 950 and 1050 °C. After the reheating stage of 3 min at 1250 °C, the austenite grains present an initial aspect ratio of approximately 1.5 , and β is close to 45°. The grains are therefore mainly equiaxed and show no particular orientations. Right after deformation, the aspect ratio of grains increases up to 1.8-1.9 and the mean value of β strongly increases up to 66-69°. It quantitatively indicates the deformation of grains and their preferential orientation perpendicular to the direction of compression.

At 1050 °C, the aspect ratio rapidly decreases down to a value of 1.6, and β returns to values close to 45° (random orientation). At 950 °C, these two parameters evolve more slowly. After 5 s at 950 °C, the aspect ratio is still high and the grains are still preferentially oriented perpendicular to the direction of compression. After 50 s at 950 °C, these parameters gets closer to the values obtained for a fully-recrystallized microstructure (20 s at 1050 °C), indicating a partially recrystallized state.

To summarize, the evolution of the austenitic microstructures during stress relaxation obtained proves that the shapes of relaxation curves are indeed directly correlated with recrystallization. At 950 °C, although it was not detected by stress relaxation (the curve exhibits a linear shape), metallographic examination of austenitic microstructures showed that an incomplete recrystallization process occurred.

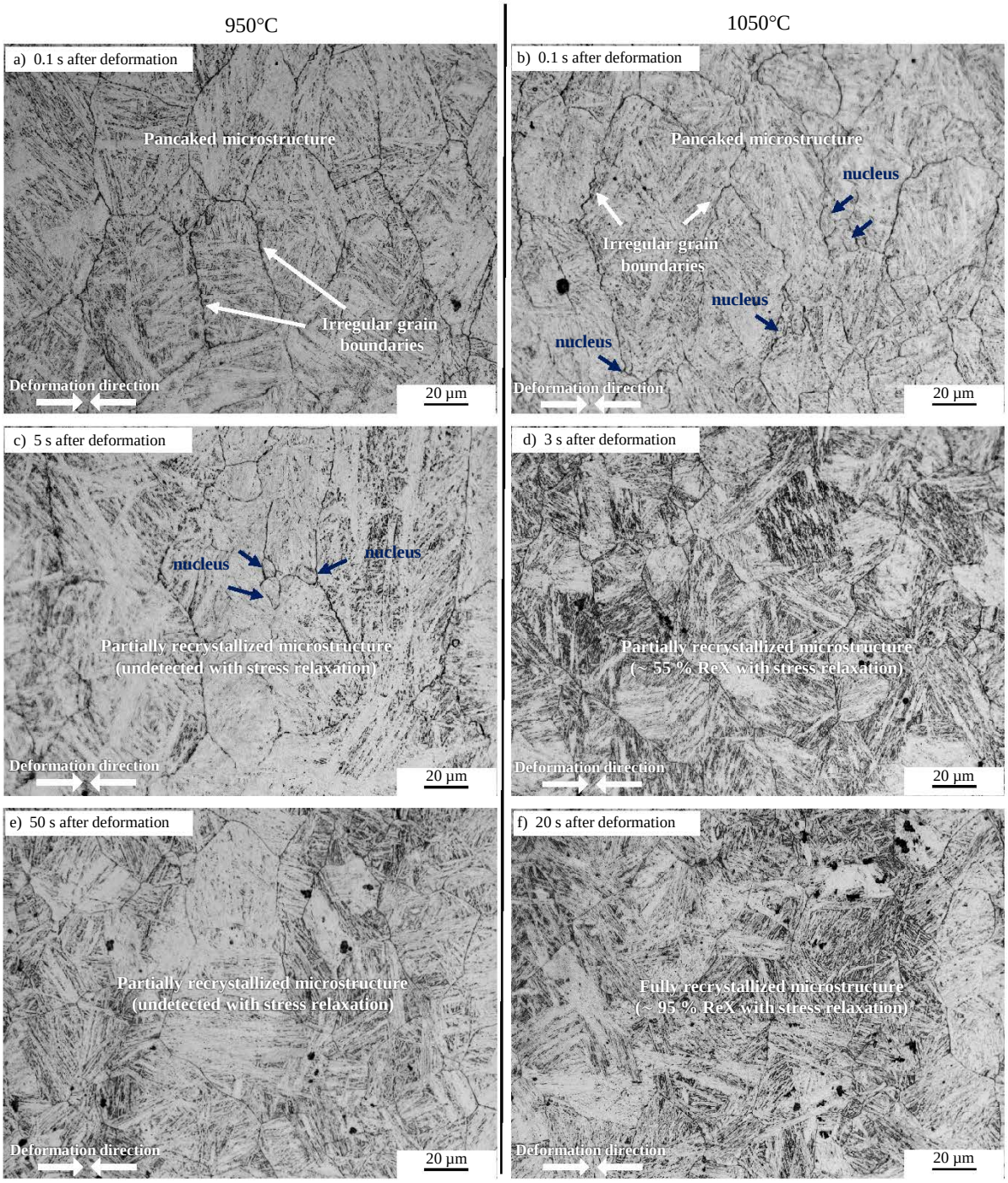

Figure 2.16: Selected austenitic microstructure revealed by Béchet-Beaujard etching for 0.04Nb-0.05Ti-0.2V steel, during stress relaxation tests at 950 and 1050 °C with $\varepsilon = 0.3$ and $\dot{\varepsilon} = 5\,s^{-1}$.

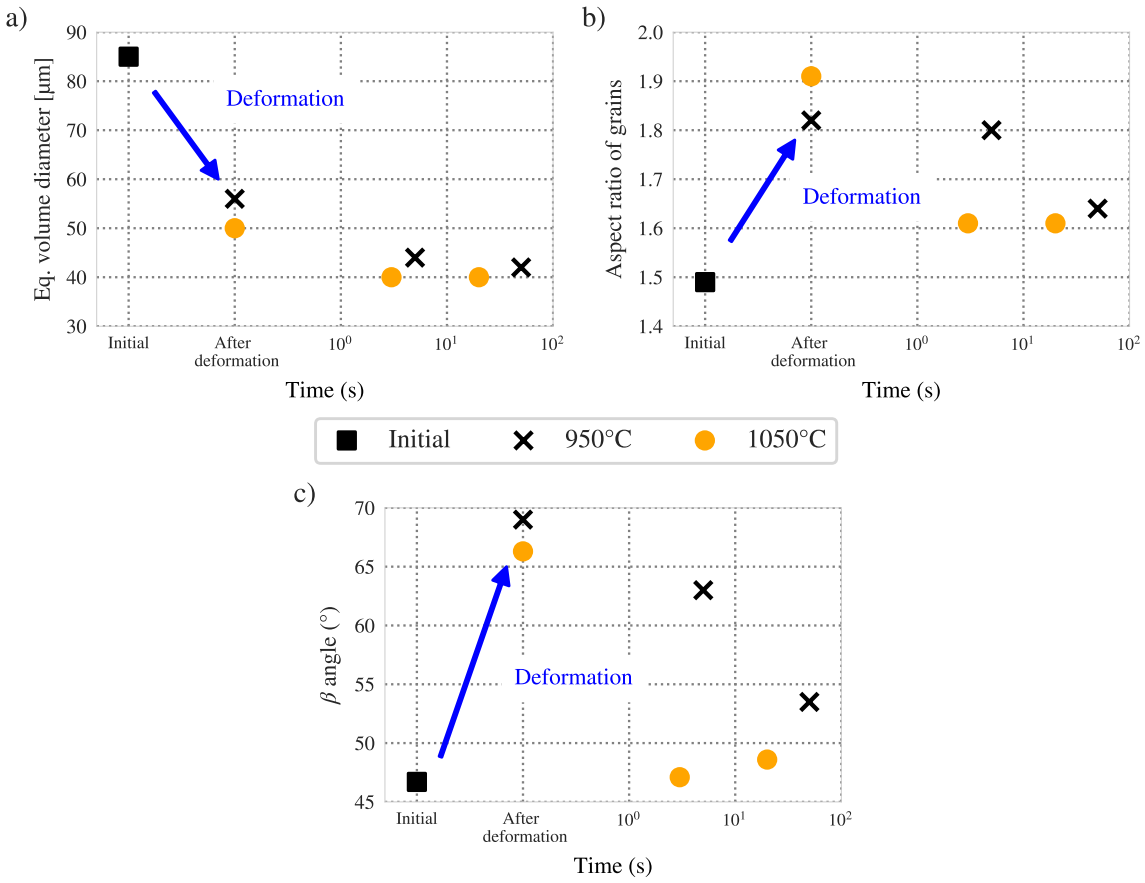

Figure 2.17: Evolution of (a) mean equivalent volume diameter, aspect ratio (b), and (c) β angle of austenite grains during stress relaxation tests at 950 and 1050 °C with $\varepsilon = 0.3$ and $\dot{\varepsilon} = 5\,\mathrm{s}^{-1}$.

2.4.3 Precipitation kinetics

The stress relaxation tests carried out on the Gleeble 3500 thermomechanical simulator proved to be unsuccessful to study the microstructural phenomena occurring for times longer than 100 s. Above 100 s, dilatation of the anvils leaded to variations in stress that erased all effects due to microstructural evolutions. As a result, precipitation phenomena were rather studied using the Bähr 805 DIL dilatometer, which is much more suited to carry out long heat treatments than Gleeble. Figure 2.18 shows the stress relaxation curves obtained for 0.04Nb-0.09Ti steel at 900, 950 and 1000 °C for an applied strain rate of $\dot{\varepsilon} = 0.1\,\mathrm{s}^{-1}$. Precipitation was detected by the apparition of a plateau in the stress relaxation curves in all conditions except for 1000 °C and $\varepsilon = 0.3$, where recrystallization occurred.

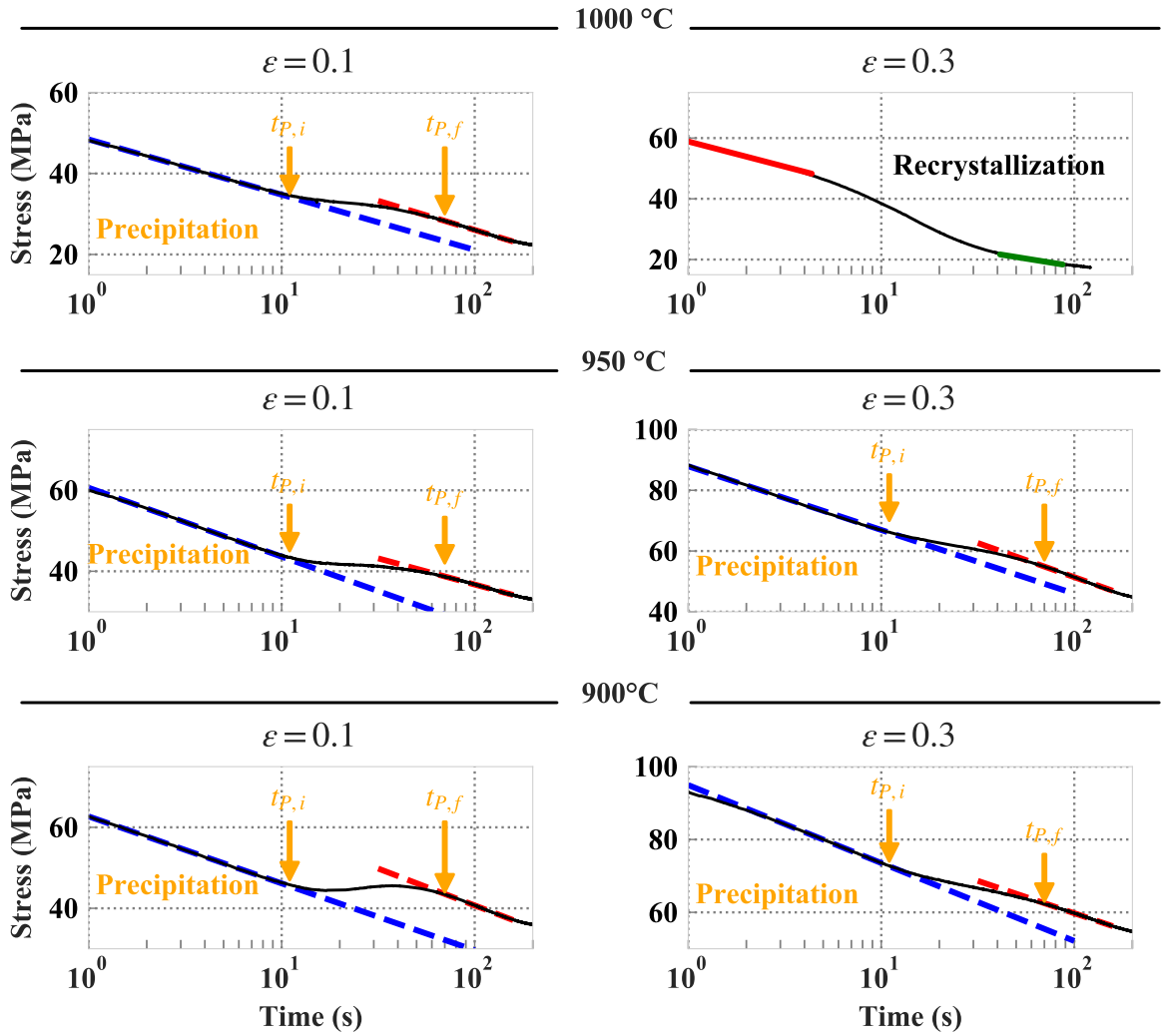

Figure 2.18: Stress relaxation curves obtained in Bähr 805 DIL dilatometer for 0.04Nb-0.09Ti steel at $\dot{\varepsilon} = 0.1\,\mathrm{s}^{-1}$.

Similar results were obtained for the two other steels studied. The determined precipitation start and finish times, respectively $t_{P,i}$ and $t_{P,f}$, are given in Table 2.4.3. Note that for each of the steels

studied, precipitation occurred in very similar time ranges. For 0.5Ti-2V steel at 950 °C, neither recrystallization nor precipitation was detected on the stress relaxation curve.

T (°C)	**900**				**950**				**1000**			
Strain	**0.1**		**0.3**		**0.1**		**0.3**		**0.1**		**0.3**	
Times (s)	$t_{P,i}$	$t_{P,f}$	$t_{P,i}$	$t_{P,f}$	$t_{P,i}$	$t_{P,f}$	$t_{P,i}$	$t_{P,f}$	$t_{P,i}$	$t_{P,f}$	$t_{P,i}$	$t_{P,f}$
0.04Nb-0.09Ti	10.6	81	9.0	79	7.0	72	10.4	69	8.3	61	ReX	
0.04Nb-0.09Ti-0.1V	9.4	98	7.8	85	9.5	76	8.1	68	10.0	73	ReX	
0.04Nb-0.05Ti-0.2V	12.0	78	9.0	69	8.0	65	-	-	10.7	61	ReX	

Table 2.4: Precipitation start $t_{P,i}$ and finish $t_{P,f}$ detected on stress relaxation curves for the three studied steels.

Stress relaxation tests, which indirectly detect precipitation but provide no direct evidence, were completed by observations in transmission electron microscopy. The precipitation state in 0.04Nb-0.09Ti steel after a stress relaxation test at 950 °C was investigated by TEM on carbon replicas. The stress relaxation test was performed under a strain of 0.3 and a strain rate of $0.1\,s^{-1}$ in the dilatometer. The sample was quenched after a 600 s holding at 950 °C. A large surface density of nanometer-sizes (Ti,Nb)C precipitates was collected on the replicas (Figure 2.19 a)). The precipitates present a mean radius of 12 ± 2 nm.

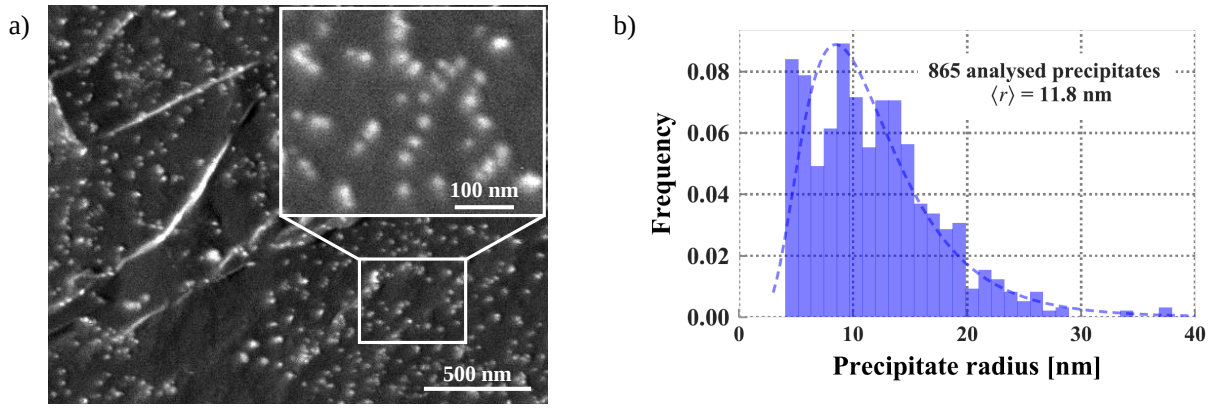

Figure 2.19: Precipitation state observed on carbon replicas in 0.04Nb-0.09Ti steel, 600 s after deformation at 950 °C with $\varepsilon = 0.1$ and $\dot{\varepsilon} = 0.1\,s^{-1}$. (a) STEM-HAADF micrograph ; (b) Precipitate size frequency distribution.

2.5 Models

The evolution of precipitation state and austenite composition in the 0.04Nb-0.09Ti steel during reheating was extensively studied in Chapter 1. This allowed to gather essential data on the metallurgical state of the steel at the end of reheating, which constitutes the preliminary step to the stress relaxation tests presented in this chapter. Here, it is proposed to extend the modeling work presented in chapter 1 by applying recrystallization and precipitation models to describe the microstructure

evolutions after hot deformation of austenite. These models are applied to the 0.04Nb-0.09Ti grade.

2.5.1 Recrystallization model

Modeling the static recrystallization of microalloyed steel using Johnson-Mehl-Avrami-Kolmogorov (JMAK) equation is a common approach in literature [CHO 01, MED 01, Gó 02, BAO 11, SHE 18]. These models are empirical and account for the effects of temperature, strain, strain rate, and initial austenite mean grain size. The recrystallized fraction is given by:

$$X = 1 - \exp\left(-0.693 \cdot \left(\frac{t}{t_{1/2}}\right)^n\right) \tag{2.9}$$

n is a material dependent constant, globally ranging from 1 to 3, and $t_{1/2}$ is the time needed to achieve 50% of recrystallization, following the expression:

$$t_{50} = A \cdot \varepsilon^p \cdot \dot{\varepsilon}^q \cdot D_0^r \exp\left(\frac{Q_a}{R_g T}\right) \tag{2.10}$$

a, p, q, r are constants, ε is the applied strain, $\dot{\varepsilon}$ is the applied strain rate, D_0 is the initial mean austenite grain size, R_g the ideal gas constant, Q_a the apparent activation energy for static recrystallization, and T the absolute temperature (K).

Although allowing to reproduce the experimental recrystallization kinetics, these empirical approaches do not make it possible to connect the JMAK law parameters with physical phenomena. In this PhD-work, a different approach is followed, based on the work presented by Zurob *et al.* [ZUR 01, ZUR 02]. The recrystallized fraction, X, is given by a modified JMAK law in which physical parameters are introduced:

$$X = 1 - \exp(-X_{ext}) \tag{2.11}$$

Where X_{ext} is the extended recrystallized volume:

$$X_{ext} = \left(N_{REX} \int_0^t M \cdot G \, \mathrm{d}t\right)^n \tag{2.12}$$

N_{REX} is the number of nucleation sites for recrystallization, M is the mobility, G is the driving force for recrystallization, and n is the exponent of the JMAK law. The mobility of grain boundaries is thermally activated:

$$M = M_0 \exp\left(\frac{-Q_{GG}}{R_g T}\right) \tag{2.13}$$

Here M_0 is a pre-exponential factor, R_g is the gas constant and Q_{GG} is the activation energy for grain boundary mobility.

The driving energy available for recrystallization, G, arises from the difference in dislocation density between a strained grain and a recrystallized grain [HUM 17]:

$$G = \frac{1}{2} \cdot \mu b^2 \Delta\rho \tag{2.14}$$

where μ is the shear modulus of austenite, b is the burgers vector, and $\Delta\rho$ is the change in dislocation density associated with the motion of a grain boundary from a deformed region to a recrystallized one. The value of $\Delta\rho$ is very difficult to measure experimentally and thus has to be estimated. The following equation is commonly used in literature [DUT 03, GÓM 05] for relating $\Delta\rho$ with the rise in flow stress during deformation, $\Delta\sigma$:

$$\Delta\sigma = M\alpha_T\mu b\sqrt{\Delta\rho} \tag{2.15}$$

Where M is the Taylor factor (3.1 for face-centered-cubic), α_T is a material constant, μ the shear modulus, and b the burgers vector. In this model, it is assumed that forest-type hardening relation links the flow stress σ, the yield stress $\sigma_{0.2\%}$, and the dislocation density ρ. Thus $\Delta\sigma$ is taken equal to $\sigma_{max} - \sigma_{0.2\%}$ (see equation 2.6). The driving force for recrystallization is thus calculated for each stress relaxation tests on the basis on the $\sigma - \varepsilon$ compression curve, and varies depending on the deformation parameters.

The number of recrystallization sites N_{REX} depends on the austenite grain size and temperature. In the present model, N_{REX} is given by:

$$N_{REX} = N^0_{REX} \exp\left(\frac{-Q_{REX}}{R_g T}\right) \tag{2.16}$$

Where N^0_{REX} is the pre-exponential factor, and Q_{REX} is the activation energy. Both are used as fitting parameters. $N^0_{REX} = 2.2 \times 10^{11}$ and $Q_{REX} = 150\,\text{kJ/mol}$ were used. Assuming that the austenite grain diameter after 10 min at 1250 °C is 400 µm according to Chapter 1, the number of austenite grains per cubic meter is approximately 2.98×10^{10}. In order to estimate the number of recrystallization sites per cubic meter, equation 2.16 needs to be corrected:

$$N_{REX/m^3} = (N_{REX})^{3/n} \tag{2.17}$$

At 1100 °C, it gives approximately 5.7 recrystallization sites per austenite grain.

All modeling parameters used in the recrystallization model are summarized in Table 2.5.

Parameter	**Value**	**Source/Comment**
JMAK law exponent, n	1.5	Best fit on experimental data.
N^0_{REX}	2.2×10^{11}	Best fit on experimental data.
Q_{REX}	150 kJ/mol	Best fit on experimental data.
M_0	10^4 $\text{m}^4\text{J}^{-1}\text{s}^{-1}$	As used in Chapter 1.
Q_{GG}	390 kJ/mol	Uhm *et al.* [UHM 04].
Taylor factor, M	3.1	For f.c.c. crystals.
α_T	0.15	As used in [DUT 92, ZUR 02, GÓM 05].
Shear modulus, μ	81×10^9[0.91 - (T(K)-300)/1810] Pa	Frost *et al.* [FRO 82].
Burgers vector, b	2.55×10^{-10} m	$a/\sqrt{2}$ with $a = 3.6 \times 10^{-10}$ m.

Table 2.5: Parameters used for recrystallization model calculations in 0.04Nb-0.09Ti steel.

2.5.2 Precipitation model

The precipitation modeling work is based on the one presented in Chapter 1. *PreciSo* [PER 08, PER 09] was applied to follow the precipitation of (Ti,Nb)C during heat treatments. The classical nucleation and growth theories implemented in *PreciSo* are detailed in part 1.5.3. The present precipitation modeling work focuses on strain-induced precipitation, occurring after compression, during stress relaxation tests. In order to compare the experimental results with the prediction of the precipitation model, the formation of (Ti,Nb)C during heat treatments in the lower temperature range of austenite stability (900 °C $< T <$ 1000 °C) is considered.

The dissolution temperature of (Ti,Nb)C_{fine} is equal to 1233 °C according to the calculations presented in Chapter 1. The initial distribution of (Ti,Nb)C_{fine} rapidly dissolves during a simulated heat treatment at 1250 °C. It is therefore considered that (Ti,Nb)C_{fine} are completely dissolved at the end of the preliminary reheating stage of 10 min at 1250 °C performed during stress relaxation tests. Thus, the initial carbon, titanium and niobium contents of austenite were estimated on the basis of the experimental investigation performed in Chapter 1.

It is assumed that after deformation, dislocations are the main nucleation sites available for the formation of precipitates. As proposed in [DUT 92], the number of nucleation sites for precipitation, N_0^P, is assumed to be related to the dislocation density by:

$$N_0^P = 0.5\rho^{3/2} \tag{2.18}$$

The dislocation density is estimated from the increase in flow stress, $\Delta\sigma$, using the same formalism as presented in part 2.5.1:

$$\rho = (\frac{\Delta\sigma}{M\alpha\mu b})^2 \tag{2.19}$$

Concerning the precipitate/matrix interfacial energy, the value given by Yong *et al.* [YON 89], used in Chapter 1, is considered as a reference. In order to fit the experimental data, this interfacial energy is multiplied by a dimensionless corrective coefficient k_P (close to 1):

$$\gamma_P = k_P \cdot [0.9545 - 4.27 \cdot 10^{-4} \cdot T(K)] \tag{2.20}$$

The other modeling parameters related to precipitation are identical to those used in chapter 1 of this PhD manuscript. The diffusion coefficient of carbon, titanium and niobium can be retrieved in Table 1.8. The modeling parameters used in the precipitation model applied to 0.04Nb-0.09Ti steel are synthesized in Table 2.6.

Parameter	Value	Source/Comment
Initial C content in austenite (wt.%)	0.0615	Based on Chapter 1.
Initial Ti content in austenite(wt.%)	0.0421	Based on Chapter 1.
Initial Nb content in austenite(wt.%)	0.0334	Based on Chapter 1.
(Ti,Nb)C solubility product	$\log_{10} K_S = -9612.4\ K/T + 0.40115$	See equation 1.24.
(Ti,Nb)C interfacial energy γ_P	$k_P \cdot [0.9545 - 4.27 \cdot 10^{-4} \cdot T(K)]$ J m^{-2}	From [YON 89].

Table 2.6: Parameters used for precipitation model calculations in 0.04Nb-0.09Ti steel.

2.6 Modeling results

2.6.1 Recrystallization kinetics

The analysis of the compression curves determined the increase in flow stress $\Delta\sigma$ for the varying deformation temperatures, strains and strain rates applied. $\Delta\sigma$ served as an input for the calculation of the driving pressure for recrystallization, G. Since recrystallization was only observed for $\varepsilon = 0.3$, G was only calculated for this strain. The determined value of G are displayed in Table 2.7.

Temperature (°C)	1000		1050		1100	
Strain rate (s^{-1})	0.1	5	0.1	5	0.1	5
Increase in flow stress $\Delta\sigma$ (MPa)	61	93	52	83	41	68
Increase in dislocation density $\Delta\rho$ ($\cdot 10^{14}$m^{-2})	3.0	6.9	2.3	6.1	1.7	5.2
Driving pressure G (MPa)	0.29	0.68	0.23	0.58	0.17	0.42

Table 2.7: Increase in flow stress during compression and resulting calculated increasing in dislocation densities and driving pressure for recrystallization for 0.04Nb-0.09Ti steel ($\varepsilon = 0.3$).

Figure 2.20 compares the recrystallization model predictions with the experimental JMAK curves obtained via stress relaxation tests. The model is able to reproduce the effects of strain rate and temperature on the recrystallization kinetics. The effect of strain rate is indirectly taken into account through the calculation of the driving pressure for recrystallization, because increasing strain rate leads to increased $\Delta\sigma$ values during the compression preceding stress relaxation.

An excellent agreement is found for the 5 slowest recrystallization kinetics. The agreement between model and experiments is weaker for the faster kinetics at 1100 °C and for $\dot{\varepsilon} = 5\,\text{s}^{-1}$. However, the recrystallization is so fast under these conditions that the experimental error on the determination of the empirical JMAK law is much more important.

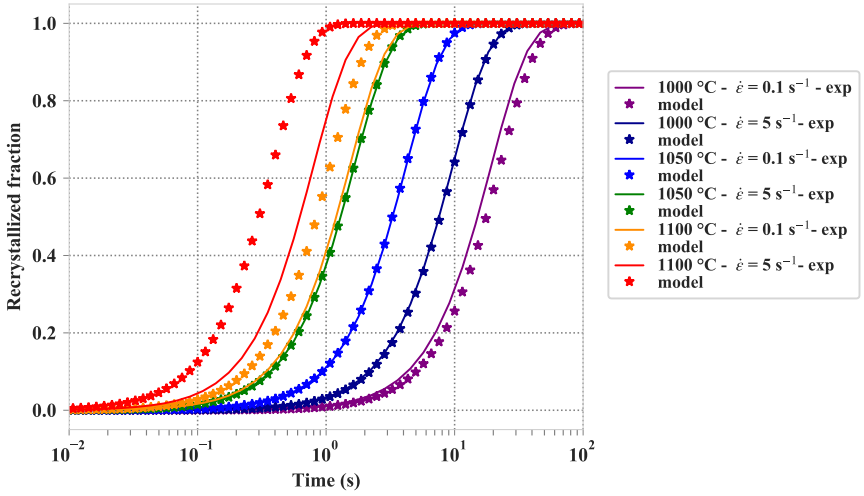

Figure 2.20: Comparison of the experimental recrystallization kinetics and recrystallization model predictions for the 0.04Nb-0.09Ti steel ($\varepsilon = 0.3$).

2.6.2 Precipitation kinetics

Stress relaxation tests coupled with TEM characterization of the precipitation state allowed obtaining a rather complete experimental study of precipitation after deformation of austenite. It is proposed to couple these experimental results with modeling results. The purpose is to determine whether the precipitation start and finish times detected by the stress relaxation tests can be obtained through modeling with physically meaningful parameters. It particularly focuses on determining whether the interface energies used are realistic or totally outside the ranges usually used.

The stress relaxation test performed at 950 °C (with $\varepsilon = 0.1$ and $\dot{\varepsilon} = 0.1\text{s}^{-1}$), and the associated TEM characterization are used to adjust the k_P interfacial energy coefficient (equation 2.20). Figure 2.21 shows the outputs of the precipitation model obtained for k_P value ranging from 0.80 to 0.90. The precipitation start and finish times determined on stress relaxation curves, $t_{P,i}$ and $t_{P,f}$, as well as the precipitate mean radius measured by TEM at 950 °C are also plotted.

The interfacial energy used has a considerable influence on the precipitation kinetics. The best agreement between the modeled mean radius and the measured one is obtained for $k_P = 0.875 \pm 0.025$ (Figure 2.21 b)). The precipitation start and finish times detected by stress relaxation tests do not seem to be related to the volume fraction or the size of the precipitates, but rather to their number density. This observation will be thoroughly analyzed in the discussion part 2.7.

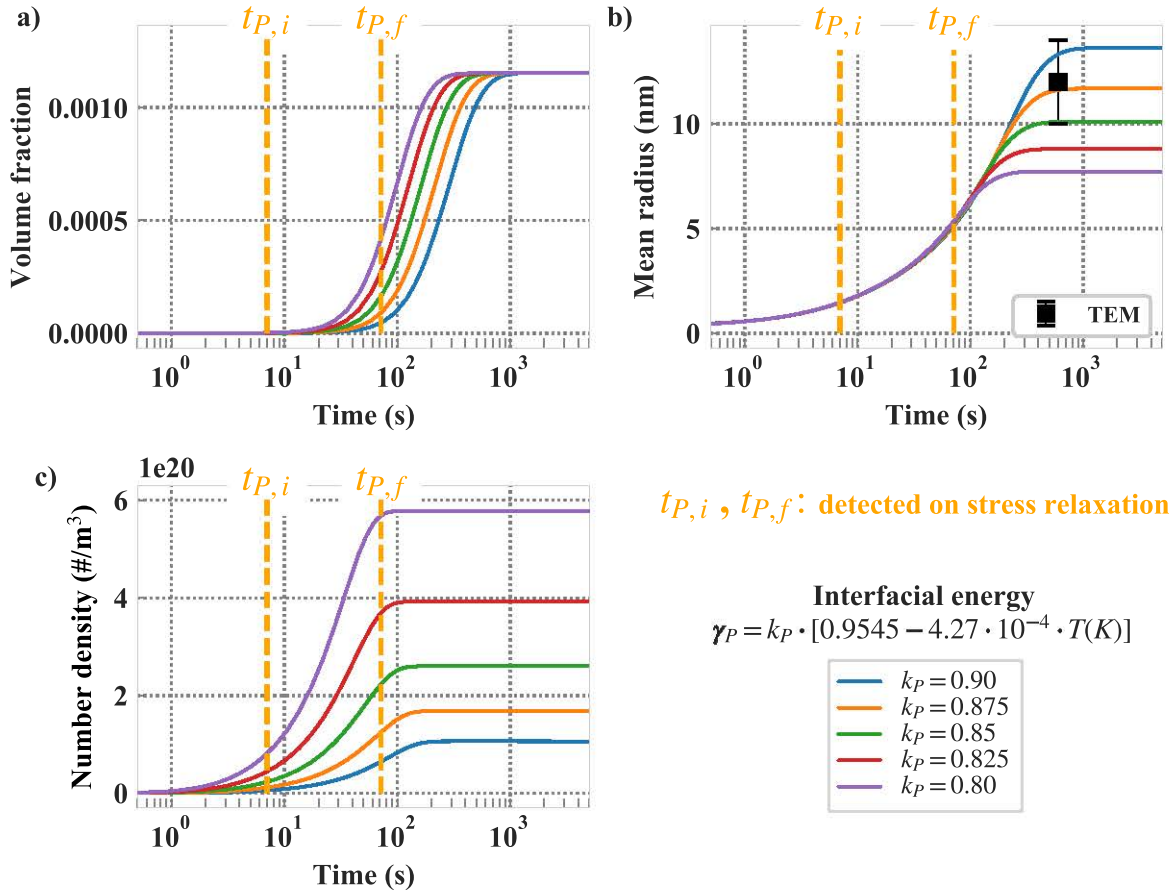

Figure 2.21: Precipitation modeling results obtained for varying interfacial energies: (a) volume fraction, (b) mean radius, and (c) number density of precipitates. k_P values ranging from 0.80 to 0.90 were applied.

2.7 Discussion and analysis

2.7.1 Influence of strain rate on recrystallization kinetics

Recrystallization start and finish times, respectively taken as $t_{REX,10\%}$ and $t_{REX,90\%}$, were determined based on the empirical JMAK laws fitted on experimental curves. Recrystallization-time-temperature diagrams are plotted in Figure 2.22 in order to highlight the effect of the strain rate on recrystallization kinetics.

For each of the three steels studied, the increase in strain rate leads to an acceleration of the recrystallization kinetics. Only one condition does not follow this rule: For 0.04Nb-0.5Ti-0.2V steel (Figure 2.22 c)), similar recrystallization kinetics are observed at 1050 °C for both applied strain rates. This general acceleration of the recrystallization kinetics is coherent with the fact that increasing $\Delta\sigma$ values are obtained when applying a higher strain rate (see Figure 2.11). As a matter of fact, the recrystallization model presented in part 2.5.1 allows reproducing the accelerating effect of strain rate, as it can be observed in Figure 2.20. When increasing strain rates are applied during compression, higher increases in flow stress $\Delta\sigma$ are achieved (Table 2.7), which means that

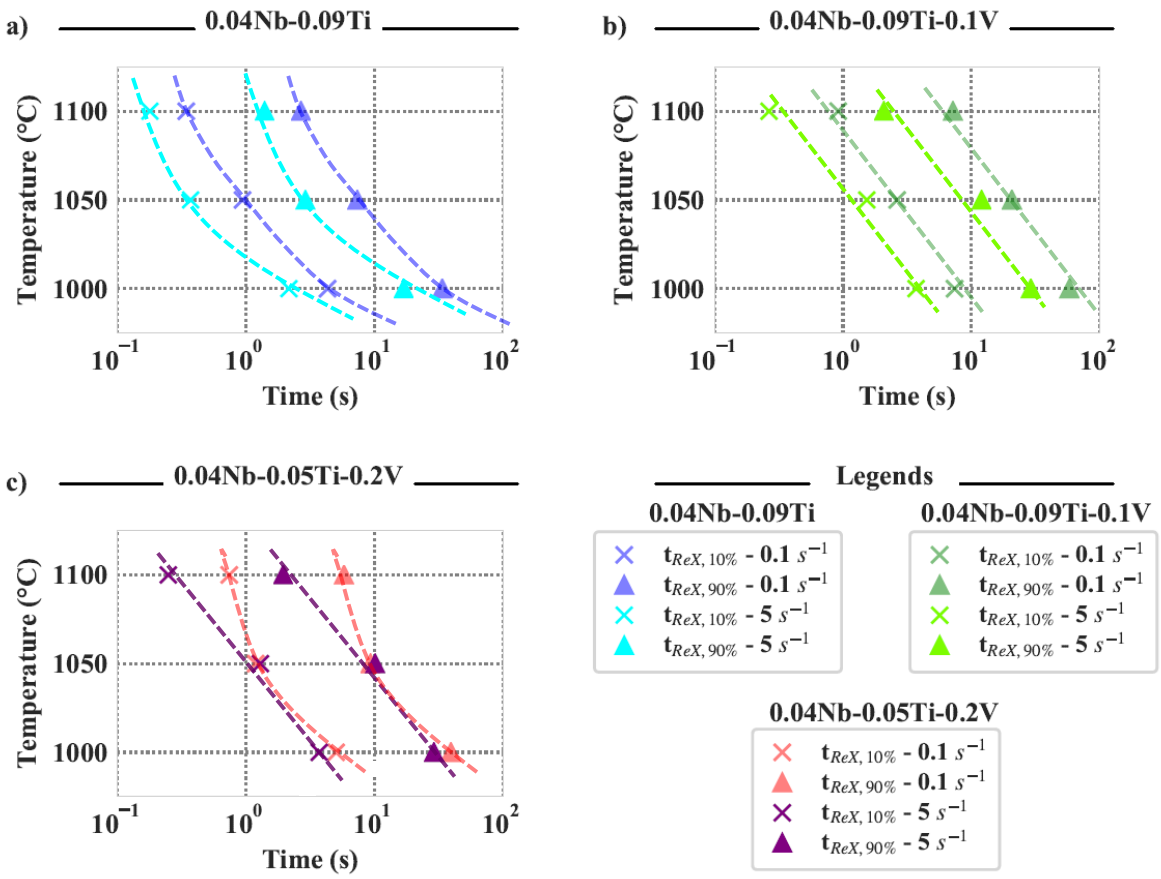

Figure 2.22: Recrystallization-Time-Temperature (RTT) diagrams showing the influence of strain rate of recrystallization kinetics for the three studied steels. The dash-dotted lines in the figure are given to guide the eye.

higher dislocation densities are obtained. Thus, the driving pressure for recrystallization increases as increasing strain rates are applied.

2.7.2 Influence of steel composition on recrystallization kinetics

In order to highlight the effect of steel composition on recrystallization kinetics, RTT diagrams are plotted in Figure 2.23. It appears that 0.04Nb-0.09Ti-0.1V and 0.04Nb-0.5Ti-0.2V steels present slower recrystallization kinetics than 0.04Nb-0.09Ti steel. The effect of vanadium additions seems to depend on the applied strain rate: while the difference between 0.04Nb-0.09Ti and 0.04Nb-0.09Ti-0.1V steel recrystallization kinetics at 1050 °C is limited for $\dot{\varepsilon} = 0.1\,\mathrm{s}^{-1}$, a larger offset is observed at the same temperature for $\dot{\varepsilon} = 5\,\mathrm{s}^{-1}$.

Figure 2.24 shows literature data[2] comparing the respective effects of Nb, Ti, and V on recrystallization kinetics. Niobium is known to be the microalloying element with the strongest delaying effect on static recrystallization, followed by titanium, and vanadium. Andrade *et al.* [AND 83] also

[2]The figures are extracted from Deardo [DEA 03b].

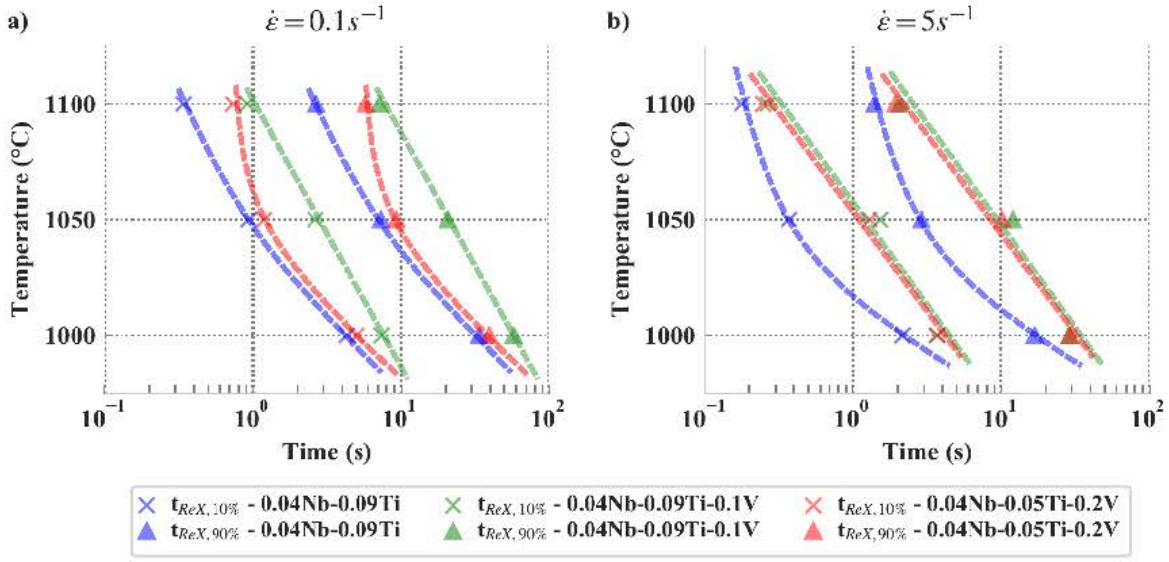

Figure 2.23: Comparison of the recrystallization kinetics of the three studied steels (Recrystallization - Time - Temperature diagrams). The dash-dotted lines in the figure are drawn to guide the eye.

reported the delaying solute drag effect of Mo, the effect of Mo laying between those of Nb and V. The three steels studied present approximately the same content of Nb and Mo, but different contents of Ti and V. The differences observed in the recrystallization kinetics are therefore due to the differences of Ti and V contents.

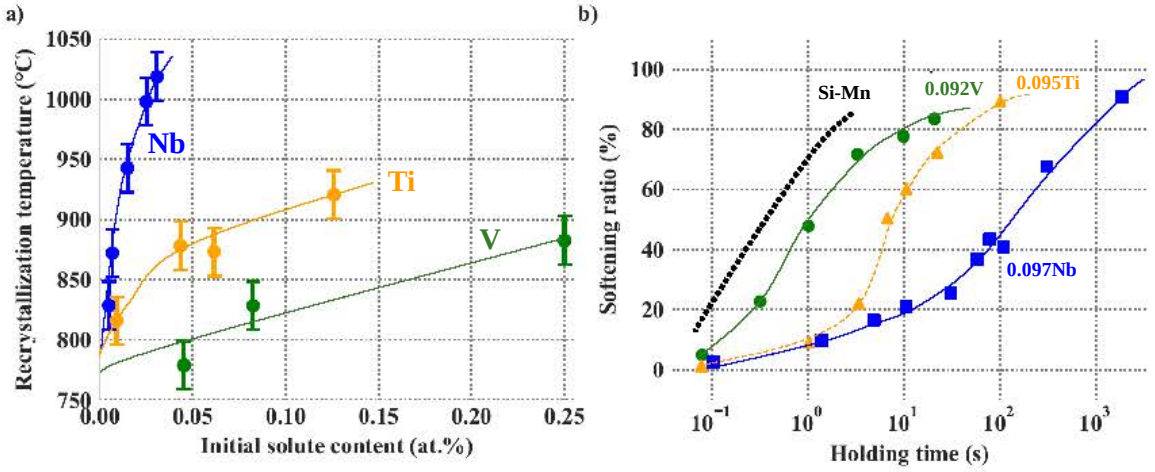

Figure 2.24: Literature data on the effects of microalloying additions on static recrystallization. (a) Increase in recrystallization temperature with increase in level of microalloy solutes in 0.07C-1.40Mn-0.25Si steel (from Cuddy [CUD 82]). (b) Effects of Nb, V, and Ti on softening behavior at 900 °C in 0.002 Cwt % (from Yamamoto *et al.* [YAM 82]).

Several studies reported delaying effects of vanadium additions on recrystallization kinetics, ei-

ther by formation of precipitates [MED 93, GAR 01, GÓM 07], or by solute drag [AND 83, GAR 01, AM 04]. The solute drag effect of vanadium is rather observed at high temperatures whereas the formation of V(C,N) retards austenite recrystallization at lower temperatures [GAR 01]. As a matter of fact, due to the high solubility of vanadium in austenite, vanadium precipitates do not form in the investigated temperature ranges (1000 to 1100 °C) for such carbon and vanadium contents. Thus, the only probable hypothesis is that V delays recrystallization kinetics by solute drag. This is consistent with the fact that precipitation is not detected on stress relaxation curves.

With an applied strain rate of $5\,s^{-1}$, the 0.04Nb-0.09Ti-0.1V and 0.04Nb-0.05Ti-0.2V present very similar recrystallization kinetics. Since both Ti and V participate to the solute drag effect, multiplying the vanadium content by 2 is counterbalanced by approximately dividing by 2 the titanium content.

2.7.3 On the recrystallization model parameters used

In the present recrystallization model, the formalism used for the determination of the driving pressure for recrystallization is based on Taylor's law. The parameters used are the same as those found in several articles dealing with austenite recrystallization [DUT 92, ZUR 02, GÓM 05]. They give rise to dislocation densities of the order of 10^{14} m^{-2} and to driving pressures of the order of 1 MPa, which are in the correct order of magnitude [HUM 17].

The grain boundary mobility used is the same as the one determined in Chapter 1, that was fitted on austenite grain growth experimental measurements. Moreover, the activation energy used, Q_{GG}, is extracted from Uhm *et al.* [UHM 04].

The number of nucleation sites for recrystallization, N_{REX}, also follows a Arrhenius law. The pre-exponential factor, N^0_{REX}, was adjusted to fit the experimental kinetics. Nucleation is related to grain boundary diffusion, since nuclei form at grain boundaries. Most of the activation energies for grain boundary diffusion of iron in austenite available in literature lies between $140\,kJ\,mol^{-1}$ and $180\,kJ\,mol^{-1}$ [KAU 90]. The activation energy used, Q_{REX} =$150\,kJ\,mol^{-1}$, falls into that range.

Medina and Fabregue [MED 91] provided an empirical formula for the apparent activation energy of static recrystallization of microalloyed austenite, Q_{app}, accounting for the contribution of steel composition:

$$Q_{app} = 83600 + 97800\frac{(\mathrm{Mn}+\mathrm{Si})^{0.537}}{\mathrm{C}^{1.269}} + 1728.7\mathrm{Mo}^{0.704} + 4952\cdot 10^5\mathrm{Ti}^{3.663} + 259.6\mathrm{Nb}^{1.256} \quad (2.21)$$

where Q_{app} is given in $J\,mol^{-1}$, and the contents of alloying elements (Mn, Si, etc.) are given in 10^3 wt.%.

Assuming effective Ti and Nb content in austenite respectively equal to 0.0415 wt % and 0.334 wt %, consistently with the atom probe tomography study presented in Chapter 1, equation 2.21 gives rise to $Q_{app} = 560\,kJ\,mol^{-1}$. Since the present recrystallization model comprises two Arrhenius laws, Q_{GG} and Q_{REX}, the apparent activation energy for static recrystallization in 0.04Nb-0.09Ti steel is $Q_{GG} + Q_{REX} = 540\,kJ\,mol^{-1}$. This value is comparable to the apparent activation energy given by equation 2.21.

To summarize, the applied modeling parameters all fall into realistic orders of magnitude, and can be related to physical phenomena.

2.7.4 On the detection of precipitation by stress relaxation trials

The classical way to plot Precipitation-Time-Temperature (PTT) diagrams is to consider the volume fraction of precipitates formed. In this approach, the precipitation start and finish times, $t_{P,i}$ and $t_{P,f}$, are respectively taken equal to the times where X % and $100 - X$ % of the maximum volume fraction are formed. This type of diagram can be built when the applied technique measures a value linked to the volume fraction of precipitates, as it is the case for thermo-electric power (TEP), electrical resistivity, or direct microstructural investigations.

In this study, stress relaxation tests are used to derive $t_{P,i}$ and $t_{P,f}$. Due to the occurrence of precipitation, the stress relaxation curve departs from its initial linear trend due to a stress increment $\Delta\sigma_{SR}$. $t_{P,i}$ is determined when $\Delta\sigma_{SR}$ starts to differ from zero, whereas $t_{P,f}$ is when $\Delta\sigma_{SR}$ reaches its maximum value [LIU 88a]. Although it is clear that the stress plateau is related to precipitation, there is no indication that $t_{P,i}$ and $t_{P,f}$ are directly related to the volume fraction of precipitates. The question is thus to determine the precipitation characteristics linked to $t_{P,i}$ and $t_{P,f}$.

Two different hypotheses can be assumed about the appearance of the plateau:

(i) The first one, as considered by [PAN 05], is to consider that precipitation stops recrystallization due to the pinning pressure induced by precipitates on moving grain boundaries. The plateau would thus be related to the pinning pressure, proportional to a f_v/r ratio.

(ii) The second hypothesis is that the stress plateau is related to the interaction of precipitates with dislocations during recovery. When precipitation starts, mobile dislocations are pinned by precipitates. Liu and Jonas [LIU 88a] initially proposed that dislocations pinning stays effective until Ostwald ripening starts, during which particles start to lose their ability to pin the dislocations.

Assumption (i) does not seem reasonable in this study, because the stress relaxation decreases linearly as a function of log (t) before the plateau, which is rather related to a recovery process. It is therefore more probable that the plateau is due to dislocation/precipitate interactions (assumption ii). Zurob *et al.* [ZUR 02] proposed for instance that the appearance of a plateau in stress relaxation is related to the number of precipitates with respect to the number of dislocation nodes. Under this hypothesis, $t_{P,i}$ and $t_{P,f}$ are thus linked to the number density of precipitates rather than to their pinning pressure exerted on grain boundaries.

This assumption seems in line with the observation made on the precipitation modeling results in Figure 2.21. The precipitation start and finish times do not appear to be linked to neither the volume fraction (Figure 2.21 a)) nor precipitate mean radius (Figure 2.21 b)) but rather with the number density of precipitates (Figure 2.21 c)). It would be interesting to deepen the precipitation modeling calculations in order to analyze the influence of precipitation on relaxation stress. In particular, it should be taken into account that the dislocation density decreases over time because of recovery, which reduces the number of nucleation sites for precipitates.

2.7.5 Interactions between precipitation and recrystallization

2.7.5.1 RPTT diagrams

The combination of stress relaxation tests performed with the Gleeble and dilatometer allowed the reconstruction of complete Recrystallization-Precipitation-Time-Temperature (RPTT) diagrams. These RPTT diagrams are drawn in Figure 2.25 for each of the three studied steels and for an applied strain rate of $0.1\,s^{-1}$. They allow an overview of the microstructural evolutions observed for this strain rate.

An applied strain of 0.1 (Figure 2.25 a), c), and e)) is insufficient to induce recrystallization but provides enough nucleation sites for the precipitation process. Precipitation is observed between 900 and 1000 °C, and recovery above 1000 °C. When a larger deformation is applied ($\varepsilon = 0.3$), recrystallization is observed above 1000 °C, and precipitation at 950 and 900 °C.

When recrystallization takes place before precipitation (as observed at 1000 °C and $\varepsilon = 0.3$), no precipitation is detected on stress relaxation curves. Recrystallization causes a decrease in the density of dislocations, which are the main nucleation sites for strain-induced precipitation. Thus, the formation of precipitates is delayed to longer times, probably larger than the duration of the stress relaxation tests carried out. After recrystallization, the relaxation stress decreases down to low levels, around 20 MPa. For such low stress levels, it becomes difficult to detect precipitation by the stress relaxation technique, which does not mean that it does not take place at 1000 °C and above.

It seems that only solute drag is limiting the progress of recrystallization at high temperatures. Indeed, pre-existing (Ti,Nb)C precipitates are fully dissolved during the reheating stage, and the other larger populations can only have a very limited pinning pressure. The times involved to reach a full recrystallization are too short to form strain-induced precipitates. For decreasing temperatures, precipitation takes place before recrystallization. It can be assumed that the newly formed fine precipitates largely delays recrystallization. As a result, recrystallization was not observed at 900 and 950 °C for the heat treatment times involved.

2.7.5.2 Comparison with existing equations for T_{NR}

In order to design the hot rolling process, the determination of the temperature of no-recrystallization, T_{NR}, is of particular interest. The most common approach to determine T_{NR} is to simulate successive rolling passes under a fixed cooling rate. After a reheating stage, the sample undergo a series of successive deformations separated by a fixed interpass time, Δt, while the sample is cooled down at a fixed cooling rate. Then, the T_{NR} is determined by representing the evolution of the mean flow stress (MFS) of each pass as a function of absolute inverse temperature for each deformation passes. T_{NR} depends both on the applied ε, $\dot{\varepsilon}$, and Δt.

Gorni [GOR 11] and Homsher [HOM 13] performed detailed reviews of the available empirical equations for T_{NR}. Most of these empirical equations focus on Nb additions. Much less were established on steels containing combined additions of Ti, Nb, and V. Additionally, none of the available equations take into account the delaying effect of Mo. Thus, of the available equations, only two of them appear to be suitable for comparison with the experimental data generated in this

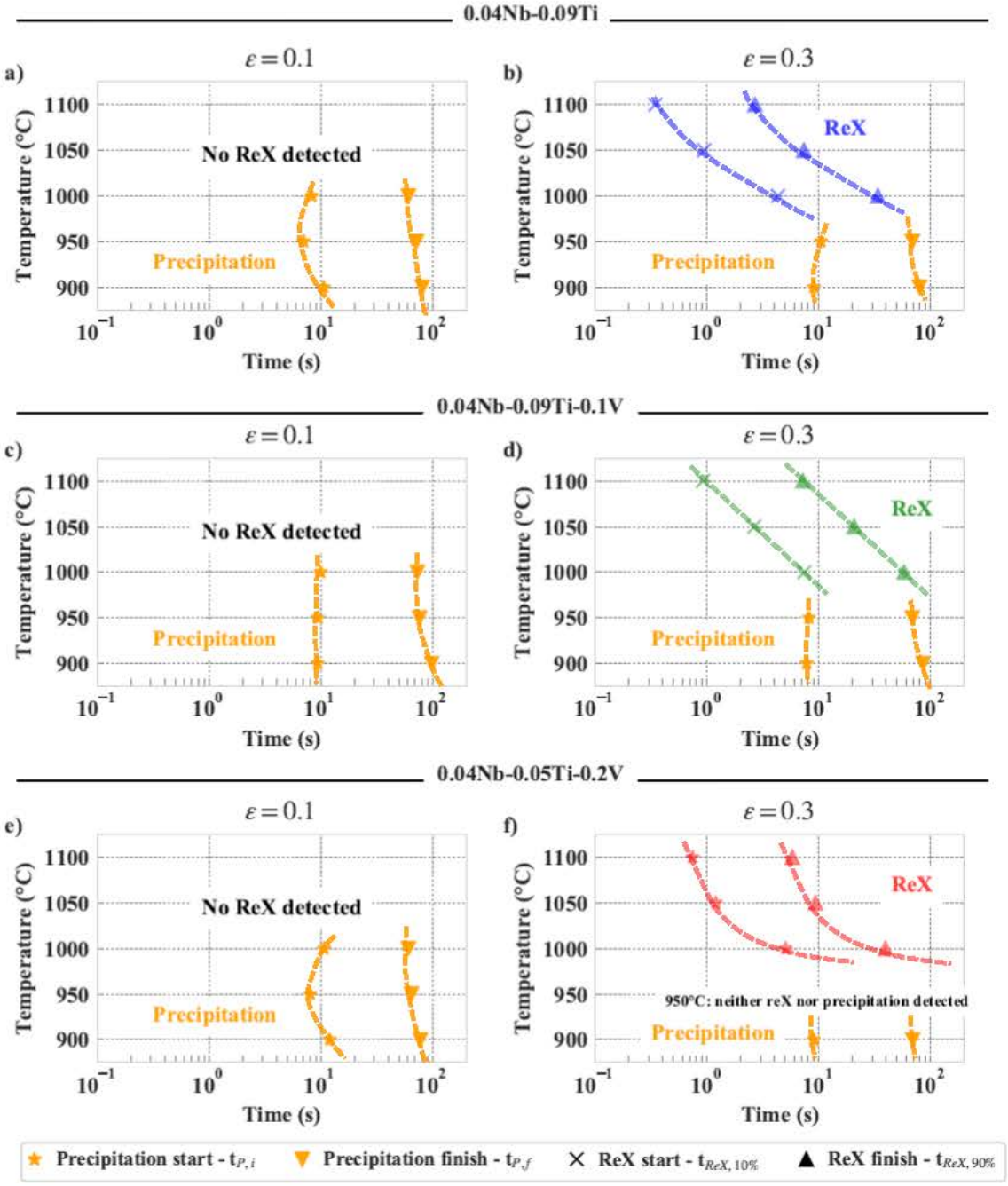

Figure 2.25: Recrystallization - Precipitation - Time - Temperature (RPTT) diagrams determined by exploitation of stress relaxation curves for the three studied steels. A strain rate of $0.1\,s^{-1}$ was applied.

PhD-work:

(i) Boratto *et al.* [BOR 88] equation:

$$T_{NR} = 887 + 464C + 6445Nb - 644\sqrt{Nb} + 732V - 230\sqrt{V} + 890Ti + 360Al - 357Si \quad (2.22)$$

This equation is the most known empirical formula used in literature to estimate T_{NR}. The composition range used by Boratto *et al.* are close to the one used in this PhD-work, and the equation includes effects of the microalloying elements (Ti, Nb, and V) present in the steels. An interpass time of 30 s was used.

(ii) Bai *et al.* [BAI 96] equation:

$$T_{NR} = (88.1 \ln(\mathrm{Nb}_{eq}) + 1156) \cdot \varepsilon^{-0.12} \cdot \dot{\varepsilon}^{-0.01} \cdot \Delta t^{-0.1} \tag{2.23}$$

where $\mathrm{Nb}_{eq} = \mathrm{Nb}{+}0.31\mathrm{Ti}{+}0.15\mathrm{Al}$ is the equivalent Nb content. This equation was determined with $1 < \Delta t < 12.5\,\mathrm{s}$, $0.2 < \varepsilon < 0.5$, and $0.2 < \dot{\varepsilon} < 10\,\mathrm{s}^{-1}$. It must be noted that this equation does not take into account the effects of V, and that the Ti levels in the studied steels are above those studied by Bai *et al.* ($\mathrm{Ti} \leq 0.026\,\mathrm{wt}\,\%$). Thus the effects of Ti additions may be poorly represented by this equation. The other alloying elements are in similar ranges of composition.

Before making a comparison of these empirical formulas with the results obtained in this chapter, it must be considered that all these equations were established with continuous cooling experiments whereas isothermal heat treatments were performed in the present study. During continuous cooling, the decrease in temperature between two applied deformation passes, ΔT, generally ranges from 25 to 30 °C, which slows down the recrystallization kinetics between two passes. Therefore, the no-recrystallization temperature determined in isothermal conditions is approximately ΔT higher than the one obtained from continuous cooling experiments [BAI 93]. In order to take that point into account, the T_{NR} empirical equations (equations 2.22 and 2.23) were increased by their corresponding ΔT values. A summary of the composition ranges and the deformation parameters for this study and for the two empirical T_{NR} equations is given in Table 2.8.

The T_{NR} is, by definition, the temperature below which recrystallization is no longer complete between two deformation passes. Thus, empirical T_{NR} equations can be compared with the times needed to reach 90 % recrystallized fraction determined by stress relaxation, in isothermal conditions. The comparison is performed using a strain rate of $5\,\mathrm{s}^{-1}$, since it is the closest from the strain rates ranges applied in industrial conditions. Figure 2.26 compares the results from the three above-cited empirical equations with the experimental data generated in this work.

The T_{NR} value predicted by Bai *et al.* [BAI 96] are significantly below the experimental values determined by stress relaxation. This equation also over-evaluates the effect of interpass time of the T_{NR}, so that the gap between Bai's equation and experimental values increases with increasing Δt. These differences seems understandable since this equation cannot properly traduce the effects of Ti and V on recrystallization kinetics.

On the contrary, although it was established with slightly lower strain and strain rates, Boratto's predictions appears to be very close from the experimental recrystallization finish times, and well describes the effects of Ti and V. This equation predicts that 0.04Nb-0.09Ti-0.1V and 0.04Nb-0.05Ti-0.2V grades have almost identical T_{NR}, approximately 30 °C higher than the 0.04Nb-0.09Ti grade. This seems consistent since the stress relaxation tests showed that these 2 steels have quasi-identical recrystallization kinetics, slower than the 0.04Nb-0.09Ti grade.

Content	**This study**		**Boratto *et al.***		**Bai *et al.***	
	min	max	min	max	min	max
C	0.062	0.087	0.04	0.17	0.021	0.125
Mn	1.91	1.95	1.46	1.48	0.43	1.80
Si	0.50		0.15	0.50	0.12	0.33
Ti	0.046	0.093	0	0.11	0	0.026
Nb	0.039		0	0.06	0	0.09
V	0.002	0.206	0	0.12	-	-
Mo	0.21		0	0.31	0	0.35
Al	0.065	0.067	0.002	0.065	0.02	0.042
N	0.006		-	-	0.003	0.01

Parameter	**This study**	**Boratto *et al.***	**Bai *et al.***	
			min	max
Strain ε	0.3	0.2	0.2	0.5
Strain rate $\dot{\varepsilon}$ (s^{-1})	5	2	0.2	10
Thermal conditions	Isothermal	Continuous cooling	Continuous cooling	
Interpass time Δt (s)	-	30	1	12.5
Cooling rate (°C s^{-1})	-	1	$30/\Delta t$	
ΔT	-	30	30	

Table 2.8: Comparison of the range of steel composition (wt. %) and deformation parameters used for this study and those used in literature for empirical T_{NR} equations.

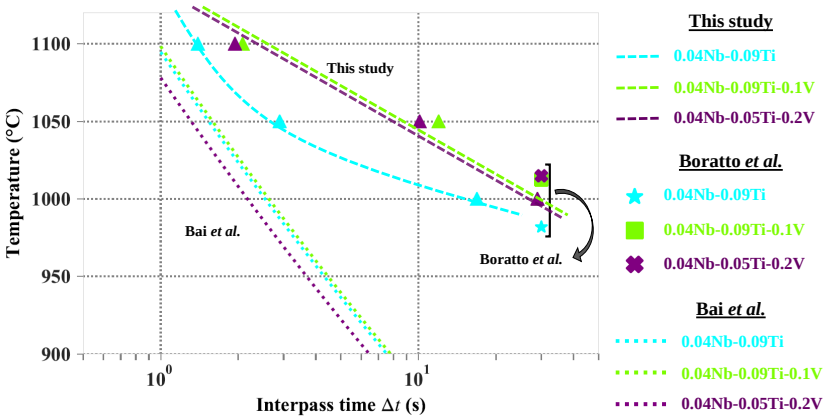

Figure 2.26: Comparison of the recrystallization finish times determined by stress relaxation with an applied strain rate of $5\,s^{-1}$, $t_{ReX,90\%}$, with empirical T_{NR} equations given by Bai *et al.* [BOR 88] and Boratto *et al.* [BAI 96].

2.8 Conclusion

This chapter aimed at characterizing recovery, recrystallization and strain-induced precipitation in austenite after deformation, for three steels presenting Nb, Ti, and V microalloying additions. After a reheating stage at 1250 °C, the progress of all the aforementioned processes were characterized by stress relaxation after compression performed every 50 °C between 900 °C and 1100 °C. Stress relaxation has been shown to be a powerful technique for indirectly detecting recovery, recrystallization, and strain-induced precipitation. These indirect characterization tests were completed by direct observations of recrystallization and precipitation states.

The kinetics of static recrystallization and strain-induced precipitation were established for the three studied steels, allowing the construction of complete Recrystallization-Precipitation-Time-Temperature diagrams. For low levels of deformations ($\varepsilon = 0.1$), it appeared that the stored energy due to deformation was too low to induce static recrystallization: only recovery and precipitation occurred. For higher levels of deformation, recrystallization took place for $T \geq 1000\,°C$, whereas only recovery and strain-induced precipitation were detected below 1000 °C.

Both solute drag effect and precipitation interacted with recrystallization. At high temperature, solute drag drives the recrystallization kinetics. A significant delay of recrystallization kinetics was observed for the too steels containing vanadium. At lower temperatures, precipitation took place fast enough ($t < 100\,s$), therefore delaying recrystallization so that it was not observed for the performed heat treatment times. Precipitation modeling work tends to confirm that the detection of precipitation by stress relaxation is related to the number of precipitates formed rather than their volume fraction or pinning pressure.

Increasing strain rates to from 0.1 to $5\,s^{-1}$ leaded to an acceleration of recrystallization kinetics. Higher strain rates lead to higher dislocation densities in the strained material. An analytical model based on JMAK theory was developed and applied to one steel. In this model, the increase in flow stress observed during compression is used to derive the dislocation density and driving pressure

for recrystallization after compression. The model was able to successfully reproduce the effects of strain rate on recrystallization kinetics.

The experimental and modeling work generated in this chapter makes it possible to clearly establish the kinetics of recrystallization and precipitation during hot rolling. This information is crucial in order to determine the metallurgical state of austenite at the end of finishing rolling, prior to phase transformations taking place during cooling (accelerated cooling and coiling stages of the hot rolling process). In the next chapter, the microstructural evolutions during the complete hot rolling process will be studied for the 0.04Nb-0.09Ti steel by investigating its phase transformation behavior during continuous cooling experiments and during lab scale hot rolling.

Chapter 3

Design of complex phase steel by hot rolling

Contents

3.1 Introduction

Numerous automotive parts are manufactured by cold forming from steel sheets. These parts may present fairly complex shapes. The ability to take different forms during forming operations, namely the formability, can be classified into four modes [SEN 01, TAK 03], as shown in Figure 3.1: deep-drawing, stretching, stretch flanging, and bending. During forming, all the parts undergo a combination of these four deformation modes. A good stretch flangeability is particularly essential for forming chassis components such as suspension arms or control arms [PAT 17], which present expanded holes. Examples of such components are given in Figure 3.2.

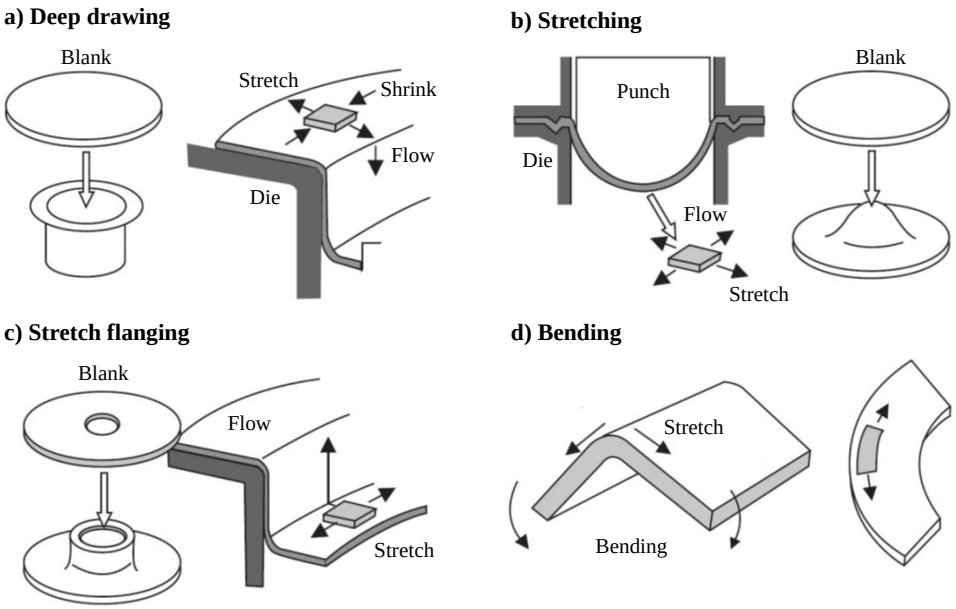

Figure 3.1: Deformation modes in press forming of sheet steels. Adapted from [TAK 03].

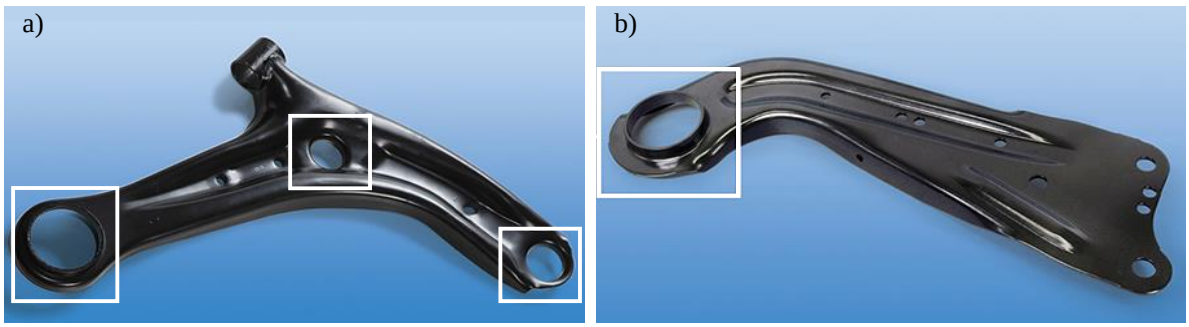

Figure 3.2: Example of parts necessitating a good stretch flangeability: (a) Transverse control arm, and (b) Trailing arm. Images are extracted from [Sal 19a].

The stretch flangeability is indicative of the formability of the edges, and is usually evaluated by the hole expansion test, during which a pierced hole of diameter D_0 is expanded with a conical

punch until a crack is observed (see Figure 3.3). Knowing the final diameter of the expanded hole, D_f, a hole expansion ratio is calculated as a key indicator of the stretch flangeability :

$$\lambda(\%) = \frac{D_f - D_0}{D_0} \times 100 \tag{3.1}$$

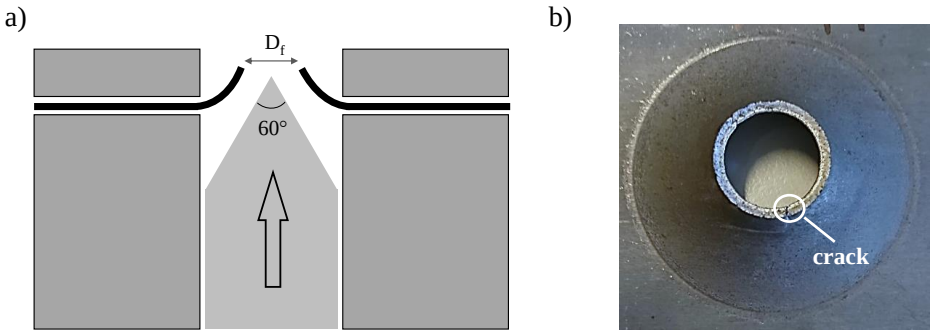

Figure 3.3: (a) Schema of hole expansion test tool and specimen, (b) Example of specimen after hole expansion test.

Before being expanded by a conical punch, the hole is machined in the steel plate, generally by punching [SEN 01]. Several studies [COM 06, KAR 09, YOO 16] have compared this reference punching method with other hole machining techniques: drilling, milling, edge surface smoothing after milling, and wire-cutting. It results from these studies that the surface quality of the hole has a major influence on the resulting hole expansion ratio (HER). Imperfections and micro-cracks introduced by the machining technique in the vicinity of the hole have a detrimental influence on the resulting HER. Therefore, machining techniques that reduce these imperfections result in higher hole expansion ratio, as illustrated in Figure 3.4 [KAR 09]. Comparison of the HER values emanating from different studies must therefore be carried out with caution regarding the experimental setup.

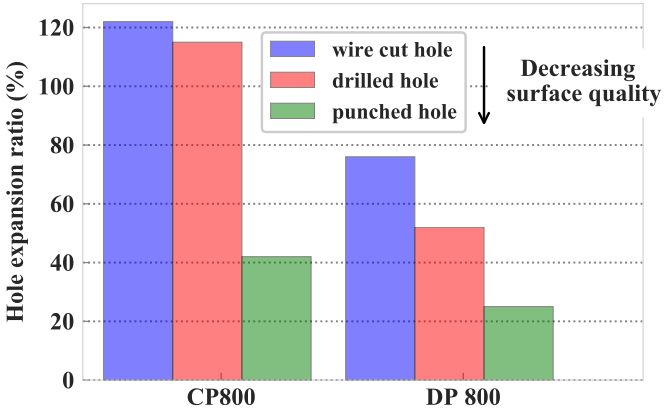

Figure 3.4: Influence of the hole edge condition on hole expansion of DP800 and CP800 steel grades. Adapted from [KAR 09].

Nowadays, car manufacturers are gradually replacing conventional steels by higher strength steels, in order to enhance the car crash performances and contribute to reduce the greenhouse gas emissions. However, the formability properties such as the stretch flangeability generally decrease with increasing strength [CHE 14, FON 15]. Thus, steels presenting high strengths but limited formability can not be used for the manufacture of complex parts. Besides, steels for the automotive sector are also constrained by the material cost, which must remain quite low. Thus, the total amount of alloying elements is generally limited to approximately 2 % [BHA 15, p. 367] and complex manufacturing processes must be avoided. Summarizing, there is a demand in automotive industry for steels presenting a good balance of strength and stretch flangeability while keeping the material cost quite low.

3.1.1 Microstructure and stretch flangeability

The steel microstructure strongly influences the stretch flangeability. Indeed, it has been shown that the stretch flangeability is sensitive to differences in hardness between the different phases present in the microstructure. Micro-cracks may form in a softer phase in the vicinity of harder phases because these are areas of concentration of stress and strain. Thus, steels with homogeneous microstructures generally present good hole expansion ratios. For reference, conventional C-Mn steels, whose ultimate tensile strengths range from 300 to 400 MPa, generally exhibit hole expansion ratios of 100-120 %, approximately [CHE 14]. Conversely, steels with inhomogeneous microstructures with large differences in hardness generally exhibit poor hole expansion ratios. For example , DP steels typically exhibit hole expansion ratios of 20 to 40 % [TSI 06, KAR 09, CHE 14].

Recently, a large effort has been made to reach a good compromise of strength and hole expansion ratio. These development strategies are mainly based on obtaining homogeneous hardness or on reducing the hardness differences between existing phases. Three main strategies can be mainly distinguished:

(i) **Fully ferritic steels reinforced by nanometer precipitates**: In recent years, researchers and industry have devoted efforts into developing fully ferritic microstructures reinforced by precipitates with nanometric sizes, obtained though interphase precipitation by additions of Nb, Ti, V, and/or Mo. These steels are sometimes referred to as *nano-steels*. These steels are specifically designed to avoid forming pearlite or large cementite particles, which are known to cause stress concentration regions. In order to reach significant strength, both fine grain sizes and considerable precipitation strengthening are required.

Most of the studies have focused on the combined additions of Ti and Mo [FUN 04, JHA 11, JHA 12, WAN 14], reporting fine ferrite grains diameters (3 to 4 µm) and precipitates of 3 to 5 nm mean radius. Outstanding combinations of properties were achieved: up to 800 MPa tensile strength, with 20 to 25 % ultimate elongation and hole expansion ratios superior to 90 %[1].

(ii) **Reducing the hardness differences between martensite and ferrite in DP steels**:

[1] Funakawa *et al.* [KAM 12] and Wang *et al.* [WAN 14] obtained HER of 120 % and 90 %, respectively, with punched holes. Higher values were reported by Jha *et al.* [JHA 11] with a drilled hole, which is known to significantly increase HER values compared to punched hole.

either by reducing the hardness of martensite, or by increasing the one of ferrite [RYD 10, FON 15]. The hardness of martensite may be reduced by tempering at higher temperatures [FAN 03, AZU 12] or reducing its carbon content. One the other hand, the hardness of ferrite can be increasing by solid solution, grain refinement [TSI 06], or precipitates [TSA 17].

However, it seems difficult to significantly increase the hole expansion properties of DP steels while maintaining tensile strengths superior to 800 MPa. One of the best compromise may have been achieved by Lee *et al.* [LEE 12], reaching 45 % hole expansion ratio with a 800-850 MPa ultimate tensile strength and a 350-400 MPa yield strength.

(iii) **Complex phase (CP) steels**

Another strategy, based on the idea of replacing martensite by bainite in DP steels, emerged in the 1980s [SUD 83]. Indeed, bainite presents a lower hardness than martensite, which reduces the hardness difference between the hard phase and the soft ferrite. Since then, numerous studies have been carried out on steels containing bainite. Efforts have been made to achieve the greatest possible proportions of bainite, with the aim of having homogeneous microstructures. A 100 % would be ideal, but it is often difficult to completely avoid the formation of secondary phase (ferrite/martensite) during manufacturing.

It has given rise to the emergence of complex phase (CP) or multi-phase steels [FON 15]. CP steels present superior stretch flangeability than dual phase steels with similar levels of tensile strength [KAR 09], as it can be observed in Figure 3.4, which compares the HER of CP800 and DP800 steels (both presenting approximately 800 MPa ultimate tensile strength). CP800 class steels typically reach a 40 % hole expansion ratio, and are already used for forming automotive parts where good stretch formability is needed [Sal 19a, Sal 19b]. Therefore, there is still a certain room for improvement of the stretch flangeability of complex phase steels.

Nano-steels are definitely a successful way to achieve a good combination of strength and stretch flangeability. However, it seems that the maximum strength achievable using an industrial process is ceiling around 800 MPa. To achieve higher resistance levels, it appears judicious to try to obtain phases with higher dislocations densities than ferrite, such as bainite or martensite. However, it seems complicated to increase the formability of DP steels while maintaining a resistance greater than 800 MPa. In addition, one of the advantages of CP steels over nano-steels and DP steels is that they globally present higher YS/UTS ratios. Thus, this PhD-work and the NANOFORM research project focus on CP steels.

3.1.2 Objectives of the chapter

The NANOFORM project aims at designing CP steels by hot rolling with a maximum fraction of bainite and with target properties of 70 % hole expansion ratio and 800 MPa ultimate strength. In order to maximize the proportion of bainite in CP steels, one can optimize the manufacturing process and/or the steel composition. In this chapter, only one steel composition was selected, but different hot rolling strategies were tested. The steel studied in this chapter is a 0.04Nb-0.09Ti microalloyed steel, of which austenite grain growth and recrystallization after deformation behavior was presented in the previous chapters. Since an industrial application is targeted, some limitations have to be respected regarding the choice of the hot rolling parameters. In particular, the coiling

temperature must be between 500 and 650 °C.

The phase transformation behavior during continuous cooling was determined, including the effect of austenite deformation. The samples used for dilatometer experiments were extracted from a first small casting ingot of 140 × 150 × 50 mm^3, as mentioned in Chapters 1 and 2.

Finally, several types of hot-rolling schedules were applied at semi-industrial scale, aiming at reproducing achievable industrial conditions. Larger quantities of material were needed for hot rolling schedules. Thus, a second 100 kg ingot of approximate dimensions 120 × 140 × 600 mm^3 was produced (Table 3.1 H-R). The 100 kg ingot was sectioned into coupons of 60 × 70 × 150 mm^3 intended to be hot-rolled. The hot rolled plates underwent mechanical and microstructural characterization, highlighting the relations between elaboration process, microstructures, and mechanical properties.

Note that slightly different compositions were obtained for these two ingots (Table 3.1), due to the use of two different vacuum induction melting furnaces. However, the observed variations in composition remained limited enough to allow comparison between laboratory tests and semi-industrial hot rolling tests.

Element	**C**	**Mn**	**Si**	**Ti**	**Nb**	**V**	**Mo**	**Al**	**Cr**	**N**
CCT	0.062	1.91	0.50	0.085	0.039	0.002	0.212	0.065	0.013	0.006
H-R	0.062	1.90	0.50	0.097	0.041	<0.001	0.208	0.053	0.093	0.0039

Table 3.1: ICP-MS composition of the microalloyed steel studied (wt.%) produced for continuous cooling experiments (CCT) and pilot plant hot-rolling (H-R) schedules.

3.2 Background

Before presenting the results obtained, a brief background part, mainly focusing on the phase transformations in steels, is given. Indeed, it appears to be essential knowledge for the understanding of this work. Quantitative techniques based on ESBD for the characterization of ferrite and/or bainite microstructures are also detailed. Finally, the influence of austenite deformation on phase transformation into ferrite and bainite is reviewed. These phases are the most likely to form regarding the hot-rolling parameters selected.

3.2.1 Phase transformation in steels

For the sake of brevity, the iron-carbon equilibrium phase diagram is not recalled here. Every austenite to ferrite solid-state transformation occurs with two steps of nucleation and growth, the parent phase (austenite) and the product phase (ferrite) being separated by an interface. Phase transformations are generally split into two categories: **reconstructive** and **displacive** ones [BHA 87, POR 92]. Although the purpose of this section is not to perform a detailed review of the numerous phase transformations in steels, it seems necessary to briefly review their main features, mainly focusing on the bainitic transformation.

3.2.1.1 Reconstructive phase transformations

Slow cooling from austenite generally promotes reconstructive phase transformation mechanisms, governed by the diffusion of elements. Austenite decomposition through reconstructive mechanisms involves the formation of ferrite and pearlite.

Ferrite can be classified in two main forms [BHA 85], that are dominating micro-constituents of a vast majority of steels:

- **Allotriomorphic ferrite**, that nucleates at austenite grain boundaries. The term allotriomorphic implies that the shape of this phase do not reflect its internal symmetry: the limiting surfaces of the crystal are not regular.
- **Idiomorphic ferrite**, formed inside austenite grains, mainly on non-metallic inclusions. The term idiomorphic means that the crystal present faces belonging to its crystalline form.

When the steel contains microalloyed additions, ferrite formation may be accompanied by a precipitation phenomenon, either after or during γ/α transformation. This later case is referred to as **interphase precipitation** [DAV 68], during which a very fine dispersion of nanometer size precipitate forms at a moving γ/α boundary, giving rise to considerable precipitation strengthening.

Pearlite, another major constituent of the microstructures of steel, forms through the eutectoid decomposition reaction of austenite, in which both ferrite and cementite grow at a common front with the austenite. A repeated nucleation mechanism from an initial nucleus leads to the formation of a well-known ferrite/cementite lamellar structure [ZHA 09].

3.2.1.2 Displacive phase transformations

Displacive transformations include **Widmanstätten ferrite**, **acicular ferrite** and **martensite**. The controversial case of **bainite** will be discussed separately. In the following, only martensite will be reviewed.

Martensite represents somehow an extreme case, which forms when high cooling rates are applied. Martensite forms by a deformation of the austenite lattice, without any diffusion of atoms. The deformation leads to a change in the transformed material, with large shear and a volume expansion. This diffusion-less mechanism is referred to as displacive [BHA 06b]. The martensite reaction occurs athermally, and only depends on the undercooling below a martensite-start temperature, M_S. In order to minimize the strain energy due to the deformation, martensite forms as highly dislocated plates or laths.

Because of the diffusion-less nature of the transformation mechanism, martensite forms with the same composition as the parent austenite phase. It is thus is supersaturated in carbon. In order to accommodate the carbon content, the crystal structure changes from body-centered cubic (BCC) to body-centered tetragonal (BCT). The tetragonality of the crystal, c/a, increases with carbon content.

Martensite is a very hard phase, but also brittle and unusable in its virgin condition. Its hardness is highly related to its carbon content. For this reason, it is necessary to modify its properties by heat treatments ranging from 150 to 700 °C called tempering [BHA 06c]. Tempering tends to lead the metastable martensitic microstructure towards the equilibrium phases (ferrite and cementite).

There exist different stages of tempering depending on the applied temperature, during which the carbon content of martensite diminishes, mainly by formation of metastable carbides or cementite. As a consequence, martensite loses its brittleness at the cost of a reduction of hardness/strength.

3.2.1.3 The controversial case of bainite

Bainite is a non-equilibrium transformation product of austenite, which forms upon cooling at intermediate rates from austenitic state, too fast for reconstructive transformations but slow enough to avoid the formation of martensite.

Bainite is probably the most complex phase present in steels, and its transformation mechanism has been extensively discussed and controverted since its first observation by Robertson [ROB 29], and Davenport and Bain [DAV 30] in 1929-1930. Citing Mats Hillert in 2002 [HIL 02]: "*The transformation of austenite to bainite is probably the phenomenon that has caused most controversy in the field of physical metallurgy. The mechanism of bainite formation has been the subject of numerous original research papers and reviews for almost a century but without any signs of controversies being resolved.*"

Before outlining some points of the controversies, it is first necessary to deal with the general, well-established characteristics of bainite [BHA 15]:

(i) **The existence of a bainite start temperature**: The formation of bainite is impossible above a specific B_S temperature, in a quite similar way to martensite start temperature. B_S is highly depending on the steel composition.

(ii) **The incomplete reaction phenomenon**: When the temperature of transformation is reduced below B_S, increasing amounts of bainite form. Nevertheless, during isothermal transformation there is a limit beyond which austenite will no longer transform into bainite, which can lead to significant amounts of untransformed austenite. The reaction is therefore considered as incomplete because it stops prematurely, and the phenomenon is referred to as transformation stasis or incomplete reaction phenomenon [CAB 09].

(iii) **The classification into upper and lower bainite**: Bainite is commonly present in two main distinguished forms: upper bainite and lower bainite. These terms refer to the temperature domain in which both types of bainite form. Upper bainite forms at relatively high temperatures, whereas lower bainite forms in a lower temperature range. Both upper and lower bainite consist of aggregates of platelets of ferrite separated in some regions by residual phases such as untransformed austenite or martensite formed subsequently to the growth of bainitic ferrite. Bainite has a characteristic morphology, consisting of platelets of ferrite called subunits, assembled into aggregates called sheaves. The principal distinction between the two microstructures relies on the localization of the carbide precipitates. In upper bainite, cementite precipitates separate the ferrite subunits, whereas in lower bainite, there is also a fine dispersion of cementite precipitate within the subunits.

Figure illustrates the differences in morphology between upper and lower bainite for a Fe-0.5C-0.7Mn steel [DUR 13]. In upper bainite (Figure a)) cementite, appearing white, is found between bainitic ferrite laths. Conversely, precipitates are found within bainite laths in lower bainite (Figure b)). Note that for steels with lower carbon contents, the amount of cementite decreases, which

changes the appearance of the microstructures.

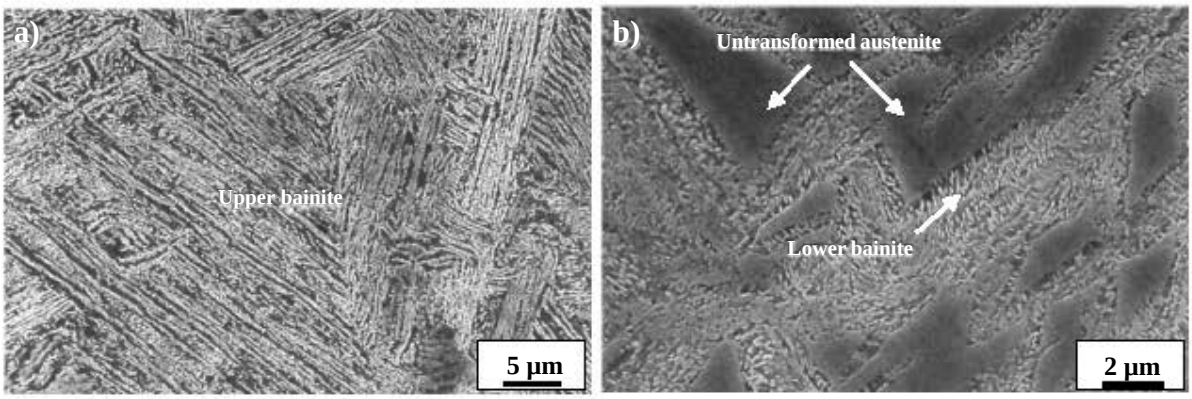

Figure 3.5: SEM micrographs of typical (a) upper bainite microstructure obtained by isothermal treatment at 500 °C and (b) lower bainite obtained by isothermal holding 325 °C with a Fe-0.5C-0.7Mn steel. Images extracted from [DUR 13].

The mechanism of bainite formation has been the subject of many discussions and controversies [HEH 72, HIL 95, FIE 13]. This is due to the fact that it shows intermediate characteristics between fully displacive and reconstructive formation mechanism. For example, bainite is morphologically close to martensite, since it forms laths or plates. However, it presents much slower growth rates than martensite. Thus, for a long time, both a reconstructive theory and a displacive theory co-existed to explain the mechanism of bainite transformation. The first one described the growth of bainite by a diffusion-controlled ledge propagation mechanism. The second one invoked a displacive, diffusion-less transformation, where bainite grows by successive nucleation and growth of displacive subunits.

Nowadays, it seems that a certain consensus has been reached, validating a displacive transformation mechanism with regard to the elements of the substitutional network. Bainite formation gives rise to surface relief, which can only be explained by a displacive mechanism. However, there is still controversy regarding the mechanism that controls the growth kinetics of bainite and the role of carbon. The controversy is now mainly on the question of whether bainitic ferrite initially forms with a supersaturation of carbon or not. There are now two hypotheses:

(i) The first one is mainly defended by Bhadeshia and co-workers [BHA 90, BHA 15]. It states that bainite forms by successive nucleation and growth of displacive sub-units. New subunits preferentially forms near the tips of existing ones, resulting in a sheaf-like structure (Figure 3.6 a)). The growth rate of bainite sheaf is not limited by any diffusion process, but by the rate of nucleation of these subunits. Plastic relaxation in the austenite adjacent to the growth front of the bainite sheaf may itself play an important role on the nucleation rate of displacive subunits. Subunits initially form with carbon supersaturation, inheriting the carbon content of austenite (Figure 3.6 b)). The excess of carbon is afterwards partitioned into the residual austenite or precipitates as carbides. The formation of carbides is thus a secondary process, similar to the one observed during the tempering of martensite. Depending on the temperature, precipitates may form either only between and/or within subunits, leading to

upper or lower bainite.

(ii) The second one [QUI 02, HIL 10, BOR 12] states that bainite grows under simultaneous diffusion of carbon into the interior of the parent austenite. Bainite does not grow with initial carbon supersaturation. Defenders of this theory argue that the transformation mechanism of bainite is of the same nature than the one of Widmanstätten ferrite, of which growth is known to by controlled by carbon diffusion despite presenting a displacive mechanism regarding substitutional elements.

In order to recognize one of the two theories, it would be necessary to prove the carbon supersaturation of bainite when it forms, and thus measure the carbon content of bainite when it forms. However, due to its high diffusion rate at the considered temperatures, carbon diffuses rapidly to austenite. Thus, it is almost impossible to measure the initial carbon content of bainitic ferrite when it forms. A recent attempt [CAB 10] measured high amounts of carbon in solid solution in bainitic ferrite at the early stages of transformation, above that predicted from para-equilibrium with austenite, but below that of the parent austenite. Thus, the mechanism of bainite transformation can be expected to be debated in the coming years.

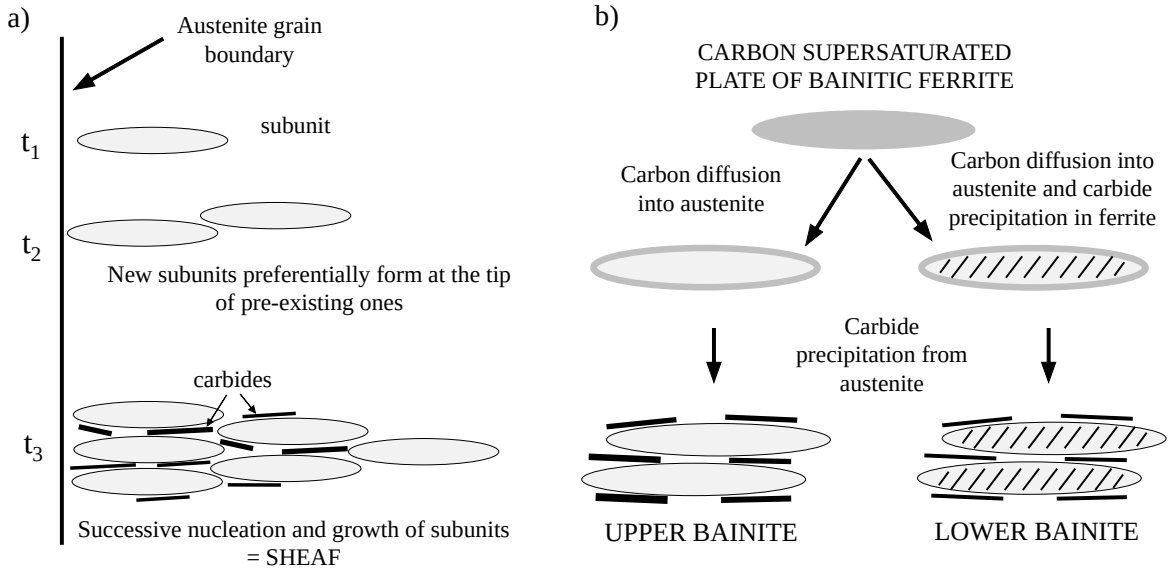

Figure 3.6: Mechanism of bainite transformation according to Bhadeshia [BHA 15]. (a) Schematic representation of formation of a bainite sheaf by repeated nucleation and growth of displacive subunits. (b) Each subunit initially forms with carbon supersaturation, and carbide precipitation occurs as a secondary process.

Acicular ferrite was not discussed previously, because it forms with the same mechanism than bainite [BHA 15]. Their microstructures differ because bainite sheaves grow as a series of parallel platelets from austenite grain boundaries, whereas acicular ferrite nucleates inter-granularly on non-metallic inclusions, leading to the growth of acicular ferrite plates in different directions [BHA 06a]. This term is particularly used in welding steels. However, it is sometimes employed to simply designate the shape of ferrite, without implying any particular mechanism of formation [BOR 12].

Another bainite morphology, designated by *granular bainite* is frequently observed in low carbon steels, particularly after continuous cooling. It is composed of irregular ferrite with martensite/austenite (MA) islands located between the irregular ferrite grains. Despite the granular shape under optical or scanning electron microscope, granular bainite do not really differ from the other types of bainite, and is constituted of bainite ferrite separated by very thin regions of austenite [JOS 88]. Figure 3.7 shows the microstructure of the 0.04Nb-0.09Ti steel after austenitizing (10 min at 1250 °C) and continuous cooling at $1\,°C\,s^{-1}$. The microstructure is almost exclusively composed of granular bainite, but upper bainite is observed in some areas, which allows to illustrate the differences in morphology between granular bainite and upper lath-like bainite in low carbon steels.

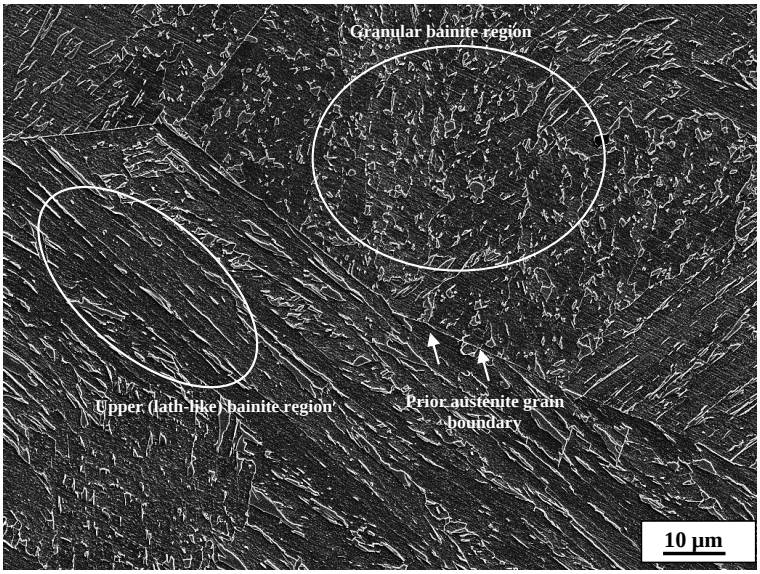

Figure 3.7: SEM micrograph of the 0.04Nb-0.09Ti low carbon steel studied in this chapter, continuously cooled down at $1\,°C\,s^{-1}$ after austenitizing 10 min at 1250 °C. Granular and upper bainite regions are observed.

3.2.2 Methodologies for phase characterization

The micrographs shown until now (Figure 3.5 and 3.7) exhibit quite easily identifiable bainite microstructures, since obtained after fairly simple heat treatments (isothermal treatment or continuous cooling), from a non-deformed austenite. When the phase transformations take place from deformed austenite and/or during more complex thermomechanical treatments, the identification of the phases can be much more difficult. After a classical nital etching and at low magnification, if the precipitates are not visible, the distinction between ferrite and bainite may not be obvious. Color metallography techniques [BAN , ZAK 09] may be a suitable option for the characterization of multi-phase steels, but they require knowledge and practice that is not necessarily present in all laboratories. Moreover, if a microstructure gradient is present, it is difficult to discriminate the different phases by observation of the morphologies, and color etching techniques can be unsuccessful.

ESBD does not allow distinguishing between ferrite, bainitic ferrite, and martensite without fur-

ther analysis because all these phases are indexed by the same body centered cubic crystallographic structure. This is why quantitative methods based on the misorientation angles determined by EBSD are used. In the following part, two of these methods are therefore detailed.

3.2.2.1 Misorientation angle distributions

Quite recently, Zajac *et al.* [ZAJ 05a, ZAJ 05b] presented a terminology in which bainite is classified into three main groups according to the morphology of ferritic phases and the distribution of second phases: granular bainite, upper bainite, and lower bainite. Zajac *et al.* also showed that these three types of bainitic microstructures found in low carbon steels present different distributions of boundary misorientation angles characterized by EBSD (see Figure 3.8). These misorientation angle distributions allow to distinguish between the different forms of bainite. Lower bainite present a high proportion of boundaries in the 50°-60° range and few boundaries below 20°. Conversely, upper bainite has a high proportion of low misorientation boundaries ($< 20°$) and fewer high angle boundaries ($> 50°$). In granular bainite, the distribution of grain boundaries is broader and more random with a broad peak around 45° or a double peak between 50° and 60°.

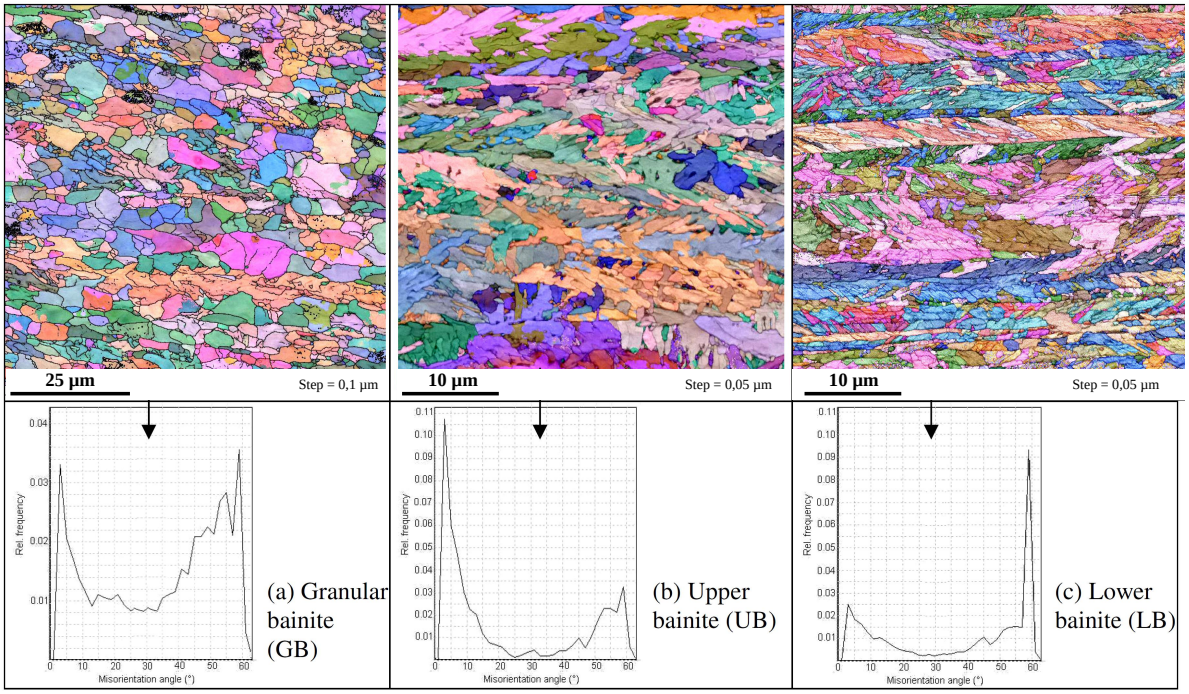

Figure 3.8: EBSD-orientation maps and distribution of the misorientation angles of ferritic grains in (a) granular bainite, (b) upper bainite, and (c) lower lath-bainite. From [ZAJ 05b].

This method was applied to the 0.04Nb-0.09Ti steel studied in this work. The microstructures resulting from CCT experiments with cooling rates of 0.05, 1, and 5 $°C\,s^{-1}$ were selected as references for EBSD characterization for ferrite/granular bainite, fully granular bainite, and fully lath bainite microstructures. The samples were cut and polished down to 1 μm. An additional polishing step was performed on a cloth soaked with a Struers OP-S colloidal suspension solution. Electron back-scatter

diffraction (EBSD) was carried out a ZEISS Supra 55VP Scanning Electron Microscope operating at 20 kV, equipped with an Oxford Symmetry EBSD camera. The post-processing analysis was performed on AZtec HKL Channel 5 software. Figure 3.9 shows the corresponding EBSD maps and misorientation orientation distributions obtained from these reference microstructures.

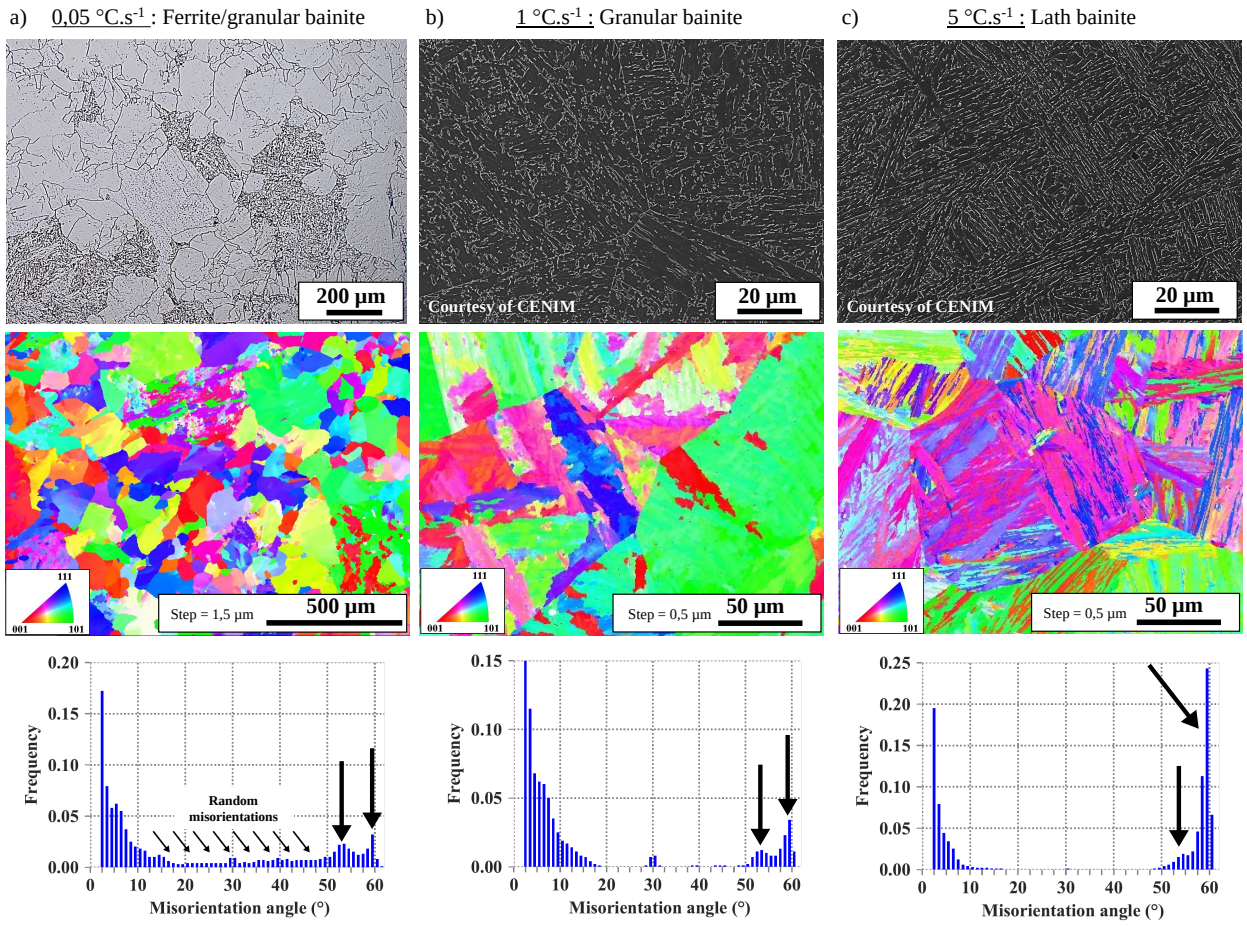

Figure 3.9: SEM/optical images of the microstructure, and corresponding EBSD (IPFZ) maps and distribution of misorientation angle on reference microstructures obtained after continuous cooling from undeformed austenite at (a) $0.05\,^{\circ}\mathrm{C\,s^{-1}}$ (ferrite + granular bainite), (b) $1\,^{\circ}\mathrm{C\,s^{-1}}$ (granular bainite), and (c) $5\,^{\circ}\mathrm{C\,s^{-1}}$ (lath bainite).

For a microstructure almost fully composed of granular bainite (Figure 3.9 b)), two clear peaks around 53° and 60° (pointed with black arrows) are identified on the misorientation angle distribution. A peak around 30° is also observed, but is actually an artifact arising from systematic mis-indexing of pseudo-symmetry patterns, as pointed out by [RYD 06, KAR 15]. These two peaks characterizing granular bainite are retrieved in the misorientation angle distribution of the mixed ferrite/granular bainite microstructure (Figure 3.9 a)). Random misorientation angles, which are probably due to the random orientations between ferritic grains, are also found between 15 and 45°.

For a lath bainite microstructure (Figure 3.9 c)), the misorientation angle distribution shows a different profile, with a large height difference between the peak around 60° and the one around

53°. The presence of a high peak around 60° thus seems to characterize lath microstructures.

3.2.2.2 Kernel average misorientation (KAM) maps

Granular bainite and ferrite can be morphologically close when observed in OM or SEM. In a recent study, Chen *et al.* [CHE 18] detailed a method based on EBSD that allows to distinguish granular bainite from ferrite grains by constructing Kernel average misorientation (KAM) maps. A KAM map is a method that indicates the differences in crystallographic orientation between neighboring points in an EBSD map. This method calculates the mean misorientation between a pixel and a number of neighboring pixels following a squared grid (filter), and then assigns this average misorientation to that pixel (see Figure 3.10 a)). The calculated KAM depends on the filter size, given by the pixel size and the number of neighboring pixels considered in the filter. Increasing the filter size leads to a smoother misorientation maps.

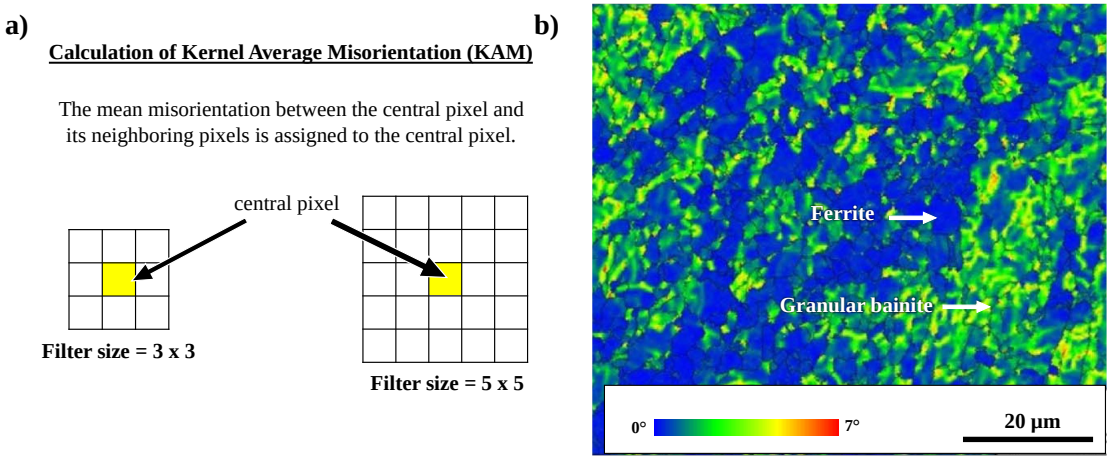

Figure 3.10: (a) Calculation of Kernel average misorientation. (b) Example of KAM map allowing to differentiate ferrite from granular bainite, from Chen *et al.* [CHE 18].

The method allows differentiating ferrite from granular bainite due to their different transformation mechanism. Within a ferrite grain, which forms by a reconstructive mechanism, no strong variation of misorientation angle is found, except if the grain is heavily deformed. Only slight variation of misorientation angle may appear if bainite forms in the adjacent region and introduce strain in the ferrite grains. On the opposite, a significant misorientation gradient is found within granular bainite, because it actually contains several subunits that form following a displacive mechanism. Thus, it is possible to distinguish ferrite from granular bainite on a KAM map, where ferrite grains present lower KAM values, as observed on Figure 3.10 b).

3.2.3 Influence of austenite conditioning on phase transformation

Most steelmaking processes start by a reheating treatment to the austenitic state, followed by deformation of austenite grains. The final microstructures and mechanical properties depend on the austenitic state (grain size, deformed or undeformed) before it begins to transform and on the thermal treatments (cooling rate, holdings) applied. The deformation of austenite enables to refine

and control the final microstructures to achieve enhanced strength, and is therefore of primary importance. In this section the effect of plastic deformation of austenite on the formation of ferrite and bainite is discussed.

3.2.3.1 Deformation in recrystallization region

When the deformation is applied in the region where austenite can recrystallize, recrystallization leads to a refinement of austenite grain sizes. A higher number density of nucleation sites for ferrite is thus obtained, leading to finer final ferrite grains. The effect of austenitic grain size on bainitic transformation is not completely understood because contradictory results have been obtained [LEE 08b]. It seems, however, that in most cases, a decrease of austenite grain sizes leads to increasing rates of bainite transformation.

3.2.3.2 Deformation in non-recrystallization region

Numerous studies have investigated the effect of austenite deformation in non-recrystallization region (at lower temperature) on phase transformations during continuous cooling experiments in low carbon steels [SMI 71, MAN 96b, ZHA 03, JUN 06]. It follows from these studies that the deformation of austenite grains tends to promote reconstructive transformation mechanisms (ferrite, pearlite) to the detriment of phases presenting displacive transformation mechanisms (bainite and/or acicular ferrite). This means that higher cooling rates must be applied to avoid the formation of ferrite and pearlite when austenite is deformed, compared with undeformed austenite. Figure 3.11 provides an example of continuous cooling transformation (CCT) diagrams starting from deformed and undeformed austenite in low carbon steels, illustrating the effect of the deformation of austenite.

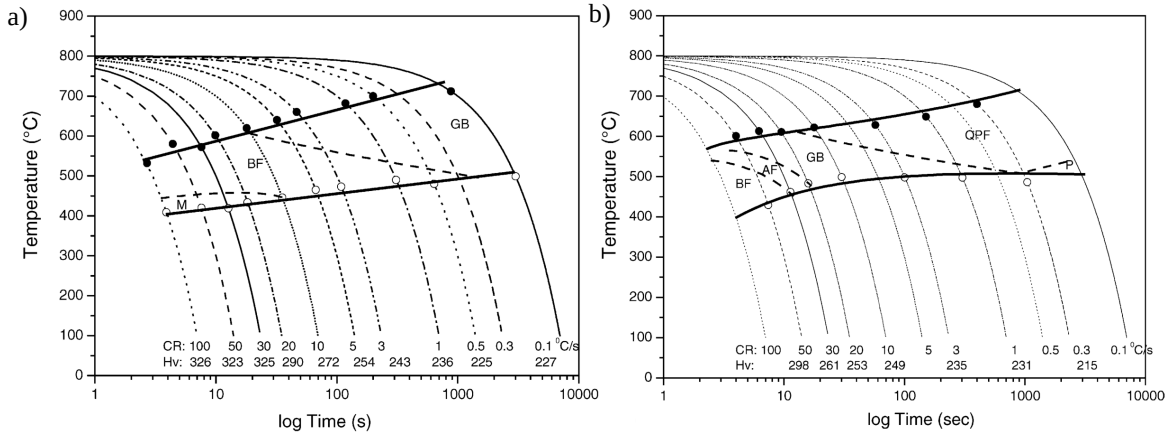

Figure 3.11: (a) Non-deformed and (b) deformed CCT diagrams of a low carbon HSLA steel. P: pearlite, QPF: quasi-polygonal ferrite, AF: acicular ferrite, GB: granular bainite, BF: bainitic ferrite, M:martensite. From [JUN 06].

If austenite deformation occurs in the non-recrystallization region, several factors can influence the formation of ferrite, listed by Singh [SIN 98]:

- Change in the grain shape: deformation induces pancaking of austenite grains, and increases the grain boundary area per unit volume, S_V. It thus results in an increase of potential nucleation sites for ferrite.

- Enhanced nucleation on deformed austenite grain boundaries: deformation not only increases S_V, but also increases the nucleation potency of the grain boundaries.

- Inter-granular nucleation sites: apart from grain boundaries, deformation creates new nucleation sites such as deformation bands or sub-grain boundaries, which increases the total number of nucleation sites for ferrite.

- Stored energy of deformed austenite: deformation puts austenite into a higher state of energy, which increases the free energy change associated with the γ/α transformation.

The combination of these factors results in accelerated ferrite transformation kinetics, and in finer ferrite grain sizes when austenite is deformed.

The effect of austenite plastic deformation on the bainitic transformation is significantly different. Indeed, bainite forms with a displacive mechanism, *i.e.* by a coordinated movement of atoms during the glide of glissile interfaces. Such movements are hindered by the presence of obstacles. This is why bainite do not cross grain boundaries, for example.

Austenite deformation has contradictory effects on bainite formation [SIN 98, BOH 19]. On the one hand, introduced dislocations favors nucleation by increasing the initial number density of potential nucleation sites or by enhancing the driving force for nucleation. On the other hand, dislocations induce a resistance against the shape deformation associated with the growth of bainite laths. This process, well-established for martensite, is referred to as **mechanical stabilization**, and is also observed for the bainite reaction [SIN 96]. Although deformation increases the nucleation rate, the overall extent of bainite transformation can be reduced because each nucleus transforms to a smaller amount of bainite [SIN 96]. Due to the contradictory effects on nucleation and growth, some investigators reported an increase in the bainite transformation temperature during continuous cooling after austenite deformation, while others reported a decrease. In the same way, some authors reported accelerated isothermal kinetics after austenite deformation while others found slower kinetics [SIN 98].

The deformation of austenite also influences the bainitic microstructures. Yamamoto *et al.* [YAM 95] reported that austenite deformation leads to increasing lath width compared to bainite formed from equiaxed austenite grains. They also reported that martensite/austenite (MA) constituents are mainly located between laths when bainite forms from undeformed austenite, whereas the shape of MA becomes blocky when austenite is deformed. Fujiwara *et al.* [FUJ 95] also reported that the lath length can significantly decrease when austenite is consequently deformed ($> 30\,\%$ deformation).

3.3 Continuous cooling phase transformation

3.3.1 Methods

Continuous cooling experiments were performed[2] using a Bähr 805 DIL dilatometer on samples of 10 mm length and 5 mm diameter. The specimens were heated from room temperature to 1250 °C at a rate of 5 °C s^{-1}, held for 10 min and cooled to ambient temperature at rates of 0.05, 1, 5, 10 and 25 °C s^{-1} (Figure 3.12 a)). Additionally a second thermal cycle was applied in order to study the effect of deformation on phase transformation. After reheating, the samples were cooled down to 950 °C, held for 30 s, deformed to $\varepsilon = 0.3$ at a rate of 10 s^{-1}, and subsequently cooled down to room temperature at rates of 0.05, 1, 5, 10 and 25 °C s^{-1} (Figure 3.12 b)). According to the study of recrystallization presented in Chapter 2, this deformation pass is performed in the non-recrystallization domain and thus results in austenite pancaking.

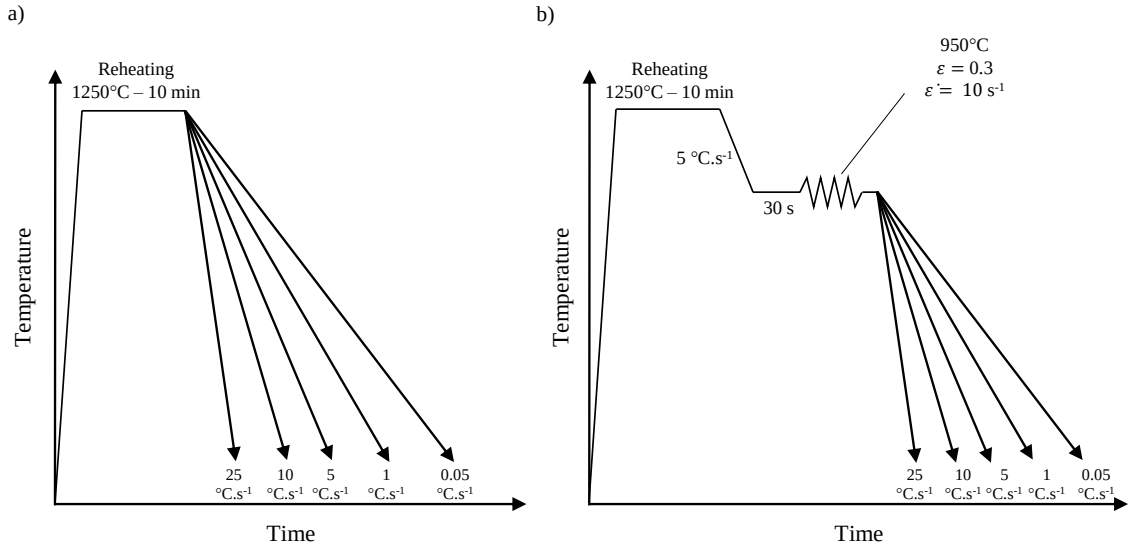

Figure 3.12: Thermal cycles applied for (a) Continuous Cooling Transformation (CCT) and (b) Deformed Continuous Cooling Transformation (DCCT) experiments.

During the thermal cycles, the transformation temperatures were determined from the dilatation curves. The determination of the critical A_{C1} and A_{C3} temperatures upon heating at 5 °C s^{-1}, as well as the transformation start and finish temperatures upon cooling were determined from the dilatometry curves, following the analysis showed in Figure 3.13. The points at which the dilatometry curves deviated from linear trend curves where used to detect phase transformation. The corresponding CCT diagrams were built. For convenience when comparing CCT and DCCT diagrams, both are plotted starting from 950 °C.

After heat treatment, samples were cut in halves and the resulting microstructures were characterized by optical and scanning electron microscopy. Vickers hardness measurements were also performed using a 10 kg load.

[2]CCT experiments were performed in CENIM.

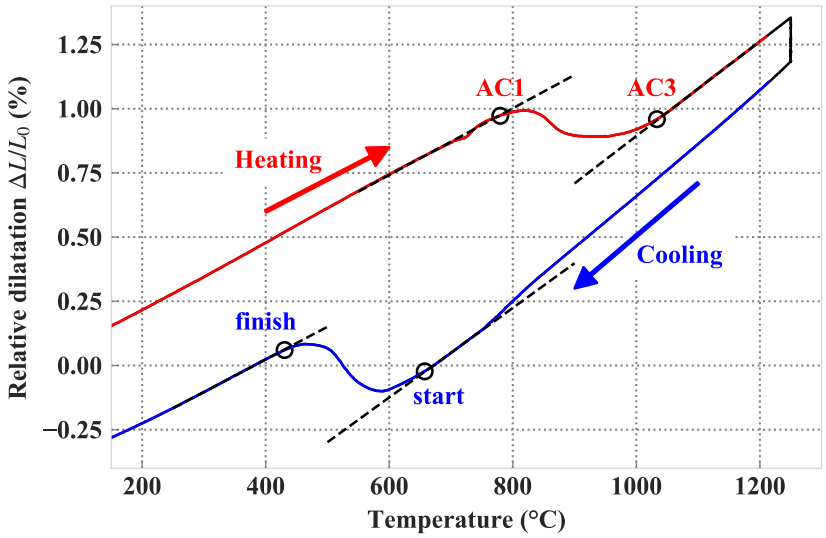

Figure 3.13: Exploitation procedure of dilatometry curves. The figure shows a CCT experiments with a $5\,°C\,s^{-1}$ cooling rate as an example.

3.3.2 Microstructures and CCT diagram

Figure 3.14 shows the microstructures obtained after continuous cooling from both undeformed and deformed austenite. The cooling rate range for which bainitic microstructures are obtained is wide. The formation of ferrite is only observed at the slowest cooling rate ($0.05\,°C\,s^{-1}$). Even at this cooling rate, granular bainite is found together with ferrite. At $1\,°C\,s^{-1}$, fully bainitic microstructures are observed. When increasing cooling rates are applied, the morphology of bainite changes gradually from a large fraction of granular bainite to fully lath-like bainite/martensitic microstructures.

Table 3.2 recapitulates the critical temperatures determined from dilatometry signal. Based on the dilatometry curves and microstructure, the continuous cooling transformation diagrams were constructed (Figure 3.15). At the highest cooling rates ($10\,°C\,s^{-1}$ and $25\,°C\,s^{-1}$), high hardnesses are obtained but M_S is not detected by dilatometry, except for DCCT at $25\,°C\,s^{-1}$, where a slope change around 453 °C might correspond to M_S. It is close to the theoretical martensite start temperature of 456 °C calculated with the MAP_STEEL_MUCG83 program [PEE 06]. Optical micrographs do not allow to easily distinguish bainite from martensite at these cooling rates, but rather high levels of hardness are obtained, indicating that martensite is probably obtained. It is likely that M_S is not detected in most cases due to the overlapping with the bainite transformation.

Note that in Figure 3.14, the terms *upper* and *lower* bainite were not employed because it is difficult to distinguish these two microstructures in SEM for such a low carbon content. *Lath bainite* was thus used as a general term to describe the global morphology. However, since it mostly forms above 400 °C according to dilatometry curves, lath bainite is most likely almost exclusively composed of upper bainite.

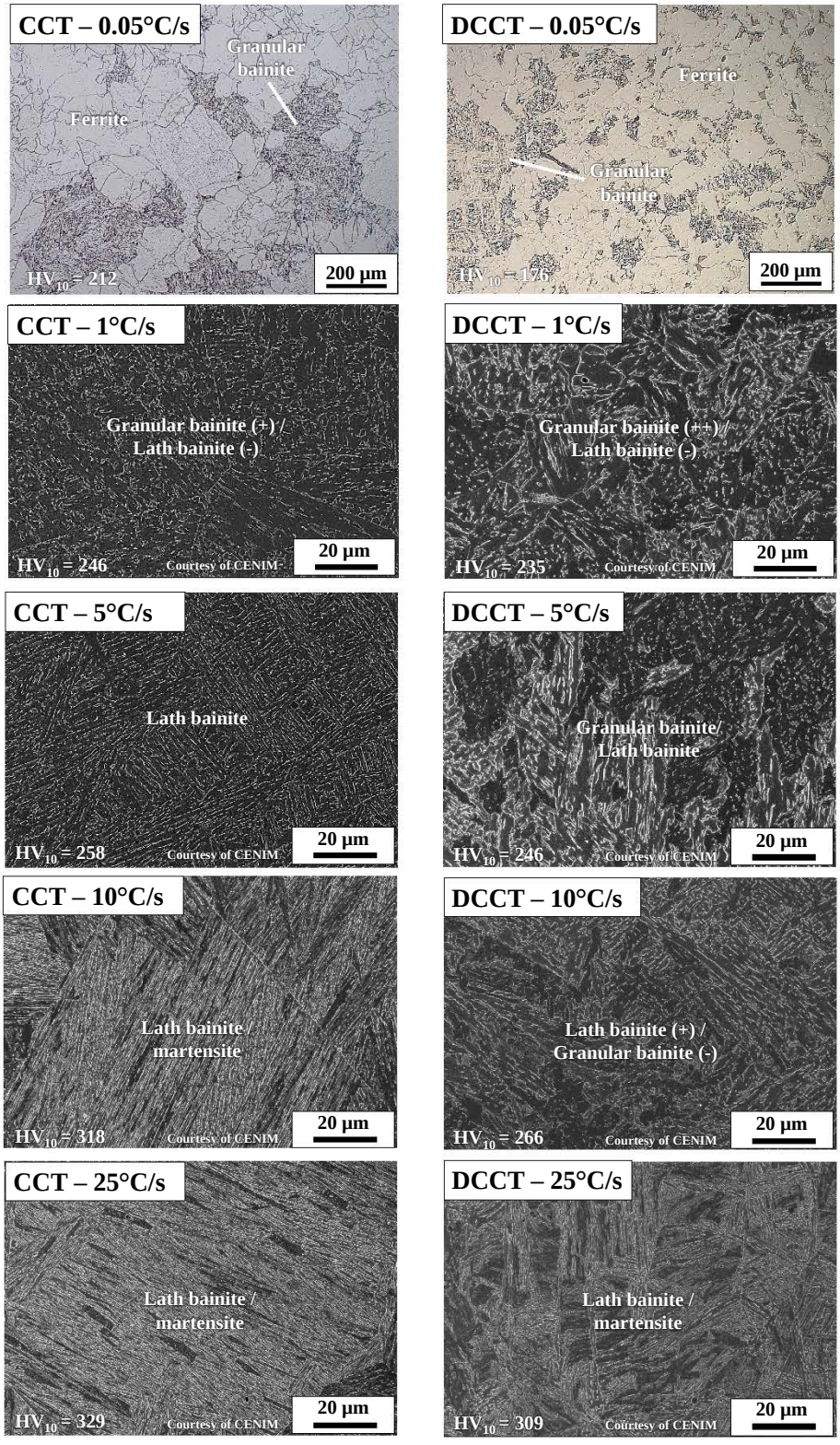

Figure 3.14: Optical/SEM images showing the microstructures resulting from CCT and DCCT experiments.

		Heating ($5\,°C\,s^{-1}$)	
		AC1 (°C)	780
		AC3 (°C)	1032
		Cooling	
		Undeformed austenite	**Deformed austenite**
$0.05\,°C\,s^{-1}$	F_S (°C)	866	837
	B_S (°C)	710	734
$1\,°C\,s^{-1}$	B_S (°C)	712	604
$5\,°C\,s^{-1}$	B_S (°C)	645	618
$10\,°C\,s^{-1}$	B_S (°C)	630	584
$25\,°C\,s^{-1}$	B_S (°C)	611	578
	M_S (°C)	Undetected	453

Table 3.2: A_{C1}, A_{C3} and F_S/B_S temperatures determined by dilatometry starting from undeformed or deformed austenite.

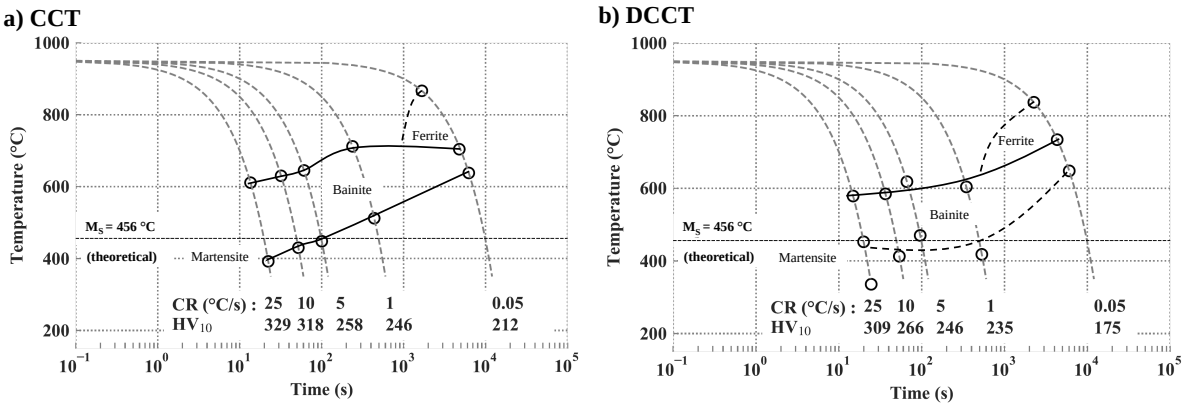

Figure 3.15: (a) Continuous cooling transformation diagram with underformed austenite and (b) after deformation at 950 °C with $\varepsilon = 0.3$ and $\dot{\varepsilon}$ =$10\,s^{-1}$.

3.3.3 Effect of austenite deformation

At a cooling rate of $0.05\,°C\,s^{-1}$, austenite deformation at 950 °C leads to significantly refined ferrite grains, as expected. The area fraction of granular bainite formed at $0.05\,°C\,s^{-1}$ is however not affected by the deformation of austenite: around 30 % of granular bainite is formed both from undeformed or deformed austenite. Despite this apparent refinement of ferrite grains, a lower hardness was obtained when austenite was deformed, which can only be explained by different precipitation hardening levels. When austenite is undeformed, it is likely that no precipitation occurs in austenite before ferrite formation. Thus, a consequent precipitation strengthening can be obtained by interphase precipitation, as reported in several studies on steels containing combined additions of Ti, Nb, and/or Mo [KAM 12, FUN 04, JHA 11, JHA 12, WAN 14]. On the opposite, due to the low cooling rate applied after austenite deformation, there is plenty of time for precipitates to form in austenite, coherently with the strain-induced precipitation kinetics determined in Chapter

2. Precipitates formed in austenite being coarser than the ones formed by interphase precipitation, the precipitation strengthening decreases for samples submitted to austenite deformation.

For increasing cooling rates ($\geq 1\,°C\,s^{-1}$), austenite deformation lowers B_S. It also tends to increase the domain of granular bainite: granular bainite is observed at $5\,°C\,s^{-1}$ when austenite is deformed whereas it is not when austenite is undeformed, which is coherent with [JUN 06]. Another effect is the decreasing hardness of the lath-like microstructures, which is related to an apparent coarsening of the lath microstructures. Shorter and wider laths are obtained from pancaked austenite, as reported by [YAM 95, FUJ 95].

3.4 Hot rolled plates

3.4.1 Hot rolling schedules

The individual coupons cutted out from the ingot were hot-rolled in SZMF [3] hot rolling pilot plant. The purpose of these hot rolling tests was to test different strategies applicable on an industrial hot rolling plant, and which one of them led to promising mechanical properties. The metallurgical state of the austenite determines the final microstructures and mechanical properties. It is therefore worth recalling the Recrystallization-Precipitation-Time-Temperature diagram[4] of 0.04Nb-0.09Ti steel (Figure 3.16) before describing in more details the various hot rolling strategies.

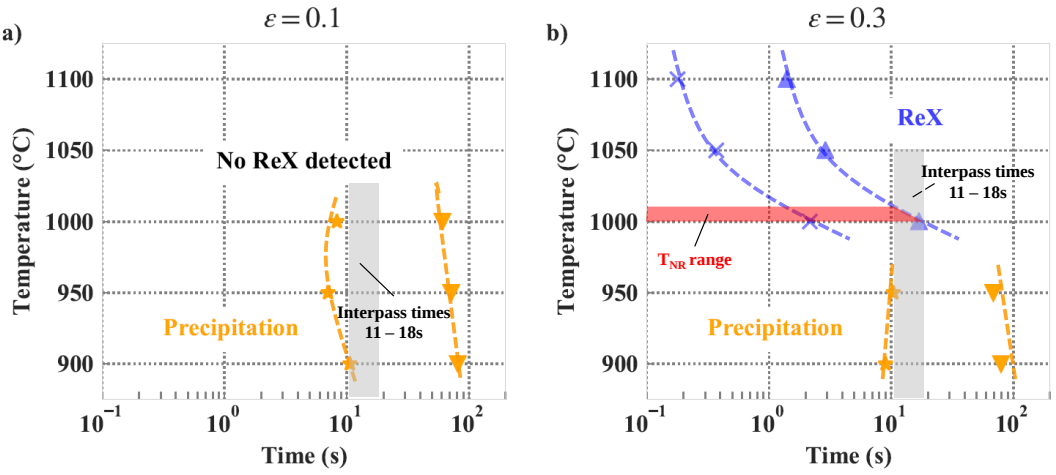

Figure 3.16: Recrystallization - Precipitation - Time - Temperature (RPTT) diagrams determined by stress relaxation for the 0.04Nb-0.09Ti steel for a strain rate of $5\,s^{-1}$.

Each hot rolling schedule entails five phases:

[3] Salzgitter Mannesmann Forschung GmbH, one of the industrial partners involved in NANOFORM project.

[4] Note that precipitation kinetics were determined by stress relaxation using a low strain rate of $0.1\,s^{-1}$, whereas recrystallization kinetics were determined using $0.1\,s^{-1}$ and $5\,s^{-1}$. The effect of strain rate on precipitation is however thought to limited because it only acts on the number of nucleation sites, but not on the driving force for precipitation. The precipitation modeling work presented in Chapter 2 tends to confirm that the increase in precipitation kinetics when the strain rate is increased from 0.1 to $5\,s^{-1}$ is limited. As a first approximation, it is considered than the precipitation kinetics are identical at 0.1 and $5\,s^{-1}$.

(i) Reheating at 1250 °C.

(ii) Rough rolling or roughing. Two deformations passes applied.

(iii) Finish rolling or finishing. Five deformations passes applied.

(iv) Accelerated cooling at 20-40 °C s^{-1} starting from the finishing rolling temperature down to the simulated coiling temperature.

(v) Slow cooling down to room temperature once the coiling temperature is reached.

The applied deformation passes for each hot rolling schedules are given in Table 3.3. The strain rate applied during hot rolling is of the order of 10 s^{-1}.

A reversing rolling mill was used to deform the plate, which resulted in rather large interpass times ranging from 11 to 18 s. For such interpass times and for a strain of 0.3, the temperature of no-recrystallization (T_{NR}) is about 1000 °C (see Figure 3.16 b)). It means that when deformations of the order of 30 % (such as R1, R2, F1, F2, and F3 passes) are applied above 1000 °C during hot rolling, austenite can statically recrystallize completely before the next pass. A higher deformation of 55.6 % is given for F4 pass, which may be large enough to induce dynamic recrystallization during deformation. Conversely, note that the last deformation (F5) of 12.5 % may not be large enough to induce recrystallization, even at elevated temperatures.

Such large interpass times also have consequences on the expected precipitation strengthening contribution. It was demonstrated in Chapter 2 that precipitation starts taking place in austenite approximately 10 s after deformation. Thus, due to the large interpass times applied, most of the precipitation probably take place in austenite, leading to limited precipitation strengthening. The strength properties of the generated hot-rolled steels should therefore mainly be related to the grain sizes and the type of phases formed. In particular, bainitic phases present high dislocation strengthening contributions.

Deformation pass	**Plate thickness (mm)**	**Deformation (%)**	**Interpass time (s)**
Initial	60	-	-
Roughing 1 (R1)	44	26.7	11-13
Roughing 2 (R2)	32	27.3	11-13
Finishing 1 (F1)	21	34.4	13-18
Finishing 2 (F2)	13	38.1	13-18
Finishing 3 (F3)	9	30.8	13-18
Finishing 4 (F4)	4	55.6	13-18
Finishing 5 (F5)	3.5	12.5	13-18

Table 3.3: Deformation passes applied for each hot rolling schedules.

It was first decided to vary the temperature domain were deformation steps were applied with respect to T_{NR}. Three schedules, represented in Figure 3.17, were tested. For convenience, they were referred to as HOT, MIXED and COLD, receptively:

(i) HOT: All deformation passes were performed above 1050 °C, above T_{NR}. This corresponds to a recrystallization controlled rolling. Austenite is expected to fully recrystallize between

each deformation passes, leading to grain refinement before cooling, excepted the last finishing pass.

(ii) MIXED: The two roughing passes are performed above 1050 °C leading to grain refinement. After a wait period of 30 seconds, the finishing stage was performed starting from 1050 °C. Therefore, most of the finishing passes were performed below T_{NR}, resulting in pancaked austenite. Note that the finishing rolling temperature (880 °C) was close to the austenite to ferrite transition equilibrium temperature, A_{e3}, equal to 860 °C according to Thermo-Calc [AND 02a]. Thus, slight amounts of ferrite could have formed during the last pass or right after it.

(iii) COLD: The two roughing passes were performed above 1050 °C. After a wait period of 90 seconds, the finishing stage is performed starting from 950 °C. This schedule is close to the MIXED schedule, but finishing passes were performed even at lower temperatures, with a finishing rolling temperature of 800 °C, 60 °C below the A_{e3} temperature. Thus increasing amounts of ferrite formed during the last finishing passes are expected.

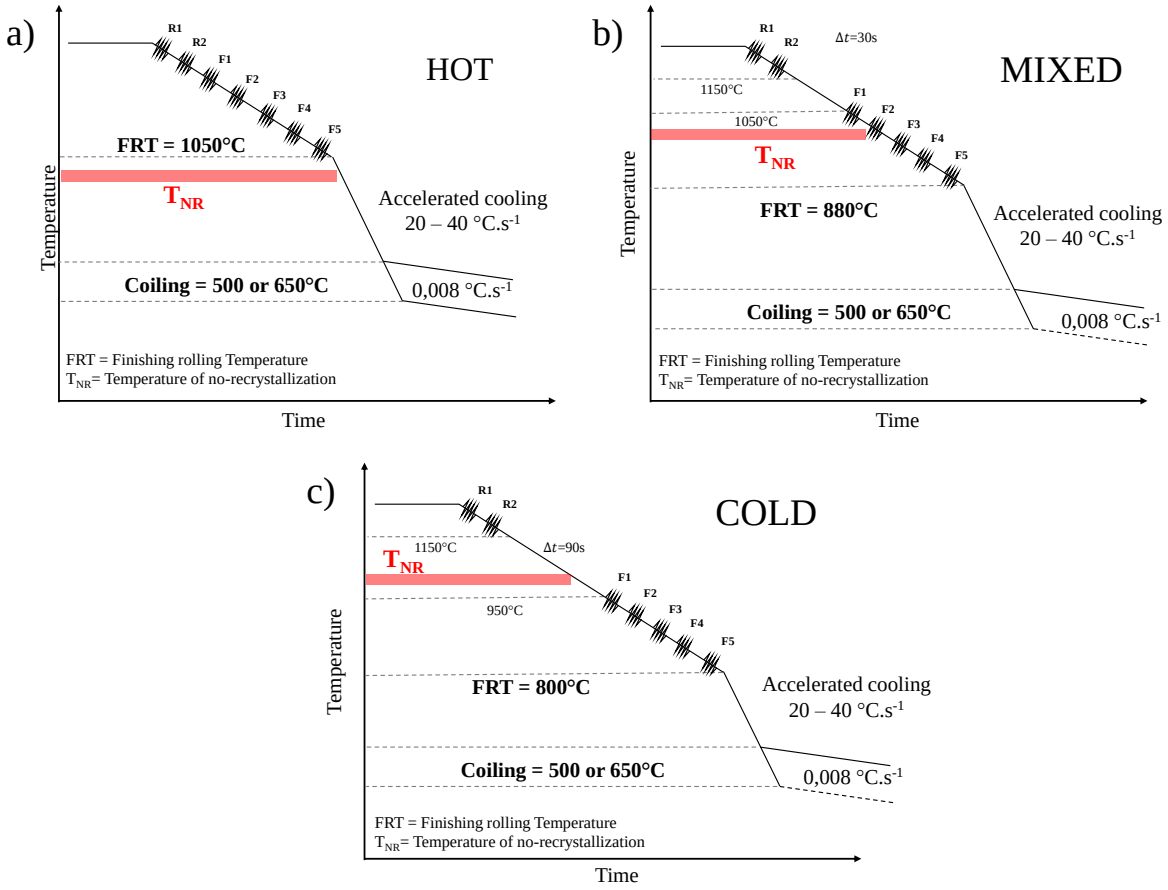

Figure 3.17: Schematic hot rolling schedules performed: (a) HOT, (b) MIXED, and (c) COLD conditions. For each hot-rolling conditions, two coiling temperatures were applied, giving a total of six different hot-rolling schedules.

After hot rolling, the plates were cooled down to the coiling temperature at a rate ranging

from 20 to 40 °C s^{-1}. Consequently, two coiling temperatures were applied: 500 and 650 °C. After reaching the coiling temperature, the hot rolled plates were stored into an insulated box in order to slowly cool down to room temperature, with an estimated cooling rate of 0.5 °C min^{-1}, which is comparable to the cooling rates reached in industrial conditions after coiling. Thus, **a total of six different hot rolling schedules were applied to generate different microstructures.** Hot rolled plates of 1050 × 160 × 3.5 mm^3 were finally obtained.

3.4.2 Characterization methods of hot-rolled plates

3.4.2.1 SEM and EBSD

For microstructural characterization, parallelepiped samples were machined from the different hot-rolled plates. Observations were performed in the plan (RD, ND), where RD and ND stands for rolling and normal direction, respectively.

After polishing down to 1 μm and nital (2 %) etching, samples were observed in a ZEISS Supra 55VP FEG Scanning Electron Microscope in secondary electron (SE) mode. For EBSD characterization, an additional polishing step was performed on a cloth soaked with a Struers OP-S colloidal suspension solution. Electron back-scatter diffraction (EBSD) was carried out a ZEISS Supra 55VP Scanning Electron Microscope operating at 20 kV, equipped with an Oxford Symmetry EBSD camera. The post-processing analysis was performed on AZtec HKL Channel 5 software.

3.4.2.2 Mechanical properties[5]

The mechanical properties of the plates obtained after hot rolling were characterized by tensile tests and hole expansion tests.

Tensile tests

The tensile tests were performed following the DIN EN ISO 6892-1 standard. The tensile properties were evaluated according to three different orientations with respect to the rolling direction: at 0°, 45°, and 90°. Two tensile samples were tested for each orientations, giving a total of 6 tensile samples per hot-rolling schedule.

The number of experiments was limited due to the low amount of material per hot rolling condition. A total of 2 samples per condition is not enough to make statistics and calculate standard deviations. However, a rather limited dispersion was observed, with an average difference between the 2 tensile tests of 15 MPa for yield stress (YS)/ ultimate tensile strength (UTS), 1.9 % for total elongation (TE), and 1.0 % for uniform elongation (UE).

Hole expansion tests

Hole expansion tests were performed following the DIN EN ISO 16630 standard. Square specimens of 90 × 90 mm^2 were machined from the plates. A hole with initial diameter D_0 of 10 mm was prepared in the center of the square samples by punching. During the test, the hole is expanded by a conical punch with a 60° top angle, until a crack at the edge of the expanding hole is observed

[5]Tensile and hole expansion tests were both performed by SZMF.

(refer to Figure 3.3). Knowing the final diameter of the hole D_f, the hole expansion ration λ was calculated through:

$$\lambda(\%) = \frac{D_f - D_0}{D_0} \times 100 \tag{3.2}$$

Three samples are tested for each hot rolling conditions. The standard error of the mean was calculated.

3.4.3 Microstructures oh hot-rolled plates

3.4.3.1 HOT schedule

The HOT schedule is characterized by the fact that all deformation passes were performed in the recrystallization region (Figure 3.17 a)), above a targeted temperature of 1050 °C. Since all passes were performed well above the ferrite start temperature, ferrite cannot form before accelerated cooling takes place. A low deformation (12.5 %) was given for the last finishing pass, F5. This may not be enough to induce static recrystallization after the last finishing pass. Indeed, it was shown in Chapter 2 that a true deformation of 10 % only led to recovery. Thus, austenite is only slightly deformed before accelerated cooling and coiling. During coiling, granular bainite is expected at 650 °C, whereas coiling at 500 °C should favor the formation of lath bainite.

Figure 3.18 shows the results from the characterization by SEM and EBSD of the microstructures obtained after coiling at 650 and 500 °C. The microstructure resulting from the HOT - 650 °C schedule appeared to mainly consist of granular bainite (HOT - 650 °C), which is confirmed by the misorientation angle distribution obtained from EBSD (Figure 3.18 g)). On the contrary, the HOT - 500 °C schedule led to large amounts of lath bainite (Figure 3.18 b)). It was confirmed by the presence of a high peak around 60° in the misorientation angle distribution (Figure 3.18 h)).

In both HOT - 650 °C and HOT - 500 °C microstructures, equiaxed ferrite grains also appeared, pointed by arrows in Figure 3.18 a) and b). The presence of ferrite was assessed from KAM maps (Figure 3.18 e) and f). Ferrite grains seem to follow a certain alignment, which shows that they were probably formed along the prior austenite grains. KAM maps also showed that the amount of ferrite seems to be larger in the HOT - 650 °C conditions. Coiling at higher temperature thus increased the amount of ferrite in the microstructure.

3.4.3.2 MIXED schedule

In the MIXED rolling schedule, two roughing passes were first given in the austenite recrystallization region, above 1050 °C. Five finishing passes were then performed in a lower temperature region with a finishing rolling temperature around 880 °C, which thus results in significant pancaking of austenite microstructure before accelerated cooling and coiling. The finishing rolling temperature is close to the austenite to ferrite transition equilibrium temperature, A_{e3}, equal to 860 °C according to Thermo-Calc [AND 02a]. Thus slight amounts of ferrite may have formed during the last pass or right after it. Similarly to the HOT schedule, granular bainite and lath bainite are expected for coiling at 650 and 500 °C, respectively.

Figure 3.19 exhibits the results from the characterization by SEM and EBSD of these microstructures. The MIXED - 650 °C microstructure mainly consisted of granular bainite according to SEM

(Figure 3.19 a)) and misorientation angle distribution (Figure 3.19 g)). The MIXED - 500 °C microstructure is mainly composed of lath bainite. The misorientation angle distribution showed a high peak around 60°. KAM maps revealed small amounts of ferrite aligned on pancaked prior austenite grains (Figure 3.19 f)), which can also be observed on SEM images (Figure 3.19 b)).

3.4.3.3 COLD schedule

The COLD schedule is close to the MIXED schedule, but finishing passes were performed at even lower temperatures, with a finishing rolling temperature of 800 °C, 60 °C below the A_{e3} temperature. Thus, as expected, increasing amounts of ferrite formed during the last finishing passes compared to the microstructures resulting from the MIXED schedules.

The microstructures resulting from COLD schedule were characterized by SEM and EBSD (Figure 3.20). The COLD - 650 °C schedule led to a microstructure mainly consisting of granular bainite with ferrite. When coiling at 500 °C, a mixture of granular bainite, lath bainite, and ferrite was obtained.

A significant amount of ferrite was obtained in both microstructures, as proved by the misorientation angle distributions that show random distributions at all angles (Figure 3.20 g) and h)), pointed by small black arrows). The microstructure resulting from COLD - 650 °C was very fine, so the filter size applied to build the KAM map was reduced. Even though, the distinction between granular bainite and ferrite remained difficult (Figure 3.20 e)). The distinction was easier on COLD - 500 °C microstructure (Figure 3.20 f)). Ferrite grains were aligned along severely pancaked PAG.

3.4.3.4 Microstructure summary

A summary of microstructures is presented in Table 3.4 for ease of reading.

	650 °C	500 °C
HOT	Granular bainite Ferrite along PAG (++)	Lath-like bainite Ferrite along PAG (+)
MIXED	Granular bainite Ferrite along PAG (++)	Lath-like bainite Ferrite along PAG (+)
COLD	Granular bainite Ferrite (+++)	Mostly granular bainite + lath-like bainite Ferrite (+++)

Table 3.4: Summary of the microstructures of hot rolled plates.

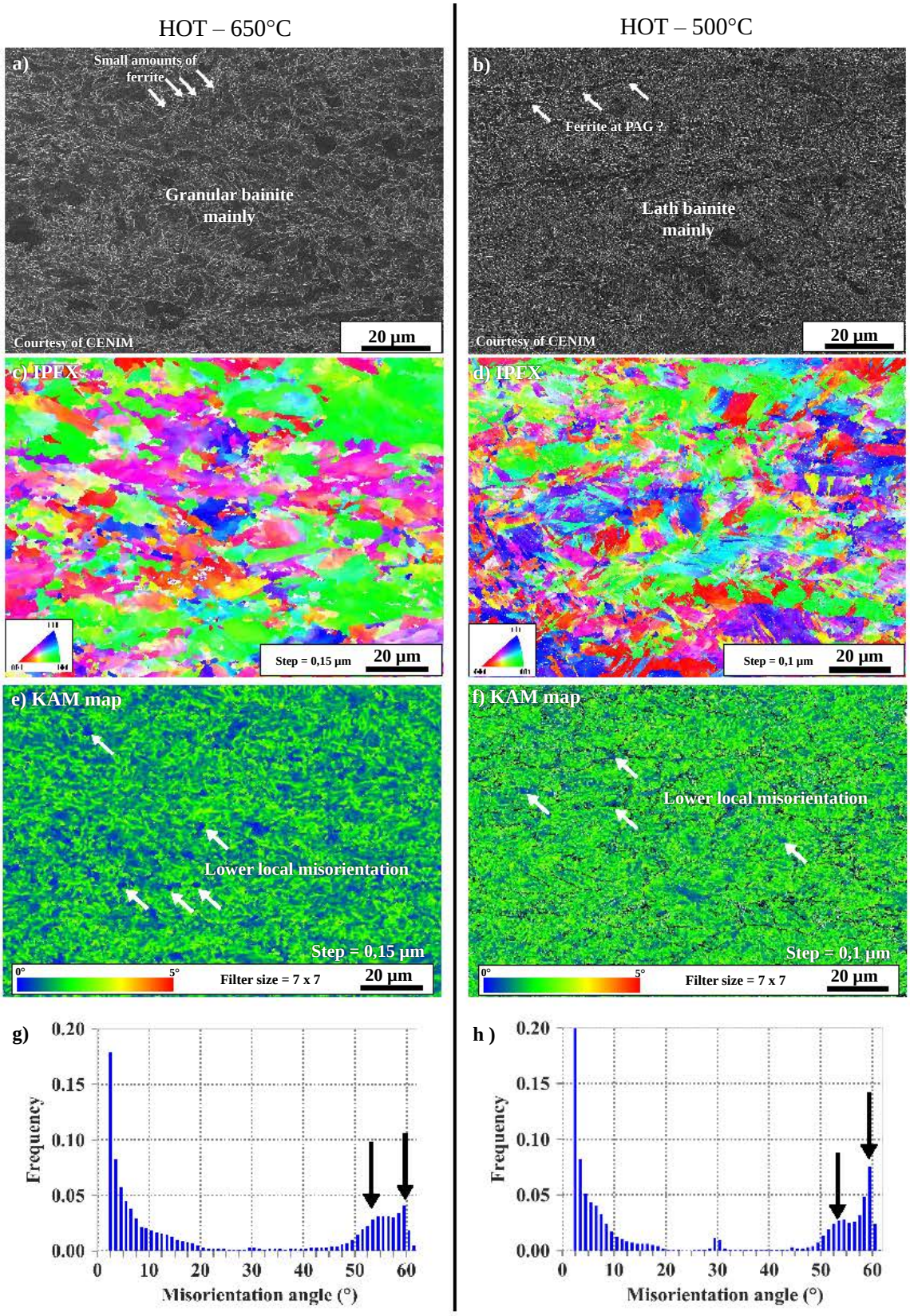

Figure 3.18: SEM and EBSD characterization of the microstructures obtained after "HOT" hot-rolling schedule, accelerated cooling and coiling at 650 and 500 °C.

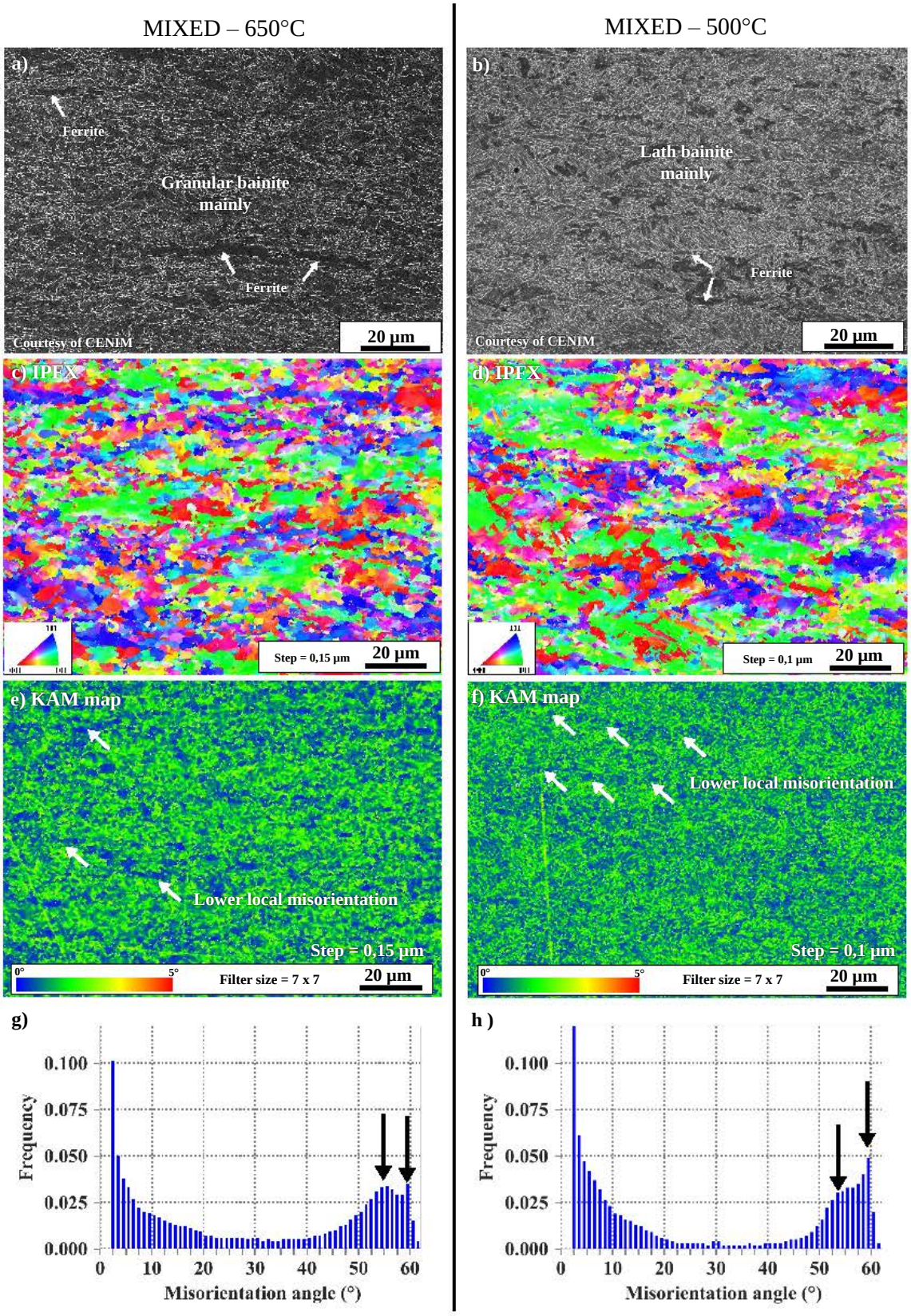

Figure 3.19: SEM and EBSD characterization of the microstructures obtained after "MIXED" hot-rolling schedule, accelerated cooling and coiling at 650 and 500 °C.

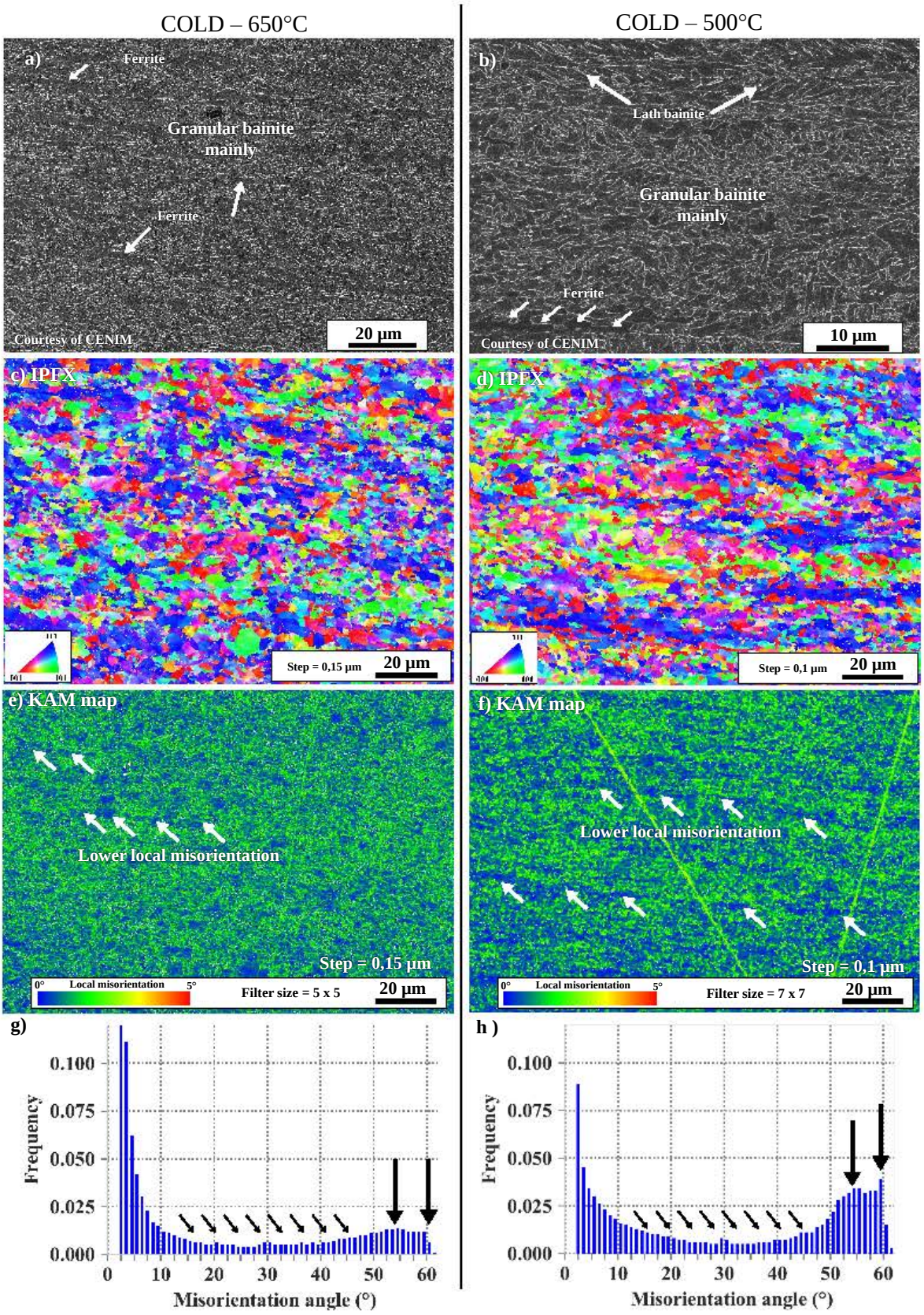

Figure 3.20: SEM and EBSD characterization of the microstructures obtained after "COLD" hot-rolling schedule, accelerated cooling and coiling at 650 and 500 °C.

3.4.4 Mechanical properties

Figure 3.21 presents the average tensile and hole expansion properties of the hot-rolled plates. The tensile properties were determined on a total of 6 samples per hot-rolling schedule (2 samples per direction with respect to the rolling direction).

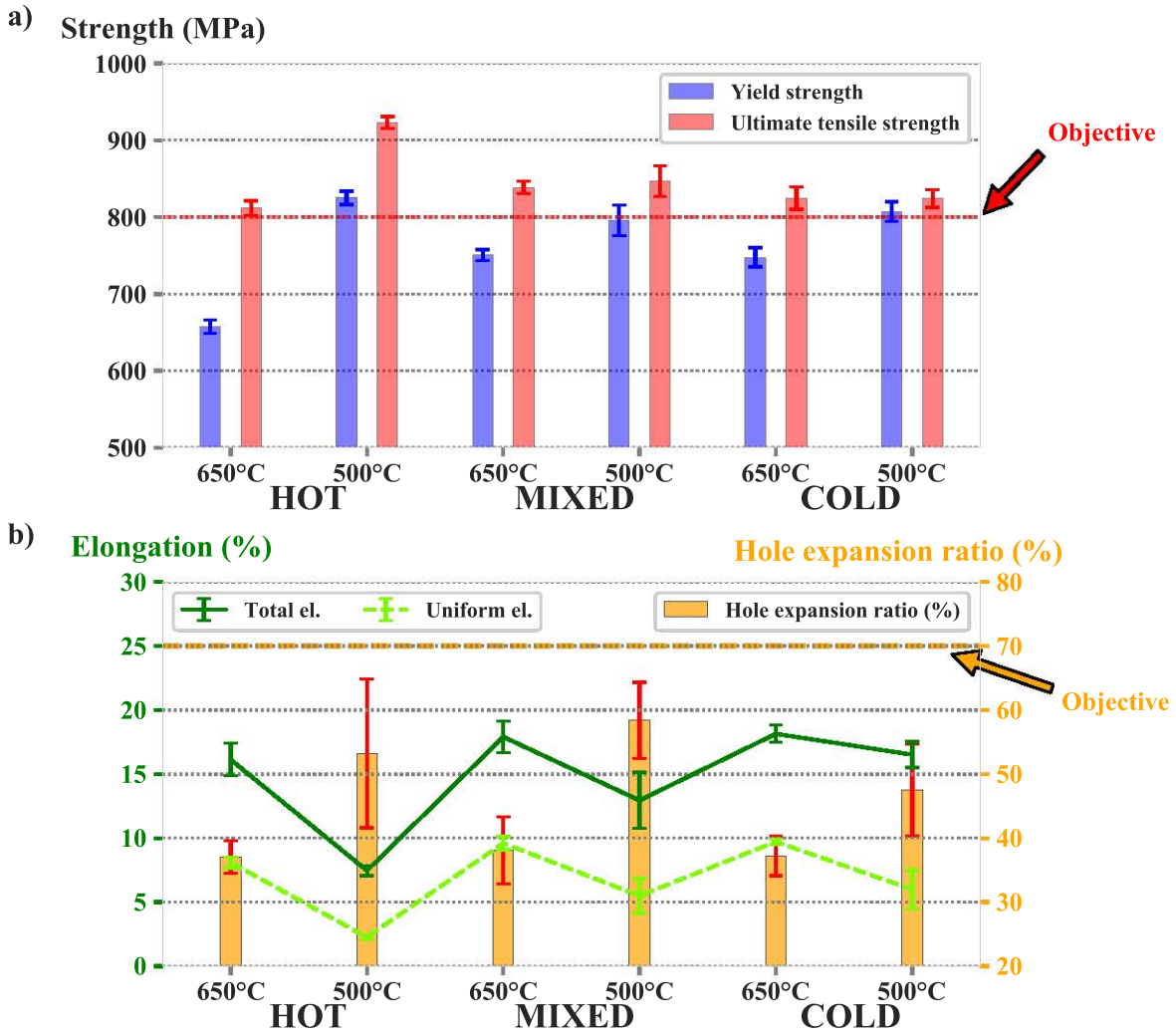

Figure 3.21: Average tensile properties and hole expansion ratios obtained on hot-rolled plates. (a) Yield and ultimate tensile strengths. (b) Ductility properties : Total and uniform elongation determined by tensile tests, and hole expansion ratios.

Each hot-rolling schedule gave rise to ultimate tensile strength equal or above 800 MPa (Figure 3.21 a)). The highest UTS was obtained for HOT - 500 °C, whose microstructures mainly consisted of lath bainite. The minimum yield strength was obtained for HOT - 650 °C with approximately 660 MPa. Rather high YS/UTS ratios were obtained, higher than 0.81. This YS/UTS ratio reached 0.97 for the COLD - 650 °C, meaning that this steel plate does not present any significant strain-hardening.

Figure 3.21 b) focuses on the ductility properties of the plates: the global ductility, evaluated by

tensile tests (uniform and total elongation), as well as the local one, evaluated by hole expansion tests. Rather low tensile ductility levels were obtained: the total elongation ranged from 7 to 18 % for all steel plates. The microstructures mainly composed of granular bainite (coiling at 650 °C and COLD - 500 °C) globally showed higher tensile ductility compared to microstructure mainly composed of lath bainite (HOT and MIXED - 500 °C). Thus, the stronger plate was unsurprisingly also the least ductile.

The opposite was observed for the hole expansion ratio, which is mainly governed by the local ductility of the plates. Steels mainly composed of lath bainite (HOT and MIXED - 500 °C) showed the best hole expansion ratios, ranging between 50 and 60 %. Conversely, the microstructures mainly composed of granular bainite (all steel plates coiled at 650 °C) showed very similar HER, with a ceiling at 40 %. The COLD - 500 °C, containing both granular and lath bainite showed an intermediate HER around 50 %.

Figure 3.22 shows the stress - strain curves obtained from tensile tests on the six different hot-rolling schedules. It can be observed that some tensile curves exhibited a plateau at constant stress during the transition from elastic to plastic domains (Figure 3.22 b) to f)), which is a phenomenon known as Piobert–Lüders bands or stretcher strains [HAL 70]. It traduces an heterogeneous deformation of the tensile samples. Piobert–Lüders bands are typically observed for mild (low-carbon) steels, whose microstructure are mainly composed of ferrite. Their observation in MIXED and COLD hot-rolled plates is thus probably due to the presence of ferrite in the microstructure. It should be noted that the MIXED - 500 °C plate was highly anisotropic, with lower strength and higher ductility at 45° with respect to the rolling direction (Figure 3.22 e)). The anisotropy was more limited for the other hot-rolled plates.

3.5 Discussion

3.5.1 Achieved strength - stretch flangeability combination

The initial goal of this study, and in a wider context, the goal of the NANOFORM project was to design low carbon complex phase steels reaching UTS superior to 800 MPa with improved stretch flangeability (HER $\geq$ 70 %). The strategy was based on obtaining homogeneous microstructures, maximizing the proportion of bainite, in order to reduce the stress concentration region at interfaces between hard and soft phases.

As explained by Bhadeshia [BHA 15, p. 367], a successful strategy to promote bainitic transformation is to use low carbon steels with additions of boron or molybdenum. Keeping a low carbon content avoid increasing the hardenability drastically, which would lead to the formation of martensite. Additions of B or Mo suppress allotriomorphic ferrite formation, and promote the formation of bainite [CIZ 02, ZHA 03, KON 06, HU 15]. Thus, the steel composition studied in this work is particularly suitable for favoring bainite transformation. As demonstrated in part 3.3, bainitic microstructures were obtained for a wide range of cooling rates, even from deformed austenite. With cooling rates as low as 0.05 °C s^{-1}, a non-negligible fraction of austenite still transforms to granular bainite. The microstructures generated by hot rolling schedules also contain a very large proportion of bainite with, in the case of MIXED and COLD schedules, small fractions of ferrite. The initial

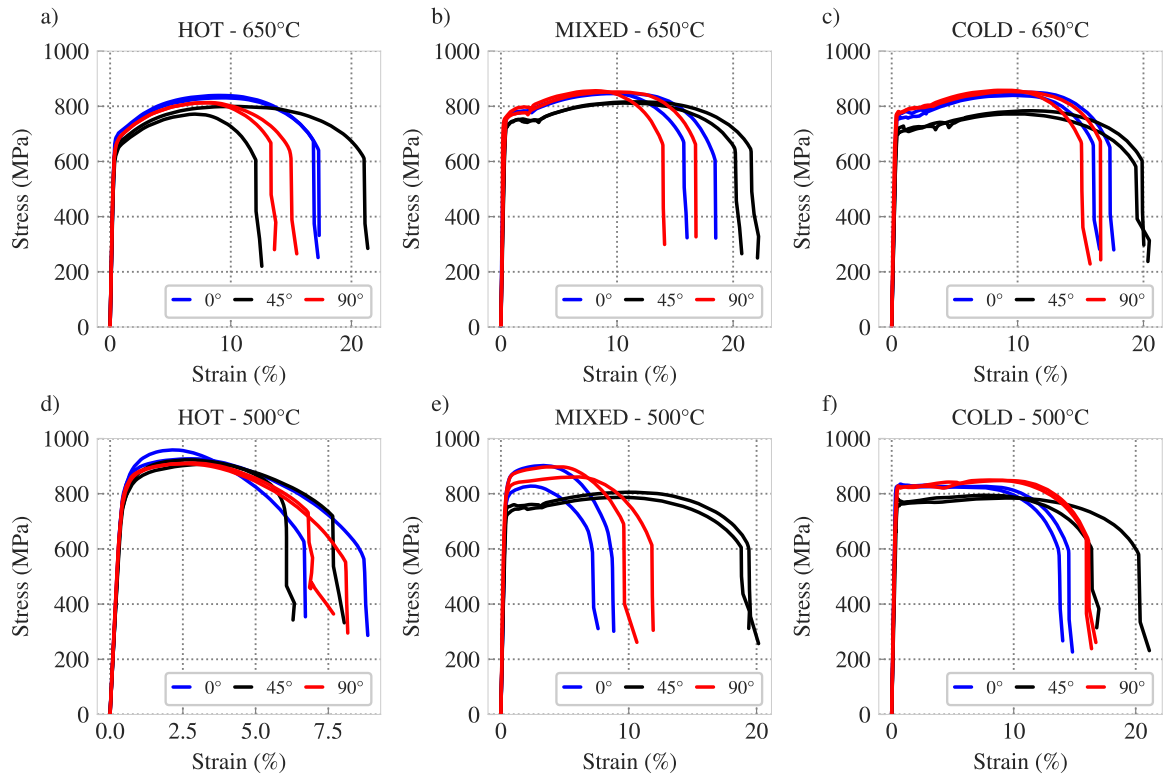

Figure 3.22: Engineering stress - strain curves obtained by tensile tests on hot-rolled plates.

goal of obtaining mainly bainitic microstructures is thus fulfilled.

The target of 800 MPa for UTS is achieved for all the hot-rolled steels produced. The maximum strength is reached for the HOT - 500 °C, which present an almost fully lath bainite microstructure. Concerning HER, none of the hot-rolled conditions reaches the objective of 70 % initially defined. However, respectable levels are still achieved, with ratios higher than 50 % for HOT - 500 °C and MIXED - 500 °C.

Figure 3.23 compares the HER and strengths of the steels obtained in this work with those of other types of steels (with carbon content lower than 0.2 wt%) presenting UTS levels that approach those of the steels designed in this study. Since the hole expansion ratio is very sensitive to experimental conditions, it was ensured that all data came from experiments performed under similar conditions, from a punched hole and using a 60° conical punch for hole expanding. However, it is worth mentioning that the steel plate thickness changes in the different studies. The steels produced in this work are compared with:

(i) Dual Phase steels, with data extracted from [HAS 04, KAR 09, HIS 12, TAY 14].

(ii) Other Complex Phase Steels, with data from [KAR 09, RYD 10, HIS 12].

(iii) Fully ferritic steels with outstanding precipitation strengthening contribution achieved by combined additions of Ti and Mo, from [FUN 04, WAN 14].

(iv) A fully martensitic steel, from [HAS 04].

It can be observed that the hot-rolled steels produced in this work globally present a higher

combination of strength and stretch flangeability than most of the DP steels with similar strength levels. Their stretch flangeability is however significantly lower than single phased steels such as precipitation-strengthened ferrite steels and martensite steels. The complex phase phases steels produced still reach higher yield and tensile strength than precipitation-strengthened ferrite steels. Although the combination of strength and HER of the fully martensitic steel is outstanding, it should be remembered than their ductility is severely limited (5 % of total elongation in the cited study [HAS 04]). The combination of properties achieved in this work is in fact quite similar to other complex phase steels for most of the tested conditions. The HOT - 500 °C and MIXED - 500 °C hot rolled plates present the most promising properties.

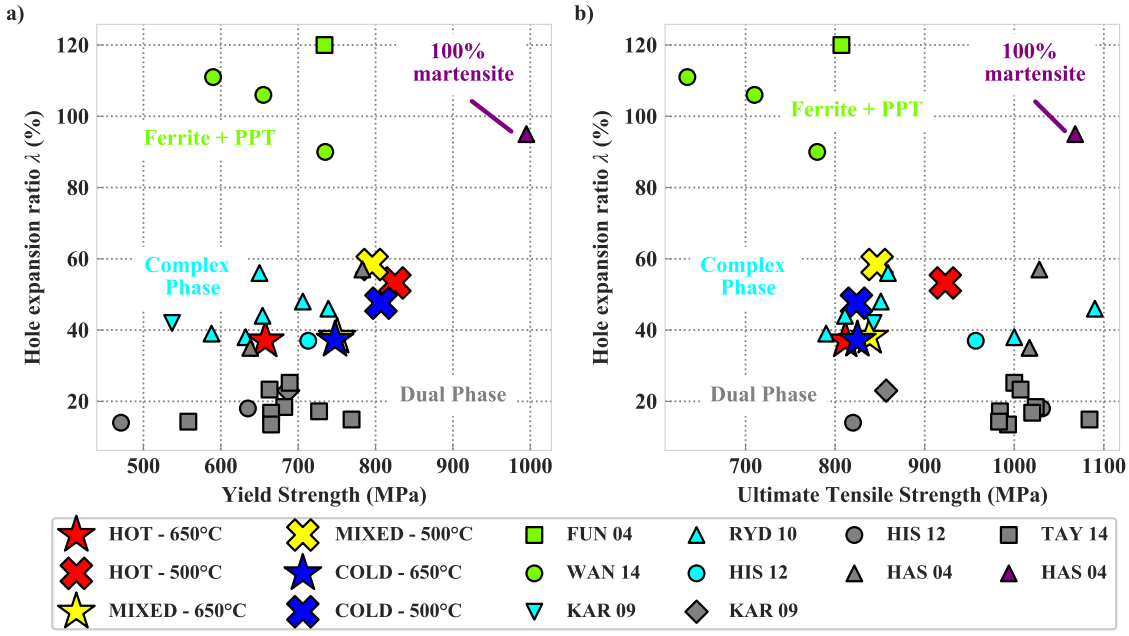

Figure 3.23: Comparison of YS, UTS, and HER of the hot-rolled steels developed in this work with other types of steels extracted from literature.

During this PhD work, and more generally during the NANOFORM project, a large part of the work focused on the microstructural evolutions of austenite during reheating and hot rolling. It should be noted, however, that the main factor affecting the nature of the phases formed during the hot rolling process is the coiling temperature. In fact, the coiling is almost equivalent to an isothermal treatment, because the cooling rate after coiling is rather low. It is therefore logical that this is the main factor influencing the microstructure. This indicates that the coiling temperature is an important lever for optimizing the microstructure, on which the project has not yet concentrated at the time of writing this manuscript: only the minimum and maximum achievable coiling temperatures were tested (500 and 650 °C). However, the hot rolling step still has a significant effect on the morphology of the phases formed and the resulting mechanical properties, as illustrated for example by the very different properties obtained for the 3 plates coiled at 500 °C.

It should also be remembered that these steels were produced on a pilot plant, *i.e.* in semi-industrial conditions. The use of an industrial process could induce significant changes in the

generated microstructures. In particular, the interpass times are much shorter than those used in this laboratory trials, which can results in increased austenite pancaking before cooling and more refined final microstructures. Shorter interpass times will also lower the amount of precipitates formed in the austenite domain. A larger proportion of precipitates forming in the ferritic phases can be expected, with a greater precipitation strengthening contribution.

To summarize, a better combination of properties could be achieved by the transition to an industrial process and the optimization of the coiling temperature.

3.5.2 Enhancing stretch flangeability

Two paths could be followed to improve the stretch flangeability of the steels designed in this project:

(i) **Avoiding the formation of granular bainite.**
It was experimentally observed that microstructures consisting mainly of granular bainite led to lower HER than those mainly consisting of lath bainite. These observations are consistent with a recent study by Weißensteiner *et al.* [WEI 18] that reported that lath bainite microstructures exhibits higher tolerance against damage during the shearing of edges, and thus higher HER, than granular bainite ones. This may be due to the presence of large MA islands in granular bainite (see Figure 3.24 a)) that act as crack nucleation sites due to stress concentration at interface between MA islands and bainitic ferrite, presenting different levels of hardness. Lath bainite microstructures do not contain these large MA islands, as illustrated in Figure 3.24 b). Thus, the formation of granular bainite should be avoided in order to achieve better HER.

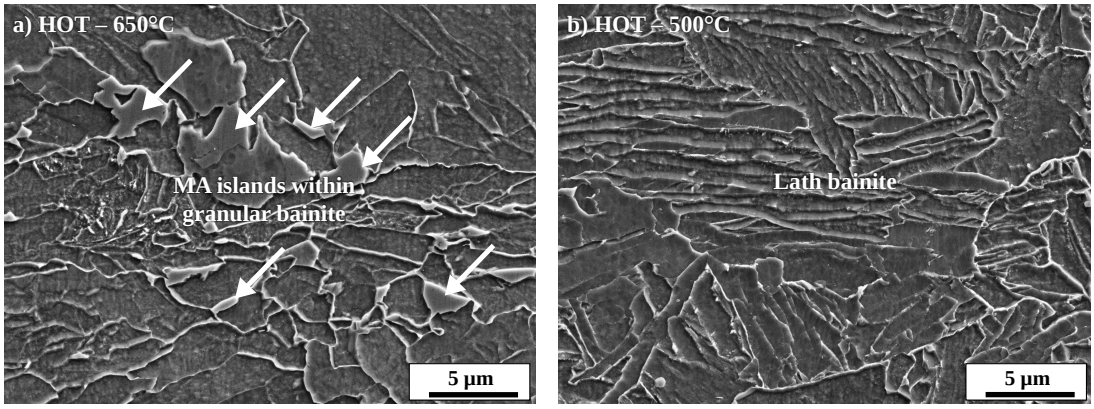

Figure 3.24: SEM observations of the microstructures of (a) HOT - 650 °C and (b) HOT - 500 °C hot-rolled plates. Nital etching.

(ii) **Limiting the amount of ferrite.**
In the same spirit of homogenization of microstructures, the process could be adapted to minimize the fraction of ferrite formed, particularly for the MIXED schedule. It would probably be necessary to slightly increase the finishing rolling temperature (FRT) in order to increase the margin between A_{e3} and FRT.

(iii) **Controlling the size of TiN.**

Two recent studies [PAT 17, KAI 17] reported that large precipitates such as micrometric TiN or cementite can act as the primary source of void nucleation in complex phase steels, which deteriorates HER. Large TiN are also known to deteriorate the toughness [GLA 02]. The steel studied in this work contains a significant amount of micrometric TiN particles, an example of which is presented in Figure 3.25.

It is known that to avoid the formation of large TiN, the formation of TiN before solidification should be avoided by maintaining Ti and N contents below the solubility product of TiN at the solidus temperature [YAN 06]. Additionally, maintaining the Ti/N ratio below 3.42 reduces the coarsening rate of TiN during reheating [YAN 06]. In this study, the Ti/N ratio was above 24 for the hot-rolling experiments, which explains the presence of coarse TiN in the microstructure. It would be interesting to try designing complex phase steels presenting compositions similar to those studied, but with Ti/N contents that avoid forming large TiN. Better hole expansion ratios should be achieved, at the cost of a limited loss of strength due to a reduction in precipitation hardening.

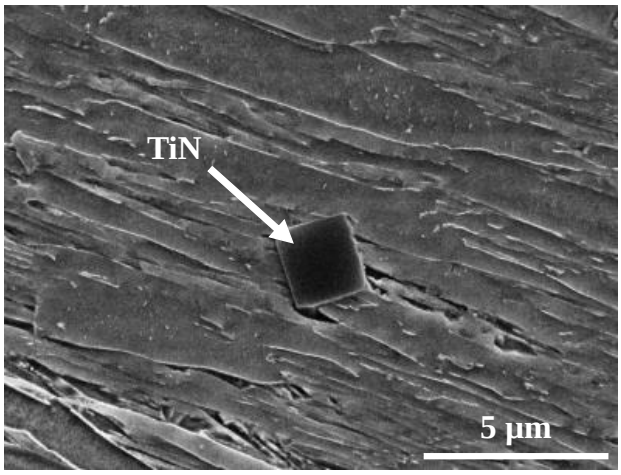

Figure 3.25: Example of large TiN precipitates observed in the studied steel. SEM observation after austenitisation at 1200 °C and quenching.

3.6 Conclusions

This work aimed at generating a complex phase microstructure mainly consisting of bainite by hot-rolling, using a low-carbon Ti-Nb microalloyed steel. A good combination of strength and stretch flangeability was targeted. The hot-rolling process consisted of deformation at elevated temperatures, followed by accelerated cooling, and coiling at 500 or 650 °C.

The phase transformation behavior of the steel was first followed by dilatometry during continuous cooling experiments. Deformation in the non-recrystallization austenite region is known to influence phase transformations during subsequent cooling. Thus, in order to establish the effect of austenite deformation, continuous cooling experiments were performed from undeformed and deformed austenite. Bainitic microstructures were obtained for a wide range of cooling rates. Cooling

rates as low as $1\,°C\,s^{-1}$ led to a fully (mainly granular) bainitic microstructure, which showed that the steel composition is particularly suitable for promoting the formation of bainite. For increasing cooling rates, lath-like microstructures were rather observed. Deformation of austenite in the non-recrystallization region favored the formation of granular bainite at the extent of lath-bainite. It also significantly coarsened lath microstructures, which thus presented decreasing hardness compared to those obtained from undeformed austenite.

Subsequently, steel plates were produced by hot rolling tests on a pilot plant reproducing industrial conditions, with the aim of testing varying hot-rolling strategies. Deformation passes were performed in various temperature regions, following three distinct sketches:

(i) HOT, for which all deformation passes were given in the recrystallization region (recrystallization controlled rolling).

(ii) MIXED, for which roughing passes were performed in the recrystallization region, and finishing passes were given between 1050 and 880 °C.

(iii) COLD, which is similar to MIXED schedule, but with the finishing passes performed in a lower temperature region, between 950 and 800 °C.

Two different coiling temperatures of 500 and 650 °C were applied, which gave a total of six different hot-rolling schedules. The tensile, hole expansion properties, and microstructures of the generated steel plates were subsequently characterized.

For all hot-rolling schedules, the microstructures mainly consisted of bainite, with low amounts of ferrite. Deformation of austenite in a low temperature region during hot-rolling favored the formation of ferrite, mainly on prior austenite grains. Microstructures mainly consisting of lath bainite were obtained for HOT-500 °C and MIXED-500 °C, whereas granular bainite dominated for the other four schedules.

Ultimate tensile strength over 800 MPa were obtained for all hot-rolled plates, reaching the initial target defined in the NANOFORM research project. High levels of yield strength were also achieved, with YS/UTS ratios ranging from 0.81 to 0.97. However, the ductility (evaluated by tensile tests) was limited.

A reasonable stretch formability was reached, hole expansion ratio being between 40 % and 60 %. The microstructures mainly consisting of granular bainite, mostly obtained though coiling at 650 °C, presented lower hole expansion ratios. Higher hole expansion ratios were obtained when lath bainite is the dominant phase, as obtained for HOT - 500 °C and MIXED - 500 °C rolling schedules. This is due to the presence of coarse MA islands in granular bainite.

Since the tested hot-rolling schedules correspond to boundary conditions, a better combination of properties could be obtained by testing intermediate conditions, such as coiling temperatures between 500 and 650 °C. Since granular bainite seems to be detrimental to hole expansion ratios, granular bainite should be avoided to enhance stretch flangeability for this composition.

Large TiN precipitates were observed in the microstructures due to the use of a high Ti/N ratio, which can act as void nucleation sites during hole expansion, leading to reduce stretch flangeability. It would be interesting to optimize the size of these TiN to determine if it leads to enhanced stretch flangeability. This could be done by adjusting the Ti/N content of the alloy with the aim of avoiding their formation in liquid state during casting.

Conclusions and Perspectives

Conclusions

This PhD-work was carried out as part of NANOFORM RFCS project aiming at developing low carbon complex phase steels produced by hot rolling. The goal of NANOFORM project was to reach a high combination of strength and stretch flangeability by optimization of the steel composition and hot-rolling process. Although a total of 11 alloys were studied in the project, this PhD work focused mainly on one of the 11 grades. Naturally, the work was built following the different stages of the hot rolling process, as illustrated in Figure 1.

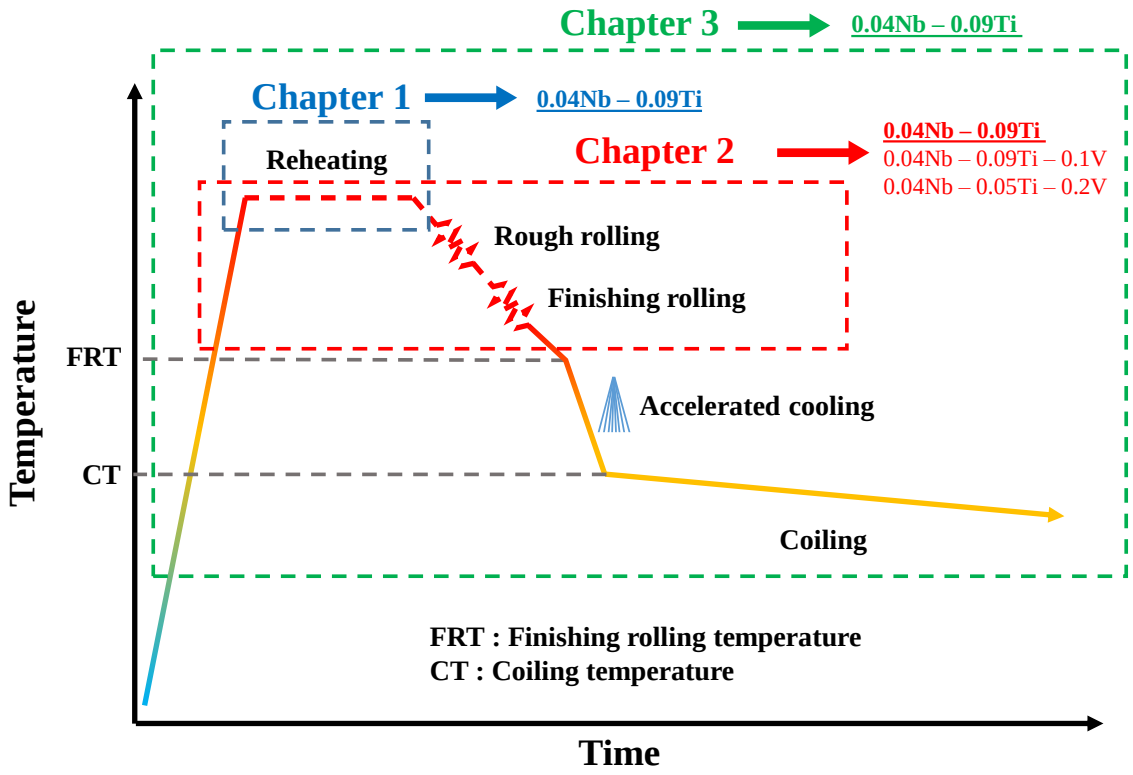

Figure 1: Structure of the PhD manuscript with respect to the different stages of the hot rolling process.

Chapter 1

The first chapter focused of the microstructural evolution occurring during the reheating stage of the process in the 0.04Nb-0.09Ti steel.

Starting from a fully precipitated as-received state, several heat treatments were performed between 950 and 1250 °C. The evolution of austenite grain sizes and precipitation state were characterized over this entire temperature range combining optical microscopy, transmission and scanning electron microscopy, and atom probe tomography. Four types of precipitates were identified in the as-received state. Of these 4 populations, only one has a sufficiently large volume fraction and fine sizes to effectively control grain growth: (Ti,Nb)C_{fine}. The characterization work thus focused on this (Ti,Nb)C_{fine} population. An original strategy was followed to measure the volume fraction of (Ti,Nb)C_{fine} by composition measurement of the matrix with atom probe tomography. This technique is made possible by the considerable evolution experienced by the tomographic atomic probe during the last 20 years.

The experimental data accumulated in this first chapter were used to inform modeling work. A multi-class precipitation model was developed and applied to describe the evolution of (Ti,Nb)C_{fine} distribution during heat treatments. The output from the precipitation model served as input parameters to a simple grain growth model based on the theory of Zener pinning, containing only one adjustable parameter. The modeled austenite grain diameters were consistent with the experiments for the investigated heat treatments.

Based on the acquired experimental data, a reheating temperature of 1250 °C was selected for the hot rolling process. A this temperature, (Ti,Nb)C_{fine} completely dissolve. Although large austenite grain sizes are obtained at the end of reheating using such a high temperature, it will be possible to refine austenite grains by recrystallization during the next hot rolling stage. Dissolving all pre-existing (Ti,Nb)C_{fine} during reheating makes it possible to form finer precipitates during the next stages of hot rolling, enabling recrystallization control and precipitation strengthening.

Chapter 2

The second chapter was related to the hot rolling stage of the process. It focused on determining the kinetics of recrystallization and precipitation occurring after deformation of austenite. Three different alloys presenting varying Ti and V contents were studied, including the 0.04Nb-0.09Ti steel characterized in the first chapter.

Stress relaxation after reheating at 1250 °C and compression tests proved to be powerful since it allowed to indirectly study recovery, recrystallization, and the precipitation in austenite. Varying temperature, strain and strain rates were applied in order to determine the influence of these parameters on subsequent microstructural evolutions. Stress relaxations tests were supplemented by direct microstructural characterization of austenite grain sizes and precipitation state.

The experimental techniques applied alloyed to establish Recrystallization-Precipitation-Time-Temperature diagrams for the three studied steels. This allowed to draw the following main conclusions:

(i) Recrystallization globally took place above 1000 °C if sufficient strain was applied ($\epsilon = 0.3$).

When a lower strain was applied ($\epsilon = 0.1$), only recovery was observed.

(ii) Increasing strain rate from 0.1 to $5\,s^{-1}$ resulted in accelerated recrystallization kinetics.

(iii) Vanadium additions delayed the recrystallization by solute-drag effect. Despite this clear effect of vanadium, the recrystallization kinetics of the three studied steels are quite similar. Indeed, the Nb content, which has the strongest retarding effect of austenite recrystallization, was kept constant is the three studied steel.

(iv) At lower temperatures, strain-induced precipitation took place before recrystallization. Due to the pinning pressure exerted by the fine precipitates formed, austenite recrystallization was delayed to longer times, so that it was not observed for the performed heat treatments times. Precipitation modeling work tended to confirm that the plateau appearing in stress relaxation curves due to strain-induced precipitation is related to the number of precipitates rather to their pinning pressure or volume fraction.

Additionally, a JMAK-based model was developed and applied to reproduce the recrystallization kinetics in the 0.04Nb-0.09Ti steel. In this model, the driving force for recrystallization was calculated from the increased in flow stress observed during compression tests prior to stress relaxation. Thus, the model was able to reproduce the effect of strain rate on recrystallization kinetics, and agreement between experimental and modeling data was obtained.

This chapter allowed a better understanding of the microstructural evolution of austenite during hot-rolling, thus helping to elaborate different hot rolling strategies that were applied in the third chapter.

Chapter 3

The third and last chapter of this manuscript was related to the complete hot rolling process. It details the relations between the processing parameters and the obtained microstructure and mechanical properties for the 0.04Nb-0.09Ti steel. Of course, the first two chapters provided essential data to understand the microstructural evolutions taking place during reheating and hot deformation. Thus, the metallurgical state of austenite right before accelerated cooling can be - at least partially - deduced from the work presented in chapter 1 and 2.

The phase transformation behavior of the steel was first investigated by dilatometry during continuous cooling experiments after reheating at 1250 °C. These experiments revealed that the steel composition is particularly suitable for obtaining bainitic microstructure over a large range of cooling rates. Ferrite was observed only for the slowest $0.05\,°C\,s^{-1}$. Starting from $1\,°C\,s^{-1}$, fully bainitic microstructures were obtained. Granular bainite was obtained at low cooling rates, whereas a lath-like bainite microstructure was rather obtained for increasing cooling rates. Deformation of austenite favored the formation of granular bainite. It also led to coarser lath microstructures, that consequently presented reduced hardnesses.

Subsequently, six different hot rolling schedules were designed and performed on a hot rolling pilot plant. These schedules aimed at reproducing various strategies that can be targeted in industrial conditions. Deformation passes were performed following three distinct sketches:

(i) HOT, for which all deformation passes were given in the recrystallization region. This was basically what is referred to as a recrystallization-controlled rolling.

(ii) MIXED, for which roughing passes were performed in the recrystallization region, and finishing passes were given between 1050 and 880 °C. Thus, pancaked austenite were obtained at the end of the finishing stage. This corresponded to a thermo-mechanical control process.

(iii) COLD, for which roughing passes were performed in the recrystallization region, and finishing passes were given between 950 and 800 °C. This schedule is similar to the MIXED one, but finishing is performed in a lower temperature region, so that ferrite formation is possible during the last deformation passes.

Following these hot deformation sketches, accelerated cooling at 20-40 °C s^{-1} and coiling at 500 and 650 °C were applied, giving at total of six different hot rolling processes.

The generated hot-rolled plates showed microstructures mainly consisting of granular/lath bainite. The MIXED and COLD rolling schedules also led to the formation of ferrite, mostly at prior austenite grain boundaries. The ultimate tensile strengths reached values above 800 MPa, while hole expansion ratios ranging from 40 to 60 % were achieved.

Four of the six hot rolled plates presented microstructures mainly consisting of granular bainite: all the plates coiled at 650 °C as well as the COLD - 500 °C. These plates presented limited hole expansion ratios, around 40 %. The presence of large martensite/austenite islands in granular bainite may limit their stretch flangeability.

The best combination of properties were obtained for the HOT - 500 °C and the MIXED - 500 °C plates, which presented both higher strength and stretch flangeability. This is due to the fact that they showed a more homogeneous microstructure mainly consisting of lath bainite. An even better combination of properties could be achieved by optimizing the process, for example by testing intermediate coiling temperatures.

Perspectives

Production of NANOFORM steels at industrial scale

The 0.04Nb-0.09Ti steel grade studied in this PhD work was selected for industrial scale production trials on Salzgitter Mannesmann Forschung GmbH hot rolling plant. Although the experimental results presented in Chapter 3 were encouraging, they do not demonstrate the industrial feasibility. The transition from lab scale hot rolling to an industrial production line induces many changes. Notably, higher strain rates and shorter interpass times are gotten. The feasible processes are not so flexible, and suffer more constraints, for example on achievable heating and cooling rates.

At the time of writing this manuscript, these industrial trials have just been successfully completed. Different hot rolling schedules were tested for the purpose of seeking an optimal combination of properties. The mechanical characterization revealed that two of these industrially produced plates showed interesting properties:

(i) The first one showed high UTS in the 900-950 MPa range, and reasonable hole expansion ratio of approximately 50 %.

(ii) The second presented an UTS of approximately 850 MPa and an excellent hole expansion ratio of 70 to 80 %.

It has therefore been demonstrated that it is possible to industrially produce the steels studied in this research project, by achieving an excellent combination of mechanical properties. The characterization of the microstructure of these two plates has not yet been realized at the time of writing this manuscript. A short-term perspective is therefore to conduct a fine microstructural characterization to understand the origin of these excellent mechanical properties. In the end of the NANOFORM project, these steel plates will undergo deeper characterization, such as weldability, galvanisability, or bendability tests. In the longer term, after further characterization of these properties, one of these steels may be on the market within a few years.

Enhancement of modeling works

In chapter 1, a fairly simple model, based on Zener pinning, was proposed to correlate the evolution of the precipitation state to austenite grain growth during isothermal treatments from the as-received state. Although it showed a correct agreement with the experimental results, this model is based on a thorough characterization of the precipitation state in the as-received state. Efforts could therefore be made to reduce the amount of experimental data needed to calibrate the model. This should include working towards the prediction of the actual amount of solute elements trapped into large precipitates such as (Ti,Nb)N, that therefore do not actively participate to austenite grain growth control. This requires modeling the formation of precipitates in the liquid phase during casting. The model could also be improved by allowing the modeling of more complex heat treatments, including non-isothermal sections.

In Chapter 2, models describing austenite recrystallization and strain-induced precipitation in 0.04Nb-0.09Ti steel grade were presented. To go further in these models, they should be coupled to account for the many interactions between recovery, recrystallization, and precipitation. Thus, this work could be extended to become a complete model of recovery, recrystallization, and precipitation, on the basis of Zurob's work [ZUR 03]. The modeling of these phenomena and their interactions should allow a better understanding of stress relaxation curves obtained experimentally. However, it would probably be wiser to carry out this study on model alloys, presenting simpler compositions, allowing a better understanding of metallurgical evolutions. In particular, the model should be able to estimate the mobility of grain boundaries, accounting for the solute-drag effect, in order to be applied to other steel compositions.

It would also be very useful to develop a complete model of recrystallization and restoration, including the modeling of restoration phenomena (dynamic recovery and recrystallization) during compression tests and the modeling of these phenomena once the deformation is complete (recovery and static or metadynamic recrystallization). For this purpose, the first step is to develop constitutive equations for the description of the hot flow stress behavior of austenite, as proposed in literature [MIR 11, AKB 15]. These equations describe the evolution of the flow stress and, indirectly, of the dislocation density during deformation. Thus, they allow to estimate the dislocation density at the end of a compression test, and consequently the driving pressure for static or metadynamic recrystallization. It would then be necessary to couple a static/metadynamic recrystallization model, which can be of the type proposed in Chapter 2.

Optimization of the steel composition

The studied 0.04Nb-0.09Ti steel present both a high Ti content and a high Ti/N ratio. Although initially intended to form hardening precipitates in the ferritic phases during cooling and coiling, it also leads to the formation of large TiN, sometimes up to a few micrometers. The strengthening contribution of precipitates is presumably limited. Cracks are prone to initiate near these large TiN, which has detrimental effects on the stretch flangeability of the plates. Thus, the composition tested may not optimal to achieve excellent level of formability.

Although it has previously been reported in the literature, it should first be experimentally confirmed that these TiN are the main source of crack propagation in the studied steel. The analysis of the fracture surfaces of post-mortem hole expansion samples should confirm this hypothesis. Once confirmed, it would be interesting to test other compositions of steels which have lower levels of Ti and N **to avoid the formation of** these large **TiN**. However, a composition prone to promote the formation of bainite must be kept, in order to reach high strength levels.

Using **combinatorial metallurgy** [DES 18], which is receiving a growing attention, would be an interesting and elegant way to find the optimal composition to produce a microstructure mainly consisting of bainite, with improved mechanical properties. It would first be necessary to produce steel slabs having a composition gradient in one or more elements. It is possible to obtain these gradient materials by assembling blocks of different alloys by hot compression and then carrying out a diffusion treatment [DES 18]. Steel plates could then be produced by applying laboratory hot rolling. It would then be possible to scan a wide range of composition in a single sample, which is the main advantage of combinatorial metallurgy. However, the production of gradient materials is a tedious experimental procedure. This strategy is schematically illustrated in Figure 2.

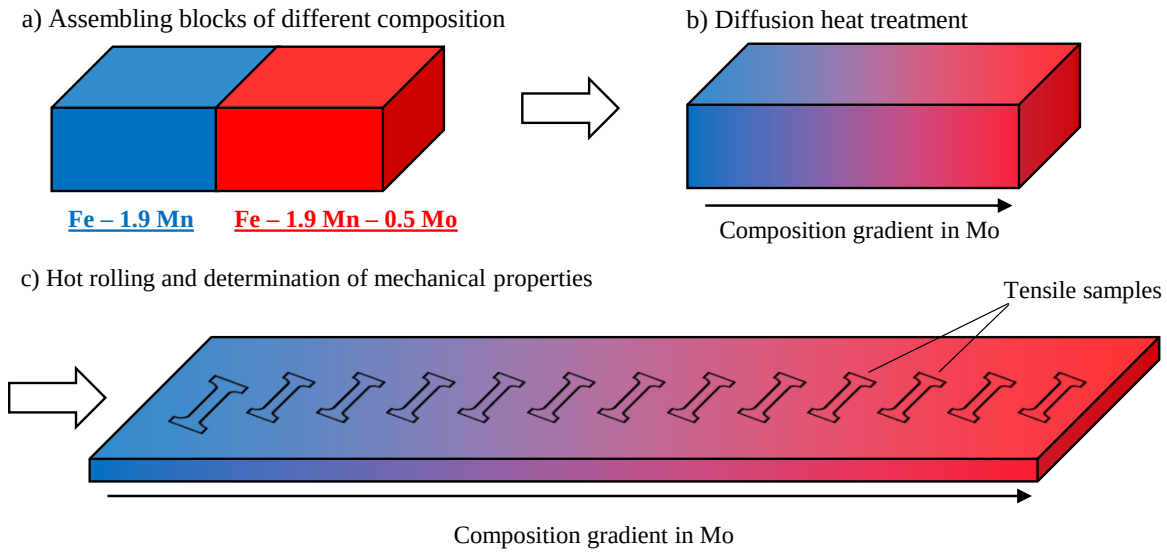

Figure 2: Schematic illustration of obtaining a composition gradient material for combinatorial metallurgy.

Appendix A

Overview of NANOFORM project

NANOFORM is a 42-month project that started in June 2016. The project was founded by the Research Found for Coal and Steel (RFCS) from the European Commission. It involved five academic and two industrial partners:

- MATEIS laboratory in Villeurbanne, France.
- Groupe de Physique des Matériaux (GPM) laboratory in Saint Etienne du Rouvray, France.
- Centro Nacional de Investigaciones Metalúrgicas (CENIM) in Madrid, Spain.
- Universitat Politècnica de Catalunya (UPC) in Barcelona, Spain.
- Eurecat Centre Tecnològic in Manresa, Spain.
- Salzgitter Mannesmann Forschung GmbH (SZMF) in Salzgitter, Germany.
- Thyssenkrupp Steel Europe (TKSE) in Duisbourg, Germany.

It is a complete project for the design of new steel grades, starting from laboratory scale up to industrial scale. The project aims to produce by hot rolling a complex phase steel presenting a good compromise of strength and stretch flangeability. A tensile strength of 800 MPa and a hole expansion ratio of 70 % are targeted. For this purpose, the steel microstructure has to be optimized by playing on two main levers: the steel composition and the process.

11 different compositions were chosen at the beginning of the project (Table A.1): six were produced by TKSE and five by SZMF. These grades present manganese contents of about 1.9 % and low carbon levels, ranging from 0.03 to 0.12 %. The contents of niobium, aluminum and nitrogen remain globally fixed for all steels. Some other alloying elements were varied in order to study their effect:

(i) The composition of TKSE steels mainly allow studying the influence of carbon and chromium contents. The use of microalloying elements are limited to Nb and Ti additions. The V content remains very low. TKS1A and TKS1B present higher molybdenum contents than other TKS steels in order to compensate their lower hardenability due to their low carbon contents.

(ii) SZMF steels present intermediate carbon contents. Their Si content is higher than TKSE steels(0.50 %), which enables to harden the ferritic phases by solid solution. The Mo content varies from 0 to 0.2 % in SZMF1A, SZMF1B, and SZMF1C steels. Vanadium is added in SZMF2A and SZMF2B, to examine the possibility of strengthening the steel by the formation

of vanadium-rich precipitates.

Element	C	Mn	Si	Ti	Nb	V	Mo	Al	Cr	N
TKS1A	0.032	1.91	0.11	0.100	0.040	0.010	0.200	0.052	0.11	0.0039
TKS1B	0.030	1.87	0.11	0.098	0.039	0.011	0.200	0.053	0.50	0.0040
TKS2A	0.054	1.88	0.10	0.071	0.037	0.001	0.100	0.051	0.50	0.0064
TKS2B	0.057	1.86	0.10	0.091	0.036	0.001	0.100	0.050	1.01	0.0071
TKS3A	0.116	1.87	0.10	0.071	0.038	0.001	0.100	0.052	0.05	0.0054
TKS3B	0.118	1.88	0.11	0.073	0.040	0.001	0.100	0.052	0.97	0.0063
SZMF1A	0.061	1.93	0.50	0.087	0.039	0.002	0.005	0.079	0.01	0.0058
SZMF1B	0.062	1.93	0.51	0.085	0.039	0.002	0.108	0.047	0.01	0.0066
SZMF1C	0.062	1.91	0.50	0.085	0.039	0.002	0.212	0.065	0.01	0.0060
SZMF2A	0.087	1.94	0.50	0.093	0.039	0.105	0.209	0.067	0.01	0.0059
SZMF2B	0.085	1.95	0.50	0.046	0.039	0.206	0.209	0.070	0.01	0.0060

Table A.1: Bulk composition (wt%) of the 11 steel grades studied in NANOFORM project (ICP-MS). The six grades highlighted in blue were selected for the second characterization iteration. The grade framed in red was selected for the final industrial tests.

The steels are intended to be manufactured by hot rolling. The various steps of the process were described in the general introduction (Figure 3 and 4). The parameters of each of these steps can be optimized according to the characterization results obtained during the project, in order to reach the best possible combination of strength and stretch flangeability.

As schematically represented in Figure A.1, the work was divided into five main work packages. MATEIS laboratory, in which this PhD-work was carried out, was almost exclusively involved in work package 3 and 4, thus dealing with thermomechanical treatments on Gleeble, and microstructure characterization and modeling. Some results produced by other project partners were also included in this manuscript.

Three distinct series of characterization took place during the project, as represented in Figure A.2. In the following parts, these series are briefly described.

A.1 First series of characterization

The study began with a first series of characterization, covering the 11 different grades. For this first stage, small ingots of approximately 10 kg were cast by the industrial partners. These ingots were intended for **laboratory tests**, mainly using dilatometers or Gleeble thermomechanical simulators. The main tasks performed are described below:

(i) The compositions were selected on the basis of the experience of the academic and industrial partners involved in the project. The precipitation behavior was first studied by performing **equilibrium calculation** using various programs: Thermo-Calc, MalCalc, Factsage and JMatPro. These calculations allowed determining which precipitates may form during the process, and estimating the temperatures ranges at which the precipitates may form.

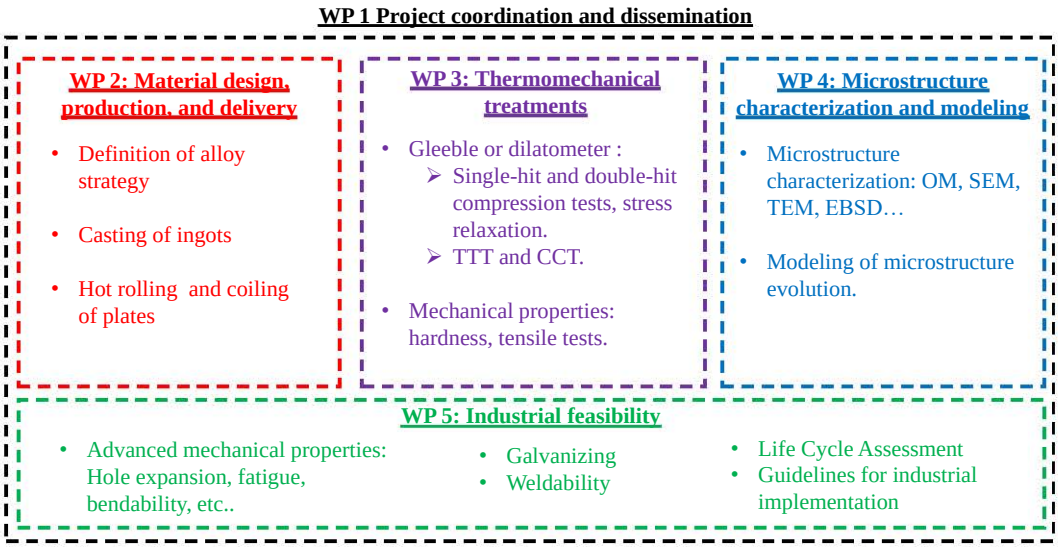

Figure A.1: Work packages of the NANOFORM project. MATEIS mostly intervened in WP3 and 4.

(ii) Then, the **austenite grain growth** behavior during reheating was studied. Isothermal holding at temperatures ranging from 950 to 1250 °C were performed, and the average austenite grain sizes were measured at the end of each of these treatments. These experiments were completed by studying the evolution of pre-existing precipitates controlling the grain growth using electron microscopy techniques. The results of this study fed the chapter 1. This allowed to select **a temperature of** 1250 °C **for the reheating step** of the hot rolling process. This high reheating temperature allows a complete dissolution of the (coarse) pre-existing precipitates to fully benefit from microalloying additions in the next steps of the hot rolling process.

(iii) Afterwards, the project focused on the microstructural evolutions of the austenite during and after hot deformation. The flow stress behavior of the steels was derived during single hit compression tests for various temperatures and strain rates. These single hit compression tests notably allowed to determine the conditions needed to induce **dynamic recrystallization**. The **static recrystallization** (*i.e.* after deformation) was also studied by stress relaxation and double hit compression tests. Stress relaxations tests also allowed to study **strain-induced precipitation** in austenite. Some of these results were presented in the Chapter 2 of this manuscript.

(iv) Finally, the phase transformation behavior of the steel grades was investigated during continuous cooling and isothermal experiments on dilatometers. Continuous cooling transformation (**CCT**) and time-temperature-transformation (**TTT**) diagrams were determined. Vickers hardness measurements were performed at the end of each heat treatment.

At the end of this first series of characterization, **six grades were selected for further characterization in a second series of tests**. The grades with moderate carbon levels (0.06 wt%), more inclined to produce bainitic microstructure, were selected: TKS2A, TKS2B, SZMF1A, SZMF1B,

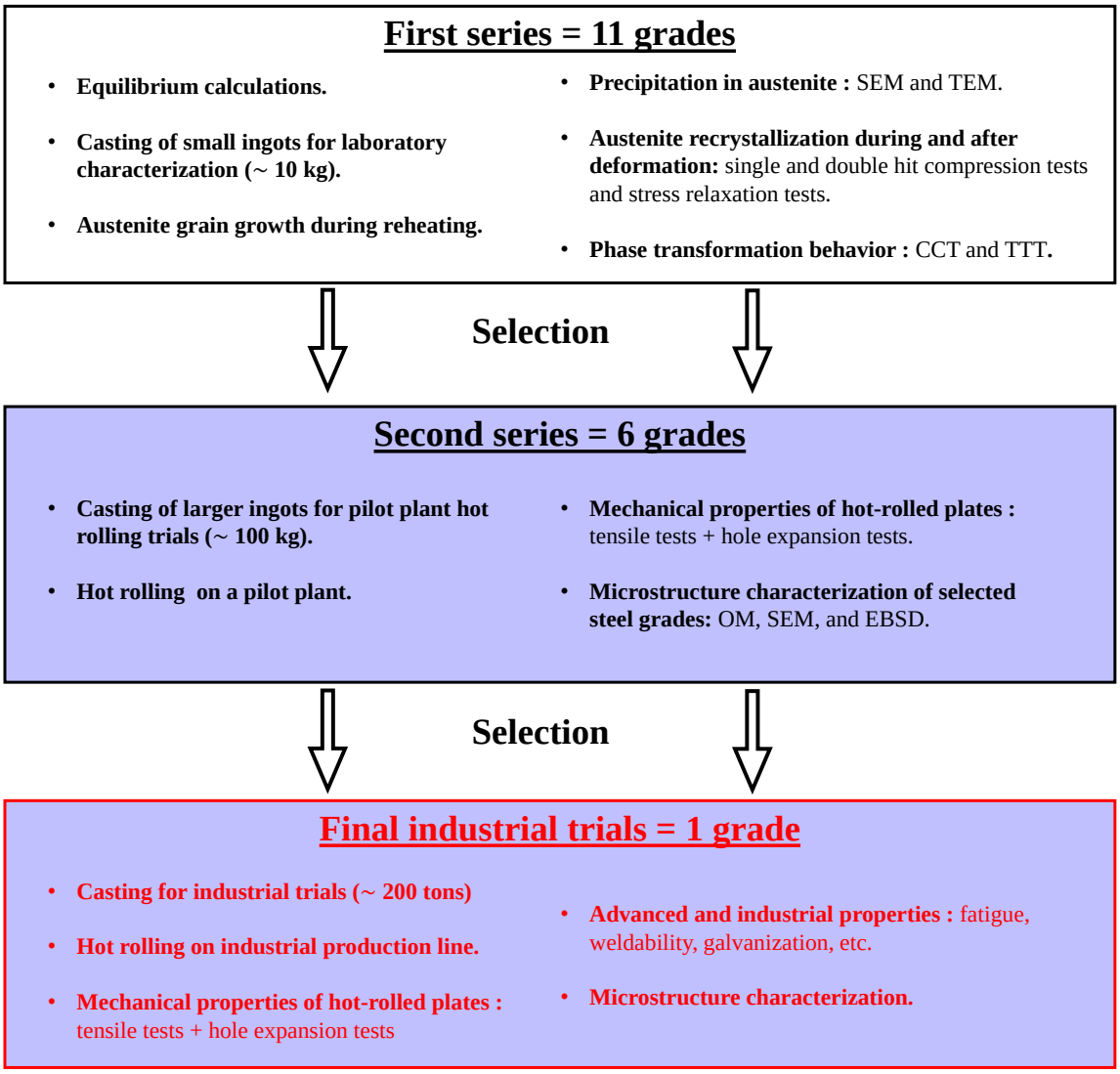

Figure A.2: Gradual selection of steel grades during the NANOFORM project. At the end of a first series of characterization, six shades were selected for further characterization in a second series. Then, the most promising grade was selected for final industrial trials.

SZMF1C, and SZMF2A (see the steels highlighted in blue in Table A.1).

TKS1A and TKS1B showed low hardness values (between 220 and 280 HV10) even after rapid cooling during CCT experiments, which is mainly due to their low carbon contents. It seemed complicated to reach the objective of 800 MPa tensile strength with these compositions. On the other hand, it was impossible to generate a purely bainitic microstructure with TKS3A and TKS3B. Due to their higher carbon contents, these two steels showed incomplete bainite transformation even after isothermal holding of 1 h between 500 and 700 °C. These four steels were consequently eliminated.

SZMF2B, presenting a higher vanadium content was also discarded. Its high vanadium content was initially intended to improved the strength by formation of vanadium-rich precipitates in the ferritic phases. However, using such V content also raises the material costs. No significant hardness improvement was obtained after the various heat treatments performed on dilatometers compared to the other SZMF compositions, which led to the exclusion of SZMF2B.

For the first series of characterization, the carbon content of SZMF2A was raised up to 0.08 wt% in order to increase the driving force for precipitation. In order to obtain a better comparability between the SZMF steels, it was decided to lower the carbon content down to 0.06 wt% in the second series of characterization.

A.2 Second series of characterization

The study was pursued by a second series of characterization on a **semi-industrial scale**. Larger steel ingots of approximately 100 kg were cast and cut into several coupons. Then **six different hot rolling schedules** were designed and applied in the **pilot hot rolling plant** of the industrial partners, in order to test different strategies applicable on an industrial production line. Three hot deformation schedules (HOT, MIXED, and COLD) coupled with coiling at two different temperatures (500 and 650 °C) were applied, giving a total of six rolling schedules. These different hot rolling strategies were described in Chapter 3 (see part 3.4.1 and Figure 3.17).

The mechanical properties of the steel plates obtained at the end of these hot rolling schedules were characterized by **tensile and hole expansion tests**. These mechanical tests were completed by the **characterization of the microstructure** of selected steel plates, in order to understand the relationships between hot rolling parameters, microstructures and mechanical properties.

As one of the final goal of the project is to demonstrate the industrial feasibility of the designed steels, one grade was selected for final tests on the SZMF industrial production line. The SZMF1C grade showed the best compromise of mechanical properties: the target utimate tensile strength of 800 MPa was fulfilled for all hot rolling schedules and reasonable hole expansion ratios (50 to 60 %) were obtained for two particular schedules. The chapter 3 mainly focuses on the description of the relationships between hot rolling parameters and obtained microstructure and mechanical properties on SZMF1C steel. Thus, **SZMF1C was selected for the final industrial tests.**

A.3 Final industrial tests

For the final tests on the SZMF industrial production line, large quantities of materials (approximately 200 tons) were cast to generate several steel slabs. The pilot plant trials performed during the second series of characterization allowed to select the most promising hot rolling strategies. Since there was no indication that the hot rolling conditions used during pilot plant trials were optimized, different hot rolling strategies were tested during these final industrial tests.

At the time of writing this manuscript, these final industrials tests have just been successfully completed. Two industrially produced steel plates showed outstanding combinations of properties:

(i) The first one showed high UTS in the 900-950 MPa range, and reasonable hole expansion ratio of approximately 50 %.

(ii) The second presented an UTS of approximately 850 MPa and an excellent hole expansion ratio of 70 to 80 %, reaching the initial objectives of the project.

The end of the project will focus on the microstructural characterization of these two steel plates and on advanced mechanical and industrial properties: fatigue, weldability, galvanization, etc.

References

[ACE 05] Acevedo Reyes D., Perez M., Pecoraro S., Vincent A., Epicier T., Dierickx P.
Vanadium carbide dissolution during austenitisation of a model microalloyed fecv steel. *Materials Science Forum*, vol. 500 Trans Tech Publ, 2005, p. 695–702.

[AI 00] AI F., Uranga P., López B.
Static recrystallization behaviour of a wide range of austenite grain sizes in microalloyed steels. *ISIJ international*, vol. 40, n° 9, 2000, p. 893–901.

[AKB 15] Akbari Z., Mirzadeh H., Cabrera J.-M.
A simple constitutive model for predicting flow stress of medium carbon microalloyed steel during hot deformation. *Materials & Design*, vol. 77, 2015, p. 126–131, Elsevier.

[ALL 81] Allen S. M.
Foil thickness measurements from convergent-beam diffraction patterns. *Philosophical Magazine A*, vol. 43, n° 2, 1981, p. 325–335.

[AM 04] AM E., Essadiqi E., Yue S.
Kinetics of metadynamic recrystallization in microalloyed hypereutectoid steels. *ISIJ international*, vol. 44, n° 4, 2004, p. 744–752.

[AND 83] Andrade H., Akben M., Jonas J.
Effect of molybdenum, niobium, and vanadium on static recovery and recrystallization and on solute strengthening in microalloyed steels. *Metallurgical Transactions A*, vol. 14, n° 10, 1983, p. 1967–1977.

[AND 95] Andersen I., Grong .
Analytical modelling of grain growth in metals and alloys in the presence of growing and dissolving precipitates—I. Normal grain growth. *Acta Metallurgica et Materialia*, vol. 43, n° 7, 1995, p. 2673–2688.

[AND 02a] Andersson J.-O., Helander T., Höglund L., Shi P., Sundman B.
Thermo-Calc & DICTRA, computational tools for materials science. *Calphad*, vol. 26, n° 2, 2002, p. 273–312.

[AND 02b] Garcia de Andres C., Caballero F., Capdevila C., San Martin D.
Revealing austenite grain boundaries by thermal etching: advantages and disadvantages. *Materials Characterization*, vol. 49, n° 2, 2002, p. 121–127.

[ARI 94] Arieta F., Sellars C.
Activation volume and activation energy for deformation of Nb HSLA steels. *Scripta Metallurgica et Materialia;(United States)*, vol. 30, n° 6, 1994.

[ASH 66] Ashby M., Ebeling R.
On the determination of the number, size, spacing, and volume fraction of spherical second-phase particles from extraction replicas. *AIME MET SOC TRANS*, vol. 236, n° 10, 1966, p. 1396–1404.

[AZU 12] Azuma M., Goutianos S., Hansen N., Winther G., Huang X.
Effect of hardness of martensite and ferrite on void formation in dual phase steel. *Materials Science and Technology*, vol. 28, n° 9-10, 2012, p. 1092–1100.

[Bé 55] Béchet S., Beaujard L.
Nouveau réactif pour la mise en évidence micrographique du grain austénitique des aciers trempés ou trempés-revenus. *Revue de Métallurgie*, vol. 52, n° 10, 1955, p. 830–836.

[BAI 93] Bai D. Q.
Effect of rolling parameters on the no-recrystallization temperature (Tnr) in Nb-bearing steels. PhD thesis, McGill University, 1993.

[BAI 96] Bai D., Yue S., Maccagno T., JJ J.
Static recrystallization of Nb and Nb-B steels under continuous cooling conditions. *ISIJ international*, vol. 36, n° 8, 1996, p. 1084–1093.

[BAK 16] Baker T.
Microalloyed steels. *Ironmaking & Steelmaking*, vol. 43, n° 4, 2016, p. 264–307.

[BAN] BANDOH S., MATSUMURA O., SAKUMA Y.
An improved tint etching method for high strength steel sheets with mixed microstructures. *Transactions of the Iron and Steel Institute of Japan*, vol. 28, n° 7.

[BAN 10] Banerjee K., Militzer M., Perez M., Wang X.
Nonisothermal Austenite Grain Growth Kinetics in a Microalloyed X80 Linepipe Steel. *Metallurgical and Materials Transactions A*, vol. 41, n° 12, 2010, p. 3161–3172.

[BAO 11] Bao S., Zhao G., Yu C., Chang Q., Ye C., Mao X.
Recrystallization behavior of a Nb-microalloyed steel during hot compression. *Applied Mathematical Modelling*, vol. 35, n° 7, 2011, p. 3268–3275.

[BEC 23] Becket F.
Some effects of zirconium in steel. *Trans. Am. Electrochem. Soc*, vol. 43, 1923, p. 261–269.

[BEI 59] Beiser C.
The effect of small columbium additions to semi killed, medium carbon steels. *ASM Preprint*, , n° 138, 1959.

[BHA 85] Bhadeshia H. K.
Diffusional formation of ferrite in iron and its alloys. *Progress in Materials Science*, vol. 29, n° 4, 1985, p. 321–386.

[BHA 87] Bhadeshia H.
Diffusional and displacive transformations. *Scripta metallurgica*, vol. 21, n° 8, 1987, p. 1017–

1022.

[BHA 90] Bhadeshia H. K. D. H., Christian J.
Bainite in steels. *Metallurgical transactions A*, vol. 21, n° 3, 1990, p. 767–797.

[BHA 06a] Bhadeshia H., Honeycombe S. R.
Acicular ferrite. *Steels*, p. 155–165 Elsevier, 2006.

[BHA 06b] Bhadeshia H., Honeycombe S. R.
Formation of Martensite. *Steels*, p. 95–128 Elsevier, 2006.

[BHA 06c] Bhadeshia H., Honeycombe S. R.
The Tempering of Martensite. *Steels*, p. 183–208 Elsevier, 2006.

[BHA 15] Bhadeshia H. K. D. H.
Bainite in steels: theory and practice. Maney Publishing, Leeds, third edition édition, 2015.

[BOH 19] van Bohemen S.
Bainite growth retardation due to mechanical stabilisation of austenite. *Materialia*, vol. 7, n° 100384, 2019.

[BOR 88] Boratto F., Barbosa R., Yue S., Jonas J.
Effect of chemical composition on the critical temperatures of microalloyed steels. *International Conference on Physical Metallurgy of Thermomechanical Processing of Steels and Other Metals. THERMEC-88.*, vol. 1, 1988, p. 383–390.

[BOR 12] Borgenstam A., Hillert M.
Kinetics of bainite transformation in steels. *Phase Transformations in Steels*, p. 468–501 2012.

[BOU 13] Bouaziz O., Zurob H., Huang M.
Driving Force and Logic of Development of Advanced High Strength Steels for Automotive Applications. *steel research international*, , 2013, p. 937–947.

[CAB 09] Caballero F. G., Garcia-Mateo C., Santofimia M., Miller M. K., De Andrés C. G.
New experimental evidence on the incomplete transformation phenomenon in steel. *Acta Materialia*, vol. 57, n° 1, 2009, p. 8–17.

[CAB 10] Caballero F. G., Miller M. K., Garcia-Mateo C.
Carbon supersaturation of ferrite in a nanocrystalline bainitic steel. *Acta Materialia*, vol. 58, n° 7, 2010, p. 2338–2343.

[CAH 62] Cahn J. W.
The impurity-drag effect in grain boundary motion. *Acta Metallurgica*, vol. 10, n° 9, 1962, p. 789–798.

[CHE 14] Chen X., Jiang H., Cui Z., Lian C., Lu C.
Hole expansion characteristics of ultra high strength steels. *Procedia Engineering*, vol. 81, 2014, p. 718–723, Elsevier.

[CHE 18] Chen Y.-W., Tsai Y.-T., Tung P.-Y., Tsai S.-P., Chen C.-Y., Wang S.-H., Yang J.-R.
Phase quantification in low carbon Nb-Mo bearing steel by electron backscatter diffraction tech-

nique coupled with kernel average misorientation. *Materials Characterization*, vol. 139, 2018, p. 49–58.

[CHO 01] Cho S.-H., Kang K.-B., Jonas J. J.
The Dynamic, Static and Metadynamic Recrystallization of a Nb-microalloyed Steel. *ISIJ International*, vol. 41, n° 1, 2001, p. 63–69.

[CIZ 02] Cizek P., Wynne B., Davies C., Muddle B. C., Hodgson P. D.
Effect of composition and austenite deformation on the transformation characteristics of low-carbon and ultralow-carbon microalloyed steels. *Metallurgical and Materials Transactions A*, vol. 33, n° 5, 2002, p. 1331–1349, Springer.

[COM 06] Comstock R., Scherrer D., Adamczyk R.
Hole expansion in a variety of sheet steels. *Journal of materials engineering and performance*, vol. 15, n° 6, 2006, p. 675–683.

[CUD 82] Cuddy L.
Thermomechanical Processing of Microalloyed Austenite, ed. by AJ DeArdo. *Ed. AJ DeArdo, GA Ratz, PJ Wray, The Metallurgical Society of AIME, Warrendale, PA*, vol. 129, 1982.

[Dž 04] Džubinský M., Husain Z., van Haaften W.
Comparison of recrystallisation kinetics determined by stress relaxation, double hit, optical metallography and EBSD approaches. *Materials Characterization*, vol. 52, n° 2, 2004, p. 93–102.

[DAN 07] Danoix F., Grancher G., Bostel A., Blavette D.
Standard deviations of composition measurements in atom probe analyses—Part II: 3D atom probe. *Ultramicroscopy*, vol. 107, n° 9, 2007, p. 739–743, Elsevier.

[DAV 30] Davenport E., Bain E. C., Paxton H. W.
Transformation of austenite at constant subcritical temperatures. *Metallurgical Transactions*, vol. 1, 1930, p. 3473–3530.

[DAV 68] Davenport A., Berry F., Honeycombe R.
Interphase precipitation in iron alloys. *Metal Science Journal*, vol. 2, n° 1, 1968, p. 104–106.

[DEA 01a] DeArdo A.
Metallurgical basis for thermomechanical processing of microalloyed steels. *Ironmaking & Steelmaking*, vol. 28, n° 2, 2001, p. 138–144, Taylor & Francis.

[DEA 01b] Deardo A.
Metallurgical basis for thermomechanical processing of microalloyed steels. *Ironmaking & Steelmaking*, vol. 28, n° 2, 2001, p. 138–144.

[DEA 03a] Deardo A. J.
Niobium in modern steels. *International Materials Reviews*, vol. 48, n° 6, 2003, p. 371–402.

[DEA 03b] DeArdo A.
Niobium in modern steels. *International Materials Reviews*, vol. 48, n° 6, 2003, p. 371–402.

[DEA 09] DeArdo A., Hua M., Cho K. G., Garcia C.
On strength of microalloyed steels: an interpretive review. *Materials Science and Technology*, vol. 25, n° 9, 2009, p. 1074–1082.

[DEG 12] De Geuser F., Deschamps A.
Precipitate characterisation in metallic systems by small-angle X-ray or neutron scattering. *Comptes Rendus Physique*, vol. 13, n° 3, 2012, p. 246–256.

[DES 13] Deschamps A., De Geuser F.
Quantitative characterization of precipitate microstructures in metallic alloys using small-angle scattering. *Metallurgical and Materials Transactions A*, vol. 44, n° 1, 2013, p. 77–86.

[DES 18] Deschamps A., Tancret F., Benrabah I.-E., De Geuser F., Van Landeghem H. P.
Combinatorial approaches for the design of metallic alloys. *Comptes Rendus Physique*, vol. 19, n° 8, 2018, p. 737–754, Elsevier.

[DOH 97] Doherty R., Hughes D., Humphreys F., Jonas J., Jensen D., Kassner M., King W., McNelley T., McQueen H., Rollett A.
Current issues in recrystallization: a review. *Materials Science and Engineering: A*, vol. 238, n° 2, 1997, p. 219–274.

[DUM 05] Dumont M., Lefebvre W., Doisneau-Cottignies B., Deschamps A.
Characterisation of the composition and volume fraction of η and η precipitates in an Al–Zn–Mg alloy by a combination of atom probe, small-angle X-ray scattering and transmission electron microscopy. *Acta Materialia*, vol. 53, n° 10, 2005, p. 2881–2892.

[DUR 13] Durand-Charre M.
Microstructure of steels and cast irons. Springer Science & Business Media, 2013.

[DUT 92] Dutta B., Valdes E., Sellars C.
Mechanism and kinetics of strain induced precipitation of Nb (C, N) in austenite. *Acta Metallurgica et Materialia*, vol. 40, n° 4, 1992, p. 653–662.

[DUT 03] Dutta B., Palmiere E.
Effect of prestrain and deformation temperature on the recrystallization behavior of steels microalloyed with niobium. *Metallurgical and Materials Transactions A*, vol. 34, n° 6, 2003, p. 1237–1247.

[DŽU 04] Džubinskỳ M., Husain Z., Van Haaften W.
Comparison of recrystallisation kinetics determined by stress relaxation, double hit, optical metallography and EBSD approaches. *Materials characterization*, vol. 52, n° 2, 2004, p. 93–102.

[FAN 03] Fang X., Fan Z., Ralph B., Evans P., Underhill R.
Effects of tempering temperature on tensile and hole expansion properties of a C–Mn steel. *Journal of materials processing technology*, vol. 132, n° 1-3, 2003, p. 215–218.

[FEI 23] Feild A.
Some effects of zirconium in steel. *Trans. Am. Inst. Mining Met. Eng*, vol. 69, 1923, p. 848–894.

[FIE 13] Fielding L.
The bainite controversy. *Materials Science and Technology*, vol. 29, n° 4, 2013, p. 383–399.

[FON 15] Fonstein N.
Complex Phase Steels. *Advanced High Strength Sheet Steels*, p. 241–258 2015.

[FRO 82] Frost H. J., Ashby M. F.
Deformation mechanism maps: the plasticity and creep of metals and ceramics. 1982.

[FUJ 95] Fujiwara K., Okaguchi S., Ohtani H.
Effect of hot deformation on bainite structure in low carbon steels. *ISIJ international*, vol. 35, n° 8, 1995, p. 1006–1012.

[FUN 04] Funakawa Y., Shiozaki T., Tomita K., Yamamoto T., Maeda E.
Development of high strength hot-rolled sheet steel consisting of ferrite and nanometer-sized carbides. *ISIJ international*, vol. 44, n° 11, 2004, p. 1945–1951.

[Gó 02] Gómez M., Medina S. F., Quispe A., Valles P.
Static Recrystallization and Induced Precipitation in a Low Nb Microalloyed Steel. *ISIJ International*, vol. 42, n° 4, 2002, p. 423–431.

[GAR 01] Garcia-Mateo C., Lopez B., Rodriguez-Ibabe J.
Static recrystallization kinetics in warm worked vanadium microalloyed steels. *Materials Science and Engineering: A*, vol. 303, n° 1-2, 2001, p. 216–225.

[GIU 99] Giumelli A. K., Militzer M., Hawbolt E. B.
Analysis of the Austenite Grain Size Distribution in Plain Carbon Steels. *ISIJ International*, vol. 39, n° 3, 1999, p. 271–280.

[GLA 02] Gladman T.
The physical metallurgy of microalloyed steels. N° 792 Book / The Institute of Materials Maney, London, 2002.

[GÓM 05] Gómez M., Medina S. F., Valles P.
Determination of driving and pinning forces for static recrystallization during hot rolling of a niobium microalloyed steel. *ISIJ international*, vol. 45, n° 11, 2005, p. 1711–1720.

[GÓM 07] Gómez M., Medina S. F., Chaves J.
Static recrystallization of austenite in a medium-carbon vanadium microalloyed steel and inhibition by strain-induced precipitates. *Materials science forum*, vol. 550 Trans Tech Publ, 2007, p. 417–422.

[GOR 11] Gorni A. A.
Steel forming and heat treating handbook. *Sao Vicente, Brazil*, vol. 24, 2011.

[GRA 09] Gražulis S., Chateigner D., Downs R. T., Yokochi A. F. T., Quirós M., Lutterotti L., Manakova E., Butkus J., Moeck P., Le Bail A.
Crystallography Open Database – an open-access collection of crystal structures. *Journal of Applied Crystallography*, vol. 42, n° 4, 2009, p. 726–729.

[HAL 63] Halliday W. I.
Determination of the austenitic grain size of steel using a thermal etching method. ISI Special Report n° 81, 1963, Iron and Steel Institute, London.

[HAL 70] Hall E. .
Yield point phenomena in metals and alloys. Plenum Press, 1970.

[HAS 04] Hasegawa K., Kawamura K., Urabe T., Hosoya Y.
Effects of microstructure on stretch-flange-formability of 980 MPa grade cold-rolled ultra high

strength steel sheets. *ISIJ international*, vol. 44, n° 3, 2004, p. 603–609.

[HEH 72] Hehemann R., Kinsman K., Aaronson H.
A debate on the bainite reaction. *Metallurgical Transactions*, vol. 3, n° 5, 1972, p. 1077–1094.

[HER 14] Hersent E., Marthinsen K., Nes E.
On the Effect of Atoms in Solid Solution on Grain Growth Kinetics. *Metallurgical and Materials Transactions A*, vol. 45, n° 11, 2014, p. 4882–4890.

[HIL 95] Hillert M.
The nature of bainite. *ISIJ international*, vol. 35, n° 9, 1995, p. 1134–1140.

[HIL 02] Hillert M.
Preface to the viewpoint set on: bainite. *Scripta Materialia*, vol. 47, n° 3, 2002, p. 137–138.

[HIL 10] Hillert M., Borgenstam A., Ågren J.
Do bainitic and Widmanstätten ferrite grow with different mechanisms? *Scripta Materialia*, vol. 62, n° 2, 2010, p. 75–77.

[HIL 15] Hilditch T., de Souza T., Hodgson P.
Properties and automotive applications of advanced high-strength steels (AHSS). *Welding and Joining of Advanced High Strength Steels (AHSS)*, p. 9–28 Elsevier, 2015.

[HIS 12] Hisker F., Thiessen R., Heller T.
Influence of microstructure on damage in advanced high strength steels. *Materials Science Forum*, vol. 706 Trans Tech Publ, 2012, p. 925–930.

[HOM 13] Homsher C. N.
Determination of the non-recrystallization Temperature (Tnr) in multiple Microalloyed steels. PhD thesis, Colorado School of Mines. Arthur Lakes Library, 2013.

[HON 02] Hong S., Kang K., Park C.
Strain-induced precipitation of NbC in Nb and Nb–Ti microalloyed HSLA steels. *Scripta materialia*, vol. 46, n° 2, 2002, p. 163–168.

[HU 15] Hu H., Xu G., Wang L., Xue Z., Zhang Y., Liu G.
The effects of Nb and Mo addition on transformation and properties in low carbon bainitic steels. *Materials & Design*, vol. 84, 2015, p. 95–99, Elsevier.

[HUA 16a] Huang K., Logé R.
A review of dynamic recrystallization phenomena in metallic materials. *Materials & Design*, vol. 111, 2016, p. 548–574.

[HUA 16b] Huang K., Logé R.
Zener Pinning. *Reference Module in Materials Science and Materials Engineering* Elsevier, 2016.

[HUM 17] Humphreys F. J., Rohrer G. S., Rollett A. D.
Recrystallization and related annealing phenomena. Elsevier, Amsterdam Oxford Cambridge, MA, third edition édition, 2017.

[JHA 11] Jha G., Haldar A., Bhaskar M., Venugopalan T.
Development of high strength hot rolled steel sheet for wheel disc application. *Materials Science and Technology*, vol. 27, n° 7, 2011, p. 1131–1137.

[JHA 12] Jha G., Das S., Lodh A., Haldar A.
Development of hot rolled steel sheet with 600 MPa UTS for automotive wheel application. *Materials science and engineering: A*, vol. 552, 2012, p. 457–463.

[JOS 88] Josefsson B., Andrén H.-O.
Microstructure of granular bainite. *Le Journal de Physique Colloques*, vol. 49, n° C6, 1988, p. C6–293.

[JUN 06] Jun H., Kang J., Seo D., Kang K., Park C.
Effects of deformation and boron on microstructure and continuous cooling transformation in low carbon HSLA steels. *Materials Science and Engineering: A*, vol. 422, n° 1-2, 2006, p. 157–162.

[KAI 17] Kaijalainen A., Kesti V., Vierelä R., Ylitolva M., Porter D., Kömi J.
The effect of microstructure on the sheared edge quality and hole expansion ratio of hot-rolled 700 MPa steel. *Journal of Physics: Conference Series*, vol. 896 IOP Publishing, 2017, Page 012103.

[KAM 12] Kamibayashi K., Tanabe Y., Takemoto Y., Shimizu I., Senuma T.
Influence of Ti and Nb on the strength–ductility–hole expansion ratio balance of hot-rolled low-carbon high-strength steel sheets. *ISIJ international*, vol. 52, n° 1, 2012, p. 151–157.

[KAR 95] Karjalainen L. P.
Stress relaxation method for investigation of softening kinetics in hot deformed steels. *Materials Science and Technology*, vol. 11, n° 6, 1995, p. 557–565.

[KAR 09] Karelova A., Krempaszky C., Werner E., Tsipouridis P., Hebesberger T., Pichler A.
Hole Expansion of Dual-phase and Complex-phase AHS Steels-Effect of Edge Conditions. *steel research international*, vol. 80, n° 1, 2009, p. 71–77.

[KAR 14] Karmakar A., Kundu S., Roy S., Neogy S., Srivastava D., Chakrabarti D.
Effect of microalloying elements on austenite grain growth in Nb–Ti and Nb–V steels. *Materials Science and Technology*, vol. 30, n° 6, 2014, p. 653–664.

[KAR 15] Karthikeyan T., Dash M. K., Saroja S., Vijayalakshmi M.
Estimation of martensite feature size in a low-carbon alloy steel by microtexture analysis of boundaries. *Micron*, vol. 68, 2015, p. 77–90.

[KAU 90] Kaur I., Gust W.
12.2.4 Interphase boundary tracer diffusion, p. 669–670. Springer Berlin Heidelberg, Berlin, Heidelberg, 1990.

[KIM 13] Kim H. C., Wallington T. J.
Life-cycle energy and greenhouse gas emission benefits of lightweighting in automobiles: review and harmonization. *Environmental science & technology*, vol. 47, n° 12, 2013, p. 6089–6097, ACS Publications.

[KOL 15] Kollamthodi S., Kay D., Skinner I., Dun C., Hausberger S.
The potential for mass reduction of passenger cars and light commercial vehicles in relation to future CO2 regulatory requirements. Report for the European Commission – DG Climate Action, 2015, Ricardo-AEA, Transport and Environmental Policy Research.

[KON 06] Kong J., Xie C.
Effect of molybdenum on continuous cooling bainite transformation of low-carbon microalloyed steel. *Materials & design*, vol. 27, n° 10, 2006, p. 1169–1173, Elsevier.

[KWO 10] Kwon O. J., Lee K. Y., Kim G. S., Chin K. G.
New Trends in Advanced High Strength Steel Developments for Automotive Application. *Materials Science Forum*, vol. 638-642, 2010, p. 136–141.

[LAA 91] Laasraoui A., Jonas J.
Recrystallization of austenite after deformation at high temperatures and strain rates—analysis and modeling. *Metallurgical Transactions A*, vol. 22, n° 1, 1991, p. 151–160.

[LEE 08a] Lee S.-J., Lee Y.-K.
Prediction of austenite grain growth during austenitization of low alloy steels. *Materials & Design*, vol. 29, n° 9, 2008, p. 1840–1844.

[LEE 08b] Lee S.-J., Park J.-S., Lee Y.-K.
Effect of austenite grain size on the transformation kinetics of upper and lower bainite in a low-alloy steel. *Scripta Materialia*, vol. 59, n° 1, 2008, p. 87–90.

[LEE 12] Lee J., Lee S.-J., De Cooman B. C.
Effect of micro-alloying elements on the stretch-flangeability of dual phase steel. *Materials Science and Engineering: A*, vol. 536, 2012, p. 231–238, Elsevier.

[LIN 08] Lin Y., Chen M.-S., Zhong J.
Study of static recrystallization kinetics in a low alloy steel. *Computational Materials Science*, vol. 44, n° 2, 2008, p. 316–321.

[LIU 88a] Liu W., Jonas J.
A stress relaxation method for following carbonitride precipitation in austenite at hot working temperatures. *Metallurgical transactions A*, vol. 19, n° 6, 1988, p. 1403–1413.

[LIU 88b] Liu W., Jonas J.
Ti (CN) precipitation in microalloyed austenite during stress relaxation. *Metallurgical Transactions A*, vol. 19, n° 6, 1988, p. 1415–1424.

[LIU 12] Liu W.
A review of the stress-relaxation method for following the kinetics of precipitation, recovery and recrystallization. *Materials Science Forum*, vol. 706 Trans Tech Publ, 2012, p. 2758–2763.

[LU 11] Lu J., Wiskel J. B., Omotoso O., Henein H., Ivey D. G.
Matrix dissolution techniques applied to extract and quantify precipitates from a microalloyed steel. *Metallurgical and Materials Transactions A*, vol. 42, n° 7, 2011, p. 1767–1784.

[MAA 12] Maalekian M., Radis R., Militzer M., Moreau A., Poole W.
In situ measurement and modelling of austenite grain growth in a Ti/Nb microalloyed steel. *Acta Materialia*, vol. 60, n° 3, 2012, p. 1015–1026.

[MAN 96a] Manohar P. A., Dunne D. P., Chandra T., Killmore C. R.
Grain Growth Predictions in Microalloyed Steels. *ISIJ International*, vol. 36, n° 2, 1996, p. 194–200.

[MAN 96b] Manohar P., Chandra T., CR K.
Continuous cooling transformation behaviour of microalloyed steels containing Ti, Nb, Mn and Mo. *ISIJ international*, vol. 36, n° 12, 1996, p. 1486–1493.

[MAN 98] Manohar P. A., Ferry M., Chandra T.
Five Decades of the Zener Equation. *ISIJ International*, vol. 38, n° 9, 1998, p. 913–924.

[MAT 09] Matlock D. K., Speer J. G.
Third Generation of AHSS: Microstructure Design Concepts. Haldar A., Suwas S., Bhattacharjee D., Eds., *Microstructure and Texture in Steels*, p. 185–205 Springer London, London, 2009.

[MAT 12] Matlock D. K., Speer J. G., De Moor E., Gibbs P. J.
Recent Developments In Advanced Hıgh Strength Sheet Steels For Automotıve Applıcatıons: An Overvıew. *Jestech*, vol. 15, n° 1, 2012, p. 1–12.

[MAU 04] Maugis P., Lanteri S., Ravaine D., Barges P., Gouné M., Bi Y., Lamberigts M., Siwecki T.
Development of Methods for the Characterisation and Modelling of Precipitation in Steels. *EUR*, , n° 20938, 2004, p. 1–230, European Commission.

[MED 91] Medina S. F., Fabregue P.
Activation energy in the static recrystallization of austenite. *Journal of materials Science*, vol. 26, n° 20, 1991, p. 5427–5432.

[MED 93] Medina S. F., Mancilla J. E., Hernandez C. A.
Influence of vanadium on the static recrystallization of austenite in microalloyed steels. *Journal of materials science*, vol. 28, n° 19, 1993, p. 5317–5324.

[MED 01] Medina S. F., Quispe A.
Improved Model for Static Recrystallization Kinetics of Hot Deformed Austenite in Low Alloy and Nb/V Microalloyed Steels. *ISIJ International*, vol. 41, n° 7, 2001, p. 774–781.

[MIL 12] Miller M. K., Kelly T. F., Rajan K., Ringer S. P.
The future of atom probe tomography. *Materials Today*, vol. 15, n° 4, 2012, p. 158–165.

[MIL 13] Militzer M., Garcin T., Poole W. J.
In Situ Measurements of Grain Growth and Recrystallization by Laser Ultrasonics. *Materials Science Forum*, vol. 753 Trans Tech Publ, 2013, p. 25–30.

[MIR 11] Mirzadeh H., Cabrera J. M., Najafizadeh A.
Constitutive relationships for hot deformation of austenite. *Acta materialia*, vol. 59, n° 16, 2011, p. 6441–6448, Elsevier.

[MOB] Thermo-Calc Software MOBFE3 Steels/Fe-alloys mobility database (accessed 30 July 2018).

[MOD 14] Modaresi R., Pauliuk S., Løvik A. N., Müller D. B.
Global Carbon Benefits of Material Substitution in Passenger Cars until 2050 and the Impact on the Steel and Aluminum Industries. *Environmental Science & Technology*, vol. 48, n° 18, 2014, p. 10776–10784.

[MOO 16] Moody M. P., Vella A., Gerstl S. S., Bagot P. A.
Advances in atom probe tomography instrumentation: Implications for materials research. *MRS*

bulletin, vol. 41, n° 1, 2016, p. 40–45.

[MUL 57] Mullins W. W.
Theory of Thermal Grooving. *Journal of Applied Physics*, vol. 28, n° 3, 1957, p. 333–339.

[NAN 16] Nanda T., Singh V., Singh V., Chakraborty A., Sharma S.
Third generation of advanced high-strength steels: Processing routes and properties. *Proceedings of the Institution of Mechanical Engineers, Part L: Journal of Materials: Design and Applications*, , 2016.

[NES 85] Nes E., Ryum N., Hunderi O.
On the Zener drag. *Acta Metallurgica*, vol. 33, n° 1, 1985, p. 11–22.

[PAL 94] Palmiere E., Garcia C., De Ardo A.
Compositional and microstructural changes which attend reheating and grain coarsening in steels containing niobium. *Metallurgical and Materials Transactions A*, vol. 25, n° 2, 1994, p. 277–286.

[PAN 05] Pandit A., Murugaiyan A., Podder A. S., Haldar A., Bhattacharjee D., Chandra S., Ray R.
Strain induced precipitation of complex carbonitrides in Nb–V and Ti–V microalloyed steels. *Scripta materialia*, vol. 53, n° 11, 2005, p. 1309–1314.

[PAT 92] Patterson B. R., Liu Y.
Relationship between grain. *Metallurgical Transactions A*, vol. 23, n° 9, 1992, p. 2481–2482.

[PAT 17] Pathak N., Butcher C., Worswick M., Bellhouse E., Gao J.
Damage evolution in complex-phase and dual-phase steels during edge stretching. *Materials*, vol. 10, n° 4, 2017, Page 346, Multidisciplinary Digital Publishing Institute.

[PEE 06] Peet M., Bhadeshia H.
Program MAP_STEEL_MUCG83. *Materials Algorithms Project. Information on http://www.msm.cam.ac.uk/map/steel/programs/mucg83.html*, , 2006.

[PER 05] Perez M.
Gibbs-Thomson effects in phase transformations. *Scripta Materialia*, vol. 52, n° 8, 2005, p. 709–712.

[PER 08] Perez M., Dumont M., Acevedo-Reyes D.
Implementation of classical nucleation and growth theories for precipitation. *Acta Materialia*, vol. 56, n° 9, 2008, p. 2119–2132.

[PER 09] Perez M., Dumont M., Acevedo-Reyes D.
Corrigendum to "Implementation of classical nucleation and growth theories for precipitation" [Acta Materialia 56 (2008) 2119–2132]. *Acta Materialia*, vol. 57, n° 4, 2009, Page 1318.

[PIC 92] Pickering F. B.
High Strength Low Alloy Steels. *Constitution and Properties of Steels*, Materials Science and Technology, p. 335–400 Wiley-VCH Verlag GmbH & Co. KGaA, Weinheim, Germany, 1992.

[POR 92] Porter D., Easterling K.Phase Transformations in Metals and Alloys, 1992.

[QUI 02] Quidort D., Bréchet Y.
The role of carbon on the kinetics of bainite transformation in steels. *Scripta Materialia*, vol. 47, n° 3, 2002, p. 151–156.

[RAZ 12] Razzak M. A., Perez M., Sourmail T., Cazottes S., Frotey M.
A Simple Model for Abnormal Grain Growth. *ISIJ International*, vol. 52, n° 12, 2012, p. 2278–2282.

[RAZ 14] Razzak M. A., Perez M., Sourmail T., Cazottes S., Frotey M.
Preventing Abnormal Grain Growth of Austenite in Low Alloy Steels. *ISIJ International*, vol. 54, n° 8, 2014, p. 1927–1934.

[RIO 87] Rios P.
Overview no. 62: A theory for grain boundary pinning by particles. *Acta Metallurgica*, vol. 35, n° 12, 1987, p. 2805–2814.

[RIO 96] Rios P.
On the relationship between pinning force and limiting grain radius. *Scripta Materialia*, vol. 34, n° 8, 1996, p. 1185–1188.

[RIO 04] Rios P., Fonseca G.
Grain boundary pinning by Al6Mn precipitates in an Al–1wt%Mn alloy. *Scripta Materialia*, vol. 50, n° 1, 2004, p. 71–75.

[RIO 10] Rios P. R., Fonseca G. C.
Grain Boundary Pinning by Particles. *Materials Science Forum*, vol. 638-642, 2010, p. 3907–3912.

[RIO 18] Rios P. R., Zöllner D.
Grain growth – unresolved issues. *Materials Science and Technology*, vol. 34, n° 6, 2018, p. 629–638.

[ROB 29] Robertson J.
The microstructure of rapidly cooled steel. *J. Iron Steel Inst*, vol. 119, 1929, p. 391–424.

[RON 92] Rong W., Andrén H.-O., Wisell H., Dunlop G.
The role of alloy composition in the precipitation behaviour of high speed steels. *Acta metallurgica et materialia*, vol. 40, n° 7, 1992, p. 1727–1738.

[RYD 06] Ryde L.
Application of EBSD to analysis of microstructures in commercial steels. *Materials science and technology*, vol. 22, n° 11, 2006, p. 1297–1306.

[RYD 10] Ryde L., Lyytinen O., Peura P., Titova M., Granbom Y. V., Hebesberger T.
Cold-rolled complex-phase (CP) steel grades with optimised bendability, stretch-flangeability and anisotropy (CP-Steels). *European Commission Research Fund for Coal and Steel, Directorate-General for Research and Innovation*, , 2010, Page 10.

[Sal 19a] Salzgitter AG. Initiative Automotive : Applications : Chassis. https://www.initiative-automotive.de/en/applications/chassis. Accessed 2019-07-11., 2019.

[Sal 19b] Salzgitter AG. Initiative Automotive : Products : Hot and cold rolled flat products : Materials : xpand. https://www.initiative-automotive.de/en/products/hot-and-cold-rolled-flat-products/materials/xpandr.html. Accessed 2019-07-11., 2019.

[SAN 10] San Martín D., Palizdar Y., Cochrane R., Brydson R., Scott A.
Application of Nomarski differential interference contrast microscopy to highlight the prior austen-

ite grain boundaries revealed by thermal etching. *Materials Characterization*, vol. 61, n° 5, 2010, p. 584–588.

[SCH 08] Schneider A., Stallybrass C., Konrad J., Kulgemeyer A., Meuser H., Meimeth S.
Formation of primary TiN precipitates during solidification of microalloyed steels – Scheil versus DICTRA simulations. *International Journal of Materials Research*, vol. 99, n° 6, 2008, p. 674–679.

[SCH 12] Schindelin J., Arganda-Carreras I., Frise E., Kaynig V., Longair M., Pietzsch T., Preibisch S., Rueden C., Saalfeld S., Schmid B., Tinevez J.-Y., White D. J., Hartenstein V., Eliceiri K., Tomancak P., Cardona A.
Fiji: an open-source platform for biological-image analysis. *Nature Methods*, vol. 9, n° 7, 2012, p. 676–682.

[SEL 79] Sellars C. M., Whiteman J. A.
Recrystallization and grain growth in hot rolling. *Metal Science*, vol. 13, n° 3-4, 1979, p. 187–194.

[SEN 01] Senuma T.
Physical metallurgy of modern high strength steel sheets. *ISIJ international*, vol. 41, n° 6, 2001, p. 520–532.

[SHE 18] Shen W., Zhang C., Zhang L., Xu Q., Cui Y., Xu Y.
A modified Avrami equation for kinetics of static recrystallization of Nb-V microalloyed steel: Experiments and numerical simulation. *Vacuum*, vol. 150, 2018, p. 116–123.

[SHO 04] Shome M., Gupta O., Mohanty O.
A modified analytical approach for modelling grain growth in the coarse grain HAZ of HSLA steels. *Scripta Materialia*, vol. 50, n° 7, 2004, p. 1007–1010.

[SIN 96] Singh S., Bhadeshia H.
Quantitative evidence for mechanical stabilization of bainite. *Materials science and technology*, vol. 12, n° 7, 1996, p. 610–612.

[SIN 98] Singh S. B.
Phase transformations from deformed austenite. PhD thesis, University of Cambridge, 1998.

[SIW 92] Siwecki T.
Modelling of Microstructure Evolution during Recrystallization Controlled Rolling. *ISIJ International*, vol. 32, n° 3, 1992, p. 368–376.

[SMI 48] Smith C. S.
Grains, phases, and interfaces: An interpretation of microstructure. *Trans. Metall. Soc. AIME*, vol. 175, 1948, p. 15–51.

[SMI 71] Smith Y., Siebert C.
Continuous cooling transformation kinetics of thermomechanically worked low-carbon austenite. *Metallurgical Transactions*, vol. 2, n° 6, 1971, p. 1711–1725.

[SUD 83] Sudo M., HASHIMOTO S.-i., KAMBE S.
Niobium bearing ferrite-bainite high strength hot-rolled sheet steel with improved formability. *Transactions of the Iron and Steel Institute of Japan*, vol. 23, n° 4, 1983, p. 303–311.

[TAK 03] Takahashi M.
Development of high strength steels for automobiles. *NIPPON STEEL TECHNICAL REPORT*, vol. 88, 2003, p. 2–7, NIPPON STEEL CORPORATION.

[TAY 14] Taylor M. D., Choi K. S., Sun X., Matlock D. K., Packard C., Xu L., Barlat F.
Correlations between nanoindentation hardness and macroscopic mechanical properties in DP980 steels. *Materials Science and Engineering: A*, vol. 597, 2014, p. 431–439, Elsevier.

[TCF] Thermo-Calc Software TCFE8 Steels/Fe-alloys database (accessed 30 July 2018).

[TSA 17] Tsai S.-P., Su T.-C., Yang J.-R., Chen C.-Y., Wang Y.-T., Huang C.-Y.
Effect of Cr and Al additions on the development of interphase-precipitated carbides strengthened dual-phase Ti-bearing steels. *Materials & Design*, vol. 119, 2017, p. 319–325.

[TSI 06] Tsipouridis P., Werner E., Krempaszky C., Tragl E.
Formability of High Strength Dual-phase Steels. *steel research international*, vol. 77, n° 9-10, 2006, p. 654–667.

[UHM 04] Uhm S., Moon J., Lee C., Yoon J., Lee B.
Prediction Model for the Austenite Grain Size in the Coarse Grained Heat Affected Zone of Fe-C-Mn Steels: Considering the Effect of Initial Grain Size on Isothermal Growth Behavior. *ISIJ International*, vol. 44, n° 7, 2004, p. 1230–1237.

[VED 17] Vedlugaitė D., European Environment Agency
Monitoring CO2 emissions from new passenger cars and vans in 2016. Eea report, 2017.

[VER 10a] Vervynckt S., Verbeken K., Thibaux P., Houbaert Y.
Characterization of the Austenite Recrystallization by Comparing Double Deformation and Stress Relaxation Tests. *steel research international*, vol. 81, n° 3, 2010, p. 234–244.

[VER 10b] Vervynckt S., Verbeken K., Thibaux P., Houbaert Y.
Characterization of the austenite recrystallization by comparing double deformation and stress relaxation tests. *steel research international*, vol. 81, n° 3, 2010, p. 234–244.

[VER 12] Vervynckt S., Verbeken K., Lopez B., Jonas J. J.
Modern HSLA steels and role of non-recrystallisation temperature. *International Materials Reviews*, vol. 57, n° 4, 2012, p. 187–207.

[WAG 05] Wagner R., Kampmann R., Voorhees P. W.
Homogeneous Second-Phase Precipitation. Kostorz G., Ed., *Phase Transformations in Materials*, p. 309–407 Wiley-VCH Verlag GmbH & Co. KGaA, Weinheim, FRG, 2005.

[WAN 14] Wang X.-p., Zhao A.-m., Zhao Z.-z., Huang Y., Li L., He Q.
Mechanical properties and characteristics of nanometer-sized precipitates in hot-rolled low-carbon ferritic steel. *International Journal of Minerals, Metallurgy, and Materials*, vol. 21, n° 3, 2014, p. 266–272.

[WEI 18] Weissensteiner I., Suppan C., Hebesberger T., Winkelhofer F., Clemens H., Maier-Kiener V.
Effect of Morphological Differences on the Cold Formability of an Isothermally Heat-Treated Advanced High-Strength Steel. *JOM*, vol. 70, n° 8, 2018, p. 1567–1575.

[WIL 09] Williams D. B., Carter C. B.
22.4 Z-Contrast. *Transmission electron microscopy: a textbook for materials science* Springer, New York, 2. ed édition, 2009. OCLC: 254591841.

[WYC 63] Wyckoff R. W. G.
Crystal Structures. Interscience Publishers, New York, 1963.

[XU 12] Xu Y., Tang D., Song Y., Pan X.
Prediction model for the austenite grain growth in a hot rolled dual phase steel. *Materials & Design (1980-2015)*, vol. 36, 2012, p. 275–278.

[YAM 82] Yamamoto S., Ouchi C., Osuka T.
Thermomechanical processing of microalloyed austenite. *Ed. AJ DeArdo, GA Ratz, PJ Wray, The Metallurgical Society of AIME, Warrendale, PA*, , 1982, Page 613.

[YAM 95] Yamamoto S., Yokoyama H., Yamada K., Niikura M.
Effects of the austenite grain size and deformation in the unrecrystallized austenite region on bainite transformation behavior and microstructure. *ISIJ international*, vol. 35, n° 8, 1995, p. 1020–1026.

[YAN 06] Yan W., Shan Y., Yang K.
Effect of TiN finclusions on the impact toughness of low-carbon microalloyed steels. *Metallurgical and Materials Transactions A*, vol. 37, n° 7, 2006, p. 2147–2158, Springer.

[YAN 14] Yang G.-w., Sun X.-j., Yong Q.-l., Li Z.-d., Li X.-x.
Austenite Grain Refinement and Isothermal Growth Behavior in a Low Carbon Vanadium Microalloyed Steel. *Journal of Iron and Steel Research, International*, vol. 21, n° 8, 2014, p. 757–764.

[YON 89] YONG Q., LI Y., SUN Z., WU B.
Theoretical Calculation of Specific Interfacial Energy of Semicoherent Interface between Microalloy Carbonitrides and Austenite. *Interface*, vol. 1, 1989, Page 1.

[YOO 16] Yoon J. I., Jung J., Lee H. H., Kim G.-S., Kim H. S.
Factors governing hole expansion ratio of steel sheets with smooth sheared edge. *Metals and Materials International*, vol. 22, n° 6, 2016, p. 1009–1014.

[ZAJ 05a] Zajac S., Komenda J., Morris P., Dierickx P., Matera S., Penalba Diaz F.Quantitative structure-property relationships for complex bainitic microstructures, 2005.

[ZAJ 05b] Zajac S., Schwinn V., Tacke K.
Characterisation and quantification of complex bainitic microstructures in high and ultra-high strength linepipe steels. *Materials Science Forum*, vol. 500 Trans Tech Publ, 2005, p. 387–394.

[ZAK 09] Zakerinia H., Kermanpur A., Najafizadeh A.
Color metallography; a suitable method for characterization of martensite and bainite in multiphase steels. *International Journal of Iron & Steel Society of Iran*, vol. 6, n° 1, 2009, p. 14–18, Iron & Steel Society of Iran.

[ZHA 03] Zhao M.-C., Yang K., Xiao F.-R., Shan Y.-Y.
Continuous cooling transformation of undeformed and deformed low carbon pipeline steels. *Materials Science and Engineering: A*, vol. 355, n° 1-2, 2003, p. 126–136.

[ZHA 09] Zhang M.-X., Kelly P.
The morphology and formation mechanism of pearlite in steels. *Materials Characterization*, vol. 60, n° 6, 2009, p. 545–554.

[ZHA 11] Zhang S., Li M., Liu Y., Luo J., Liu T.
The growth behavior of austenite grain in the heating process of 300M steel. *Materials Science and Engineering: A*, vol. 528, n° 15, 2011, p. 4967–4972.

[ZUR 01] Zurob H., Brechet Y., Purdy G.
A model for the competition of precipitation and recrystallization in deformed austenite. *Acta materialia*, vol. 49, n° 20, 2001, p. 4183–4190.

[ZUR 02] Zurob H., Hutchinson C., Brechet Y., Purdy G.
Modeling recrystallization of microalloyed austenite: effect of coupling recovery, precipitation and recrystallization. *Acta materialia*, vol. 50, n° 12, 2002, p. 3077–3094.

[ZUR 03] Zurob H.
Effects of precipitation, recovery and recrystallization on the microstructural evolution of microalloyed austenite. PhD thesis, McMaster University, 2003.

FOLIO ADMINISTRATIF

THESE DE L'UNIVERSITE DE LYON OPEREE AU SEIN DE L'INSA LYON

NOM : GRAUX DATE de SOUTENANCE : le 13 Décembre 2019

Prénoms: Alexis

TITRE : Microstructure evolution during hot rolling of low carbon microalloyed steels

NATURE : Doctorat Numéro d'ordre : 2019LYSEI120

École doctorale : ED 34 Matériaux de Lyon

Spécialité: Matériaux

RÉSUMÉ :

There are nowadays major driving forces for the development of Advanced High Strength steels presenting enhanced formability properties for automotive applications. This PhD-work is part of a research project that aims at producing complex phase (CP) steels by hot rolling, seeking for an enhanced combination of strength and stretch flangeability. Thus, this PhD-work focused on the description and the understanding of the microstructural evolutions during the various steps of the hot rolling process of low carbon microalloyed steels.

First, the evolution of the precipitation state and austenite grain sizes during the reheating stage of hot rolling were studied. A precipitation model was developed and coupled to a simple grain growth model based on Zener pinning to describe microstructural evolutions that occurs during reheating.

Then, the microstructural evolutions occurring after the hot rolling deformation passes were analyzed. The kinetics of austenite recrystallization and strain-induced precipitation were determined by stress relaxation and direct microstructural observations. Models were also developed for describing these microstructural evolutions.

A final chapter focused on establishing the relationships between the hot rolling parameters, the microstructures, and the mechanical properties obtained. The phase transformation during continuous cooling was established, including the effect of austenite deformation. Then, six different hot rolling processes were applied, and the resulting microstructures and mechanical properties were extensively characterized.

This PhD-work provided a better understanding of the microstructural evolutions taking place during hot rolling and of the resulting microstructures and mechanical properties. The modeling work presented could extended to the study of other alloys. Several strategies for improving the combination of strength and stretch flangeability were proposed.

MOTS-CLÉS: Complex Phase steels, Hot rolling, Phase transformation, Precipitation, Recrystallization, Bainite.

Laboratoire (s) de recherche : MATEIS – UMR CNRS 5510
INSA de Lyon
25 Avenue Jean Capelle
69621 VILLEURBANNE CEDEX

Directeur de thèse : Sophie CAZOTTES (MCF), Michel PEREZ (PU) et Damien FABREGUE (PU).

Président de jury : Yves BRECHET (Professeur)

Composition du jury :

Sébastien ALLAIN	(Professeur)
Francisca G. CABALLERO	(Research Professor)
Carlos CAPDEVILA	(Research Scientist)
Frédéric DANOIX	(Directeur de recherches)